Air-sea momentum fluxes in the vicinity of the sea surface : a theoretical study of the coupling between turbulence and wind-waves

Alex Ayet

DOCTORAT SCIENCES BRETAGNE DE LA MER LOIRE ET DU LITTORAL

UBO Université de Bretagne Occidentale

THESE DE DOCTORAT DE

L'UNIVERSITE
DE BRETAGNE OCCIDENTALE

ECOLE DOCTORALE N° 598
Sciences de la Mer et du littoral
Spécialité : « *Océanographie physique et Environnement* »

Par

Alex AYET

Flux de quantité de mouvement à l'interface air-mer : Approche théorique du couplage entre turbulence et vagues de vent

Thèse présentée et soutenue à Plouzané, le 9 septembre 2020
Unités de recherche : Laboratoire d'Océanographie Physique et Spatiale/ Laboratoire de Météorologie Dynamique

Rapporteur.ice.s avant soutenance :

Luc DEIKE	Assistant professor, Princeton University, New Jersey
Bérengère DUBRULLE	Directrice de Recherche CNRS SPEC, Gif sur Yvette

Composition du Jury :

Président du Jury

Fabrice ARDHUIN	Directeur de recherche CNRS LOPS, Brest
Fleur COUVREUX	Chercheuse Météo-France CNRM, Toulouse
Luc DEIKE	Assistant professor, Princeton University
Bérengère DUBRULLE	Directrice de Recherche CNRS SPEC, Gif sur Yvette
Sarah GILLE	Full professor, Scripps Institution of Oceanography, California

Directeur de thèse

Jean-Luc REDELSPERGER	Directeur de recherche CNRS LOPS, Brest

Co-directeur de thèse

Guillaume LAPEYRE	Directeur de recherche CNRS LMD Paris

Invités

Co-encadrants de thèse:

Bertrand CHAPRON	Chercheur IFREMER LOPS, Brest
Louis MARIE	Chercheur IFREMER LOPS, Brest

REMERCIEMENTS

Je voudrais exprimer toute ma reconnaissance à celles et ceux qui, au travers d'échanges formels et informels, ont permis la construction du travail collectif qu'est cette thèse. Les allers-retours fréquents entre Brest et Paris, ainsi que les quelques séjours aux États-Unis m'ont permis, par la diversité des points de vue que j'y ai rencontrés, d'approcher un peu plus les nombreuses facettes, analytiques et poétiques, des vagues de vent.

Je tiens à remercier les deux rapporteur.ice.s Luc Deike et Bérengère Dubrulle pour avoir accepté de relire ce manuscrit, ainsi que Fabrice Ardhuin, Fleur Couvreux et Sarah Gille d'avoir accepté d'être membres du jury. Merci également à Olivier Kimmoun et à Roger Lewandoski d'avoir été membres du comité de suivi de thèse.

Merci aux participant.e.s de l'école de Physique des Houches et du programme de recherche KITP "Boundary Layers", deux évènements qui ont marqué mes années de thèse. En particulier, je tiens à remercier Freddy Bouchet, Tapio Schneider et Antoine Venaille pour l'organisation de ce premier évènement, et Baylor Fox-Kemper ainsi que Brad Marston pour m'avoir accueilli à Santa Barbara pendant le second. Ces deux séjours ont grandement contribué à forger mon intérêt pour le domaine, et ont amené de nombreuses collaborations passionnantes.

Je tiens également à remercier Gabriel Katul pour m'avoir accueilli dans son équipe. L'intensité du travail intellectuel qui a été fourni au cours de ce séjour a été une expérience très enrichissante, et la qualité de son accueil sans égal.

Cette thèse n'aurait pas eu lieu sans mes directeurs qui ont, chacun à leur façon, contribué à ce que ma curiosité pour l'interaction air-mer se transforme en une véritable fascination pour cette question, dont la (parfois désespérante) complexité à de quoi encore nourrir de nombreuses années de recherche. Au-delà de vos nombreuses qualités scientifiques, je tiens à vous remercier, Bertrand, Guillaume, Jean-Luc et Louis, pour votre bonne humeur, votre motivation, et la liberté que vous m'avez accordé.

Merci à mes collègues et ami.e.s de Scripps: Momme Hell, Bia Villas Bôas, Nick Pizzo, pour les nombreux moments passés ensemble, et pour les échanges scientifiques stimulants. Merci également à mes collègues et ami.e.s du LOPS pour ces années partagées: Gwendal, Hugo, Ivane, Luc, Léo, Lisa, Manuel, Marie, Sophia... La liste est trop longue pour me permettre d'être exhaustif.

Je remercie également mes colocataires brestois qui, malgré mes nombreux allers-retours, ont su offrir de nombreux moments de partage et d'échange.

Merci à mes parents Rita et Lluis pour l'ouverture d'esprit qu'ils ont su me transmettre au cours de toutes ces années, et, plus récemment, pour leur soutien pendant les périodes de rédaction.

Enfin merci, Jeanne, pour ta présence, et pour avoir su remettre en question, en perspective, de nombreux éléments de ma vie, et de mon rapport à la recherche.

Insomma, non si può osservare un'onda senza tener conto degli aspetti complessi che concorrono a formarla e di quelli altrettanto complessi a cui essa dà luogo. Questi aspetti variano continuamente, per cui un'onda è sempre diversa da un'altra onda; ma è anche vero che ogni onda è uguale a un'altra onda, anche se non immediatamente contigua o successiva; insomma ci sono delle forme e delle sequenze che si ripetono, sia pur distribuite irregolarmente nello spazio e nel tempo.

Italo Calvino, Palomar, lettura di un'onda, 1983.

RÉSUMÉ ÉTENDU EN FRANÇAIS

La compréhension du couplage entre turbulence et vagues de vent est essentielle pour la description des interactions air-mer, car celui-ci contrôle les flux de quantité de mouvement, de chaleur, d'humidité et de CO2: ceux-ci jouent un rôle clef dans les modèles de prévision numérique, autant aux échelles de la couche limite atmosphérique qu'aux échelles climatiques [Shimura et al., 2017]. L'influence des vagues de vent sur ces flux a été paramétrée à partir de mesures, sous la forme d'une relation non-linéaire entre le vent moyen et les flux turbulents à 10m de hauteur [par exemple, la paramétrisation COARE, Edson et al., 2013]. Cependant, malgré une bonne compréhension théorique de cette relation, lorsque moyennée sur différentes conditions de vent, de vagues et de courant, sa variabilité pour un vent moyen donné est mal expliquée. Cette compréhension pourrait être améliorée par un meilleur échantillonage des interactions air-mer pour différentes conditions environnementales. Cependant, du fait de la complexité des mesures en mer et de la difficulté à identifier des signaux reliés aux vagues [Hristov and Ruiz-Plancarte, 2014], la mise en place et l'interprétation de ces mesures nécessite également une compréhension théorique de la physique à l'interface air-mer [Villas Boas et al., 2019].

D'un point de vue théorique, la turbulence au-dessus des vagues de vent présente des caractéristiques uniques, comparée à la turbulence au-dessus d'autres obstacles tels que les collines et les tôles ondulées. Ceci provient de la nature multi-échelle et couplée de la surface de la mer. Comme le montre la figure 1, des vagues de différentes échelles spatiales interagissent avec le vent sur des échelles de temps différentes. Historiquement, ce couplage a été modélisé par la modification des lignes de courant moyennes, qui est qualitativement différente selon l'échelle de la vague (lignes de courant noires dans le plan (x,z) de la Fig. 1). Cette modification affecte la turbulence par le biais d'une interaction onde/champ moyen. Ces travaux théoriques ont été simplifiés pour guider le paramétrage du flux de quantité de mouvement uniquement en fonction de mesures moyennées de la turbulence et des statistiques des vagues, indépendantes de l'échelle. En particulier, l'accent a été mis sur l'analyse de la modification de la covariance des fluctuations turbulentes en présence de vagues et sur sa sensibilité à la stabilité dans le cadre de la théorie de similitude de Monin-Obukhov.

Cette approche moyennée capture une partie de la variabilité des flux de quantité de mouvement due à des variations de vent moyen et de stabilité, mais ne fournit d'informations ni

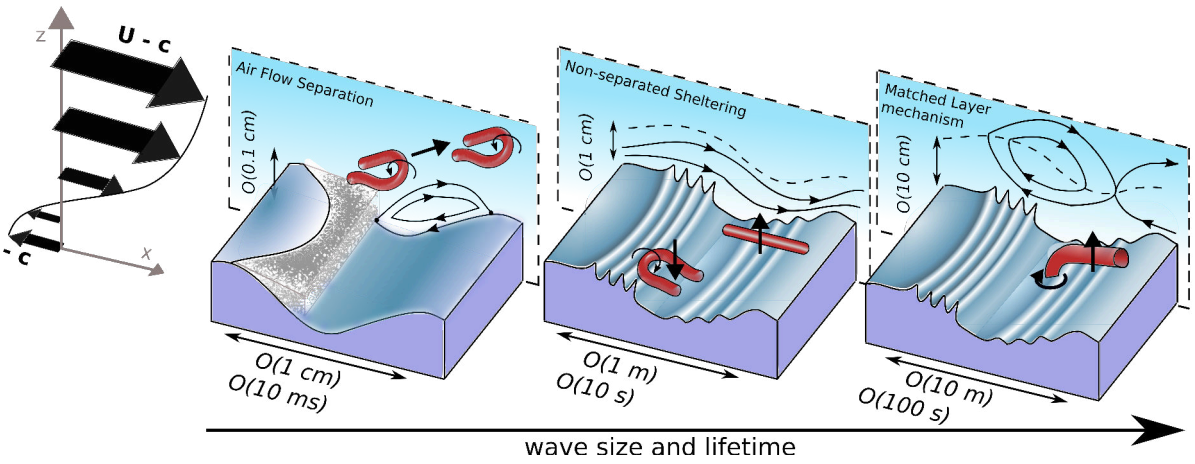

Figure 1: Schéma résumant le couplage multi-échelle entre le vent et les vagues, dans le référenciel en mouvement de ces dernières: **U** est la vitesse de vent moyenne et **c** est la vitesse de phase de la vague. Le schéma n'est pas à l'échelle. Les vagues de vent courtes (à gauche), interagissent avec la turbulence majoritairement à travers le déferlement. Les vagues de vent intermédiaires (au milieu) et longues (à droite) modulent la pente des vagues plus courtes, et leurs effets respectifs sur la turbulence sont qualitativement différents. Les traits noirs dans le plan (x,z) et les tubes de vorticité en rouge sont, respectivement, les lignes de courant affectées par les vagues et les structures cohérentes turbulentes.

sur leur dépendance aux échelles spatiales et temporelles du moyennage, ni sur leur sensibilité à d'autres paramètres environnementaux, tels que les courants et les fronts de température [Kudryavtsev et al., 2012, Wang et al., 2019]. En outre, des études numériques récentes ont montré que les vagues modifient directement les propriétés de la turbulence, par un autre biais que celui de l'interaction avec les lignes de courant déformées: elles affectent la forme des structures cohérentes qui la composent [voir, par exemple, Yang and Shen, 2009, et les tubes rouges dans la Fig. 1]. Toutes ces études questionnent les limites du cadre traditionnel présenté ci-dessus, et dans le Chapitre 1 de cette thèse, pour décrire les interactions entre le vent et les vagues et le développement de paramétrisations de flux turbulents.

L'objectif de cette thèse a été de revisiter ces modèles théoriques en étudiant la réorganisation des tourbillons énergétiques au-dessus d'une surface multi-échelle, mouvante et couplée (la surface de la mer). Les tourbillons énergétiques désignent ici ceux dont les propriétés déterminent les flux turbulents à une hauteur donnée. Cette question a été abordée en utilisant un modèle phénoménologique développé pour décrire la turbulence proche de paroi [Gioia et al., 2010, Katul et al., 2011]. Le Chapitre 2 de cette thèse s'attache à comprendre quelles sont les limites de ce modèle phénoménologique, en étudiant ses hypothèses physiques sous-jacentes pour une paroi lisse et des conditions de stabilité variables. Le modèle phénoménologique a ensuite été étendu au cas des vagues de vent longues et leur impact géométrique sur les tourbillons énergétiques (Chapitre 3) ainsi qu'au couplage dynamique de ces mêmes tourbillons avec des vagues courtes et déferlantes (Chapitre 4).

CHAPITRE 2: VERS UN LIEN SPECTRAL POUR LA VITESSE TURBULENTE VERTICALE?

Comme mentionné ci-dessus, dans cette thèse nous avons revisité l'interaction entre le vent et les vagues en utilisant un modèle phénoménologique, développé à l'origine pour décrire les modifications des propriétés moyennes de la turbulence proche d'un mur plat sous l'influence de la stabilité atmosphérique [Katul et al., 2011]. Ce modèle phénoménologique relie les mesures de spectres et co-spectres turbulents à des mesures de quantité de mouvement et de flux de chaleur. Ce lien est établi par un bilan spectral, c'est-à-dire un budget pour chaque longueur d'onde de la turbulence, qui implique de choisir des fermetures appropriées pour les termes composant ce bilan. La compréhension des implications de tels choix fait l'objet de ce chapitre.

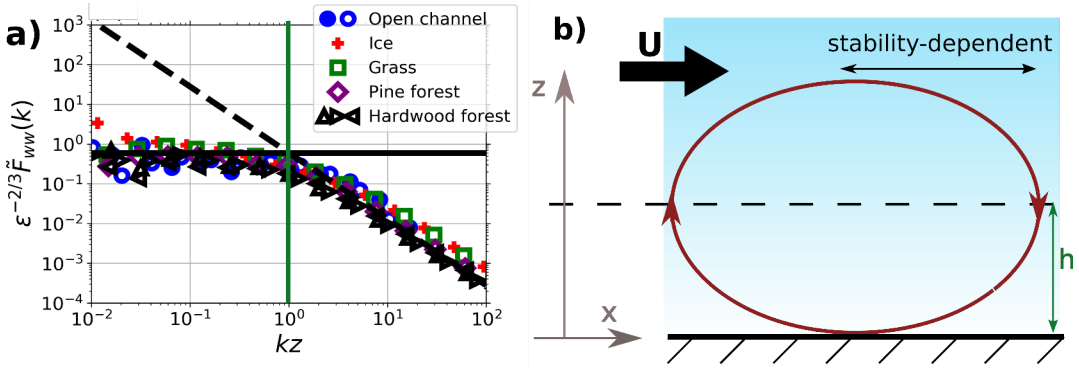

Figure 2: (a) Observations de spectres de vitesse verticale pour différents types de surfaces. Ces spectres révèlent l'existence de deux régimes (separés par la ligne verticale verte). (b) Représentation phénoménologique de la turbulence proche d'une paroi au travers d'un tourbillon représentatif (cercle rouge) dont la taille (en vert, **h**) correspond à la longueur d'onde séparant les deux régimes présentés dans (a), et détermine la dissipation d'énergie cinétique turbulente et le flux de quantité de mouvement à une hauteur donnée du mur (tirets horizontaux).

Dans un premier temps, nous avons proposé un budget spectral pour la vitesse turbulente verticale, qui permet de faire le lien entre son spectre et sa variance moyennée. La vitesse verticale est une grandeur qui devrait en effet être fortement affectée par la présence d'une paroi, puisque les mouvements verticaux sont inhibés par la présence d'une surface rigide horizontale. L'étude de ce budget a révélé que l'efficacité des tourbillons à redistribuer de l'énergie entre les différentes composantes turbulentes doit dépendre de leur échelle et des conditions de stabilité: ce résultat remet en question les fermetures standard [par exemple, Rotta, 1951], utilisées dans les modèles numériques ainsi que dans les budgets spectraux.

Ces résultats sont importants pour la modélisation, et montrent que des travaux théoriques sont encore nécessaires pour comprendre pleinement la dépendance de la vitesse turbulente verticale proche d'une paroi. Dans la deuxième partie du chapitre, nous avons donc étudié comment le budget spectral d'énergie cinétique turbulente peut être utilisé pour construire

un modèle phénoménologique qui permette de prédire les propriétés du spectre de la vitesse verticale en fonction de mesures moyennées. Le bilan d'énergie cinétique turbulente ne contient aucune information sur la redistribution de l'énergie entre les composantes turbulentes: il ne présente donc pas les problèmes rencontrés avec le bilan de vitesse verticale. Notre étude a ainsi montré que, pour que le budget soit suffisamment contraint pour reproduire les observations, il fallait prendre en compte la coupure du spectre aux hautes fréquences (coupure due à l'instrument de mesure utilisé).

Au cours de ce chapitre, nous avons donc étudié plusieurs budgets spectraux, visant à relier les propriétés spectrales de la turbulence à ses propriétés moyennées. Mais quelles propriétés spectrales avons-nous examinées? Près d'un mur, les spectres de vitesse turbulente présentent deux régimes: pour les petites échelles, un régime isotrope est atteint avec une dépendance en $k^{-5/3}$, alors que pour des grandes échelles la dépendance est en k^0 (voir la Fig. 2a, k étant le nombre d'onde dans la direction du flot moyen). La longueur d'onde à laquelle ce changement de pente se produit peut être vue comme la taille des tourbillons énergétiques mentionnés ci-dessus, qui détermine le flux de quantité de mouvement à une distance donnée de la paroi (voir la Fig. 2b). Ces tourbillons sont attachés à la paroi, et leur taille correspond à la hauteur à laquelle les flux sont calculés. Dans la suite de la thèse, nous avons utilisé cette représentation phénoménologique des flux de quantité de mouvement pour étudier l'effet des vagues sur les propriétés moyennes de la turbulence.

Chapitre 3: L'impact géométrique des vagues sur la turbulence

Le modèle phénoménologique a tout d'abord été étendu pour comprendre comment la géométrie d'une frontière mobile et multi-échelle peut affecter la structure des tourbillons énergétiques. En effet, comme le montre la Fig. 2b, le modèle phénoménologique permet de modéliser les flux turbulents comme étant liés à des tourbillons représentatifs, dont la taille est proportionnelle à la hauteur, par rapport à la surface, à laquelle les flux sont calculés.

Dans ce chapitre, nous avons supposé que, en raison des variations de la hauteur de la surface de la mer, la taille du tourbillon représentatif varie (comme illustré dans la Fig. 3a pour une onde monochromatique). La taille effective du tourbillon représentatif résulte donc de la moyenne de toutes les tailles de tourbillon possibles, qui dépend des propriétés de la surface de la mer. Nous avons démontré que cela affectait essentiellement la dissipation d'énergie cinétique turbulente à des hauteurs de 10 m ou plus, d'un facteur proportionnel à la pente des vagues de longueur d'onde d'environ 10 m.

Ce résultat a trois conséquences importantes. Premièrement, la pente des vagues de 10 m de longueur d'onde étant modulée par les courants de surface [voir par exemple Rascle et al., 2016], le résultat de ce chapitre montre que les courants peuvent affecter la dissipation d'énergie cinétique turbulente en modulant la taille des tourbillons représentatifs. Ensuite, nous avons montré que ce changement de dissipation d'énergie cinétique turbulente induisait une variabilité significative du flux de quantité de mouvement. Cette modulation pourrait donc être un mécanisme capable d'expliquer la variabilité des flux de quantité de mouvement mentionnés au début de cette introduction, au travers de l'effet des courants sur les vagues de 10 m. Enfin, nous avons montré que les vagues de vent pouvaient potentiellement avoir une signature (i) non seulement sur le flux de quantité de mouvement, (ii) mais aussi sur la

dissipation d'énergie cinétique turbulente (et, en utilisant le budget spectral du chapitre 2, sur le spectre de la turbulence). Ces travaux ont donc révélé des variables associées à la turbulence atmosphérique dont la mesure précise pourrait améliorer notre compréhension des interactions entre le vent et les vagues.

CHAPITRE 4: L'IMPACT DYNAMIQUE DES VAGUES SUR LA TURBULENCE

Dans la dernière partie de cette thèse, nous avons revisité l'échelle de Beaufort en se posant la question suivante : le couplage local entre le vent et les vagues peut-il être caractérisé par une vitesse ou une longueur horizontale associée à la surface de la mer ? En effet, lorsque l'on observe une mer ventée, on peut remarquer, comme l'ont fait F. Beaufort et G. Simpson, que malgré la nature multi-échelle de la surface, les conditions de vent peuvent être caractérisées par une échelle de vagues horizontale, ou une vitesse, associée à un changement des propriétés de la surface de la mer. En particulier, pour des vents suffisamment forts, celle-ci est reliée à la taille et à la durée de vie de l'écume résultant des déferlements. Cette échelle horizontale est donc une mesure du couplage local multi-échelle entre le vent et les vagues.

Ainsi, dans ce chapitre, nous avons d'abord déterminé cette échelle horizontale en analysant des mesure de statistiques de déférlements [Sutherland and Melville, 2013]. Ces mesures forment un jeu de données unique, qui capture non seulement la densité des fronts déferlants associés à la présence d'écume, mais également celle associée à des vagues plus courtes, qui n'entraînent pas d'air et ne laissent donc pas de trace visible (et ceci grâce à l'utilisation de caméras infrarouges). L'analyse de cet ensemble de données a permis de déterminer la taille des vagues dont la densité de fronts déferlants varie le plus pour un changement de vent moyen à 10m, et qui sont donc celles qui, visuellement, traduisent le plus un changement de l'intensité du couplage vent-vagues: celles-ci vont des vagues centimetriques pour les vents faibles, jusqu'à des vagues de quelques mètres pour les vents de 10 m/s.

Indépendamment de cette analyse expérimentale, nous avons également utilisé le modèle phénoménologique présenté ci-dessus pour obtenir une estimation théorique de cette longueur d'onde horizontale. En effet, s'il existe une échelle de longueur horizontale caractérisant le couplage vent-vagues, il est raisonnable de supposer que celle-ci laisse également une empreinte sur les propriétés de la turbulence atmosphérique proche de la surface. Nous avons donc supposé que les fronts déferlants associés à cette échelle horizontale déterminent la taille des tourbillons représentatifs du modèle phénoménologique, comme illustré dans la Fig. 3b. En utilisant cette contrainte sur la taille des tourbillons dans le modèle phénoménologique et en nous appuyant sur des mesures de flux de quantité de mouvement, nous avons démontré que l'échelle horizontale ainsi obtenue est en accord avec celle obtenue à partir de l'analyse expérimentale.

Ce travail montre donc que le système couplé vent-vagues peut être représenté par l'échelle horizontale des vagues déferlantes qui sont les plus sensibles aux changements de vent. Cette échelle de longueur horizontale laisse une empreinte sur les statistiques de turbulence dans les premiers centimètres de la couche de surface de l'atmosphère, régulant l'amplitude du flux de quantité de mouvement air-mer. C'est un résultat important qui fournit une quantité (l'échelle horizontale, de quelques dizaines de centimètres) qui est mesurable à la fois avec des techniques de détection in-situ ou satellite, et qui permettrait de fournir des estimations

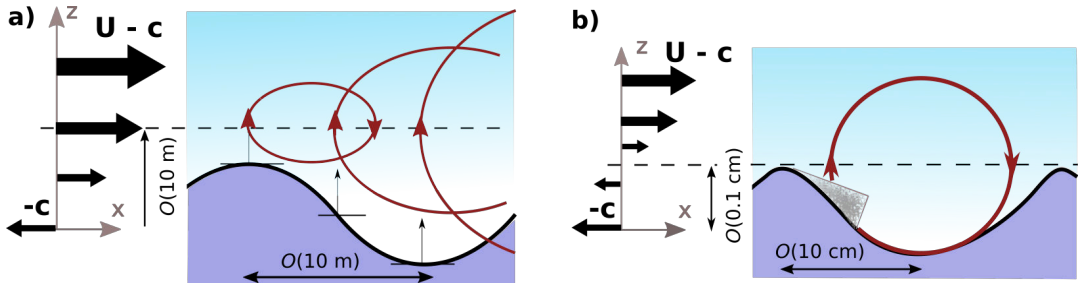

Figure 3: Modèle phénoménologique de la turbulence (Fig. 2b) étendu à deux situations reliées à l'interaction vent-vagues. (a) Les vagues de vent longues, donc la pente est sensible entre autre aux courants, changent la géométrie des tourbillons représentatifs, modifiant par la même la dissipation d'énergie cinétique turbulente et pouvant expliquer la variabilité des flux de quantité de mouvement pour un vent moyen donné. (b) L'échelle et la vitesse des vagues courtes et déferlantes est couplée à celle des tourbillons représentatifs proches de la surface. Ce couplage caractérise l'état de mer et le flux de quantité de mouvement pour une vent donné.

précises de la vitesse du vent, des flux turbulents et de l'état de mer local.

CONCLUSION

Cette thèse porte sur la question de l'interaction entre le vent et les vagues en utilisant un cadre théorique qui permet une description de la turbulence proche de la surface échelle par échelle. Cette méthode a été utilisée pour aller au-delà de la description traditionnelle des flux air-mer, qui repose sur la théorie de similitude de Monin-Obukhov, en montrant que la signature des interactions vent-vague sur la turbulence atmosphérique peut être importante sur des variables autres que la covariance des vitesses horizontales et verticales. Un tel cadre théorique est utile pour l'interprétation de mesures satellite et in-situ de la surface de la mer. Il l'est également pour l'étude du lien entre les petites échelles turbulentes et les flux moyennés à des échelles spatiales et temporelles plus grandes. Ces derniers sont notamment nécessaires pour les paramétrisations des flux air-mer dans les modèles de prévision climatiques.

CONTENTS

INTRODUCTION

In a recent perspective article, J. Jiménez made the following statement: "turbulence research, in common with other sciences at some point in their development, has changed from a subject driven by the need for good data, to one driven by the need for new ideas" [Jiménez, 2018]. For low-Reynolds number turbulent flows, which are the subject of Jiménez's article, and for which Direct Numerical Simulations are now massively available, this statement is certainly accurate. Is that the case for open-ocean turbulence close to the sea surface, which is coupled to wind-waves? Such a question is crucial, since turbulence close to the sea surface, or, more broadly, wind-and-wave interactions, is at the heart of parameterizations of air-sea fluxes for heat, gases, humidity and momentum [e.g. Fairall et al., 2003], used in numerical weather prediction models, both at the synoptic and at the climate scale [e.g. Shimura et al., 2017].

In this thesis we focus on the momentum flux for moderate winds (lower than 20 m s^{-1}). Its time- or space-averaged value, used in parameterizations, results from a zoology of turbulent motions, which depend on the scale and the steepness of the underlying surface undulations. Two examples are shown in Figs. 4a,b for laboratory scale waves [Buckley and Veron, 2016], and demonstrate that, as steepness increases, detachment of the flow can occur. This complex picture becomes even more fascinating in open-ocean conditions. As shown in Fig. 4c, a windy sea is a multiscale rough surface, in which the scales of the waves actively coupled to the wind span several orders of magnitude (from a few millimeters to tenths of meters). These wind-waves act as individual roughness elements which grow and decay as they interact (i) with the multiscale and intermittent wind field above, and (ii) among themselves through non-linear processes [e.g. wave breaking, Kudryavtsev et al., 2014]. The resulting zoology of turbulent motions is hence more complex than what can be observed in laboratory conditions, and calls for field experiments to be unraveled.

However, field experiments suffer from limitations. First, they are subject to oversampling specific environmental conditions due to practical issues (deployment in a limited set of areas, technical issues for strong seas, etc.). Hence, quantification of the sensitivity of wind-and-wave interactions to environmental parameters other than stability is difficult, and would require a global coverage of wind and waves [e.g. from remote sensing techniques, see Villas Boas et al., 2019]. In fact, the geometry of wind-waves can be modulated by the presence of swell, slicks, ocean currents and non-stationary winds, to only cite a few [Vandemark et al., 1997, Grodsky

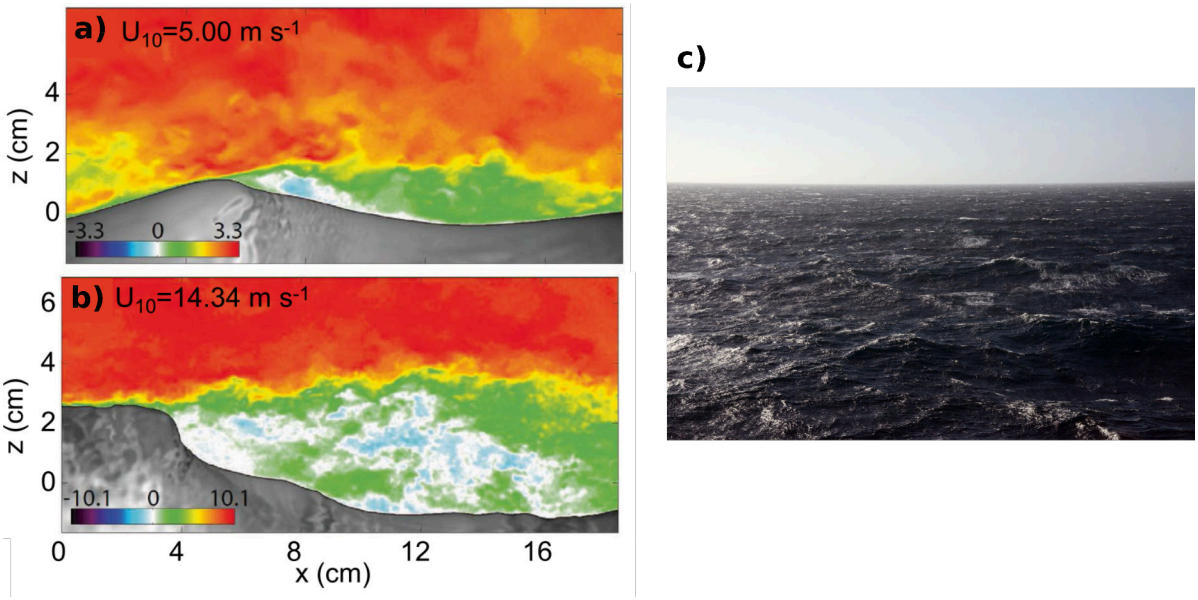

Figure 4: [(a), (b)] Snapshots of the streamwise wind field (i.e. blowing from left to right in the figure) above laboratory-scale waves. As the wave steepness increases, the flow becomes increasingly detached on the downwind face of the wave [figure adapted from Buckley and Veron, 2016]. (c) Example of a wind-driven sea surface off the coast of San Clemente Island, west of San Diego, CA, USA. The sea-surface consists of a superposition of waves of multiple scales, some of which are breaking. Courtesy of Laurent Grare.

et al., 2012, Kudryavtsev et al., 2012, Melville, 2018]. This is illustrated in Fig. 5a which compiles a large number of measurements from field campaigns, and where effects of stability have been removed [Edson et al., 2013]. While on average, a one-to-one relation between the time-averaged 10-m wind speed and momentum flux can be defined, the data is scattered around this mean value. It is unclear what are the parameters driving this spread, and to which extent this spread is underestimated. The second limitation is the difficulty to test theories for wind-and-wave interactions in the field, because (i) as mentioned above, the range of scales to be sampled is wide, while typical experimental settings (see Figs. 5c,d,e) only measure time series of the flow at some specific heights; (ii) theoretical models [Miles, 1957, Belcher and Hunt, 1993] predict that the most active part of the coupling, which is believed to occur for short and steep wind-waves [Munk, 1955], should have a signature in the first meters above the sea surface, which are difficult to sample above a windy sea. Several field experiments have nonetheless found conclusive evidence of wind-and-wave interactions at greater heights, giving support to the seminal Miles [1957] theory of wave growth, for large wind-waves [Hristov and Ruiz-Plancarte, 2014, Grare et al., 2013, 2018]. However, due to these difficulties many features of the wind-and-wave coupling are still elusive to observations and hence to theory [e.g. Soloviev and Kudryavtsev, 2010, Hristov, 2018]

The standard wind-wave-interaction theories on which these experiments are based [Miles,

1957, Belcher and Hunt, 1993] are valid under a certain number of assumptions. In particular, only a single monochromatic wave, with low steepness, is considered. Even though some extensions for steep waves have been proposed [e.g. Melville, 1977, Csanady, 1985, Kudryavtsev and Makin, 2001, Kukulka and Hara, 2008a], there is still no theoretical framework capable of consistently relating the multiscale wind and wave fields and the time-averaged momentum flux. Given the difficulties presented above, such a theory is important, since it can help designing and interpreting open-ocean measurements. Hence, rephrasing Jiménez's statement, it seems more fair to state that turbulence close to the sea surface is a subject driven by the need for *both* new data and new ideas.

In this thesis, we address the last of these two needs, by bringing a spectral framework, developed to describe turbulence over a flat wall [Katul et al., 2011], to the problem of wind-and-wave interaction. We take a step towards the evaluation of the parameters governing the relation between turbulent motions and averaged quantities, and hence towards assessing the validity of the bulk algorithms in use today. In Chapter 1, we review the characteristics of flows above a flat wall and the sea surface, and the theories used to describe them. In Chapter 2 we then address several questions regarding the use of the spectral framework, for flow over a flat wall. Finally, in Chapters 3 and 4 we use the spectral framework to investigate how long wind-waves and short breaking waves affect the properties of turbulence.

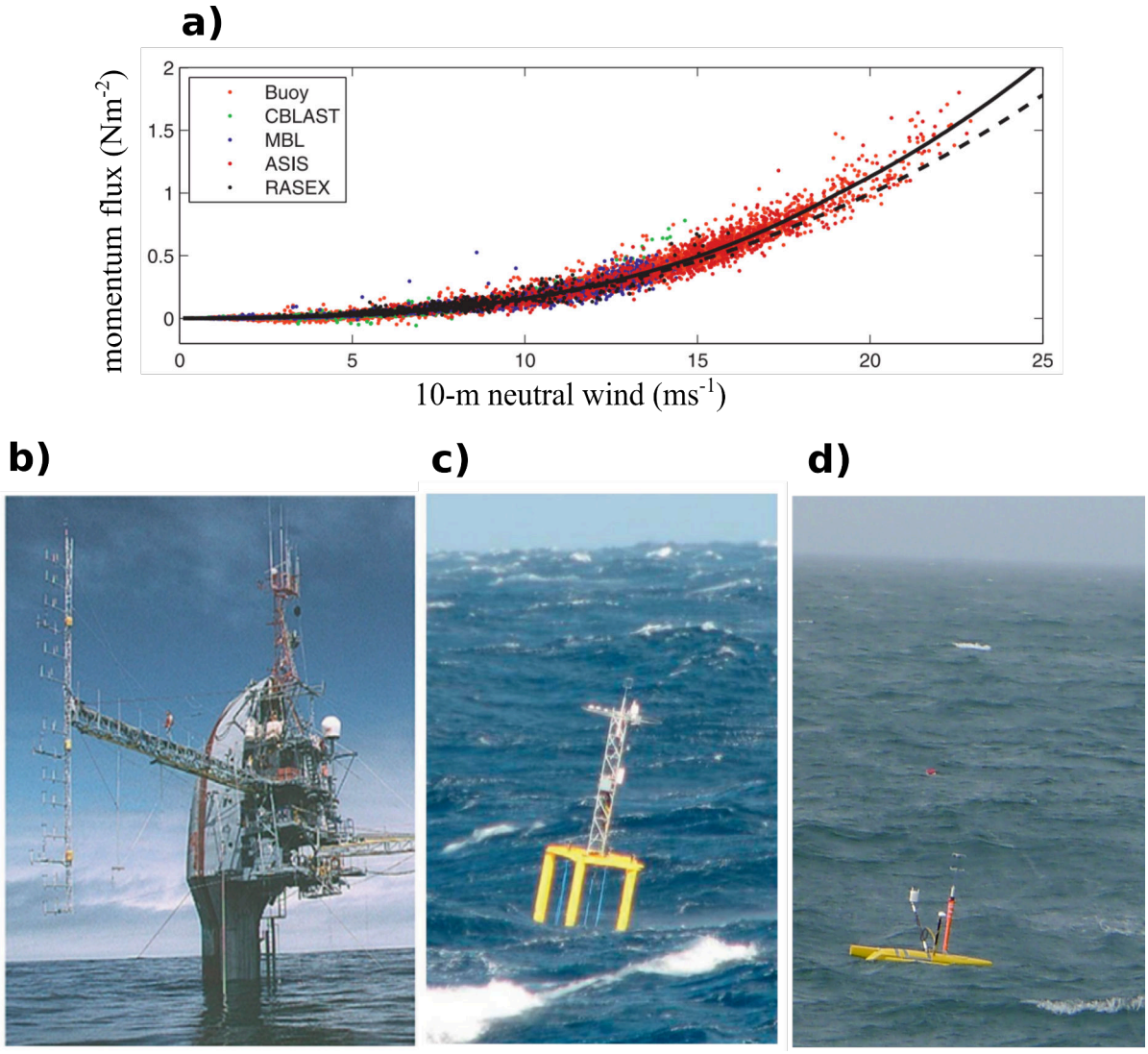

Figure 5: (a) Large set of measurements of momentum flux from field campaigns vs 10-m wind speed (dots). Effects of stability have been removed. The dashed and solid lines are fits to the data, used for the computation of fluxes in the COARE 3.0 and 3.5 algorithms respectively. Notice the spread of the data around those fits [figure from Edson et al., 2013]. [(b),(c),(d)] Example of measuring devices, with anemometers measuring wind at increasingly lower heights. (b) The R/P Flip used in e.g. the MBL experiment [Hristov et al., 2003], with an array of anemometers (on the left) going down to a height of 4 m. (c) ASIS moored buoy with a 3-m high mast, used during the CLIMODE experiment. (d) Wave-following OCARINA platform, carrying a 1.5-m mast Bourras et al. [2014, 2019]. (b) and (c) are adapted from [Edson et al., 2013], and (d) is courtesy of Louis Marié.

CHAPTER 1

TURBULENCE AND WAVES: A LITERATURE REVIEW

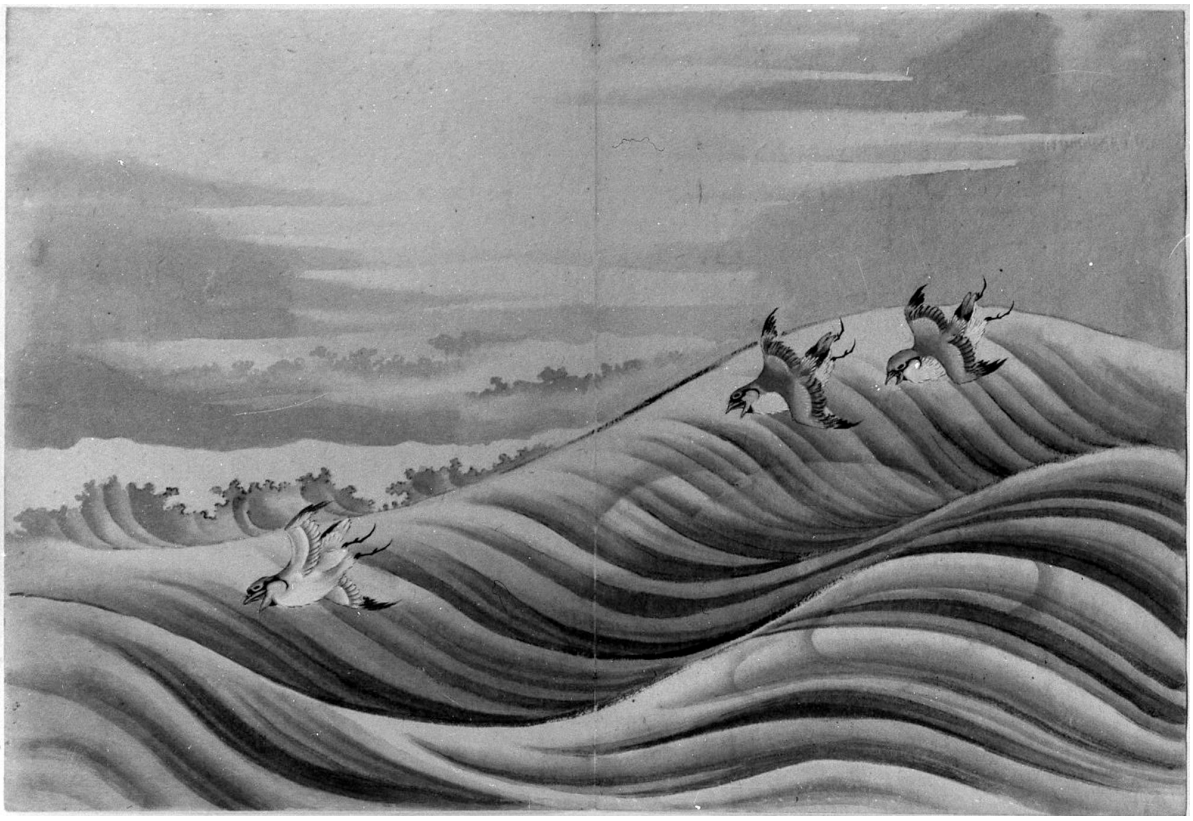

"Chidori Birds", School of Katsushika Hokusai (1615–1868).
The Metropolitan Museum of Art, Gift of Annette Young, in memory of her brother, Innis Young, 1956.

From an atmospheric perspective, the coupling between wind and waves can be seen as a (very) particular case of a turbulent flow over a rough surface. In this chapter we thus begin (Sec. 1.1) by a broad overview of wall-bounded turbulence, both over smooth and rough surfaces. Emphasis is put on dimensional analysis and on the somewhat "empirical" understanding of the flow by means of coherent structures and eddies, without discussing mathematical techniques. The phenomenological model of turbulence, used in the rest of this thesis, relies on this physical view, and is presented in Sec. 1.2. We then move to the wind-wave problem by critically reviewing historical and state-of-the-art theories of the coupling between turbulence and wind-waves (Sec. 1.3). Finally, we present the objectives of this work (Sec. 1.4). Our interest lies in the description of turbulence properties that are relevant for the determination of the momentum and energy fluxes. We do not describe heat and gas transfer, which are equally important and interesting problems.

1.1 WALL-BOUNDED TURBULENCE WITH STRATIFICATION

The literature on wall-bounded turbulence is vast, and, in this section, only a few selected elements, necessary for the rest of the thesis, are described. Included are also concepts that, arbitrarily, seem interesting for the study of turbulence on top of waves. More precisely, we focus on the description of the Atmospheric Surface Layer (ASL), which lies at the bottom of the atmospheric boundary layer. While, in the atmospheric boundary layer interior, the Coriolis force induces a rotation of the mean wind with height (the Ekman spiral), in the ASL the *direction* of the mean wind is constant with height and the Coriolis force can be neglected. This defines the streamwise (x) direction of a Cartesian coordinate system, aligned with the mean (ageostrophic) wind U. The flow is further assumed to be horizontally homogeneous, i.e. horizontal gradients, and in particular advection, cancel. All quantities are thus invariant with respect to the streamwise and spanwise (y) directions, and vary only with height above the surface z. The Reynolds-averaged streamwise momentum balance then reads

$$\frac{\partial U}{\partial t} = -\frac{\partial p}{\partial x}\bigg|_L - \frac{\partial \overline{u'w'}}{\partial z} - \nu \frac{\partial^2 U}{\partial z^2}. \tag{1.1}$$

We have introduced the (zero-mean) fluctuations of streamwise (u') and vertical (w') velocity, and $\overline{\cdot}$, the ensemble Reynolds average (the spanwise fluctuation of velocity is denoted by v'). We have also introduced the air viscosity ν, and a large scale pressure gradient $(\partial p/\partial x)_L$ resulting from a bulk atmospheric boundary layer forcing due to a large scale geostrophic equilibrium. Sufficiently far from the bottom boundary (see below), the viscous stress (the last term on the RHS) can be neglected with respect to the Reynolds stress (the penultimate term on the RHS).

The above equation shows that the Eulerian acceleration of the mean flow is related to turbulence through the vertical gradient of the anisotropic component of the Reynolds stress tensor $\overline{u'w'}$. This bulk anisotropy results from a multiscale zoology of turbulent motions, which are described, in what follows, in terms of statistical eddies [Townsend, 1972]. This anisotropic component can be interpreted as a vertical flux of momentum, providing an incentive for its understanding in terms of events (or coherent motions) which transport momentum through the

boundary layer. Some elements of the latter view will also be presented below.

We further consider a stationary ASL ($\partial U/\partial t = 0$), and neglect the large-scale pressure gradient, which leads to the following momentum balance

$$\frac{d\overline{u'w'}}{dz} = 0. \tag{1.2}$$

This defines the friction velocity u_*, as the square root of the (constant) turbulent momentum flux in the ASL $(-\overline{u'w'})^{1/2}$ (following the meteorological convention, a negative momentum $\overline{u'w'}$ flux is here a downward flux). [1]

We now proceed by first presenting a broad overview of the ASL and its eddies for neutral conditions. We then focus on Monin-Obukhov Similarity Theory (MOST) for the description of a stratified ASL. This second part is motivated by MOST being at the heart of modern parameterizations of surface fluxes in the presence of waves.

1.1.1 General considerations for neutral conditions

This section is inspired from several reviews and books, which contain more details and references than what follows: (i) the reviews about smooth- and rough-wall flows of Raupach et al. [1991] and Jiménez [2004], (ii) the reviews on coherent structures in low-Reynolds number flows [Jiménez, 2012, 2018] and on top of (forest) canopies [Finnigan, 2000] and, (iii) the classic textbooks about turbulence of Pope [2000] and Wyngaard [2010].

Flat wall The description of a turbulent boundary layer in the vicinity of a flat wall relies on several basic quantities. These are (i) the friction velocity u_*, (ii) the air viscosity ν, and (iii) the height of the boundary layer δ_{BL}. If the atmosphere is neutral, those ingredients define two dimensionless scales: the inner scale $l_{in} = zu_*/\nu$ and the outer scale $l_{out} = z/\delta_{BL}$. The inner scale can be interpreted as the Reynolds number for the attached, energetic eddies at a height z, while a friction Reynolds number can be introduced as $Re_\nu = \delta_{BL}u_*/\nu$, i.e. as the Reynolds number of the largest eddies of the boundary layer. For the ASL, $\nu = \mathcal{O}(10^{-5}$ m^2 s$^{-1})$, $\delta_{BL} = \mathcal{O}(100 - 1000$ m) and $u_* \sim 0.5$ m s^{-1}. The ASL is hence a high Reynolds-number flow, i.e. with Re_ν ranging from 10^6 to 10^8 (the latter being for a convective ASL).

The scales l_{in} and l_{out} define different layers, in which the mean wind shear scales differently (see Fig. 1.1) . The inner layer, where the mean wind shear is independent of δ_{BL} and of the free stream velocity ($U(z = \delta_{BL})$), is defined for $l_{out} \leq 0.1$. At the bottom of the inner layer lies the viscous sublayer ($l_{in} < 5$) where the Reynolds stress is negligible with respect to the viscous stress, and the mean wind shear is constant[2]

$$\frac{dU}{dz} = \frac{u_*^2}{\nu} \text{ and } U(0) = 0. \tag{1.3}$$

[1] Note that, in Tennekes [1973] neglecting the large-scale pressure gradient, which, for mid-latitude ASLs, is related to neglecting the Coriolis force, was shown to require an ASL height of the order $0.03u_*/f = \mathcal{O}(100$ m), with f the Coriolis parameter. This is a *practical estimate* of the ASL height, which ensures that momentum flux decreases of about 10 % from its surface value.

[2] This is readily obtained from Eq. (1.1) which, in the viscous sublayer, reads $\nu(d^2U/dz^2) = 0$.

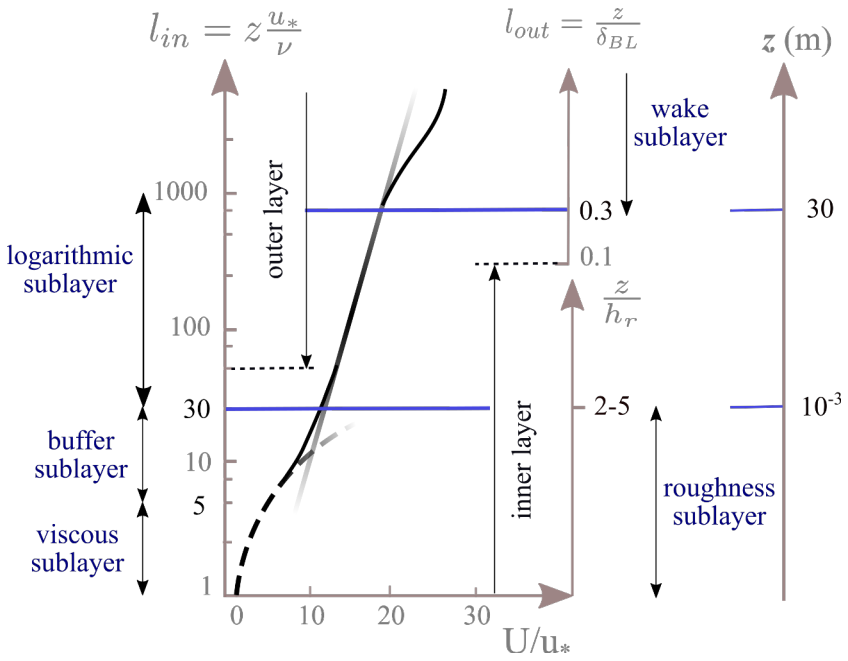

Figure 1.1: Schematic of the different layers and dimensionless quantities on which the mean wind profile of a wall-bounded flow depends. For a smooth wall, the definition of the layers depends on l_{in} and l_{out}, and the values given here follow Pope [2000]. For a rough wall, l_{in} is replaced by z/h_r where h_r is the height of the roughness sublayer (bottom right axis). The value U/u_* is an order of magnitude, corresponding to pipe flows over a smooth wall. The height of the logarithmic layer (rightmost axis) is estimated for an ASL of height 100 m and $u_* \sim 0.5$ m s^{-1}.

As height increases, for $l_{in} > 50$, effects of viscosity become negligible, which marks the bottom of the outer layer. At the overlap between the inner and outer layers (for $l_{in} > 30 - 80$ and $l_{out} < 0.2 - 0.3$, according to Pope [2000] and Jiménez [2012]), the only relevant quantity is the height z, and the mean wind follows a logarithmic profile [Townsend, 1976]

$$U(z) = \frac{u_*}{\kappa}\log(z/z_0), \qquad \frac{dU}{dz} = \frac{u_*}{\kappa z}. \tag{1.4a,b}$$

Following the meteorological convention, we have introduced the roughness height z_0 which, for a flat surface, is $0.14\nu/u_*$. The Von Kármán constant $\kappa \sim 0.4$ is a universal constant (here, we will not discuss its variations). The logarithmic region exists for sufficiently turbulent flows, for which the separation between the largest turbulent eddies and the smallest viscous eddies is broad [e.g. $Re_\nu > 750$, Jiménez, 2012]. For an ASL of height 100 m, the logarithmic sublayer range $30 < l_{in}$ and $l_{out} < 0.3$ corresponds to 6×10^{-4} m $< z < 30$ m. Note that above the logarithmic region lies the wake region, which won't be discussed here, and where the effects of the boundary layer height cause a deflect of the mean wind profile from the logarithmic law.

Kraus [1967] proposed an interesting interpretation of the Von Kármán constant. By requiring continuity of the wind shear on top of the viscous sublayer (between the linear and logarithmic

profiles), the inner Reynolds number at the top of the viscous sublayer reads $l_{in}^{\nu} = 1/\kappa$. Note that with the usual value $\kappa \sim 0.4$, this yields $l_{in}^{\nu} \sim 2.5$, of the same order of magnitude than the value $l_{in} = 5$ of Pope [2000]. This simplified picture neglects however the presence of the buffer layer, located in between the viscous and logarithmic sublayers ($5 < l_{in} < 50$) and where the linear wind velocity profile gradually merges into the logarithmic profile. The buffer layer is especially important in low-Reynolds number flows [$Re_{\nu} = \mathcal{O}(10^3)$ or lower, Smits et al., 2011], where it is home of a "viscous cycle" in which low momentum streaks destabilize periodically [Jiménez and Moin, 1991] and act as a TKE source for the boundary layer aloft [Jiménez, 1999].

ROUGH WALL Smooth walls are almost never encountered in geophysical flows. More precisely, the presence of surface roughness alters the above picture by introducing at least an additional scale, the height of the roughness elements h_r, which defines the roughness Reynolds number $Re_r = h_r u_* / \nu$ [see the review Raupach et al., 1991]. From this, three regimes can be defined: aerodynamically smooth flows for $Re_r < 5$, transitional for $5 < Re_r < 70$ and aerodynamically rough flows for $Re_r > 70$ [from the sand-grain experiments of Nikuradse, 1933][3]

We hence see that, for an ABL flow not to be considered as aerodynamically rough, h_r should be of the order of 10^{-3} m. As an example, for wheat, typical Re_r are of 10^4, and up to 10^6 for 23-m high forest canopies such as the Kondo forest [Jarvis, 1976]. In the aerodynamically rough regime ($Re_r \to \infty$), the flow becomes independent of Re_r (i.e. of viscosity), and the relevant parameters are then those of the surface geometry (streamwise and spanwise aspect ratios, density of roughness elements ....). Their determination is strongly dependent on the nature of the roughness elements, and, as will be seen in the rest of the thesis, is remarkably difficult for the ocean surface. [4]

With respect to the mean flow scaling discussed above, the viscous and buffer sublayers are, for an aerodynamically rough flow, replaced by the *roughness sublayer*, in which the mean wind speed does not depend on viscosity but on the geometry of the roughness elements. Its height is generally between $2h_r$ and $5h_r$ [see Raupach et al., 1991, and Fig. 1.1]. In this layer, the mean wind profile deviates from the logarithmic law reflecting, among others, the effect of airflow separation behind roughness elements, and the presence of *dispersive fluxes*, resulting from the spatio-temporal heterogeneity of the surface (see Sec. 1.3). For flow over forest canopies, it is generally accepted that this deviation results in an exponential law [Finnigan, 2000]. It can be derived theoretically from the momentum balance, by including an additional form drag, quadratic with wind speed [e.g. Finnigan and Belcher, 2004]. Note that this is similar to the description of the impact of breaking waves on the wind profile (as described in Sec. 1.3) even though, for wind-waves, additional sources of form drag are also present that are not quadratic with wind speed.

[3] Note that, as shown in the sand-grain experiments of Bandyopadhyay [1987], these bounds are dependent on the surface geometry. Jiménez [2004] suggests that the lower bound for an aerodynamically rough flow, is more broadly $Re_r > 50 - 100$.

[4] This is why, in the wind-wave literature, the roughness Reynolds number is more commonly defined from z_0, i.e. $Re_r^{z_0} = z_0 u_* / \nu$. In this case, aerodynamically rough flow begins for $Re_r^{z_0} > 2.2$ (and, as mentioned above, for a smooth flow, $Re_r^{z_0} = 0.14$).

In the logarithmic layer, the essential question, posed here following the meteorological conventions, is then to determine which geometrical parameters control z_0. Here we only mention the study of Lettau [1969] which has been influential in theoretical works about wind-wave interactions [Csanady, 1985, Kitaigorodskii et al., 1995]. By studying the flow over three-dimensional bushel baskets on a frozen lake [Kutzbach, 1961], Lettau [1969] showed that $z_0/h_r = 0.5 h_r h_y/D^2$, where the roughness frontal area par unit surface (or roughness density) $h_r h_y/D^2$ depends on h_r, on the mean separation distance between roughness elements (D) and on their spanwise extension (h_y). Note however that, as mentioned by Raupach et al. [1991], for roughness densities high enough, the ratio z_0/h_r decreases with roughness density. This reflects the mutual sheltering of roughness elements. An extreme case of such a sheltering, first highlighted by Perry et al. [1969], are *d-type* surfaces, for which z_0 depends only on the boundary layer height δ_{BL}.

TKE BALANCE IN THE LOGARITHMIC LAYER Townsend [1961] suggested that the logarithmic layer (above flat or rough surfaces alike) is an equilibrium layer, in which the dissipation of Turbulence Kinetic Energy (TKE) ϵ is balanced by mechanical production

$$u_*^2 \frac{dU}{dz} = \epsilon. \tag{1.5}$$

The above equation assumes that the flow is stationary and horizontally homogeneous (which are the ASL hypotheses), but neglects in addition the vertical transport of TKE (due to vertical gradients of skewness and of velocity-pressure covariance). Numerous experiments in a near-neutral ASL have shown that this balance is generally valid in the logarithmic sublayer [e.g Bradley et al., 1981].

For a low Reynolds-number flow above a smooth surface, Jiménez [1999] further suggested that this equilibrium layer, in which the energy flux is constant, is fed by the buffer sublayer, which acts as a source of energy from below, and that this energy in then dissipated in the overlying wake sublayer (for $l_{out} > 0.2$). This analysis was quantified by Cimarelli et al. [2016] using a budget for the second order structure function (interpreted as energy of the dominant eddies) on DNS data. It hence suggests an upward inverse energy cascade, as energy goes from small viscous motions to large wake motions.

This picture reversed for ASL flows in the presence of a roughness sublayer. Within the roughness sublayer, transport terms were shown to be significant, moving TKE from the top of the roughness sublayer down to the surface where energy is dissipated in the wake of the roughness elements [Raupach et al., 1991]. This mechanism requires the presence of an additional term in the TKE budget, the so-called wake production term, resulting from dispersive fluxes. It will be discussed at length in Sec. 1.3, in the case of the sea surface.

THE ATTACHED EDDY HYPOTHESIS By using the logarithmic wind profile (1.4) in equation (1.5), the TKE dissipation reads $\epsilon(z) = u_*^3/\kappa z$. This scaling is consistent with the seminal *attached eddy hypothesis* formulated by Townsend [1976] which states that, in the logarithmic layer, the characteristic size of the dominant momentum-transporting eddies scales with distance from the surface. This length is defined by considering that ϵ is the ratio of the cube of an eddy

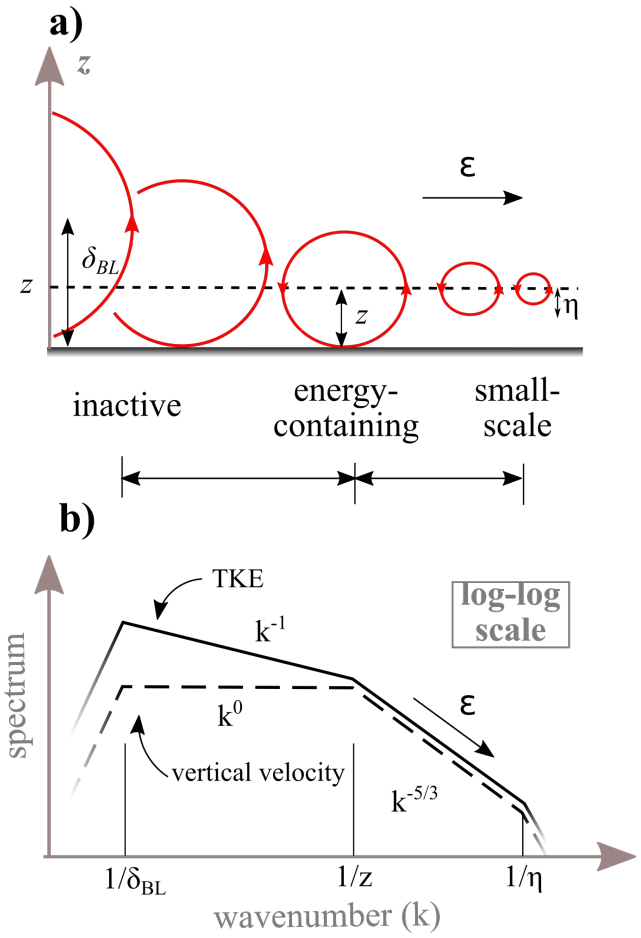

Figure 1.2: Schematic of the separation of motions in the logarithmic sublayer. (a) From large to small scales, eddies at a height z from the surface are separated into inactive motions which contribute only to the horizontal velocity, energy-containing eddies which carry most of the momentum flux and small-scale eddies which transfer energy, in the spectral space, down to the dissipation subrange (at a scale η) at a rate ϵ. (b) Idealized spectra of total kinetic energy (solid line) vertical kinetic energy (dashed line) and for the neutral ASL. The spectra exhibits two regimes: the inertial subrange, at the overlap between energy-containing and small-scale eddies, and the energy-containing subrange at the overlap between energy-containing and inactive motions. Note that, since inactive motions do not contribute to vertical motions, the spectrum of vertical velocities is flatter than the spectrum of TKE.

turnover velocity (u_*) and of its size (z). This corresponds to the size of so-called "energy-containing eddies", which extract energy from the mean shear at a given height z, before it cascades down to the Kolmogorov scale $\eta = (\nu^3/\epsilon)^{1/4}$ through a 3D isotropic cascade.[5] Across

[5]Note that η, the size of the smallest eddies of the flow, defines an estimate of the separation between the smallest and largest scales of the flow as $\delta_{BL}/\eta \propto Re_\nu^{3/4}$ [e.g. Wyngaard, 2010]. This quantity dictates the resolution

this spectral cascade, the energy flux is constant, and the dissipation rate ϵ of η-scale eddies is hence equal to the rate at which energy-containing eddies inject energy in the cascade (see Fig. 1.2a).

Eddies can hence be separated into two kinds: attached (or energy-containing, or active) eddies, which interact with the mean shear and whose size scales with height z, and small-scale eddies which transfer energy down to the scale η where it is dissipated. Bradshaw [1967] further proposed that eddies larger than z act, at a given height, as inactive motions. Those eddies, unlike energy-containing eddies, do not contribute to vertical motions at a height z, but only to horizontal motions. Several works have proposed methods for the identification of attached eddies and their separation from inactive motions, e.g. using wavelet transform [Katul and Vidakovic, 1996], a watershed algorithm [Srinath et al., 2018], conditional sampling [Lozano-Durán et al., 2012] or a clustering method [Cheng et al., 2020].

This separation of motions was used by Perry and Abell [1977] to explain the behaviour of the longitudinal turbulent spectrum, which exhibits two main regimes, shown in Fig. 1.2b, for the related TKE spectrum, as a function of the streamwise wavenumber k (solid line): a low-wavenumber regime (the energy-containing subrange) with a k^{-1} dependence, at the overlap between the scales of inactive eddies and energy-containing eddies, and a $k^{-5/3}$ high-wavenumber regime, indicative of 3D cascade where motions are isotropic[6].

The separation between the two regimes occurs at a wavenumber proportional to $1/z$, representative of the size of energy-containing eddies. Perry and Abell [1977] further used this model to recover the scaling behaviour of the horizontal velocity variances, as also done by Banerjee and Katul [2013] using a phenomenological model similar to the one presented in Sec. 1.2 . The presence of a k^{-1} regime has been observed in a variety of ABL studies [e.g. Drobinski et al., 2007, and references therein], but it is still unclear under which conditions it emerges. Note that, since energy-containing motions do not contribute to vertical motions, the spectrum of vertical velocity (dashed line) lacks the k^{-1} overlap regime, which is instead replaced by a k^0 regime [see Wyngaard, 2010, p. 234 for a theoretical argument]. The latter scaling has been more consistently observed than the k^{-1} regime of the TKE spectrum, indicative of its robustness to variations in external parameters.

Panchev [1971] (pages 219-223) proposed an interesting argument for the emergence of a k^{-1} regime in the TKE spectrum. He considered the budget for the spectrum of TKE at a given wavenumber, assumed to be a balance between mechanical injection of energy, non-linear transfer of energy from large to small scales [modeled following Heisenberg, 1948], and viscous dissipation. With respect to its scale-averaged counterpart (1.5), the spectral balance contains an additional non-linear transfer of energy term, whose integrated contribution to the averaged balance is zero. Panchev [1971] showed that the k^{-1} regime emerged in the limit where, following Tchen [1953, 1954] the mechanical injection of energy occurs only by interaction of small-scale turbulent vorticity with the *mean wind vorticity*. This limit is opposed to the case where mechanical injection of energy results from the interaction between small and large

required for a Direct Numerical Simulation (DNS) of the full boundary layer, and is also related to the number of degrees of freedom of the flow [Landau and Lifshitz, 1959].

[6] Here we do not discuss the very-low-wavenumber regime ($k < \delta_{BL}^{-1}$), where large and very-large scale motions cause a decay in the spectra, nor the very-high-wavenumber dissipation subrange ($k > \eta^{-1}$) where the spectrum also becomes steeper [see Saddoughi and Veeravalli, 1994].

scale turbulent vorticity [Tchen, 1953]. The former limit occurs when the ratio between the large- and Kolmogorov-scale vorticity is small $(dU/dx)(\nu/\epsilon)^{1/2} \ll 1$. In the logarithmic layer, this condition is valid, and can be expressed equivalently as $l_{in}^{1/2} \gg 1$ or as $(z/\eta)^{2/3} \gg 1$. A suggested interpretation of this analysis is that energy-containing eddies in the logarithmic sublayer should be viewed as an imprint of the mean flow on turbulence statistics, giving a justification for their scaling with mean-flow variables.

In the viscous sublayer, the scale of energy containing-eddies and the scale at which viscous dissipation occurs are similar, and the above picture does not hold. Note that this is used by Jiménez [2018] to determine the bottom of the logarithmic sublayer (see its figure 3a).

What is more interesting for the following is what happens in the roughness sublayer, where the scale of energy-containing eddies is fixed and depends solely on the roughness sublayer height [Raupach et al., 1991, Gioia et al., 2010, Bonetti et al., 2017]. This is at the core of Chapter 4 of this thesis. A possible explanation for this scaling is reviewed below. Finally, the presence of airflow separation events in the roughness sublayer has a last important impact, as it creates small-scale eddies, shortcutting the Kolmogorov cascade. Large-scale energy is then directly transported at the dissipation scale, which can have impact on the shape of the inertial-subrange spectra [Finnigan, 2000].

COHERENT STRUCTURES So far we have described the properties of statistical eddies in the roughness and logarithmic sublayers, which represent the *most likely* state of the flow with respect to some of its properties. The flow can also be described in terms of coherent structures, which are *representative* structures of the flow with intrinsic dynamics [Jiménez, 2018].[7] This gives an interesting insight on the dynamics of turbulence, with the hope that the properties of coherent structures are related to the statistical properties of the flow, and hence to the eddies described above. Here we discuss some of these coherent structures, summarized in Fig. 1.3.

Energy-containing eddies have been introduced above as "momentum-transporting eddies", which support most of the turbulent momentum flux $-u_*^2$ in the logarithmic and roughness sublayers. A widely-used tool to go beyond this scaling description is quadrant analysis, in which instantaneous contributions to the momentum flux are separated into four quadrants (see Fig. 1.3a). The first (Q1, $u' > 0$ and $w' > 0$) and third (Q3, $u' < 0$ and $w' < 0$) quadrants correspond to outward and inward interactions respectively, interpreted as a slow interaction induced by a momentum-transporting vertical motion w'. The second (Q2, $u' < 0$ and $w' > 0$) and fourth (Q4, $u' > 0$ and $w' > 0$) quadrants correspond respectively to *ejections* (or bursts) of low momentum fluid upwards and to *sweeps* of high momentum fluid downwards. In wall-bounded flows, since the momentum flux $\overline{u'w'}$ is downwards (negative), most of the contributions to its intensity arise from ejections and sweeps.

In the roughness sublayer above forest canopies, the distribution is skewed towards sweeps (Fig. 1.3a). As mentioned above, this indicates that the dominant events in the roughness sublayer of canopies are downward intrusions of high momentum fluid, which transport TKE down in the roughness elements where it is dissipated. It is interesting to note that, even though the contribution of sweeps to $\overline{u'w'}$ is higher than that of bursts, they are less frequent [Finnigan,

[7] Eddies are also often associated to a cascade of energy in spectral space, which is not necessarily the case of coherent structures.

2000]. This is an example of the statistical properties of turbulence being set by intense and intermittent events (another one is breaking of ocean surface waves, discussed in Sec. 1.3).

Low-Reynolds-number studies give an interesting insight on the coherent structures associated with these events. In the logarithmic sublayer, the DNS of Lozano-Durán et al. [2012], Lozano-Durán and Jiménez [2014] showed that Q2 and Q4 events come in pairs of counter-rotating vortices, with a statistically significant asymmetry (see Fig. 1.3b) and a long lifetime in which they grow in a self-similar manner. Interestingly, these pairs have a size and a velocity similar to Townsend's attached eddies (z and u_* respectively). Alternative candidates to these events are hairpin vortices (see Fig. 1.3c) which originate from a near-wall instability and grow in packets, transporting momentum and TKE upwards in the logarithmic layer [Adrian, 2007]. This is a much more organized scenario than Lozano-Durán and Jiménez [2014], where Q2-Q4 pairs do not necessarily originate near the wall, but has been very useful in building theoretical models of near-wall turbulence [Marusic and Monty, 2019].

Some of these structures have been shown to follow a self-sustaining cycle, i.e. they are observed in DNS without the presence of larger scale flow, and are sufficient to reproduce the bulk flow statistics. While it is well known that, in buffer-layer, coherent structures are modulated by the outer flow [e.g. Marusic et al., 2010, Squire et al., 2016], this point is less clear in the logarithmic layer. As Jiménez [2012] mentions, "we can expect some modulation of the logarithmic layer, including possibly long-range ordering, from the global modes above it". This modulation by outer flow eddies is of major importance, since this interaction governs the general response of wall-bounded flows to external influences. In particular, in the presence of a roughness sublayer, it has been recently shown that these modulations are particularly strong [Anderson, 2016].

It should be noted that, besides this bottom-up view of the logarithmic sublayer, other interpretations exist, such as the top-down approach presented in Hunt and Morrison [2000] for high-Reynolds number flows. This approach draws on observations of cat's paws [e.g. Dorman and Mollo-Christensen, 1973, on top of water], and describes the downward advection of upper layer eddies down to the surface, which generates ejections and logarithmic-layer vortices through various mechanisms (an example of such a mechanism is given in Fig. 1.3d). It is however out of the scope of this introduction to compare those two views in more detail.

We end this discussion on coherent structures by describing a model, first introduced by [Raupach et al., 1996], to explain the scaling of energy-containing eddies in the roughness sublayer. The model draws on the analogy between the roughness sublayer top and a plane mixing layer, supported by data on top of forest canopies. In both cases, the presence of an inflection point in the mean wind speed generates streamwise rolls by Kelvin-Helmoltz instability. Secondary instability around these rolls lead to coherent structures of similar spanwise and streamwise extensions (see Fig. 1.3e). Their extension is dictated by the scale of the mean wind shear, which is similar to the roughness-sublayer height. Hence this "mixing layer analogy" describes the scale $(2-5h_r)$ of energy-containing eddies in the roughness sublayer as being set by instabilities near the roughness sublayer top.

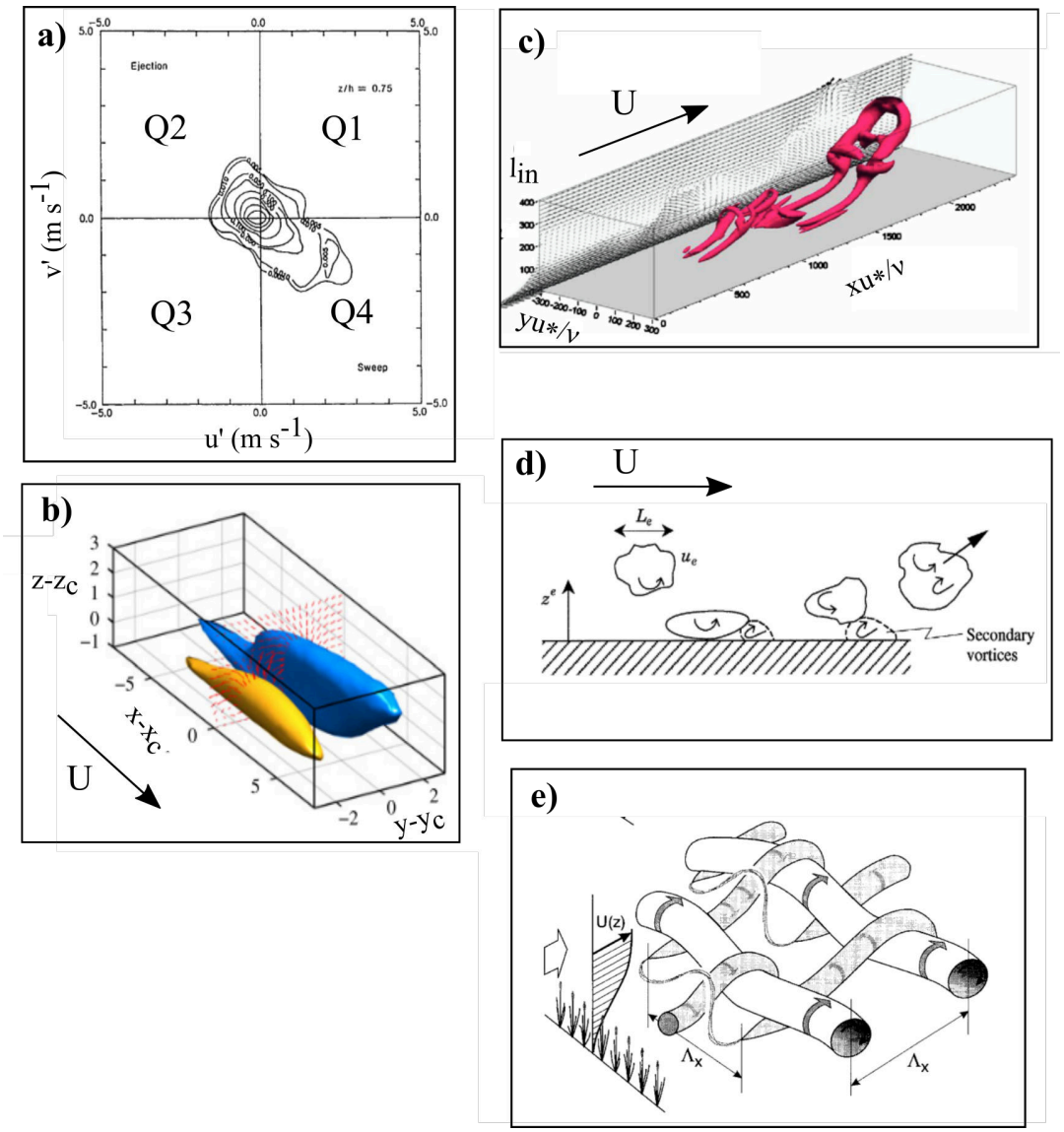

Figure 1.3: Example of coherent structures and their analysis. (a) Quadrant analysis on top of a canopy, showing the predominance of sweep events with respect to ejections [from Gardiner, 1994]; (b) Conditional surfaces associated with Q2-Q4 pairs in the logarithmic sublayer, from a low-Reynolds-number DNS. The iso-surfaces are perturbations to the streamwise velocity. Yellow is the low-speed ejection ($u' = -0.5u_*$) and blue is the high speed sweep ($u' = 0.5u_*$). The coordinates are relative to the center of the structure [from Jiménez, 2018]; (c) Snapshot of the last stage of the evolution of a packet of hairpin vortices, generated after a Q2 event in a DNS. At this stage, the scale and velocity of the packet become similar to Townsend's attached eddy. The surface is an iso-surface of "swirling strength", a quantity similar to vorticity [from Adrian, 2007]; (d) Example of a top-down mechanism: interaction of an outer-layer vortex with the wall, generating an ejection [from Hunt and Morrison, 2000]; (e) Coherent structures resulting from a Kelvin-Helmoltz instability and secondary instabilities on top of a roughness sublayer [from Finnigan, 2000]

1.1.2 Effect of stability: Monin-Obukhov Similarity Theory

Scaling and underlying hypothesis So far, we have described wall-bounded turbulent flow in neutral conditions. However, in the ASL the presence of buoyancy forces alters the scaling of the previous section by introducing an additional scale, the Obukhov scale [Obukhov, 1946, Monin and Obukhov, 1954]

$$L = -\frac{\theta_0}{\kappa g}\frac{\overline{u'w'}^{3/2}}{\overline{w'\theta'}}, \tag{1.6}$$

where g is gravity acceleration, and θ_0 and θ' are a reference potential temperature and its turbulent deviation respectively. This length accounts for a non-zero turbulent heat flux $\overline{w'\theta'}$, which is positive (upwards) for an unstable atmosphere, and negative (downwards) for a stable atmosphere. [8] Scaling the height with the Obukhov length defines the stability parameter $\zeta = z/L$, positive for a stable atmosphere and negative for an unstable atmosphere. The absolute value of this dimensionless length is characteristic of (i.e. proportional to) the height of the "dynamical sublayer", below which the effect of stratification is negligible [Obukhov, 1971].

This scale, forms the basis of the Monin-Obukhov Similarity theory [MOST, see the review by Foken, 2006]. Using the Buckingham Π theorem, the following dimensionless relations were posited

$$\frac{\kappa z}{u_*}\frac{dU}{dz} = \phi_m(\zeta), \qquad \frac{\kappa z u_*}{\overline{w'\theta'}}\frac{d\theta}{dz} = \phi_h(\zeta), \tag{1.6a,b}$$

where ϕ_m and ϕ_h are the so-called MOST universal functions for momentum and heat fluxes respectively, equal to one for neutral conditions. It is interesting to highlight that these relations can be interpreted as a modification of the diffusion properties of turbulence in the presence of heat fluxes. In fact, the momentum K_m and heat K_h turbulent diffusion coefficients

$$u_*^2 = K_m\frac{dU}{dz}, \qquad \overline{w'\theta'} = -K_h\frac{d\theta}{dz} \tag{1.7a,b}$$

can be expressed as

$$\begin{aligned} K_m &= \phi_m(\zeta)^{-2}(\kappa z)^2\frac{dU}{dz} \\ K_h &= \mathrm{Pr}^{-1}K_m = \frac{\phi_m(\zeta)}{\phi_h(\zeta)}K_m \end{aligned} \tag{1.8}$$

where we have the turbulent Prandtl number Pr, the ratio between momentum and heat turbulent

[8] In the presence of moisture and hence latent heat fluxes, the potential temperature is replaced by the virtual potential temperature (θ_v). The heat flux then reads

$$\overline{w\theta_v} = \frac{H_s}{\rho_a c_p} + 0.61\,T_0\frac{H_l}{\rho_a L_e},$$

where L_e is the latent heat of vaporization of water, c_p the heat capacity of dry air, T_0 a reference temperature, ρ_a the air density and H_s and H_l are the potential temperature and latent heat flux respectively [e.g. Fairall et al., 1996]. For simplicity, moisture is neglected in the following.

diffusion coefficients. Equation (1.8) shows that (i) ϕ_m accounts for the stability-dependent deviation of the turbulent diffusion coefficient from its neutral value in the logarithmic sublayer $(\kappa z)^2(dU/dz)$ [9] (ii) ϕ_h accounts for the influence of stability on the dissimilarity between turbulent transport of momentum and heat (see the recent analysis of Li et al. [2012, 2015] and the review of Li [2019]).

This interpretation indirectly highlights two of the fundamental assumptions of MOST. The first assumption is the existence of linear gradient-flux relationship (i.e. the fact that turbulent fluxes are related to the local properties of their averaged counterparts, Eq. (1.8)). It is well known that this assumption may not be valid in the presence of large scale convection or in the roughness sublayer, where non-local (counter-gradient) fluxes are present [e.g. Kaimal and Finnigan, 1994].

The second assumption is the existence of a logarithmic-law scaling, which relies on several other conditions. As shown in Eq. (1.5) (and the related discussion) those are the ABL hypothesis and Townsend's view of energy-containing eddies scaling with z (Fig. 1.2). The ABL hypothesis can be violated for inhomogeneous and non-stationary ABLs. According to Wyngaard [2010], for a typical height $z = 10$ m corresponding to standard measurements, the horizontal length scale on which the ABL has to be homogeneous should be larger than a few kilometers, while the time scale of variation should be greater than 5 minutes. The ASL constant-stress assumption can also be invalidated by the presence of pressure gradients or of dispersive fluxes, which change the momentum balance (1.2).

With respect to the validity of Townsend's view of energy-containing eddies, let us first mention that, while the presence of stratification should obviously alter the length scale of the eddies, it is still proportional to z in MOST, consistent with Townsend's scaling. Nonetheless, additional non-local scales can enter the problem for several reasons. First, strong inner-outer layer interactions, in particular in the presence of large convective structures, introduce outer-layer or environmental parameters in the similarity theory [e.g. Li et al., 2018, Fodor et al., 2019]. Additional scales can also be introduced due to the presence of roughness elements [e.g. Garratt and Hicks, 1990, Zilitinkevich et al., 2006]. Note that in the limiting free convective conditions [of strong instablity, Tennekes, 1970] and very stable conditions [z-less conditions, Wyngaard, 1973], which overlap some of the cases mentioned above, MOST scaling is also invalidated. Here and in the rest of the thesis, the discussion will be restricted to mildly stable and unstable conditions, defined for $|z/L| \leq 1$.

THE O'KEYPS EQUATION Empirical forms of ϕ_m and ϕ_h have been derived in numerous experiments, in particular by Businger et al. [1971] using data from the Kansas experiment. Those are not presented here, and can be found in Appendix A of Sec. 2.2. Note however that the general behavior is an increase of ϕ_m and ϕ_h with ζ, reminiscent of a decrease of turbulent intensity for stable conditions and an increase for unstable conditions.

To match the Businger empirical functions, several authors proposed the so-called O'KEYPS equation (after Obukhov, Kaimal, Elliot, Yamamoto, Panofsky, Sellers, see Panofsky [1963]

[9] Note that this neutral value is readily obtained from the logarithmic law Eq. (1.4).

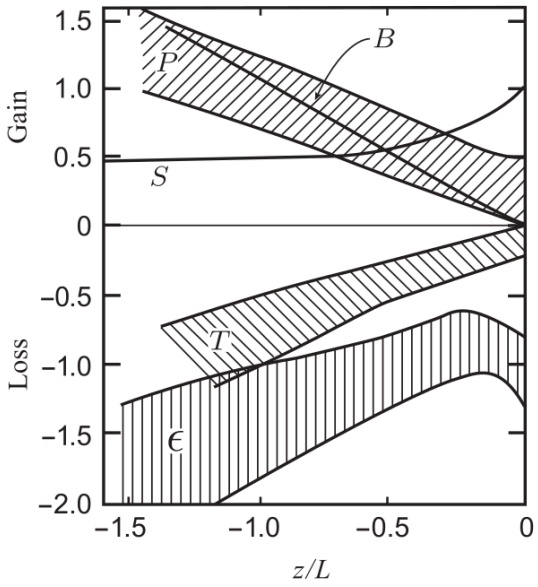

Figure 1.4: Summary of ABL measurements of the TKE budget for unstable conditions. S is the mechanical production by interaction with mean wind shear, B is the production by buoyancy, ϵ is TKE dissipation, and T and P are the turbulent and pressure transport terms respectively. The pressure transport term has not been directely measured, but is deduced from the TKE imbalance. The figure is originally from Wyngaard [1992], and here we show the reprinted version from Wyngaard [2010].

and Businger [1988]). The equation reads

$$\phi_m^4 - \gamma \frac{z}{L} \phi_m^3 = 1, \tag{1.9}$$

where γ is a "universal" constant which varies, depending on the experiments, between 5 and 18.

The O'KEYPS equation was derived in Ellison [1957] to fit two limiting regimes mentioned above: the free convective regime for $\zeta \ll -1$ (where wind shear can be neglected) and the stable regime for $\zeta \gg 1$. Alternative heuristic derivations where presented in Panofsky [1961] and Sellers [1962], considering that shear- and buoyancy-induced turbulence contribute independently to the total turbulent diffusion, in which case γ appears as a proportionality coefficient between these two processes. Using these hypothesis, these studies stress that the O'KEYPS equation is valid only for an unstable atmosphere. Further, these derivations show that γ is proportional to the turbulent Prandtl number Pr. Hence the stability-independence of γ implies that of Pr, which can be questioned in ABLs [Li, 2019]. The "universality" of γ was discussed in Katul et al. [2011], who related γ to turbulent transport and to properties of energy-containing eddies, showing its sensitivity to stability and environmental conditions.

TKE BALANCE We have mentioned that MOST accounts for the change in turbulent intensity due to buoyancy. The origin of this modification can be traced back to the TKE equation (1.5) (page 30) which, in the presence of stratification, reads

$$-\overline{u'w'}\frac{dU}{dz}+\frac{g}{\theta_0}\overline{w'\theta'}=\epsilon. \tag{1.10}$$

The additional term with respect to Eq. (1.5) is production or destruction of TKE by buoyancy forces. This additional term explains the changes in turbulence properties when stability is included. It defines the flux Richardson number Ri_f

$$\mathrm{Ri}_f=\frac{\frac{g}{\theta_0}\overline{w'\theta'}}{\overline{u'w'}\frac{\partial U}{\partial z}}.$$

The flux Richardson number can be related to the gradient Richardson number $\mathrm{Ri}=(g/\theta_0)[\partial_z\theta/(\partial_z U)^2]$ and to ζ using the flux gradient relations (1.7), and reads

$$\mathrm{Ri}_f=\frac{K_h}{K_m}\mathrm{Ri}=\zeta\phi_m^{-1}. \tag{1.11}$$

This gives another interpretation of ζ in terms of the energetic properties of turbulence, as a the ratio between energy production/destruction by buoyancy and mechanical energy production.

The TKE balance can be rewritten in dimensionless form by multiplying Eq. (1.10) by $\kappa z/u_*^3$, and reads

$$-\phi_m(\zeta)+\zeta+\frac{\kappa z}{u_*^3}\epsilon=0, \tag{1.12}$$

In the above TKE balance, transport terms have again been neglected. Measurements for mildly unstable conditions, shown in Fig. 1.4, indeed show that the two components of turbulent transport (transport by turbulent fluctuations and by pressure fluctuations) almost compensate each other. For mildly unstable conditions, a first order correction can nonetheless be included in this budget, by replacing ζ by $(1+\beta_2)\zeta$, where $\beta_2\sim 1$ is a proportionality coefficient relating the dimensionless transport to ζ [e.g. Katul et al., 2011].

1.2 A PHENOMENOLOGICAL SPECTRAL LINK

In the previous section, the description of wall-bounded turbulence has been related to statistical eddies, transporting momentum and energy both in physical space (the downward turbulent momentum flux) and in spectral space (the 3D isotropic cascade). In particular, the central role of "attached eddies", which interact with the mean wind shear at a given height, has been emphasized. Relying on this phenomenology, several authors have proposed a model, termed "spectral link", relating the averaged (or bulk) properties of turbulence to its spectral properties. The original model of Gioia et al. [2010] and its extension for a stratified flow by Katul et al. [2011] are first reviewed to introduce their use in the modeling of the mean velocity and MOST functions. They rely on the geometry of the eddies, without necessity of discussing spectral budgets. The latter are then discussed, along the lines of Katul et al. [2013] and Katul and

Manes [2014].

BULK MODEL At the core of the concept of an attached eddy is the concept of a momentum-transporting eddy, i.e. which supports $\overline{u'w'}$ at a given height. This was made explicit by Gioia et al. [2010] by expressing the momentum flux across a horizontal surface at a height z as the product of an energy-containing eddy turnover velocity v_e, depending on the streamwise scale of the eddy s_h, and a streamwise momentum difference transported by the eddy across a vertical distance s_v. To first order, the momentum difference $u(z+s_v)-u(z-s_v)$ reads $2\frac{\partial U}{\partial z}s_v$, which yields the following expression for the momentum flux

$$-\overline{u'w'}(z) \propto v_e[s_h(z)]\frac{\partial U}{\partial z}(z)s_v(z). \tag{1.13}$$

Using the same phenomenology as for $\epsilon = u_*^3/z$, the eddy turnover velocity was further expressed as $v_e(s_h) \propto (\epsilon s_h)^{1/3}$. The validity of this scaling, which requires that s_h lies in the inertial subrange, has been verified experimentally by Salesky et al. [2013] using ABL data.

Using this expression in Eq. (1.13), the TKE dissipation finally reads

$$\epsilon \propto u_*^6\left(\frac{\partial U}{\partial z}\right)^{-3} s_v^{-3}s_h^{-1}. \tag{1.14}$$

If the mean wind speed follows a logarithmic law (Eq. (1.4)), the scaling $\epsilon = u_*^3/(\kappa z)$ is recovered by requiring $s_v(z) = s_h(z) = z$ in Eq. (1.14) [Gioia et al., 2010]. This can be seen as indicative that eddies considered in this model are related to Townsend's attached eddies, since both have sizes which scale height from the ground (see Fig. 1.2a). Note that, for consistency, the proportionality factor in Eq. (1.14) has to be in this case κ^{-4}.

For a stratified atmosphere, the mean wind profile deviates from the logarithmic scaling (as mentioned in the previous section). In addition, Katul et al. [2011] argued that, while the height of the energy-containing eddies s_v should still be equal to z (since they are attached to the surface, as in Fig. 1.2a), their horizontal extension, and hence energy, can vary due to buoyancy forces. The authors hence introduced the so-called anisotropy factor $f_a(\zeta) = s_h(\zeta)/z$, larger than one for an unstable atmosphere (in which eddies are more energetic) and smaller than one for a stable atmosphere (in which eddies are "squeezed" due to the restoring buoyancy forces). [10]

Using MOST universal functions, the dissipation then reads

$$\epsilon = \frac{u_*^3}{\kappa z}\phi_m^{-3} f_a(\zeta)^{-1}. \tag{1.15}$$

Katul et al. [2011] noticed that, using this relation for ϵ in the TKE equation (1.12), a general-

[10] The anisotropy factor introduced here reflects a geometrical anisotropy in the shape of energy-containing eddies, which should not be confused with turbulence anistropy, i.e. the difference in energy between turbulent components and the fact that they are correlated (e.g. a non-zero $\overline{u'w'}$).

ized form of the O'KEYPS equation (1.9) is obtained

$$\phi_m^4 - \zeta\phi_m^3 = f_a(\zeta)^{-1}. \tag{1.16}$$

For unstable conditions, the anisotropy factor can be experimentally determined as a change in the ratio between the spanwise and streamwise integral length scales of vertical velocity Salesky et al. [2013]. For stable conditions, Li et al. [2016] showed that a more appropriate estimate is the Ozmidov length scale (the size of the largest eddy unaffected by buoyancy). In both cases, using empirical estimates for $f_a(\zeta)$, the authors were able to predict experimentally-consistent values of ϕ_m, giving support for the capacity of the phenomenological model to predict mean flow variables.

THE SPECTRAL LINK The underlying idea of the phenomenological model is to relate the bulk properties of the flow (here TKE dissipation) to its spectral properties, i.e. the energy and size of energy-containing eddies. In fact, Gioia et al. [2010] had suggested that the eddy turnover velocity $v_e(s)$ should be computed as an integral of the TKE spectrum, truncated at the energy-containing eddy wavelength. Katul and Manes [2014] went one step further by using a co-spectral budgets, i.e. budgets of co-spectrum amplitude at a given eddy scale, to derive Eq. (1.13).

More precisely, the authors considered $\tilde{F}_{uw}(k)$, the (one dimensional) streamwise Fourier transform of $-\overline{u'w'}$, where k is the streamwise wavenumber (or inverse eddy size). This momentum flux co-spectrum satisfies the normalizing condition $-\overline{u'w'} = \int_0^\infty \tilde{F}_{uw}(k)dk$. It can be shown [Panchev, 1971, Bos et al., 2004] that $\tilde{F}_{uw}$ satisfies a spectral budget which can be obtained as the Fourier transform of the budget for the correlation tensor (called the Kármán–Howarth-Monin equation). For stationary and planar-homogeneous flows close to a wall, in the absence of subsidence (the ASL hypothesis), Katul and Manes [2014] suggested that the co-spectral budget is a balance between mechanical production, pressure-strain sink ($\tilde{R}_{uw}$) and viscous dissipation:

$$\frac{\partial \tilde{F}_{uw}(k)}{\partial t} = 0 = \frac{dU}{dz}\tilde{F}_{ww}(k) - \tilde{R}_{uw}(k) - 2\nu k^2 \tilde{F}_{wu}(k), \tag{1.17}$$

where we have introduced the vertical velocity spectrum $\tilde{F}_{ww}$, such that $\overline{w'^2} = \int_0^\infty \tilde{F}_{ww}(k)dk$. The pressure-strain term R_{uw} is an essential component of the budget, acting against the presence of turbulent anisotropy, in this case against $\tilde{F}_{uw}$. A standard model for this "return-to-isotropy" tendency is the linear Rotta model [Rotta, 1951], for which $\tilde{R}_{uw} \propto \tilde{F}_{uw}$. Katul and Manes [2014] used a refined version, called the LRR-IP model [Launder et al., 1975], which reads

$$\tilde{R}_{uw}(k) = \frac{C_R}{\tilde{\tau}(k)}\tilde{F}_{uw}(k) + C_l\frac{dU}{dz}\tilde{F}_{ww}(k). \tag{1.18}$$

In addition to the first Rotta term, the model contains an "Isotropization of Production" (IP) correction (the second term). The Rotta constant C_r has a value close to 1.8 (from numerical simulations) and the second constant C_l is equal to 3/5 (from rapid-distortion theory). Note that, in its original formulation, the LRR-IP model describes return-to-anisotropy for the bulk

budget (integrated over all scales). In this case the proportionality constant in front of the Rotta term reads C_R/T, with $T = (\overline{u'^2} + \overline{v'^2} + \overline{w'^2})/(2\epsilon)$ the characteristic timescale of return to isotropy. Besnard et al. [1996], Bos et al. [2004] and Katul and Manes [2014] proposed a spectral version of the LRR-IP model with a scale-dependent timescale $\tilde{\tau}(k)$ (Eq. (1.18)). In the case of Bos et al. [2004] and Katul and Manes [2014], this dependence reads $\tilde{\tau}(k) = \epsilon^{-1/3}k^{-2/3}$.

The co-spectral budget relates the vertical velocity spectra to the momentum flux co-spectrum, and, using the normalization condition $-\overline{u'w'} = \int_0^\infty \tilde{F}_{uw}(k)dk$, hence establishes the following spectral link between $-\overline{u'w'}$ and $\tilde{F}_{ww}(k)$

$$-\overline{u'w'} = \frac{dU}{dz}\frac{1-C_l}{C_R}\epsilon^{-1/3}\int_0^\infty \frac{k^{-2/3}\tilde{F}_{ww}}{1+2(\eta k)^{4/3}/C_R}dk. \tag{1.19}$$

In this equation, the effect of viscosity is scale dependent, expressed as the ratio between the considered scale k^{-1} and the Kolmogorov microscale η. Hence the total contribution of viscosity to the momentum flux depends on the shape of the vertical velocity spectrum, presented below. Note that the DNS presented in Katul et al. [2014] show that the co-spectral budget, and hence Eq. (1.19), are still valid for mildly unstable and stable conditions.

Finally, an idealized vertical velocity spectra, presented in Fig. 1.2, was used by Katul and Manes [2014] to express the momentum flux in Eq. (1.19), and hence TKE dissipation, under the same form than the bulk spectral link, Eq. (1.15). The idealized spectra has two ranges, separated by the so-called spectral peak wavenumber k_p:

$$\tilde{F}_{ww}(k) = \begin{cases} C_{ww}\epsilon^{2/3}k_p^{-5/3}k^0, & k \le k_p \\ C_{ww}\epsilon^{2/3}k^{-5/3} & k > k_p \end{cases}, \tag{1.20}$$

where $C_{ww} = 0.65$ is the Kolmogorov constant for the vertical velocity energy spectrum [Saddoughi and Veeravalli, 1994]. [11] As mentioned previously, the peak wavenumber is proportional to $1/z$. Hence, in the logarithmic sublayer $\eta k_p \ll 1$, and viscosity can be neglected in the above integral [unlike in the buffer or viscous sublayers, not discussed here, see Katul and Manes, 2014]. Integrating over the idealized vertical velocity spectra then yields

$$\epsilon \propto u_*^6\left(\frac{dU}{dz}\right)^{-3}k_p^4 \tag{1.21}$$

where the integration as well as the Kolmogorov and return-to-isotropy constants are not explicitly written here for simplicity.

This derivation demonstrates that the horizontal extension of the energy-containing eddy $zf_a(\zeta)$, defined above (page 40), is related to the inverse wavenumber of the spectral peak k_p^{-1}, as in Townsend's imagery of attached eddies. Further, several experiments have shown that the spectral peak k_p varies with stability about $1/z$ [e.g. Kaimal and Finnigan, 1994],

[11] The term "spectral peak wavenumber" originates from the presence of a spectral peak in the *premultiplied* spectrum $k\epsilon^{-2/3}\tilde{F}_{ww}(k)$. Note also that Katul et al. [2013] discussed the inclusion of intermittency corrections to the inertial subrange of the above spectrum. The authors showed that the spectral link was unaffected, but that the resulting mean wind profile no longer follows a logarithmic law but a power law.

which is consistent with the posited stability-dependent anisotropy factor $f_a(\zeta)^{-1}$. Equations (1.19) and (1.21) establish a "spectral link" relating spectral properties of the flow to its bulk characteristics. They show that the latter are in fact not only determined by properties of the eddies whose size is commensurate to z, but by a weighted contribution of eddies of all scales.

With respect to the bulk analysis of Gioia et al. [2010] and Katul et al. [2011], the co-spectral budget unravels the physical hypothesis and shortcomings of the phenomenological model. The first assumption concerns the terms retained in the co-spectral budget. While, as for its bulk counterpart, the spectral budget is expected to be satisfied in flat-wall ASLs, the flux-transport term (the spectral analogue of the vertical transport term in the bulk budget) has been ignored. It can be expected that this term becomes important for some other type of flows, e.g. in the roughness sublayer, even if measurements for its quantification are lacking. Setting aside that assumption, the spectral link relies on two models: for the vertical velocity spectrum (Eq. (1.20), which sets the production of co-spectrum, and for the return-to-isotropy term (Eq. (1.18)). Both models are expected to be valid for mildly stable and unstable conditions, in a variety of ASL flows [see the references in Katul et al., 2013, Katul and Manes, 2014]. Nonetheless, it is important to stress that the LRR-IP model can fail for strongly inhomogeneous flows, in which the timescale of return to isotropy can exceed the modeled T or $\tilde{\tau}$.

As a final note, let us mention that, herein, we have discussed the spectra only in the wavenumber domain. Conversion to the frequency domain requires a dispersion relation for turbulent motions. The simplest conversion relies on Taylors' hypothesis of frozen turbulence [Taylor, 1938] which assumes that the advection time of turbulent motions of wavenumber k is smaller than their development time (defined as the time for turbulent structures to change significantly in their frame of reference, see Phillips [1957]). For turbulent structures advected at the mean wind speed U, the conversion is then

$$\omega = kU. \tag{1.22}$$

However, more complex models have been used [see the review Wallace, 2014], including e.g. the turbulent advection of eddies of a given scale by larger eddies [Wilczek et al., 2015]. Finally, the presence of surface roughnesses can invalidate Taylor's hypothesis. Squire et al. [2017] and references therein used measurements to demonstrate that the advection of small scale structures can be modified, but it is uncertain to which extent. The signature is especially important on the vertical velocity spectrum. This should be carefully considered when using the spectral link in complex flows, since the latter relies on spectra expressed in the wavenumber domain, which are often measured in the frequency domain.

FINAL REMARKS The phenomenological model relates the bulk turbulent momentum flux to the spectrum of the vertical velocity, whose properties can be represented by means of an idealized attached eddy. This statistical eddy has dimensions which should be the expression of the complex instantaneous features of turbulence, e.g. the coherent structures discussed in Sec. 1.1. This model allows recovering some of the "universal" MOST functions, and gives hints on their non-universal behavior. It goes beyond MOST scaling arguments, which gives support to its applicability to establish other spectral links.

As an important example of such a link, the phenomenological model has been used to

predict the properties of rough pipe flows, using its bulk formulation [Gioia and Bombardelli, 2001] and the co-spectral budget [Bonetti et al., 2017]. The effect of roughness elements has been included by assuming that, in the roughness sublayer, the size of the energy-containing eddy s_h (or the spectral peak wavenumber k_p) is constant with height and equal to the size of the roughness elements. This is consistent with the measurements presented by Raupach et al. [1996], and their interpretation as indicative of energy-containing eddies being mixing-layer eddies, whose size is set by the height of the roughness elements (see Fig. 1.3e).

The model is hence an interesting candidate for a simplified description of the complex properties of turbulence over rough surfaces, of which the windy sea is an example of. With this in mind, we first review below the properties of turbulence on top of waves, from the theoretical modeling perspective.

1.3 THE DYNAMICAL INTERACTION BETWEEN NEAR-SURFACE TURBULENCE AND WAVES

Understanding the properties of turbulent motions close to the sea surface is of uttermost importance for air-sea interactions, and is a complex problem due to the presence of ocean surface waves [see, e.g., the recent reviews on wind-wave interactions in Jones et al., 2001, Janssen, 2004, Sullivan and McWilliams, 2010, LeMone et al., 2019]. Field observations [e.g. Edson et al., 2013] indicate that, in the presence of surface waves and for sufficiently strong winds, the turbulent momentum flux on top of the so-called wave boundary layer (WBL), of height of about 10 m, is increased with respect to a flat surface, and has a one-to-one dependence on the mean wind speed (for averaging periods of about 30 minutes). Hence the disturbances generated by surface waves, whose amplitude is coupled to atmospheric motions, result in an overall change in the properties of turbulence in the WBL, for a prescribed mean 10m-wind [see experiments of Edson and Fairall, 1998, Sjöblom and Smedman, 2002]. In the following we review the dynamical properties of the WBL, with emphasis on theoretical (and, when possible, analytical) models for the interaction between atmospheric turbulence and waves. What follows is by no means an exhaustive or historical review, but rather one with a specific focus theoretical studies of the WBL.

Flow over surface waves, while sharing some similarities with flow with hills and wavy boundaries, exhibits some unique features due to the intrinsic properties of surface waves [see the review by Belcher and Hunt, 1998, where both flows are compared].

First, surface waves are moving undulations of the sea surface, which follow a dispersion relation. More precisely, the phase speed $c = \omega/k$ of a monochromatic wave depends on its wavenumber k and frequency ω, which are linked as $\omega^2 = gk + T_{sw}k^3$, where g is the gravity acceleration and T_{sw} is the dynamical surface water tension. The phase speed has a minimum for waves of wavelength ($\lambda = 2\pi/k$) of 1.6 cm, which marks the transition between capillary (smaller) and gravity (larger) waves. The phase speed of gravity waves increases with their size, as opposed to capillary waves. This first feature implies that the the impact of waves on atmospheric turbulence should depend not only on their geometry, but also on relative velocity of the wave with respect to the airflow, and hence on the scale of the wave [see for instance Kitaigorodskii, 1973, p. 27 to 36, where the surface is modelled as a linear superposition of moving roughness elements]. The relative velocity of the wave is termed wave age, c/u_*, with

u_* the friction velocity (the square root of the momentum flux on top of the WBL).

Second, the airflow bottom boundary condition is non-uniform, and depends on the wave steepness. As explained by Kraus [1967], the difference in dynamic viscosity between the air and the water results in the air-sea interface moving at the wave orbital velocity.[12] The wave orbital velocity varies periodically in the reference frame of the wave, and its magnitude, akc, depends on the wave steepness ak (a is the wave amplitude). As waves grow and decay locally under the action of the wind, their steepness changes [Longuet-Higgins, 1987]. Hence the airflow bottom boundary condition is non-uniform, and is dynamically coupled to the wind and wave fields.

Third, the growth and decay of waves under the action of the wind is a complex mechanism. It cannot be simply explained by Kelvin-Helmoltz type of instability [as originally proposed by Lord Kelvin, Thomson, 1871]. Indeed, the suction on top of wave crests required to overcome the gravity restoring force can only be strong enough for winds of about 6-7 m s^{-1}, for which waves are already present [Ursell, 1956]. In addition, wave breaking is an essential component of the sea surface, which is associated with intense energy dissipation events from the wave field towards ocean currents, but also to intense ejection events and momentum flux spikes in the atmosphere [Banner and Melville, 1976, Kawamura and Toba, 1988, Melville, 1996].

Finally, a realistic sea surface is described by a broadband wave spectrum: it is a multiscale interface which can be, to some extent, viewed as a sum of individual sinusoidal components, each moving at a different phase speed. This implies three additional difficulties: (i) the roughness properties of waves of different sizes (quantified by e.g. the roughness Reynolds number) span a wide range of regimes, and hence the overall effect of the multiscale sea surface is non trivial [Kitaigorodskii, 1973]; (ii) the response of a given wave component to the airflow depends on its non-linear interaction with other wave components, which redistributes energy among different wavenumbers [Phillips, 1985]; (iii) the response of the turbulent airflow to a multiscale surface can be qualitatively different from the superposition of responses to individual wave components [Deardorff, 1967].

From a practical point of view, it is interesting to represent the impact of those various features on the atmosphere through a roughness height z_0 (the level at which the mean wind speed, following a logarithmic law, cancels). A very influential scaling was proposed by Charnock [1955] for sufficiently high winds: $z_0 \propto u_*^2/g$, where g is the gravity acceleration. This scaling can be interpreted in light of the observations of Francis [1954] and Munk [1955], which indicate that the wind stress (equivalent to z_0) should essentially depend on short wind-waves (smaller than 1m). As argued by Phillips [1977] (p. 194), the amplitude of short wind-waves depends on wind-induced surface drift (related to u_*) and wave breaking, and hence scales with u_*^2/g, explaining the Charnock relation. An important consequence of this

[12] To understand why, let us consider how the mean flow speed of air and water should match at the interface, given their bulk values outside of the viscous sublayer. For Stokes waves, the bulk velocities are of opposite sign (wind bulk speed is negative at the wave crest and positive at the wave through, and conversely for the water). Hence, the matching at the interface generates a layer of high vorticity. The size of this layer depends on viscous diffusion, which gradually matches vorticity to its bulk value, and is about 5 times larger for the air than for the water. The speed of the interface is thus, to a good approximation, close to the bulk water speed. Note that Kraus [1967] stresses that this argument works for wavelengths greater than 0.1 m, corresponding to wavelengths smaller than the size of the atmospheric vorticity layer $\sqrt{2\nu/\omega}$.

argument is that wind stress is related to the *mean square slope* of the sea surface, which is mainly driven by short wind-waves, and not to its mean square height, which is mainly set by larger, uncoupled waves.

This bulk Charnock scaling, verified experimentally, and commonly used in forecast and climate models, gives a first intuition on the fact that the steepness of short wind-waves is important in the coupling of the sea-surface with the atmosphere. While this represents an aspect of the coupling, in an averaged sense, it does not highlight the physical processes at stake in the interaction between the highly fluctuating turbulent and wave motions. In the following, we are interested in reviewing models that go beyond this description, focusing on theoretical models of a stationary and horizontally-homogeneous WBL, where the turbulent airflow has balanced with locally-generated wind-waves (i.e. without swell). Those hypothesis imply that the WBL is a constant-flux layer, described in Sect. 1.3.1. An essential element of this constant-flux layer is wave-induced stress, resulting from wave-coherent perturbations of the airflow moving at the waves phase speed. Wave-induced stress is intrinsically related to wave growth, and we discuss its modeling in Sect. 1.3.2. The interaction of turbulence with wave-induced motions for a realistic sea surface is then discussed in Sect. 1.3.3. Note that we only consider the case of waves aligned with the mean wind direction (denoted by U, in the streamwise, x, direction). In those coordinates, the mean wind speed is zero in the spanwise (y) and vertical (z) directions.

1.3.1 Momentum balance in the wave boundary layer

As mentioned above, in the following we focus on the properties of the WBL, which is stationary and homogeneous, and above which the impact of waves on turbulent motions can be regarded as negligible. In this section we discuss its momentum balance.

Wave-induced motions At the core of the coupling between wind and waves is the existence of perturbations of atmospheric quantities which are correlated to waves, and that can extract or lose energy either to the mean flow or to turbulent motions, leading to wave growth or decay. As described in Stewart [1961], as these motions carry energy down to the surface, their coherency must increase, in the sense that the different components of the motions become increasingly correlated. The existence of such motions is similar to that of internal waves in stably stratified turbulence [e.g. Zilitinkevich et al., 2008], or to flow over inhomogeneous surfaces, such as canopies [see Kaimal and Finnigan, 1994, p. 84]. In the presence of waves, the flow, for example the streamwise velocity, is linearly decomposed into a mean component $\langle\overline{u}\rangle = U$, a wave-induced component $\overline{u} = u_w$, and a turbulent component u':

$$u = U + u_w + u', \tag{1.23}$$

where $\overline{\cdot}$ is a Reynolds average, filtering the turbulent motions, and $\langle\cdot\rangle$ is a wave average, i.e. filtering wave-induced motions [Phillips, 1977, p. 118].

Defining wave-induced motions is a non-trivial task from a theoretical point of view, and this is even more complicated in data (where all the state variables of the flow are often not observed). For flow over canopies, the existence of a third component in the flow [denoted by

u'' in e.g. Kaimal and Finnigan, 1994, p. 84] results from the spatial inhomogeneities of the canopy, which are fixed in time (at least on the timescales of turbulence). If an observer was to stand at two different positions in the same horizontal plane, it would see differences in the time- (or Reynolds-) averaged flow. Those differences then define a space-dependent deviation of atmospheric quantities from their time and space average [i.e. $\overline{u}(x,y,z) = U(z) + u''(x,y,z)$]. The ocean surface is however non-stationary, and its height is on average zero. Hence the same observer would, in the case of ocean waves, not see differences in the time-averaged flow. Hence the previous definition cannot be applied in a straightforward manner to wave-induced perturbations of the airflow.

This difficulty has led to the development of several methods to define the wave average $\langle\cdot\rangle$. From a theoretical point of view, considering only a single monochromatic wave propagating in one direction allows analysis of the flow in the frame of reference moving with the wave, where the undulations of the sea surface are stationary. In this reference frame, deviations from a Reynolds-averaged flow can, as for flow over canopies, be identified by defining the wave average $\langle\cdot\rangle$ as a space average in the direction of the wave propagation [Phillips, 1977, p. 119]. Wave-induced motions are, in this frame of reference, periodic with respect to the wave period. Note that the Reynolds average, although sometimes considered as a time average [Makin et al., 1995, Makin and Mastenbroek, 1996, Hara and Belcher, 2002, 2004], can also be defined as an average in the direction perpendicular to the wave propagation [Phillips, 1977, Kudryavtsev and Makin, 2004].

In a realistic setting, the surface is described by a continuous spectrum of waves. Assuming that each wavelength generates airflow perturbations traveling at its speed, identification of wave-induced motions requires a space-time Fourier transform, to separate Fourier components advected at the flow speed from components traveling at the wave speed, as done in LES by Hao and Shen [2019]. However, simultaneous temporal and spatial measurements of the flow are seldom available in field experiments. Cross-correlations between the surface displacement and temporal measurements of the wind field have been used to identify the dominant wave-coherent motions [Hristov et al., 1998, 2003] and, when detailed measurements of the sea surface are available, their frequency spectra [Veron et al., 2007, 2008, Grare et al., 2013, 2018].

WAVE-INDUCED STRESS The existence of wave-induced motions and of an undulating surface has important consequences on the momentum balance of the mean flow. More precisely the Reynolds- and wave-averaged horizontal momentum balance can be written, for a stationary and horizontally homogeneous flow, as

$$\tau_t(z) + \tau_w(z) + \tau_v(z) = u_*^2. \tag{1.24}$$

This equation expresses the momentum conservation in the constant-flux WBL. The total momentum flux divided by air density (u_*^2) is split between turbulent (τ_t), wave-induced (τ_w), and viscous (τ_v) stresses [Janssen, 1989, Makin et al., 1995]. At the top of the WBL, the momentum flux is supported by turbulent stresses ($\tau_w = \tau_v = 0$) and, at the surface, the turbulent stress vanishes, and the flux is supported by wave-induced and viscous stresses. Note that in the following we consider only the case of wind-waves, extracting momentum from

the mean flow (i.e. no swell), and hence $\tau_w \geq 0$. The additional stress component τ_w is the analogue of the "dispersive flux" for flows in the roughness sublayer of canopies [Wilson and Shaw, 1977].

The presence of an undulating surface implies that the momentum balance should be written in surface following coordinates [see, e.g. Phillips, 1977, Chalikov and Makin, 1991, Kudryavtsev and Makin, 2004, Hara and Sullivan, 2015, for several surface-following coordinate choices]. In these coordinates, the turbulent and wave-induced stresses are expressed as

$$\tau_t = -\langle \overline{u'W'} \rangle \tag{1.25a}$$

$$\tau_w = -\langle u_w W_w \rangle + \rho_a^{-1} \langle p_w \partial_x \eta \rangle, \tag{1.25b}$$

where $W = w - (\partial\eta/\partial x)u - (\partial\eta/\partial y)v - (\partial\eta/\partial t)$ is the contravariant vertical velocity (η is the sea-surface height displacement, i.e. $\langle\eta\rangle = 0$), p_w is the wave-induced pressure, and ρ_a is the air density. [13]

Wave-induced stress (Eq. 1.25b) contains two terms: correlations between wave-induced motions and correlations between wave-induced pressure and surface slope. At the surface, the main contribution to wave-induced stress is the pressure-slope correlation, termed “form drag” by Phillips [1977], which is responsible for the wave growth and hence maintenance of wave-induced motions [Makin and Mastenbroek, 1996]. In a pioneering work, Longuet-Higgins [1969a] further showed that form drag, and hence wave growth, results not only from pressure-slope correlations, but also from wave-induced variations in surface turbulent stress in phase with the wave height (i.e. in quadrature with the wave slope), which were shown to act as wave-induced pressure variations in phase with wave slope. Those are included implicitly in the pressure-slope correlation term, at the surface.

THE VISCOUS SUBLAYER In the momentum balance discussed above, the viscous stress τ_v acts only at the bottom of the WBL, in the so-called viscous sublayer. In wind-over-wave models of the WBL, described below, it represents the “unresolved” (small scale) processes. These small scale processes include viscous friction, but also wave-induced stresses due to waves too small to be explicitly included in τ_w, due to lack of knowledge about their impact. Historically, the WBL model of Chalikov and Makin [1991] included high frequency gravity waves in the unresolved processes. They were described through a “background” roughness coefficient, tuned to observations. Following ideas of Janssen [1989], Makin et al. [1995] extended the model, with the hypothesis that all surface undulations can be described by a wave spectrum. This eliminates the need for a background roughness parameter, which was then set

[13] Note that this expression of wave-induced stress is as presented in recent works [e.g Kudryavtsev and Makin, 2004]. In the original work of Chalikov and Makin [1991], turbulent stress is defined without the contravariant velocity field and hence the previous equation reads

$$\tau_t = -\langle \overline{u'w'} \rangle$$

$$\tau_w = -\langle u_w w_w \rangle + \langle \widetilde{p} \partial_x \eta \rangle + \langle \overline{u'^2} \partial_x \eta + \overline{u'v'} \partial_y \eta \rangle$$

to the height of the surface viscous sublayer z_0^v

$$z_0^v = 0.14 \frac{\nu}{\tau_t^{1/2}(z_0^v)}. \tag{1.26}$$

Evaluation of Eq. 1.26 requires specification of the turbulent stress on top of the viscous sublayer. Makin et al. [1995] further assumed that wave-induced stress is constant with height in the viscous sublayer [$\tau_w(z_0^v) = \tau_w(0)$]. This is equivalent to the assumption that all waves with lengths smaller than z_0^v do not contribute to the wave induced stress. Hence, by using Eq. 1.24 on top of the viscous sublayer (where the viscous stress cancels), the surface turbulent stress can be expressed as a function of the surface wave-induced stress, i.e. form drag. Note that it is not expected that the behavior of the flow in this viscous layer is equivalent to the flow in the viscous layer of smooth-wall flows. In the former, small-scale smooth and breaking waves act as roughness elements, and most likely perturb the turbulent organization present in the latter [streaks, or self-sustaining coherent motions, Jiménez, 2012].

To summarize, above the height z_0^v, the wave-averaged momentum balance in the WBL is a balance between turbulent and wave-induced stresses, which sum-up to a height-independent total momentum flux (u_*^2). Close to the surface, turbulent stress vanishes, and wave-induced stress is responsible for the momentum flux to the waves, through form drag.

1.3.2 Theoretical models of wave-induced stress

The previous section highlighted that the impact of waves on the WBL momentum balance occurs through wave-induced stress. As an energy balance reveals (see Sect. 1.3.3), wave-induced stress is related to the extraction of mean-flow energy by waves, and hence to wave growth. Historically, the determination of wave growth begins with the "separated sheltering" mechanism of Jeffreys [1925], according to which airflow separation on the leeside of the wave leads to a pressure drop and hence to wave growth. However, the growth rates predicted by this mechanism did not match measurements. Phillips [1957] and Miles [1957] proposed two mechanisms which aim at explaining the initial and later stage of wave growth, respectively. The mechanism of Phillips [1957] considers the effect of turbulent pressure fluctuations on the surface, leading to a linear wave growth. The mechanism proposed by Miles [1957] considers the inviscid growth of wave-induced motions and waves in the context of stability analysis and neglects turbulent Reynolds stresses, leading to an exponential wave growth. Belcher and Hunt [1993] later argued that the Miles mechanism might not be valid for short waves, for which the effect of turbulence becomes important. This led to the "non-separated sheltering" mechanism, whereby, even without airflow separation (which requires waves to be steep), the presence of waves results in a pressure anomaly correlated to wave slope. In the following, we discuss in more details the Miles [1993] and Belcher and Hunt [1993] mechanisms, since our interest lies in the description of a stationary wind-over-waves system, and not in the initial stages of wave growth described by Phillips [1957].

To understand the dependence of wave-induced stress on sea state, it is interesting to recast it in terms of vortex force. For a stationary flow, the Reynolds-averaged horizontal momentum

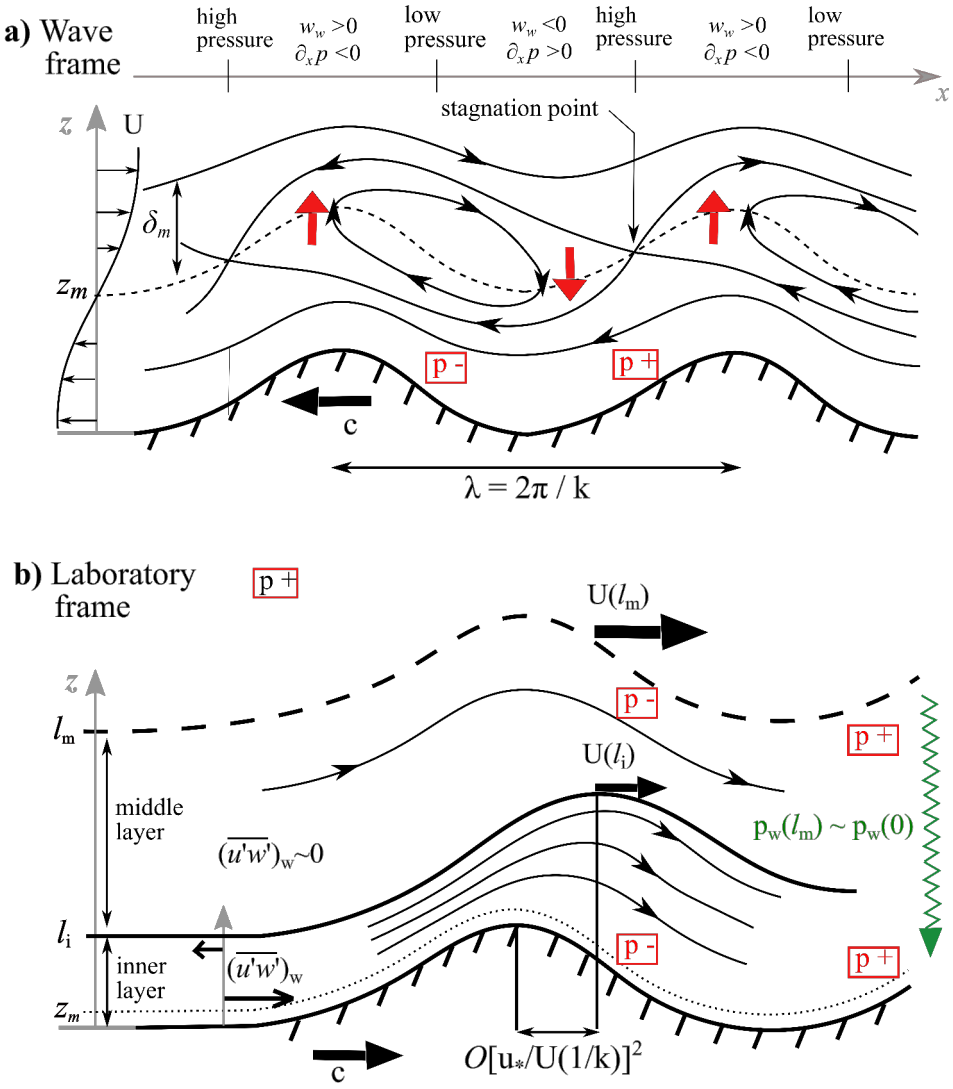

Figure 1.5: Two models of wind-wave interactions. a) Laminar and inviscid matched layer mechanism [Miles, 1957, in the wave frame of reference] and b) non-separated sheltering mechanism for a turbulent flow [Belcher and Hunt, 1993, in the laboratory frame of reference]. a) The closed loops formed by the streamlines around the matched height generate pressure-slope correlations due to vertical velocity (red arrows), which result in vortex force at the matched height, and wave growth. b) In the inner (turbulent) region, surface undulations cause, through turbulent stresses ($(\overline{u'w'})_w$), a displacement of the streamlines downwind. This results in a pressure anomaly at the top of the (inviscid) middle layer, which induces (green arrow) pressure-surface slope correlations at the surface (in red) , and a vortex force at the top of the inner region. Note that in b), the matched height lies in the bottommost layer of the flow, called the internal boundary layer.

.

balance (before wave averaging) can be written as

$$\frac{\partial \overline{u}}{\partial t} = 0 = -\frac{1}{\rho_a}\frac{\partial p_w^{\text{tot}}}{\partial x} - \Omega_w w_w + \frac{1}{\rho_a}\frac{\partial \eta}{\partial x}\frac{\partial p_w}{\partial z} + \frac{\overline{\tau}_{x,x_j}}{\partial x_j}, \tag{1.27}$$

where we have introduced $\overline{\tau}_{x_i,x_j}$, the Reynolds-averaged turbulent and viscous stress tensor (i.e. such that $\langle \overline{\tau}_{x,z} \rangle = \tau_t + \tau_v$), $\Omega_w = \partial_z u_w - \partial_x w_w$, the spanwise component of the wave-induced vorticity, and with $p_w^{tot} = p_w + \frac{1}{2}(u_w^2 + w_w^2)$ the wave-induced total pressure. The term $\Omega_w w_w$ is called the vortex force [Lighthill, 1962].

If Eq. 1.27 is wave-averaged, the horizontal pressure gradient term cancels, due to the streamwise periodicity of wave-induced motions, and Eq. 1.24 is obtained, with the vertical gradient of wave-induced stress expressed as

$$\frac{\partial \tau_w}{\partial z} = -\langle \Omega_w w_w \rangle. \tag{1.28}$$

In the following, we discuss models for the computation of the vortex force: Miles [1957] matched layer theory for a laminar flow and Belcher and Hunt [1993] non-separated sheltering mechanism for a turbulent flow. In both cases, the wave-induced motions are computed for a monochromatic wave, of wavenumber k, amplitude a, and phase speed c, traveling in the wind direction, and small slopes are considered ($ak \ll 1$). Airflow separation for steep slopes, along with more recent developments, are discussed in Sect. 1.3.2.3.

The notation $\mathrm{d}_k\langle \Omega_w w_w \rangle$ is used hereinafter to designate wave-averaged vortex force for a single monochromatic wave, also called spectral density of vortex force. In the case of a realistic sea surface, it corresponds to the wave-averaged vortex for waves of wavenumber between k and $k + \mathrm{d}k$, and is hence related to the total wave-averaged vortex force as

$$\langle \Omega_w w_w \rangle = \int_k \mathrm{d}_k \langle \Omega_w w_w \rangle. \tag{1.29}$$

1.3.2.1 The matched layer inviscid theory

Miles [1957] proposed a laminar and inviscid theory for the generation of the vortex force in the WBL. By considering the growth of wave-induced perturbations generated by a monochromatic wave, he was able, using stability analysis, to derive the wave growth rate, and hence the vortex force. This analysis was rather mathematical, and in a later work, Lighthill [1962] discussed Miles' results using physical arguments.

It is first instructive to consider the following expression, derived by Davis [1972]

$$-k^2[U(z) - c(k)]\langle \mathrm{d}_k \Omega_w w_w \rangle = \left\langle \frac{\partial \mathcal{S}}{\partial x} w_w \right\rangle \tag{1.30}$$

which links the wave-averaged vortex force to the variations of the Reynolds stress tensor anisotropy ($\mathcal{S}$ is defined as $\mathcal{S} = -(\partial_x^2 - \partial_z^2)\langle \overline{u'w'} \rangle + \partial_x \partial_z (\langle \overline{u'^2} \rangle - \langle \overline{w'^2} \rangle)$). For a laminar flow, the RHS of the above equation vanishes, and wave-averaged vortex force is localized at the *matched*

height z_m, where $U(z_m) = c$. However, for a turbulent flow, the zone where wave-averaged vortex force is non-zero might extend around the matched height, according to Eq. 1.30. This is why, following Phillips [1977], z_m is termed the "matched height" instead of the "critical height", as originally used by Miles: this emphasizes that, unlike the high-vorticity and thin critical layer of laminar instability theory, the thickness and intensity of the vortical layer around the matched height depend on turbulence anisotropy.

Neglecting turbulent stress, Miles [1957] found a vortex force

$$\mathrm{d}_k \langle \Omega_w w_w \rangle|_{\mathrm{Matched}} = \underbrace{-\frac{\pi}{k}\frac{U''(z_m)}{U'(z_m)}}_{\mathrm{I}} \underbrace{\langle w_w^2 \rangle(z_m)}_{\mathrm{II}} \delta(z - z_m), \tag{1.31}$$

where δ is the Dirac function. This expression was obtained by assuming a small wave slope ($ak \ll 1$), a wavenumber lying between the boundary layer depth (D) and the matched layer height ($1/D \ll k \ll 1/z_m$), and a small friction velocity ($u_* \ll U(1/k)$).

The wave-averaged vortex force is localized at the matched height z_m and is the product of two terms. Term I depends on the mean wind curvature ($U'' = d^2U/dz^2$) and shear ($U' = dU/dz$) at the matched layer height, and reveals that, in order to have a net transfer of momentum from wind to waves (a positive vortex force), their ratio should be positive. This is usually the case in the surface boundary layer, in particular for a logarithmic wind profile. Term II depends on the wave-induced vertical velocity variance at the matched height $\langle w_w^2 \rangle(z_m)$. An expression for $\langle w_w^2 \rangle(z_m)$ was obtained by Miles, first by an approximate [Miles, 1957] and then by an exact [Miles, 1959] solution of the small-perturbation equations. Lighthill [1962] derived a similar expression than Miles [1957] by using a simple balance between wave-induced pressure perturbations and vortex force. In either case, the resulting vertical velocity was found proportional to the wave amplitude, i.e. $\langle w_w^2 \rangle(z_m) \propto a^2\omega^2/2$, yielding an exponential wave growth, unlike the linear Phillips [1957] mechanism. [14] Note that the matched layer mechanism vortex force was also derived more recently by Hristov and Ruiz-Plancarte [2014], in a a more

[14] The link between wave growth and wave-induced stress can be understood by considering atmospheric energy density ($\rho_a \frac{1}{2}\int U^2 dz$), whose rate of change due to waves is proportional to the integrated work of wave-induced stress gradient against the wave-averaged horizontal wind $\int (d\tau_w/dz) U dz$ (this follows from the non-stationary version of Eq. 1.24). This variation can be equated to the variation of wave energy which, for a wave of amplitude a, reads $\frac{1}{2}\rho_w(g + T_{sw}k^2)a^2$. For gravity waves growing exponentially under the action of the wind

$$\frac{\partial}{\partial t}\left(\frac{a^2}{2}\right)\bigg|_{wind} = \beta\frac{a^2}{2},$$

the wave growth rate β can be expressed as

$$\beta = -\frac{\rho_a}{\rho_w}\frac{2}{ga^2}\int \frac{d\tau_w}{dz} U dz.$$

Anticipating the next subsection, this is related to the flux of atmospheric energy to the waves, Π^w, as $\Pi^w = \int (d\tau_w/dz) U dz$.

Now, in the case of Miles' theory, if the wave-induced velocity variance is expressed as $\langle w_w^2 \rangle(z_m) =$

general framework.[15]

The vortex force Eq. 1.31 results from the dynamical structure of the wave-induced flow around the matched layer, which is described here following Lighthill [1962] and Phillips [1977]. Assuming that the flow is two-dimensional (in the x,z plane), streamlines of the wave-induced flow form, in the frame of reference moving with the waves, closed loops (cat's-eye patterns) centered at the matched height (see Fig. 1.5a). Outside of the closed loops, the wave-induced vorticity and vertical velocity are in quadrature, and the contribution of those regions to the wave-averaged vortex force is zero. Inside of the cat's eye, fluid elements are trapped and transport the mean flow vorticity, which results in a wave-induced vorticity proportional to the mean flow curvature U'' (appearing in term I) times the width of the cat's eye. This width depends on the efficiency of fluid elements to diffuse vorticity inside the closed loop region. A diffusion coefficient can be estimated as $\langle w_w^2 \rangle / U'$, which, upon multiplication by the wave-induced vorticity U'', explains Eq. 1.31. Hence Miles' vortex force can be interpreted as resulting from the mean flow vorticity variations, transported by fluid elements trapped in the cat's-eye patterns. It is important to highlight that the above picture should be amended when turbulent motions are considered: turbulence increases vorticity diffusion (increasing vortex force) and decreases the mean vorticity gradient transported by fluid particles (decreasing vortex force) [note, however, that Lighthill, 1962, argued that both effects should compensate, and hence that the wave-averaged vortex force should be unchanged]. It also changes the horizontal dependence of the vortex force which becomes distributed around the matched height (Eq. 1.30). Last but not least, while in the laminar case the streamlines defined above can be interpreted as fluid particle trajectories; this is not true for a turbulent flow.

The time-dependent dynamics of fluid particles inside the cat's eyes were further analyzed by Reutov [1980]. It was argued that the oscillation of the particles inside the cat's eyes leads to a mixing of vorticity, which causes a decrease in the wave-averaged vortex force. This quenching of the momentum transfer from wind to waves leads to a stabilisation of the wind-over-waves coupled system over time. Although in the original analysis of Reutov [1980] the saturated wave amplitude, at equilibrium, was found to be too small compared to observations, this concept was recast by Fabrikant [1976] and Janssen [1982] in their quasi-linear theory of wave generation, explained in Sec. 1.3.2.3.

So far, only the wave-averaged vortex force ($\langle \Omega_w w_w \rangle$) has been discussed. It is however also interesting to discuss the link between wave-induced pressure (p^w) and the Reynolds-averaged vortex force ($\Omega_w w_w$). For heights sufficiently far from the wavy surface, Eq. 1.27 can be

---

$\mathcal{W}^2 a^2 \omega^2/2$, the growth rate reads

$$\beta_{\text{Miles}} = -\frac{\rho_a}{\rho_w}\pi\mathcal{W}^2 \frac{U''(z_m)}{U'(z_m)} U(z_m) = -\omega \frac{\rho_a}{\rho_w} \frac{\pi\mathcal{W}^2}{k} \frac{U''(z_m)}{U'(z_m)}$$

where the equality $U(z_m) = c$ has been used.

[15] More precisely, the vortex force reads

$$d_k \langle \Omega_w w_w \rangle|_{\text{Hristov}} = \delta(z - z_m) \frac{c\,\text{Im}(u_w)(z_0)}{k\eta} (ka)^2$$

With the wave-induced velocity u_w (a complex number in their model) stasifying a Taylor-Goldstein equation, where stability effects could be incorporated.

simplified by neglecting the pressure-slope term (the third term). Neglecting turbulence (i.e. the fourth term of Eq. 1.27), the equation is reduced to a balance between the horizontal gradient of wave-induced pressure and the vortex force. Hence, as depicted in Fig. 1.5a, wave-induced pressure and vortex force should be in quadrature. If the vortex force is further approximated, as above, by the product of the wave-averaged shear and the wave-induced vertical velocity ($\Omega_w w_w \sim U' w_w$), then the wave-induced updrafts and downdrafts should also be in quadrature with wave-induced pressure. For wave-induced streamlines described by Miles' cat's-eye pattern, the updrafts and downdrafts are located in between the edges and the middle of the cat's-eye (vertical red arrows in Fig. 1.5a). Hence, for Miles' mechanism to describe wind-waves, i.e. waves that receive momentum from the atmosphere, the center of the cat's eyes should be (at least partly) in phase with the wave slope, to induce pressure-slope correlations [see e.g. Sullivan et al., 2000].[16]

As a final remark, Eq. 1.31 can be rearranged by (i) introducing the proportionality relation between $\langle w_w^2 \rangle$ and wave amplitude a mentioned above ($\langle w_w^2 \rangle(z_m) \propto (akc)^2/2$) and, (ii) using a logarithmic mean wind profile to express U''/U' at the matched height[17]:

$$\mathrm{d}_k \langle \Omega_w w_w \rangle|_{\text{Matched}} \propto \underbrace{\frac{\exp(-\kappa c/u_*)}{z_0 k}}_{\text{I}} \underbrace{\frac{(akc)^2}{2}}_{\text{II}} \delta(z - z_m). \tag{1.32}$$

where κ is the Von Kármán constant. This expression shows that term I, originating from U''/U', expresses the dependence of the wave-averaged forced force on wave age: as the underlying wave becomes longer (i.e. faster), the vortex force decreases. Term II originates from $\langle w_w^2 \rangle$, and is related to the wave orbital velocity (akc) which, as mentioned in the introduction, is one of the defining characteristics of surface waves when compared to immobile roughness elements. More importantly, term II also reveals that the wave-averaged vortex force depends on the slope (ak) of the underlying wave, and not on its amplitude. This dependency, formulated by Munk [1955], reflects the increase in contact area between air and water due to the presence of an undulating surface, which increases the momentum flux from wind to waves, and hence vortex force. Note that the assumption that U follows a log profile, which results in the wave-age dependence of term I, is not entirely valid in the WBL (see Sect. 1.3.3) and is used here for illustrative purposes only.

[16] This displacement x_D of the center of the cat's eye with respect to the wave crest can be in fact more precisely related to the wave growth rate as $x_D k = \beta/[kU(1/k)]$ [Belcher and Hunt, 1998].

[17] assuming a logarithmic profile, $U = (u_*/\kappa)\ln(z/z_0)$ leads to $c/u_* = (1/\kappa)\ln(z_m/z_0)$ and to $U''(z_m)/U'(z_m) = -1/z_m$.

1.3.2.2 Inclusion of turbulence: the non-separated sheltering (NSS) mechanism

The work of Miles [1957] assumed a laminar and inviscid flow. More precisely, let us write the momentum balance *for wave-induced motions*, neglecting the effects of surface curvature, as

$$\frac{Du_w}{Dt} = -\frac{1}{\rho_a}\frac{\partial p_w}{\partial x} - \frac{\partial\left(\overline{u'w'}\right)_w}{\partial z}, \tag{1.33}$$

where D/Dt denotes the Lagrangian derivative, and $\left(\overline{u'w'}\right)_w = \overline{u'w'} - \langle\overline{u'w'}\rangle$ the wave-induced variations of turbulent stress [see e.g. Belcher and Hunt, 1998]. The linear analysis of Miles [1957] derived an expression for wave-induced motions from the above balance by neglecting turbulence, i.e. $\left(\overline{u'w'}\right)_w$.

Following this development, several works included turbulent motions in the derivation of the wave-averaged vortex force [Townsend, 1972, Jacobs, 1987, Van Duin and Janssen, 1992, Belcher and Hunt, 1993, Belcher, 1999]. In particular, Belcher and Hunt [1993] found that, for short (i.e. young) waves, effects of turbulence overcome Miles' mechanism in the determination of the vortex force. More precisely, they argued, following Townsend [1972], that there exists a layer close to the surface, called the *inner region*, in which eddies have a turnover time smaller than their advection time across the wave.[18] In the inner region, of height l_i of about $0.1k^{-1}$ for a short wave, eddies are in equilibrium with the mean flow and hence wave-induced variations of turbulent stress can be modeled with a mixing-length model

$$\left(\overline{u'w'}\right)_w = 2\kappa z u_* \frac{\partial u_w}{\partial z}, \tag{1.34}$$

In the outer region, for heights $z > l_i$, the eddies follow rapid distortion theory, and Belcher and Hunt [1993] found that the flow can be considered as being inviscid (in the sense that $\left(\overline{u'w'}\right)_w = 0$).

The analysis of Belcher and Hunt [1993] resulted in a mechanism for the generation of wave-averaged vortex force called "non-separated sheltering" (NSS) mechanism. It is summarized in Fig. 1.5b for slow waves. To start with, in the presence of an undulating surface, the streamlines are bent, which creates pressure gradients higher on the crest than on the trough of the wave. In the inner region, as those horizontal pressure gradients develop they induce vertical gradients of wave-induced turbulent stress (from Eq. 1.33). This results in higher stress at the surface

[18] The turnover and advection timescales were defined respectively as

$$T_L = \frac{z}{2\kappa u_*}, \quad T_A = \frac{1}{k|U(z) - c|}$$

And hence the inner region height, where $T_L > T_A$, is defined by

$$l_i = \frac{2\kappa u_*}{k|U(z_i) - c|}.$$

than at the top of the inner region (bottom-left part of Fig. 1.5b). Hence, in the inner region, the flow is decelerated as it reaches the surface (from Eq. 1.27) which causes a displacement of the streamlines downwind by a distance which can be shown to be proportional to $[u_*/U(1/k)]^2$ (middle of Fig. 1.5b). This "sheltering" effect of the flow then causes pressure differences in the inviscid outer region, at the so-called middle layer height l_m, which are slightly in phase with the wave slope. Those pressure differences affect, at leading order, the pressure at the surface (green arrow in Fig. 1.5b), causing wave growth, and hence a vortex force. At leading order in $u_*/U(1/k)$, it reads

$$\mathrm{d}_k\langle\Omega_w w_w\rangle|_{\mathrm{NSS}} = -\underbrace{\mathcal{C}_\beta \frac{u_*^2}{c^2}}_{\mathrm{I}} \underbrace{\frac{(akc)^2}{2}}_{\mathrm{II}} \delta(z-l_i), \tag{1.35}$$

where the vortex-force coefficient $\mathcal{C}_\beta^{(0)}$ depends on the mean wind speed in the frame of reference of the wave $U_c(z) = U(z) - c$, and reads

$$\mathcal{C}_\beta = \frac{U_c^2(l_m)}{U_c^2(l_i)}\left(2\frac{U_c(l_m)^2}{U_c(l_i)^2} - \frac{U_c^2(l_i)}{U_c^2(l_m)} + 1\right). \tag{1.36}$$

The NSS vortex force is localized at the inner layer height, and its magnitude depends on two terms, similar to the matched layer vortex force (Eq. 1.32). Term I depends on wave age, and on the mean wind shear in the middle layer $[U_c(l_m)/U_c(l_i)]$. The quadratic dependence on inverse wave age is an important result, that was originally proposed by Plant [1982] on the basis of measurements. Term II again expresses the dependence of the vortex force on wave slope. Note that the estimates of C_β by Plant [1982] are larger than those found from the analytical theory of Belcher and Hunt [1993] by a factor of two. [19] Recent works, presented below [Kudryavtsev and Chapron, 2016], show that this mismatch can be corrected by accounting for short wind-wave modulations by longer waves.

The NSS mechanism is valid for slow $c/u_* < 15$ and fast $c/u_* > 25$ waves [Belcher and Hunt, 1993, Belcher, 1999]. Common to both situations is the matched layer height being different from the inner region height. For slow waves, the matched layer lies in the inner layer (see Fig. 1.5b), where wave-induced variations of turbulent stress are the dominant term in the momentum balance Eq. 1.33. This is true in particular at the matched height, which is then of little dynamical importance (in the sense that the linear advection terms, on the left-hand-side of Eq. 1.33, are negligible).[20] For intermediate waves, with $15 \leq c/u_* \leq 30$, the matched layer and inner region heights are similar. Belcher and Hunt [1993] mention that, for this configuration, the matched layer should be significant in the determination of vortex force, and that the effect of the inner layer dynamics is to tilt the streamlines of the cat's-eye patterns: streamlines below and above z_m are displaced upwind and downwind, respectively. Note that

[19] Plant [1982] predicted $C_\beta = 40$. Other theories predicted coefficients of similar magnitude: 15 for Townsend [1972] and 40, for high winds, in Stewart [1974].

[20] In Belcher and Hunt [1993]'s theory, the matched layer is simply affecting the height at which the solutions should start.

Janssen [2004] has suggested that the matched height mechanism could be valid for all wave ages. This results from using a different scaling for eddy-turnover time than the one used in the original work of Belcher and Hunt [1993]. In the following we focus on slow and short waves which, as mentioned in the introduction, are more determinant in setting the wind-over-waves equilibrium described in Sect. 1.3.3. We hence do not discuss the case $c/u_* > 25$.

In addition to wave age, there is another limitation to the NSS mechanism. When the underlying wave is too steep, the downwind thickening of the streamlines can cause a detachment of the flow on the leeside of the wave, similar to the separated sheltering mechanism [Jeffreys, 1925]. Such airflow separation events, which can occur e.g. for breaking waves, are discussed below.

1.3.2.3 Further developments

Following the works of Miles [1957] and Belcher and Hunt [1993], other expressions for the vortex force were presented, which we discuss below. Before, we should note that in Eqs. 1.32 and 1.35, the wave amplitude a was used. For a realistic sea surface, the amplitude of an individual wave component can be related to the wave spectrum $S(k)$ as $a^2 = S(k)kdk$. Upon replacement in Eqs. 1.32 and 1.35, the total wave-averaged vortex force for a realistic sea can then be obtained by summation over all wave components (Eq. 1.29). In addition, for waves whose direction of propagation is at an angle with the mean wind direction, directional dependencies for the vortex force have been proposed [Plant, 1982, Mastenbroek et al., 1996] and, for simplicity, are not discussed here.

Quasi-linear theory Following Miles [1965] and the analysis of Reutov [1980], Fabrikant [1976] and Janssen [1982] proposed a quasi-linear theory of wave generation, where a broadband wave spectrum and a time-dependent wind were considered. They considered a continuum of matched layers with random phase, each corresponding to a wave component. The destructive interference between matched layers resulted in a quenching of the vortex force which was much larger than found by Reutov [1980], and closer to measurements. [21] The numerical studies of Janssen [1982, 1989] further revealed that wave growth was quenched due to the extraction of momentum from the mean component, which reduces the mean wind curvature (term I in Eq. 1.31): this effect was found to be particularly important for short

[21] More precisely, a multiscale expansion of quantities as a function of $(\rho_a/\rho_w)^{1/4}$ was performed. Oscillations of waves occur on the linear time scale τ_0, the mean wind speed changes on a timescale $\tau_1 = (\rho_a/\rho_w)^{1/2}t$, while wave growth (wind energy input on a scale) occurs on a timescale $\tau_2 = (\rho_a/\rho_w)t$. This follows from the expression of the growth rate (see the footnote 14), where it is evident that the growth rate is proportional to the ratio of water to air density. The resulting vortex force, which governs the evolution of the mean wind profile on the intermediate timescale τ_1, reads

$$\mathrm{d}_k\langle\Omega_w w_w\rangle|_{\mathrm{QL}} = -\frac{\pi c^2 k_c^2}{2\Delta c}\mathcal{W}(k_c)^2 U''(z_m)S(k)k\delta(k-k_m)\mathrm{d}k$$

where $\mathcal{W}$ is a normalized wave-induced velocity satisfying a Rayleigh equation, depending on the mean wind profile, and Δc is the difference between the gravity waves phase and group speed, equal to $1/2$ for gravity waves. Note that this expression is singular when approaching the transition between capillary and gravity waves, and is hence suited for longer, dispersive waves.

waves (small c/u_*). This is discussed in more details below in the context of the non-separated sheltering mechanism. Note that those numerical simulations were then used in Janssen [1991] to derive a parameterization of vortex force, with the aim to couple numerical weather and wave prediction models.

IMPACT OF LONGER WAVES ON THE NSS MECHANISM The analysis of Miles [1965] (which led to the quasi-linear theory) highlighted that the coexistence of multiple wave frequencies could result in a reduction of the vortex forces generated by each of the wave components. More precisely, the existence of a vortex force, and hence of wave-induced stress, results in a change of turbulent stress in the WBL (Eq. 1.24). Hence the NSS mechanism, which results from variations of turbulent stress in the inner region, should be affected by this modification.

This "sheltering" effect was formalized by Makin and Kudryavtsev [1999] and later by Belcher [1999]. Based on numerical simulations Mastenbroek et al. [1996], Makin and Kudryavtsev [1999] suggested using the local turbulent stress on top of the inner region in place of the friction velocity in the computation of the NSS vortex force (Eq. 1.35), i.e.

$$\mathrm{d}_k\langle\Omega_w w_w\rangle|_{\text{NL-NSS}} = \mathcal{C}_\beta \frac{\tau_t[l_i(k)]}{c^2(k)} c^2(k)k^2 S(k)\delta[z - l_i(k)]k\mathrm{d}k. \tag{1.37}$$

Hence, as longer waves grow they generate vortex force, and hence wave-induced stress, that "shelters" the shorter waves, reducing the turbulent stress on top of their inner region. The reduced vortex force of the shorter waves, and hence of their growth leads to a non-linear stabilization of their amplitude, similar to the quenching mechanism put forth by Janssen [1982].

IMPACT OF BREAKING WAVES Both the matched layer and the NSS mechanisms require waves that are not steep. For steep waves, airflow separation can occur, resulting in a sharp pressure drop on the forward face of the wave associated with a recirculating pattern [see the experimental work by Banner and Melville, 1976, Banner, 1990, Reul et al., 1999, 2008]. Those transient events are associated with waves whose slope is generally confined between 0.1 and 0.5, which are also often breaking waves [Melville, 1996]. Field measurements indicate that the wave-breaking distribution is strongly correlated with the wind speed, and hence that it can be an important parameter in the determination of the wind-and-waves equilibrium [see the measurements Sutherland and Melville, 2013, which cover a wide range of wave scales]. Note that recently, Husain et al. [2019] found, using Large Eddy Simulations and laboratory measurements, that for strong winds, a significant fraction of airflow separation events could also be associated with non-breaking waves.

Airflow separation events have been modeled as additional sources of vortex force by Kudryavtsev and Makin [2001] and later by Kukulka et al. [2007]. As the airflow separates over a wave of steepness ϵ_b and wavenumber k, it creates a pressure difference Δp between its forward and backward faces. The wind force per unit surface area at the top of the wave is then $-\Delta p 2k\epsilon l_b(k)$, where l_b is the length of of the breaking crest (i.e. perpendicular to the direction

of wave propagation). Hence a vortex force results

$$\mathrm{d}_k\langle\Omega_w w_w\rangle|_{\mathrm{AFS}}(z) = \rho_a^{-1}\Delta p 2\epsilon_b\delta(z-\epsilon_b k^{-1})l_b(k). \tag{1.38}$$

The pressure difference was further parameterized (based on experiments) as a function of a drag coefficient c_d^b, i.e. $\Delta p = \rho_a c_d^b[U(\epsilon_b k^{-1}) - c(k)]^2$ (and $\Delta p = 0$ if the wind on top of the breaking crest, $U(\epsilon_b k^{-1})$, is smaller than the speed of the wave, c). Note that, similarly to the reduction of the NSS sheltering mechanism presented above, Kukulka et al. [2007], Kukulka and Hara [2008b] and Mueller and Veron [2009] proposed a sheltering associated with airflow separation events: smaller waves, on the leeward side of a breaking wave are sheltered from the mean flow, leading to a strong reduction of their vortex force and viscous stress. This sheltering mechanism was found to be important for growing and very young seas, as found mostly in laboratory conditions [Kukulka and Hara, 2008b].

For a realistic sea surface, $l_b(k)$ is replaced by $\Lambda(k)\mathrm{d}k$, the length of breaking crests of a given wavenumber per unit area of surface and per unit time. This quantity, introduced by Phillips [1985], represents the scale-dependent distribution of transient wave-breaking events. It is stressed that, even if a small fraction of ocean waves are breaking (5%), their impact on atmospheric turbulence is significant [Banner, 1990, Kudryavtsev et al., 2014]. In addition, Csanady [1985] argued, on the basis of laboratory measurements of Kawai [1981] and Okuda et al. [1977], that airflow separation on top of centimeter-scale breaking waves could in fact be three-dimensional, due to realistic sea-surface waves being short-crested. This has influences on the properties of the recirculating region, which is no longer isolated from the rest of the flow, but can lead to a "reversed-horseshoe" kind of motion, with entrained fluid escaping from the sides of the wave before being advected forward again.

Finally, besides supporting the vortex force, airflow separation events also have a profound impact on turbulence spectra. As demonstrated by the LES of Suzuki et al. [2013], airflow separation events shortcut the inertial-subrange energy cascade through two processes. First, the energy they extract from the mean flow through wake production (see below) is directly converted to small-scale eddies instead of being injected at the energy-containing scale. Second, large eddies are transformed into small scale eddies in the wake of the air-flow separation events. Both processes could change the properties of the energy cascade of the inertial subrange in the vicinity of the elements causing air-flow separation. While this has been extensively investigated for flow inside canopies and in their roughness sublayer [Finnigan, 2000], it remains both a theoretical and experimental challenge for flows over the wind-waves.

IMPACT OF SHORT WAVE MODULATIONS The NSS mechanism (Eq. 1.35) resulted in a coefficient $\mathcal{C}_\beta$ which is too low compared to measurements Plant [1982]. Following Longuet-Higgins [1969b] and Davis [1972], Kudryavtsev and Chapron [2016] recently included the impact of short wave modulations by longer waves in the NSS mechanism to correct this deficiency. The orbital velocity of a given wave indeed induces a modulation of the steepness of shorter waves, larger on the crests than in the troughs of the modulating wave. Hence the short-wave breaking statistics change (wave breaking becomes more intense on the lee side of the wave). This asymmetric variation induces additional turbulent stress variations in the inner region, leading to an enhanced vortex force for the long, modulating wave. Kudryavtsev

and Chapron [2016] used a wind-over-waves model [Kudryavtsev et al., 2014] to compute the variation of short-wave breaking statistics along the longer wave, and found a significant enhancement of the vortex force, consistent with Plant [1982] measurements.[22]

This indicates that, for a realistic sea surface, the vortex force provided by a single wave component according to the NSS mechanism is significantly dependent on the existence of shorter waves, whose amplitude is modulated by that larger wave component.

1.3.2.4 Discussion

In this section we have discussed theoretical models for the generation of vortex force for slow monochromatic waves (i.e. $c/u_* < 30$). All models result in a vortex force localized either at the matched layer height or at the inner region height. This implies, from Eq. 1.28, a wave-induced stress which is constant up to the matched or inner region height. This discontinuous picture must be amended for realistic conditions. As mentioned in Sect. 1.3.2.1, inclusion of turbulence in the matched layer formalism results in a broadening of the area where the wave-averaged vortex force is non-zero. In the case of the NSS mechanism, numerical simulations have shown that the vertical distribution of wave-induced stress is best described by an exponential function, with a sharp decay on top of the inner region [Mastenbroek et al., 1996]. In addition, in the case of a broadband wave spectrum, the total wave-induced stress (Eq. 1.29) is smoother than contributions from individual wave components, even if those are discontinuous [e.g. Kudryavtsev et al., 2014].

There is no definite consensus on the mechanism responsible for wave-induced stress. However the matched layer mechanism seems to be dynamically important for long waves, while the NSS mechanism is significant for shorter waves. Belcher [1999] defined the transition between the two regimes for waves whose phase speed is $c/u_* = 15$. Kihara et al. [2007] found, using DNS over a single monochromatic wave, that the transition occurs for $c/u_* \sim 4$, and that for $c/u_* \geq 16$, the NSS mechanism becomes again the dominant mechanism. The authors mention that they expect their results to be significantly sensitive the the Reynolds number of the DNS ($\propto u_*/(k\nu)$), which in their case was ~ 150 [consistent with an earlier DNS analysis at similar Reynolds numbers, Sullivan et al., 2000]. The Reynolds-number dependence of the vortex force was also discussed by Meirink and Makin [2000] using a second-order turbulent closure. The authors found a strong increase of form drag with decreasing Reynolds number. This was related, among others, to an increase of the inner layer height with viscosity,

[22] More precisely, if higher order terms are kept, the asymptotic analysis of Belcher and Hunt [1993] leads to the following vortex force caused by the long modulating wave of wavenumber k

$$\mathrm{d}_k\langle\Omega_w w_w\rangle|_{\mathrm{KC16}}(z) = \frac{\tau_t(l_i)}{c^2(k)}\frac{U_c^2(l_m)}{U_c^2(l_i)}\Bigg[\underbrace{2\frac{U_c(l_m)^2}{U_c(l_i)^2} - \frac{U_c^2(l_i)}{U_c^2(l_m)} + 1}_{\text{non-separated sheltering}} - \underbrace{\frac{\hat{u}_w}{U_c(l_i)}\left(1 + \frac{U_c^2(l_i)}{U_c^2(l_m)}\right)}_{\text{impact of surface drift}}\Bigg](ak)^2\delta(z-l_i)$$

where, for simplicity, the dependencies of l_i and l_m with respect to k have been dropped, and U_c denotes the wind speed in the reference frame moving with the wave ($U - c$). The second term accounts for the impact of the surface drift ($\hat{u}_w$) on the vortex force. The surface drift is here the maximal variation of wave-induced horizontal velocity along the crest of the wave. If the variations in the surface drift are evaluated through a Charnock relation, as in Belcher and Hunt [1993], the result is negligible.

which in addition results in an increase of the wave-age threshold between NSS and matched layer mechanisms. Finally, a recent LES study by Åkervik and Vartdal [2019] revealed that the wave-induced perturbations to turbulence increase with Reynolds number, which seems to indicate that the NSS mechanism is a high-Reynolds number mechanism, as originally suggested by Belcher and Hunt [1993]. This Reynolds-number dependence of processes is not anecdotal since, as mentioned in the introduction, in realistic conditions, the Reynolds number associated with different wave components can vary greatly with respect to the overall Reynolds number of the flow.

The matched layer mechanism has been identified in field measurements by Hristov et al. [2003], for waves such that $16 < c/u_* < 40$, using the wave-coherent motion extraction technique of Hristov et al. [1998]. This result has been confirmed by Grare et al. [2013, 2018] using the spectral analysis of Veron et al. [2007, 2008]. In both cases two critical features of the matched layer mechanism were identified, as also confirmed by the DNS of Sullivan et al. [2000] over monochromatic waves: (i) a jump in the phase relation between wave-coherent wind components and the surface elevation when the matched layer height is crossed; (ii) a step-like distribution of wave-induced stress, which vanishes very fast above the matched layer height. For smaller waves, the field measurements compiled by Plant [1982] provided a dependence of wave growth rate with wave age consistent with the NSS mechanism [but with a difference in magnitude, explained by Kudryavtsev and Chapron, 2016]. These are an indirect test of the NSS mechanism, and direct measurements of the inner region in field conditions remain a formidable challenge, due to its size. The Reynolds-averaged Navier-Stokes equation (RANS) numerical simulations of Makin and Mastenbroek [1996], which included rapid-distortion effects through the LRR closure scheme [Launder et al., 1975], also confirmed the NSS mechanism and the vertical distribution of wave-induced perturbations of turbulent stress. As mentioned above, Kihara et al. [2007] also investigated the NSS mechanism using a DNS.

To these difficulties is added the complexity emerging from a realistic wave field, where the sheltering and modulation of small waves by long waves, and the transient wave breaking events play an important dynamical role in the total wave-induced stress. The multiscale structure of wave-induced stress results, for a stationary wind-over-waves system, from the coupling between the broadband wave field and atmospheric turbulence at all heights in the WBL, which is described in the next section, in the context of wind-over-waves models.

1.3.3 Turbulence in the wave boundary layer

As emphasized above, the equilibrium in the WBL results from a multiscale coupling between wind and waves, through wave-coherent motions, which change the properties of near-surface turbulence. In this section we first briefly discuss wind-over-waves models for the description of this equilibrium (Sect. 1.3.3.1), before discussing how the energetic (Sect. 1.3.3.2) and instantaneous (Sect. 1.3.3.3) properties of turbulence are modified in the WBL.

1.3.3.1 WIND-OVER-WAVES MODELS AND THE EQUILIBRIUM RANGE

Several wind-over-waves models have been developed for the description of the local equilibrium between turbulence and and waves in the WBL. Within a one-dimensional vertical column, those models couple an atmospheric component, e.g. a momentum balance and TKE equation, to a wave component, i.e. a balance equation describing the evolution of the wave spectrum under the action of the wind. The coupling between those two components occurs through wave-induced stress, which characterizes both the changes in the atmospheric momentum balance (Eq. 1.24) and the momentum input from the wind to the waves (the impact of wave-induced stress on the TKE balance is described in Sect. 1.3.3.2 below). Assuming that both the wind and wave systems are stationary, the wind-over-waves models thus describe the equilibrium between turbulence and locally-generated wind-waves.

More precisely, the range of gravity waves crucial to determine the stationary wind-over-waves system, described by the wave component of the wind-over-waves model, is the so-called equilibrium range. It covers wavelengths between the ten-meter scale and the centimeter scale, when surface tension starts to be important [Kitaigorodskii, 1983, Phillips, 1985]. In this range, wind input to the wave field is balanced by dissipation, mainly due to wave breaking. This results in a wave spectrum with a shape as k^{-4} [see the theoretical works of Phillips, 1958, 1985, Belcher and Vassilicos, 1997]. More recently, the role of centimeter-to-millimeter waves in the determination of the wind-and-waves equilibrium has been emphasized, as their amplitude is very sensitive to mean wind speed [Yurovskaya et al., 2013], and those scales might support a significant fraction of wave-induced stress [Kudryavtsev et al., 1999, 2014]. Larger waves result mostly from an inverse energy cascade due to wave-wave interactions, and are not directly coupled to the local wind. Their amplitude depends on the history of the wave field (e.g. on fetch). It is out of the scope of this review to discuss the impact that these long gravity waves can have on the atmospheric momentum budget, or their impact on the local wind-over-waves equilibrium through a change in the properties of the overall wave spectrum, the latter being still an open question.

Following the quasi-linear theory of Fabrikant [1976] and Janssen [1982], Janssen [1991] developed a wind-over-waves model in which a simple spectrum describing the equilibrium range was coupled to the atmospheric momentum balance. It was then extended in Janssen [1991] as being coupled with a numerical wave prediction model. More recently, Hristov et al. [2003] followed a similar approach, coupling a linearized atmospheric momentum balance with a simplified wave spectrum of the equilibrium range, with some degree of freedom in the slope of the spectrum. In those models, wave-induced stress is described by the matched layer mechanism (and its extension for the quasi-linear theory).

A second set of wind-over-waves models based on the NSS mechanism has been proposed, with a focus on obtaining the detailed properties of the sea surface, as measured from remote sensing techniques. In particular, Cox and Munk [1954] made optical measurements of the mean square sea surface slope, and found a linear increase with wind speed, due to short gravity and capillary waves, and related to the Charnock relation mentioned in the introduction. [23] This

[23] This conclusion was reached by comparing measurements of a normal and oil-slick covered surface, in which short waves are damped. Further remote-sensing studies revealed the link between those short wind-waves and wind speed [Vandemark et al., 2004]

triggered the development of a series of one-dimensional wind-over-waves models [starting from Makin and Kudryavtsev, 1999, Kudryavtsev et al., 1999], in which the whole range of wave scales is described with, among others, the constraint of having a mean squared sea surface slope consistent with the measurements of Cox and Munk [1954]. In these models, wave-induced stress is described by the non-linear NSS mechanism (Eq. 1.37, page 58), with $C_\beta = 40$, following measurements by Plant [1982]. More recently, Kudryavtsev et al. [2014] included airflow separation (Eq. 1.38, page 59) as an additional source of wave-induced stress, together with a consistent spectral wave balance equation for the description of equilibrium-range and capillary waves in which the effect of breaking waves is included.

These series of models, although simplified, do not provide an analytical solution to the wind-over-waves equilibrium. Such a solution was obtained by Hara and Belcher [2002, 2004], but requires waves smaller than 6 cm to be included in the viscous sublayer (see the discussion at the end of Sect. 1.3.1). This allowed Hara and Belcher [2002] to discuss the range of waves that are significantly sheltered by long waves (i.e. for which the Reynolds stress used to compute the vortex force in Eq. 1.37 is reduced with respect to u_*^2). They found that this effect started affecting gravity-range waves for winds of 12 m s^{-1}, and could be important for waves up to the meter scale for winds of about 18 m s^{-1}. Following those developments, Kukulka et al. [2007] and Kukulka and Hara [2008a,b] included the effect of airflow separation in the wind-over-waves model, which required the use of numerics to solve the coupled system of equations. As discussed, the Kudryavtsev et al. [2014] and Kukulka and Hara [2008a] models differ in their description of the wave spectra. Additional differences, in the atmospheric component of the wind-over-waves models, are discussed in Sect. 1.3.3.2 below.

An example of vertical profiles of wave-induced stress from two wind-over-waves models is shown in Fig. 1.6a, for a prescribed u_* of 0.7 m s^{-1} (corresponding to a 10m-wind of about 16 m s^{-1}). Wave-induced stress from the matched layer mechanism [solid line, Janssen, 1982] is compared to wave-induced stress from the NSS mechanism [Kudryavtsev et al., 2014], without and with airflow separation (dashed line and grey shading respectively). Wave-induced stress decays fast with height, and is confined within the first meters of atmospheric surface layer (the figure only shows the first 0.5 m for clarity). For heights above 0.1 m (upper panel), the order of magnitude predicted by both models is similar. However, as shown in Fig. 1.6b, wave-induced stress is not caused by the same range of waves. Waves whose matched layer height lies in the range 0.1-0.5 m (solid line in Fig. 1.6b) have a wavelength between 30 and 70 m, while waves whose inner region height is in the range 0.1-0.5 m (dashed line in Fig. 1.6b) have a wavelength between 5 and 20 m. [24]

These differences in wave scale are important when describing the sensitivity of the wind-and-waves system to external parameters such as ocean surface currents, fetch and slicks, since the response of the wave field to those forcings differs depending on the scale of the waves considered. Note that for the value of u_* considered here, the separation between a regime

[24] More precisely, the wave scale corresponding to an inner layer of height z is, as mentioned before, $0.1z^{-1}$. For a logarithmic layer, the wave scale corresponding to a matched layer of height z is

$$k = \frac{g\kappa^2}{u_*^2 \ln^2(z/z_0)}.$$

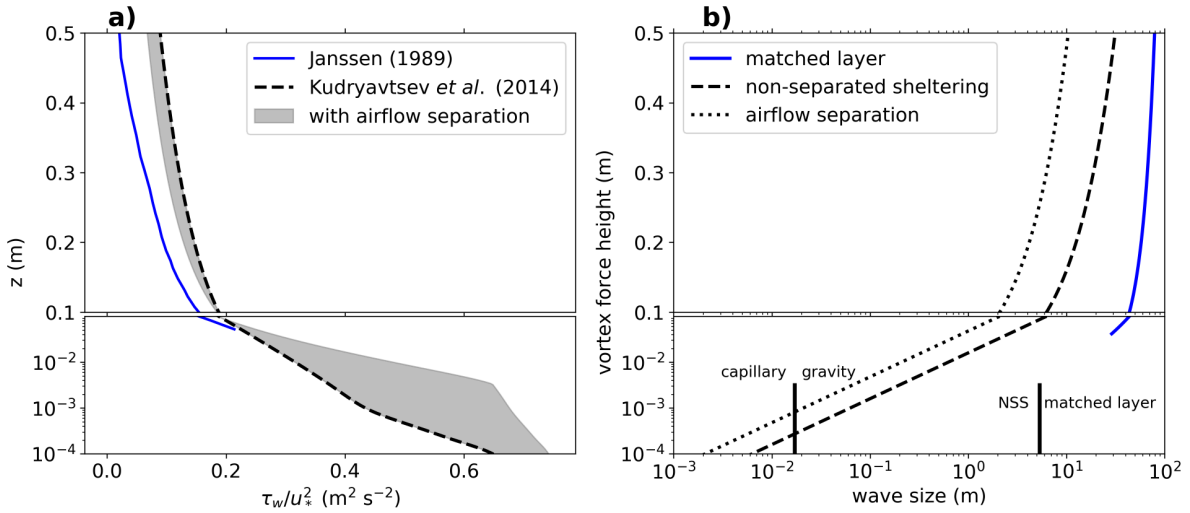

Figure 1.6: (a) Comparison of normalized wave-induced stress in the WBL for the matched layer mechanism (solid line), the NSS mechanism (dashed line) and the NSS sheltering mechanism with addition of airflow separation (grey shading). The solid line has been digitized from Janssen [1989], and the dashed line and grey shadings have been computed from the model of Kudryavtsev et al. [2014], both for $u_* = 7$ m s^{-1}. (b) Height of the wave-induced vortex force, as a function of the size of the underlying wave. Solid line is the matched layer height for a logarithmic wind profile (with roughness length of about 10^{-3}), dashed line the inner region height (set to $0.1k^{-1}$) and dotted line is the top of the breaking wave crest (set to $0.3k^{-1}$). The leftmost vertical bar denotes the wave length where the minimum in phase velocity occurs. The rightmost vertical bar denotes the wave age threshold $c/u_* = 4$ of Kihara et al. [2007] separating domains of validity of the NSS and the matched layer mechanism.

where NSS or the matched layer are dynamically important is for waves of 5 m [owing to Kihara et al., 2007, vertical line in Fig. 1.6b] or 85 m [Belcher and Hunt, 1998]. This shows, as mentioned earlier, that there exists a great range of uncertainty regarding the relative importance of the matched layer and NSS mechanisms in the determination of wave-induced stress.

The model of Kudryavtsev et al. [2014] describes wave-induced stress caused by millimeter-to-meter waves, which is important for heights below 0.1 m. As shown in Fig. 1.6a (bottom panel), this range of waves support, in the model, a significant fraction of the stress (which can be larger than 60% of the total momentum flux). As further shown in grey shadings, airflow separation (i.e. wave breaking) impacts mainly wave-induced stress for this range of waves (compare top and bottom panels of Fig. 1.6a), by causing a significant increase in wave-induced stress. It is interesting to note that airflow separation at a given height is associated with a similar but slightly different wavelength than the NSS mechanism (compare dashed and dotted lines in Fig. 1.6b). This implies, when both effects are included, that the wind field at a given height is coupled with several wave scales.

Hence it is seen that in the above models, the wind-and-wave system results from multiscale interactions between wind and waves, due to the presence of wave breaking and of the competing NSS and matched layer mechanisms. It must be emphasized that these models give an averaged description of the WBL, which, in reality, emerges from the transient coupling between wind and waves, punctuated by wave breaking events. Before focusing again on the description of the properties of the WBL without swell, it is interesting to highlight that gravity waves coupled to the wind appear to reach saturation very fast, in the sense that their elevation spectrum collapses to the k^{-4} slope for very short fetches, below what is typical of open-ocean conditions [Vandemark et al., 2004]. As Banner and Donelan [1992] mention, this saturation, reached both for low and moderate winds, is surprising, since it is unlikely that in the former regime, gravity-wave breaking plays an important role in maintaining a saturated spectra. This again demonstrates the complexity of wind-and-wave system, whose transient coupling might be qualitatively different depending on the wind speed. Note that, from a purely atmospheric perspective, for low winds where swell is usually present, Kudryavtsev and Makin [2004], Jiang et al. [2016] have, among others, shown that there exists an inverse transfer of momentum from the waves to the wind, associated with the emergence of a low-level jet. [25]

1.3.3.2 Energy balances in a stationary WBL

Among the quantities characterizing turbulence, TKE is a statistical measure of its intensity. Discussing the impact of waves on TKE requires analyzing the energy balances in the WBL. In wind-over-waves models those balances, and the models chosen for the parameterization of higher order terms, are essential to link turbulent stress to the mean wind speed U. Historically, Janssen [1982], Chalikov and Makin [1991] and Makin et al. [1995] used an eddy viscosity model, a first-order closure. However, simulations of Makin and Mastenbroek [1996], using a two-equation eddy viscosity model, showed that this simple closure was not sufficient. Building on these results, Makin and Kudryavtsev [1999] extended the model of Makin et al. [1995] using a TKE budget, which includes the effect of waves. This approach has been used in subsequent work [Hara and Belcher, 2002, 2004, Kukulka et al., 2007, Kukulka and Hara, 2008a,b, Kudryavtsev et al., 2014] . In the following we discuss the TKE budget to understand some of the statistical properties of turbulence in the WBL.

Mean, wave-induced, and TKE balances As discussed in Sect. 1.3.1, in the WBL the flow is separated into three components. The kinetic energy balance can be expressed

[25] As a side note, let us mention that the concept of equilibrium range discussed above is based on Phillips [1985] idea that, in this range of wavenumbers, the wind injects energy in the wave field at all scales, and it is balanced by dissipation and non-linear interactions. However, it is important to note that other approaches exist for the description of the equilibrium range. In particular, Zakharov and Filonenko [1966], Hasselmann et al. [1973] and Kitaigorodskii [1983] introduced the idea that wind injects energy at a bulk scale, and that wave spectrum in the equilibrium range is dominated by non-linear interactions, up to the scale where energy dissipates [see the discussion in Gemmrich et al., 1994]. This approach hence considers wind-wave interaction in a bulk sense, as opposed to the Phillips [1985] approach which however requires understanding of both the wind-wave coupling and wave-wave interactions (through wave breaking and non-linear interactions) at each wave scale [Kudryavtsev et al., 2014].

separately for each component [e.g. Makin and Mastenbroek, 1996]. The mean energy balance

$$\frac{d}{dz}(u_*^2 U) - P_t - P_w = 0 \tag{1.39}$$

is between the divergence of mean energy flux ($u_*^2 U$), and the loss of energy to turbulent (P_t) and wave-induced (P_w) motions, where

$$P_t = \tau_t \frac{dU}{dz}, \quad P_w = \tau_w \frac{dU}{dz}. \tag{1.40a,b}$$

The wave-induced motions energy balance

$$\frac{d}{dz}\Pi_w + P_w - D = 0 \tag{1.41}$$

is between the divergence of wave-induced energy (Π_w), mechanical production (P_w) and energy loss to turbulence (D), where

$$\Pi_w = \langle u_w \tau_w - \rho_a^{-1} p_w W_w \rangle, \quad D = \left\langle (\overline{u'w'})_w \frac{du_w}{dz} \right\rangle. \tag{1.42a,b}$$

Finally, the TKE balance

$$P_t + D - \epsilon = 0 \tag{1.43}$$

is between mechanical production (P_t), energy uptake from wave-induced motions (D) and TKE dissipation (ϵ, discussed below). In this last balance, diffusive fluxes are neglected (in the WBL), following Chalikov and Belevich [1993] and Janssen [1999].

With respect to a stationary and homogeneous surface boundary layer, the presence of wave-induced motions alters the WBL energy balance in three ways. First, there is an additional sink of energy for the mean flow, resulting from wave-induced stress (P_w). Second, there is an additional term (D), accounting for the transfer of energy between TKE and wave-induced energy. This term depends on the vorticity of wave-induced motions and on the wave-induced variations of turbulent stress, showing their importance not only for the NSS mechanism (Sect. 1.3.2.2) but also in the energetic balance of the WBL. Upon summation of Eqs. 1.41 and 1.43, D can be eliminated, and the energy balance for wave-induced and turbulent motions reads

$$(\tau_t + \tau_w)\frac{dU}{dz} + \frac{d\Pi_w}{dz} - \epsilon = 0. \tag{1.44}$$

It reveals that the net effect of wave-induced motions is to act as an additional source for TKE by extracting energy from the mean flow, by a mechanism similar to wake production of TKE over canopies [Kaimal and Finnigan, 1994]. The last alteration resulting from wave-induced motions is the presence of a flux of wave-induced energy Π_w. It is related to the energy loss from wave-induced motions to the waves. More precisely, summation of Eqs. 1.39, 1.41 and 1.43 and integration over the WBL (of height H) results in the following balance [discussed in

Hara and Belcher, 2004]

$$u_*^2 U - \Pi_w(z = z_0^v) - \int_{z_0^v}^{H} \epsilon dz = 0. \tag{1.45}$$

This equation describes the balance for the total energy integrated over the WBL, and shows that the flux of energy at the top of the WBL is balanced by the flux to the waves at the surface and TKE dissipation in the WBL (terms from left to right, respectively). The flux of wave-induced energy is usually related to wave-induced stress of individual wave components $\mathrm{d}_k\tau_w$ as $\Pi_w = \int c(k)\mathrm{d}_k\tau_w$, and as mentioned in Sect. 1.3.1, is mainly related to the work of wave-induced pressure against the surface vertical velocity $\langle \rho_a^{-1} p_w W_w \rangle$.

Several models for the vertical structure of Π_w have been proposed. Makin and Kudryavtsev [1999] [and subsequent work Kudryavtsev et al., 2014] , based on the numerical simulations of Mastenbroek et al. [1996], suggested that Π_w is constant within the WBL, and zero above. Hence its divergence is zero in the WBL, and Π_w only appears in the total balance (Eq. 1.45) and not in the modified TKE balance (Eq. 1.44). Hara and Belcher [2004] [and subsequent works Hara and Belcher, 2002, 2004, Kukulka et al., 2007, Kukulka and Hara, 2008a,b] assumed that that $d\Pi_w/dz$ is important in the TKE balance over the whole WBL, due to the decay of Π_w with height that should follow that of wave-induced stress [Belcher, 1999]. Finally, note that Janssen [1999] and Cifuentes-Lorenzen et al. [2018] considered that, very close to the surface, the divergence of the momentum flux is significant in Eq. 1.41, and balances the wake production of wave-induced energy P_w, which is then transfered directly to the wave field. Those different choices are related to either numerical or theoretical models and their underlying assumptions. Anticipating on the next paragraph, and Fig. 1.7b), we choose the approach of Makin and Kudryavtsev [1999] to compare the effect of different TKE dissipation parameterizations on the mean wind speed.

To summarize, the presence of wave-induced motions alters the energy budget in the WBL by extracting energy from the mean flow, which is then transfered to turbulent motions and surface waves. In particular, this energy transfer results, for a fixed mean wind speed, in an increase of the turbulent stress at the top of the WBL (u_*^2), with respect to a smooth flow [Edson et al., 2013]. In order to close the balances presented above, a parameterization of TKE dissipation is needed.

DISSIPATION OF TURBULENT KINETIC ENERGY Several vertical profiles of TKE dissipation and mean wind speed are shown in Fig. 1.7. In particular, dashed and dotted lines correspond to two choices of TKE dissipation parameterizations

$$\epsilon_{\mathrm{Hara}} = (\kappa z)^{-1}\tau_t^{3/2}, \quad \epsilon_{\mathrm{Makin}} = (\kappa z)^{-4}\tau_t^3\left(\frac{dU}{dz}\right)^{-3}, \tag{1.46a,b}$$

used in the wind-over-waves models of Hara and Belcher [2004] and Makin and Kudryavtsev [1999], respectively. The mean wind speed profile is computed from the modified TKE balance Eq. 1.44, where $d\Pi_w/dz$ has been neglected. The turbulent intensity, required to compute the mean wind speed, is obtained from the momentum balance Eq. 1.24 by using a vertical profile

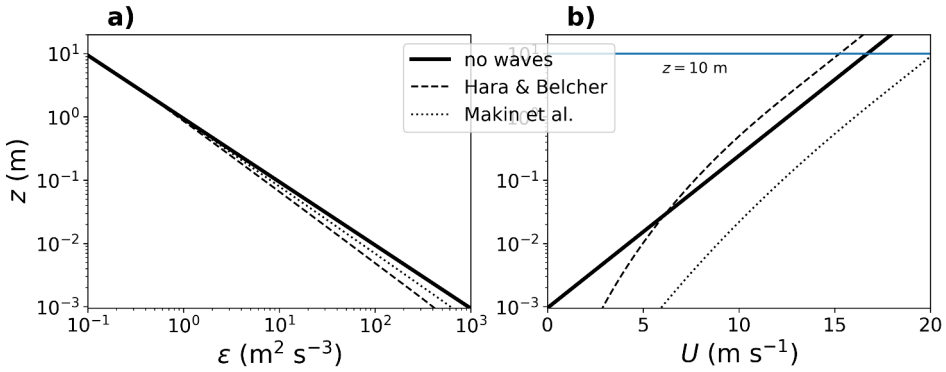

Figure 1.7: Comparison of vertical profiles of (a) TKE dissipation and (b) mean wind speed for three parameterizations of TKE dissipation, with wave-induced stress computed from the model of Kudryavtsev et al. [2014] (Fig. 1.6a). Dashed lines are the model of Hara and Belcher [2004], dotted lines the model of Makin and Kudryavtsev [1999].

of wave-induced stress from the model of Kudryavtsev et al. [2014] (Fig. 1.6a). Once the mean wind speed profile is computed, TKE dissipation can be diagnosed from the above formulas or from the modified TKE balance.

First, note that in the absence of waves, i.e. $\tau_t = u_*^2$ and $dU/dz = u_*/\kappa z$, both TKE dissipation parameterizations are equivalent to the logarithmic-law scaling (solid line). The two parameterizations of TKE dissipation are local, depending on the turbulent stress or turbulent viscosity ($u_*^2(dU/dz)^{-1}$) respectively, and on a mixing length κz. Inclusion of waves results in a decrease of TKE dissipation, which is slightly weaker for ϵ_{Hara} (dashed line) than for ϵ_{Makin} (dotted line). This decrease results from the presence of wave-induced stress, which reduces turbulent stress for a fixed u_* (see the momentum balance Eq. 1.24). The decrease is stronger close to the surface, where wave-induced stress is larger (Fig. 1.6a).

As a consequence, the mean wind speed is also affected by the presence of waves (Fig. 1.7b). As found by Stewart [1961] and Miles [1965], in order to reach their equilibrium with the wind, waves extract energy from the mean flow (through P_w) and the wind profile deviates from a logarithmic law towards a linear profile (compare the solid line with the dashed or dotted lines). This deviation is stronger close to the surface, and follows the changes in TKE dissipation. Fig 1.7b indicates that 10m-wind speed, which is a commonly measured quantity in experiments, ranges from 15 to 20 m s^{-1} depending on the choice of the parameterization for TKE dissipation. This shows the importance of choosing an appropriate closure for the TKE budget, to have a realistic description not only of the turbulent statistics but also of the mean flow quantities.

To summarize, the presence of waves impacts the production, and hence also the dissipation of TKE, with uncertainties on its modeling in the presence of waves. This is further confirmed by the LES of Hara and Sullivan [2015], which show the presence of a TKE dissipation anomaly (excess) in the WBL above a sinusoidal wave. From a spectral perspective, TKE dissipation is related to the turbulence energy cascade, and to the shape of the TKE spectrum. Hence, accurate understanding of these changes is essential both to describe the bulk properties of

turbulence, but also to understand the multiscale coupling between the turbulence and wave spectra, which, as pointed out in Benilov et al. [1974] and more recently in Ortiz-Suslow and Wang [2019], is not well understood.

1.3.3.3 Impact of waves on turbulent structures

Following the discussion on the changes of TKE in the presence of waves, below we briefly review some recent numerical work on the modulation of instantaneous, coherent turbulent structures by the presence of waves. The motivation for this review is twofold. First, coherent turbulent structures are important in the determination of the turbulent stress both for smooth-wall [Robinson, 1991, Jiménez, 2012, 2018] and rough-wall [Raupach et al., 1991, Jiménez, 2004] flows. A wave-induced change in their properties hence reflects the impact of waves directly on turbulence statistics, and not indirectly as is the case for wave-induced stress . Second, modifications of the properties of turbulent stress impact vortex force, both when described through the critical layer mechanism (through Eq. 1.30, page 51) or the NSS mechanism (through Eq. 1.33, page 55).

As an example of the importance of coherent structures, it is interesting to consider the case of transitionally rough surfaces. For these surfaces, the Reynolds number similarity, expected for aerodynamically rough surfaces, is not attained, but the geometry of the roughness elements impacts the flow. For flow over the sea surface, this transition occurs for winds between 3 and 7.5 m s^{-1} [Kitaigorodskii and Donelan, 1984], and this results in a minimum of surface drag ($u_*^2/U(10)^2$) for winds of about 3 m s^{-1} [Edson et al., 2013]. For generic surfaces, Jiménez [2004] suggested that this minimum could result from two competing mechanisms: (i) an increase of surface drag due to additional form drag from the roughness elements (ii) a decrease of surface drag due a randomisation of coherent structures in the viscous sublayer which, in the aerodynamically smooth case, act as a source of turbulence for the logarithmic layer [the so-called viscous sublayer cycle Jiménez and Moin, 1991, Jiménez, 1999]. In the case of transitional surfaces, mechanism (ii) can overcome mechanism (i), explaining the observed decrease of surface drag.

Along these lines, several experiments, including DNS [Sullivan et al., 2000], LES [Sullivan et al., 2014] and observations [Buckley and Veron, 2016], reveal that the streaky structure of viscous-layer turbulence above flat walls [e.g Kline and Runstadler, 1959, related to the viscous sublayer cycle] is affected by the presence of waves. Close to the surface, streaks are disrupted, and their length appears to be constrained by the wave size. The use of low-Reynolds number DNS [Sullivan et al., 2000, Yang and Shen, 2009, 2010] allows to further investigate those changes by analysis of coherent structures. For a slow wave ($c/u_* = 2$), Yang and Shen [2009] found that the negative turbulent stress is induced mainly by contributions from sweep events in the trough of the wave, and ejection events on the windward face of the wave. This is consistent with early experimental work of Kawamura and Toba [1988]. Those events were associated with reversed horseshoe vortices (for sweeps), and to quasi-streamwise vortices (for bursts). For faster waves, with a high enough matched layer, near surface coherent structures are advected upwind in the reference frame of the wave. In this situation, quadrant analysis [Sullivan et al., 2000] reveals that positive contributions to turbulent stress become significantly higher (Q3, or inward interactions). Those are associated with the bending of quasitreamwise

vortices as they are advected downwind, which generates vertical vorticity [Yang and Shen, 2009]. Even though these results provide an indication of the mechanisms at stake, they should however not be readily extrapolated to field-condition flows, due to the low Reynolds number of the simulations.

The impact of wave breaking on coherent structures was analyzed by means of LES by Suzuki et al. [2011, 2013]. Suzuki et al. [2011] modeled the effect of a windy sea with breaking wave crests as an anisotropy in surface drag, stronger in the streamwise (perpendicular to the crests) than spanwise direction. The authors found an enhancement of the intensity quasi-streamwise vortices with respect to an isotropic situation, resulting in more intense turbulence mixing. Suzuki et al. [2013] focused on the impact of airflow separation events on turbulence. The simulations revealed that due to the separation of the near-surface sheared boundary layer, near surface streaks (and coherent vortices) were inhibited. Finally, note that the boundary layer detachments above a breaking crest also result in the creation of vortical structures which are ejected upwards in the fluid [Reul et al., 2008].

These different studies show that waves certainly affect turbulent coherent structures (as summarized in Fig. 1.8), suggesting that their accurate modeling might improve the understanding of wind-over-wave interactions. We end this review by mentioning two theoretical works. First, Eifler [1993], who developed a theoretical model of the near-surface WBL (for heights from 1 to 10 cm) including instantaneous properties of the turbulent flow and multiscale wave effects. His model was based on the analogy between the WBL flow and flow within the viscous sublayer over a flat wall. The later has been described by Kline and Runstadler [1959] and Blackwelder and Eckelmann [1979] as a sequence of growing and collapsing laminar sublayers, associated with the destabilization of quasi-streamwise vortices. Those growth and collapses were proposed as a model for observed burst and sweep events. Eifler [1993] discussed how the spatial distribution of those transient events was constrained by the presence of an individual surface wave: as the laminar sublayer grows along the wave, near-surface wind intensity increases, generating small wavelets which act as roughness elements. This triggers the collapse of the sublayer, hence constraining the spatial distribution of burst and sweep events. Along similar lines, the theoretical work of Csanady [1985] emphasized the role of airflow separation events on top of steep and short waves ($\mathcal{O}(10\text{cm})$) for their coupling with wind. The author argued that, following an airflow separation event, the reattachment of the airflow on the windward face of such a wave is necessary to maintain a balance between momentum input to the wave [by means of a shear-stress spike at the point of reattachment, observed by Okuda et al., 1977] and dissipation of wave energy to the near-surface turbulent water field. This allows trains of such small-scale waves to be long-lived, and hence to be coupled by wind through air-flow separation. These works, although conceptual, emphasize the role of multiscale and transient coupled processes in the wind-and-waves coupling, which is not covered by the DNS and LES results presented above

1.3.4 Concluding remarks

Starting from historical models of the vortex force in the WBL, we have discussed the properties of turbulence in the WBL. Emphasis was placed on the fact that a realistic sea surface is a multiscale surface, whose roughness results from transient events (both breaking and non-

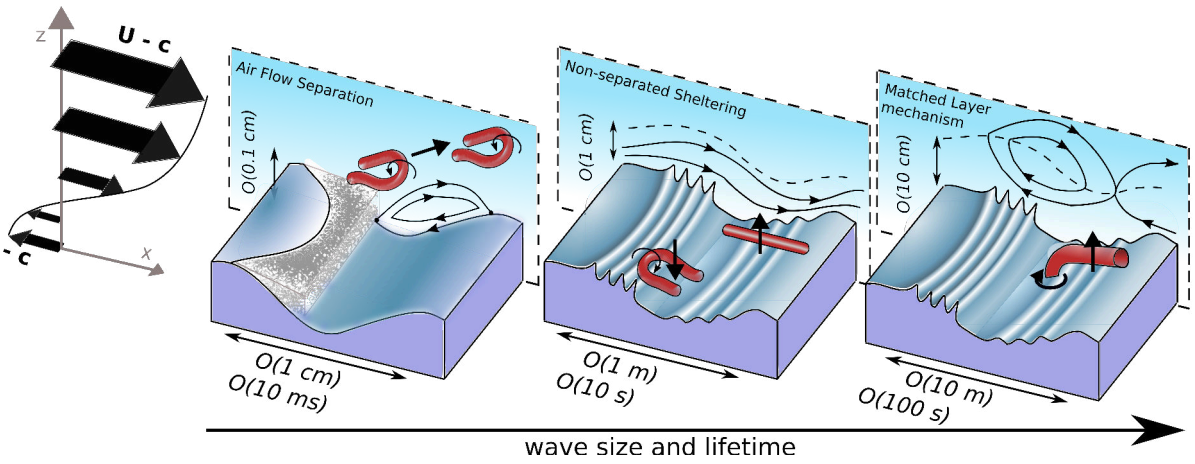

Figure 1.8: Summarizing scheme presenting a multiscale and three-dimensional view the dynamical impact of wind-waves on turbulence. The presence of waves results in both wave-coherent motions (background streamlines) and modification of the instantaneous properties of turbulence (foreground vortex tubes), which are transient events. The latter are deduced from laboratory observations (for the case of breaking waves) and low-Reynolds number DNS, and are hence possible processes, not observed in field conditions. The drawing is in the reference frame of the moving waves, whose speed increases with wave scale, and the scale of the waves is not respected. Airflow separation events (left) are mainly associated with short-crested breaking waves, resulting in inhibition of near surface streaks downwind of the breaking crest, and ejection of vortical structures in the interior of the fluid. Short waves (middle) are associated with the non-separated sheltering mechanism of vortex force, and to intensified sweeps and ejections on the trough and windward face of the wave. Longer waves (right) are associated with the matched layer mechanism of vortex force, and to positive contributions to turbulent stress resulting from the horizontal bending of quasi-streamwise vortices (Q3 events). Finally, both vortex force mechanisms are dependent on the modulation of the steepness of shorter waves along the long wave .

breaking waves) which are strongly coupled to the turbulent properties airflow. Figure 1.8 summarizes the multiscale nature of the surface, by showing that depending on the wave size, wave-induced motions and instantaneous turbulence properties can be significantly different.

Several other problems related to wind-wave interactions have not been reviewed here, among others: (i) heat fluxes, which are affected by the change in turbulent diffusion in the WBL [e.g. Kitaigorodskii and Donelan, 1984, Makin and Mastenbroek, 1996, Veron et al., 2008]; (ii) swell, which, if travelling faster than the wind, can result in a momentum transfer from waves to the wind [Kudryavtsev and Makin, 2004, Sullivan et al., 2008]; (iii) very strong winds (above 20 m s^{-1}), under which the surface might be disrupted and the flow becomes increasingly detached from the waves [Soloviev et al., 2014].

1.4 OBJECTIVES OF THE PRESENT WORK

In Sec. 1.3 we have emphasized that the interactions between wind-waves and turbulence occur not only through wave-induced motions, but also possibly through the direct modification of the instantaneous properties of turbulence. To this aim, several laboratory measurements [Kawamura and Toba, 1988, Buckley and Veron, 2016] and numerical simulations [Sullivan et al., 2000, Yang and Shen, 2009, Suzuki et al., 2011, 2013] have been highlighted. Additional complexity arises from (i) the fact that these modifications should be coupled with local changes in the wave field, due to the local and transient variations in wind speed; (ii) the nature of wind-and-wave coupling for a multiscale sea surface, where cross-scale interactions occur both in the turbulent and wave fields; (iii) the difficulties in defining the correct averaging and coordinates for a rough surface whose average height is zero. Hence, quantification of these interactions in wind-and-wave theories remains a challenge.

Yet these changes, if occurring in field conditions, are expected to have a profound impact on the averaged properties of turbulence in the WBL. As reviewed in Sec. 1.1, transient events are important in the determination of the overall momentum flux, both for flows over smooth and rough boundaries. Their modification by the geometry of the roughness elements can also have consequences on the drag coefficient, i.e. the relation between the mean wind and the turbulent momentum flux, and on turbulent transport. And what about the interaction between inner and outer layer structures, which has been shown to be sensitive to surface roughness? These modifications are all the more important for stratified field conditions, questioning why and when MOST hypotheses are satisfied. To be clear, what is at sake here is not the improvement of bulk formulations for wind stress, but the understanding of their limitations, conditions of applicability, and dependency to environmental conditions.

These instantaneous properties of turbulence can, to some extent, be related to the various turbulent spectra (by doing so, we obviously completely disregard their phase). The questions above can then be rephrased by asking what are the interactions between the spectral properties of turbulence and waves [e.g. Benilov et al., 1974, Ortiz-Suslow and Wang, 2019]. In this thesis, we take a first step towards this understanding by focusing on a particular spectral property of turbulence: the wavelength of the peak of the vertical velocity spectrum, or the size of energy-containing eddies. Both are related through the phenomenological model presented in Sec. 1.2, which relies on the use of spectral budgets. Hence, in Chapter 2, we question the hypothesis upon which the spectral budget relies, for a flat-wall and stratified flow. We aim, more specifically, at understanding the crucial ingredients which determine the value of the spectral peak wavelength.

In regard to turbulence above a sea surface, a first question is to know what should be the link between energy-containing eddies and the *geometrical* properties of the sea surface. This question, addressed in Chapter 3, is related to the uncertainty in the parameterization of TKE dissipation within the WBL, mentioned in Sec. 1.3. Indeed the phenomenological model links TKE dissipation (related to the Kolmogorov cascade) to the geometry of energy-containing eddies (see Sec. 1.2). Finally, in Chapter 4, we explore the *dynamical* impact of wind-waves on energy-containing eddies, through modification of the local mean wind shear. The work of Raupach et al. [1996], presented in Sec. 1.1, indicated that above canopies, this dynamical interaction can constrain the scale of energy-containing eddies. In Chapter 4 we consider the

most obvious candidates for the definition of an "effective canopy" above a windy surface, which are breaking waves [Melville, 1977].

CHAPTER 2

TOWARDS A "SPECTRAL LINK" FOR THE VERTICAL VELOCITY SPECTRUM?

"Wheat Field with Cypresses", Vincent van Gogh (1889).
The Metropolitan Museum of Art, purchase, The Annenberg Foundation Gift, 1993.

2.1 INTRODUCTION

GENERAL MOTIVATION Turbulence close to a wall exhibits many distinctive features, one of which is anisotropy. Indeed, for mildly stable and unstable conditions in the Atmospheric Surface Layer (ASL), numerous experiments have shown that the horizontal turbulent motions contain more energy than their vertical counterpart ($\overline{u'^2}+\overline{v'^2} \geq \overline{w'^2}$), and that both are correlated, which translates into a vertical momentum flux ($\overline{u'w'} \neq 0$). This can be attributed to (i) differences in energy pathways, as buoyancy only acts on the vertical component while, for a horizontally homogeneous flow, mechanical production is a source only for the horizontal components; (ii) wall-related effects, i.e. the blocking of the vertical velocity near the wall, and the presence of inactive motions, that only contribute to the horizontal component of the turbulent field [see, e.g. Katul et al., 1996]. Investigating how energy is redistributed among the various components of the turbulent field is hence an interesting way to unravel the mechanisms at play in wall-bounded turbulence.

From a spectral standpoint, this anisotropy is reflected in a difference between the Turbulence Kinetic Energy (TKE) and vertical velocity spectra at each scale k (k is here the streamwise wavenumber). In both cases the spectra exhibit two regimes, separated by a transition, or spectral peak wavenumber k_p (see Fig. 1.2b on page 31). The large wavenumber range ($k > k_p$) is isotropic, corresponding to the Kolmogorov cascade (it is called the inertial subrange). Scalewise anisotropy is contained in the low wavenumber range ($k < k_p$, the energy-containing range) where the exponents of the power law for TKE and the vertical velocity spectra are respectively -1 and 0. [1] Hence most of the bulk (i.e. integrated over all scales) anisotropy can be explained by the contribution from energy-containing scales, and depends on the value of k_p. For neutral conditions, the spectral peak is inversely proportional to height z, reflecting the effect of the wall on turbulent eddies (see Townsend's hypothesis on page 30). For mildly stable and unstable conditions, several measurements have shown that this spectral peak can still be defined in the vertical velocity spectrum, and that it varies with stability around $1/z$ (see Fig. 2.1 for an example). This variation should reflect the change in the balance between energy pathways as buoyancy changes.

From a practical perspective, we have introduced, in Chapter 1, a phenomenological model, which establishes a "spectral link" between the spectrum of vertical turbulent velocities F_{ww} and the turbulent momentum flux $u_*^2 = -\overline{u'w'}$. In the logarithmic sublayer, and using the canonical shape of the vertical velocity spectrum, it reads

$$u_*^2 \propto \frac{dU}{dz}\epsilon^{1/3}k_p^{-4/3}, \tag{2.1}$$

where ϵ is TKE dissipation and U is the mean wind speed. This model hence links a spectral

[1] Here two comments should be made. First, the value of the transition wavenumber differs slightly depending which spectrum is considered. Here we disregard these differences for simplicity, and because we are not interested in quantitative predictions. Second, the shape of the spectra drawn in Fig. 1.2b are canonical, in the sense that they are an idealized representation of realistic spectra, which retains only their essential features. Nonetheless, the existence of a -1 power law for the vertical velocity spectrum, and hence for the TKE spectrum, is still an ongoing debate, at it is unclear under which conditions, in field experiments, this law can be observed [see e.g. Drobinski et al., 2007].

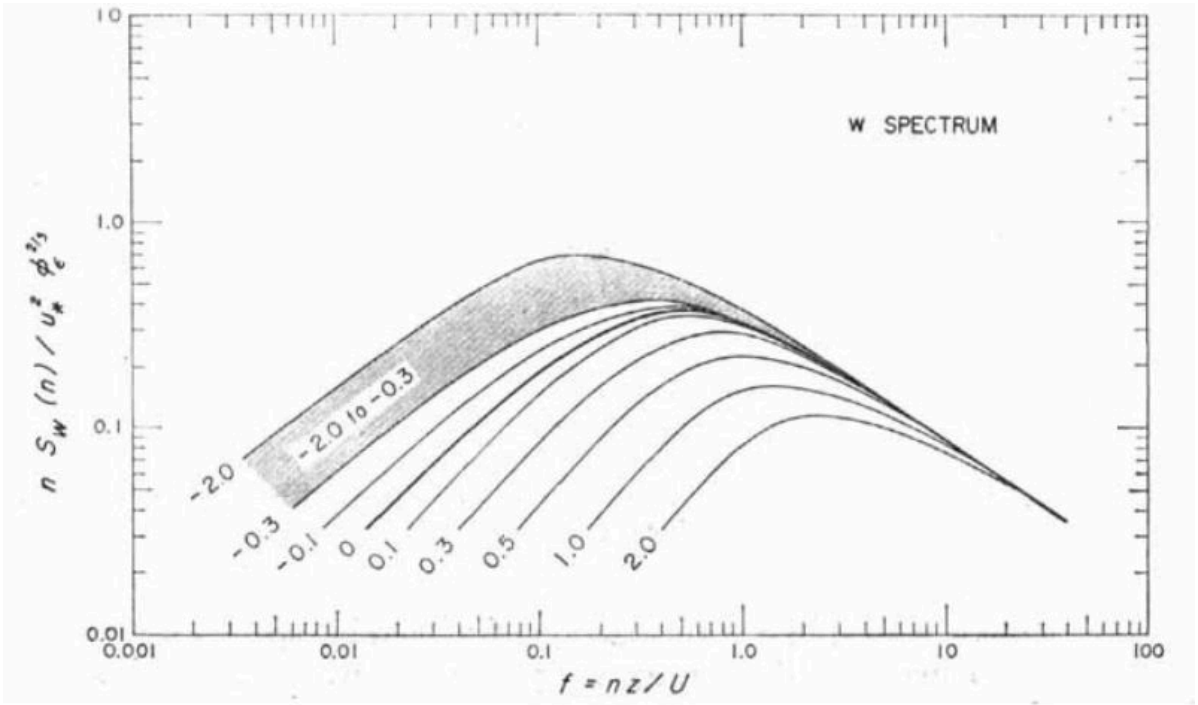

Figure 2.1: Premultiplied vertical velocity spectra from the Kansas experiment (on top of a uniform wheat field) as a function of frequency [from Kaimal et al., 1972]. The different curves indicate various values of the stability parameter ζ (negative for an unstable atmosphere, and conversely). The spectra exhibit a peak, which varies with stability.

property of anisotropy (k_p) to one of its bulk values (u_*). For a neutral ASL in the logarithmic sublayer, with $k_p \propto 1/z$, the scaling $\epsilon \propto u_*^3/z$ is recovered. The stability-dependent variations k_p derived from data (Fig. 2.1) were then used [Katul et al., 2011] to predict MOST stability functions.

Nonetheless, the spectral link (2.1) is based on a spectral budget, which relies on a certain number of assumptions (see discussion in Chapter 1). Hence this link is certainly far from being a universally valid relation. Relations of the type (2.1) might indeed well be valid to predict some bulk quantities, such as MOST stability functions, but fail in other situations. With the aim to extend such relations to wind blowing above a sea surface, we investigate in the present chapter both fundamental and practical issues related to the spectral link.

THE VERTICAL VELOCITY SPECTRAL BUDGET As mentioned above, the spectral peak wavenumber is essential in the characterization of scalewise anisotropy. Using a scaling analysis, we now show that its value (k_p) cannot be predicted using standard closures for the vertical velocity spectral budget. This indicates missing physics, setting the frame for the rest of the Chapter.

A spectral budget for the vertical velocity spectrum $\tilde{F}_{ww}$, derived in Annex A, reads, under

the ASL hypothesis,

$$\frac{1}{2}\frac{\partial \tilde{F}_{ww}(k)}{\partial t} = \tilde{B} + \tilde{R}_w - \tilde{T} - \tilde{\epsilon}. \tag{2.2}$$

In this budget, the buoyancy source/sink ($\tilde{B}$) is balanced by the interscale transfer of energy ($\tilde{T}$), viscous dissipation ($\tilde{\epsilon}$) and the return-to-isotropy term $\tilde{R}_w$. This last term, together with $\tilde{B}$, is essential in the determination of the bulk value of anisotropy, since it accounts for the redistribution of energy among the different turbulent components, due to pressure-strain correlations. Several expression of $\tilde{R}_w$, with different conventions, are compared in Annex B.

The terms in the RHS of (2.2) can be scaled using the few parameters characterizing spectral properties of the vertical velocity in the logarithmic sublayer. These are k_p, ϵ, ν (which only enters $\tilde{\epsilon}$) and $(g/\theta_0)d\theta/dz$ (which only enters $\tilde{B}$)[2] . The scalings are then

$$\tilde{B} \propto \frac{g}{\theta_0}\frac{d\theta}{dz}\epsilon^{1/3}k_p^{-7/3}, \quad \tilde{T} \propto \tilde{R}_w \propto \epsilon k_p^{-1}, \quad \tilde{\epsilon} \propto \nu\epsilon^{2/3}k_p^{1/3}. \tag{2.3}$$

In the above equation, z does not appear explicitly, and is contained in the dependence of k_p to $1/z$. The same holds for the Obukhov length, or the dimensionless stability parameter ζ, on which k_p depends. Note that, in Appendix B of the paper in Sec. 2.2, the balance (2.2) and the scaling of the different terms (2.3) are derived from canonical spectra, yielding the proportionality coefficients of (2.3).

The scalings for $\tilde{T}$ and $\tilde{R}_w$ assume that these two terms depend only on inertial-subrange variables. This is indeed the case for the widely used Rotta model of $\tilde{R}_w$ [Rotta, 1951] and its spectral equivalents [Besnard et al., 1996, Bos et al., 2004], presented in Annex B. This assumption is also common to many models for the energy transfer term $\tilde{T}$, such as the ones of Obukhov [1941], Heisenberg [1948] and Leith [1967], as reviewed in Panchev [1971] (p. 198-219). These models are valid far from the bottom of the logarithmic layer, i.e. for $k_p \ll \eta^{-1}$ (where $\eta = (\nu/\epsilon^{1/3})^{3/4}$ the Kolmogorov microscale).

However, for neutral conditions, where $\tilde{B} = 0$, the spectral balance (2.2) combined with (2.3) yields $k_p \propto \eta^{-1}$. This inconsistency suggests a missing Reynolds-number dependence in the above scaling. For sufficiently stratified conditions, for which viscosity can be neglected in (2.2) the balance yields

$$k_p z \propto \frac{\phi_h^{3/4}}{(\phi_m^{2/3} - \zeta)^{2/3}} \tag{2.4}$$

where ϕ_m and ϕ_h are the MOST functions introduced in Chapter 1, page 36. This result is inconsistent with values of k_p reported in the literature[3], and again suggests some missing dependence of (2.3) with stability.

This last inconsistency motivates the work presented in Sec. 2.2, in which a modification to the Rotta scaling of $\tilde{R}_w$ is proposed. Then, in Sec. 2.3 we suggest an alternative means of computing the stability-dependent value of $k_p z$, which does not require the spectral budget.

[2] We recall that θ and θ_0 are the potential temperature and its reference value, respectively, and that g is the gravity acceleration.

[3] This is not shown here, but can be easily seen by comparing the expressions of $k_p z$ and of ϕ_m proposed by Kaimal et al. [1972], which are both listed in Appendix A of the paper in Sec. 2.2.

2.2 ARTICLE: "SCALEWISE RETURN-TO-ISOTROPY IN STRATIFIED BOUNDARY LAYER FLOWS"

Manuscript submitted to *Journal of Geophysical Research* on 10/03/2020.

JGR Atmospheres

RESEARCH ARTICLE
10.1029/2020JD032732

Scalewise Return to Isotropy in Stratified Boundary Layer Flows

A. Ayet[1,2], G. G. Katul[3], A. D. Bragg[4], and J. L. Redelsperger[1]

[1]Ifremer, CNRS, IRD, Univ. Brest/ Laboratoire d'Océanographie Physique et Spatiale (LOPS), IUEM, Brest, France, [2]LMD/IPSL, ENS, PSL Université, École Polytechnique, Institut Polytechnique de Paris, Sorbonne Université, CNRS, Paris, France, [3]Nicholas School of the Environment, Duke University, Durham, NC, USA, [4]Department of Civil and Environmental Engineering, Duke University, Durham, NC, USA

Key Points:
- Linear return-to-isotropy (RTI) models are routinely used to describe boundary layer turbulence in mesoscale models
- Their ability to describe idealized boundary layer turbulence at different scales and stability regimes is investigated
- A phase space of eddy sizes and stability regimes is identified that shows where existing RTI models are physically unrealistic

Correspondence to:
A. Ayet,
alex.ayet@normalesup.org

Citation:
Ayet, A., Katul, G. G., Bragg, A. D., & Redelsperger, J. L. (2020). Scalewise return to isotropy in stratified boundary layer flows. *Journal of Geophysical Research: Atmospheres*, *125*, e2020JD032732. https://doi.org/10.1029/2020JD032732

Received 9 MAR 2020
Accepted 18 JUL 2020
Accepted article online 22 JUL 2020

Abstract Anisotropic turbulence is ubiquitous in atmospheric and oceanic boundary layers due to differences in energy injection mechanisms. Unlike mechanical production that injects energy in the streamwise velocity component, buoyancy affects only the vertical velocity component. This anisotropy in energy sources, quantified by the flux Richardson number Ri_f, is compensated by a "return to isotropy" (RTI) tendency of turbulent flows. Describing RTI in Reynolds-averaged models and across scales continues to be a challenge in stratified turbulent flows. Using phenomenological models for spectral energy transfers, the necessary conditions for which the widely-used Rotta model captures RTI across various Ri_f and eddy sizes are discussed for the first time. This work unravels adjustments to the Rotta constant, with Ri_f and scale, necessary to obtain consistency between RTI models and the measured properties of the atmospheric surface layer for planar-homogeneous and stationary flows in the absence of subsidence. A range of Ri_f and eddy sizes where the usage of a conventional Rotta model is prohibited is also found. Those adjustments lay the groundwork for new closure schemes.

Plain Language Summary In the atmosphere and in oceans, turbulence dominates much of the exchanges of momentum, heat, water vapor, and scalars such as carbon dioxide, ozone, or methane. Representing turbulence in numerical models of the Earth and climate system remains a first-order problem, requiring the development of simplified approaches to describe the energetics of the flow. One such representation is based on the universal tendency of all turbulent flows to attain an isotropic state, where kinetic energy is equi-partitioned among its three velocity components, labeled "return to isotropy." However, the presence of buoyancy forces and mechanical generation of turbulence causes the flow to be anisotropic at a wide range of eddy sizes. To what degree this additional layer of complexity invalidates the use of existing models based on the aforementioned universal attainment of an isotropic state is explored here. Common representation of such phenomenon within existing climate- and meso-scale models are shown to be satisfactory only for a restricted range of density stratification. The analysis unfolds conditions where adjustments to existing representations are required and others where their use is prohibited. Novel physical processes are also unfolded, providing guidance toward improved turbulence representation in a plethora of models.

1. Introduction

The significance of boundary layer turbulence in the ocean and the atmosphere is not in dispute given its control on a plethora of processes related to the exchange of momentum, heat, and scalars. The description of key flow properties, however, remains a formidable task due to the need of closing the Reynolds-averaged Navier-Stokes equations using appropriate physical models (Canuto et al., 2001; Cuxart et al., 2000; Mellor & Yamada, 1982). Among the minimal ingredients characterizing turbulence are the sources and sinks of turbulent kinetic energy (TKE): shear and buoyancy. Shear production (P_m) impacts the streamwise turbulent velocity component (of variance σ_u^2) whereas buoyancy production/destruction (B) impacts the vertical turbulent velocity component (of variance σ_w^2). A dimensionless quantity used to measure the relative strength of these two energy injection mechanisms is the flux Richardson number $Ri_f = -B/P_m$. The differences in energy injection mechanisms introduce anisotropies in the component-wise turbulent velocity fluctuations (Lane & Sharman, 2014; Lovejoy et al., 2007), with $\sigma_u^2/\sigma_w^2 > 3$ across a wide range of Ri_f (Kaimal & Finnigan, 1994; Sorbjan, 1989).

Despite being anisotropic, turbulence exhibits a universal tendency to relax to an isotropic state where TKE is equally partitioned among its three velocity components. This universal tendency of turbulence has been used to describe pressure-strain interactions that redistribute energy between the three components and hence partially compensate for the anisotropy caused by energy injection mechanisms. This premise forms the basis of numerous turbulence modeling schemes in use today (Abid & Speziale, 1993; Canuto et al., 2001; Cuxart et al., 2000; Drobinski et al., 2007; Launder et al., 1975; Lumley & Newman, 1977; Mellor & Yamada, 1982), especially within meso-scale models such as the Weather Research and Forecasting (or WRF) system. The common closure scheme in use is the Rotta model (Rotta, 1951) that assumes that the magnitude of the energy redistribution among velocity components is directly proportional to the degree of energy anisotropy, which defines the so-called Rotta constant. This scheme continues to draw research attention in the engineering and geophysical fluid dynamics communities alike (Bou-Zeid et al., 2018) since the modeling of the pressure-strain term is key for turbulent closure schemes used in both atmospheric and oceanic models.

A less-studied aspect of this universal tendency of turbulence is the connection between anisotropies appearing in the component-wise turbulent energy spectra at large scales and the attainment of local isotropy at inertial to small scales (Brugger et al., 2018). The "state of the science" to operationally describe such redistribution of energy between differing velocity components at a given scale remains a spectral version of a linear return to isotropy scheme put forth by Rotta (Besnard et al., 1996; Katul et al., 2013). Such a scheme rectifies the absence of a local balance between production and nonlinear transfer across scales for a given velocity component (since the action of viscous dissipation of kinetic energy is small at large scales). It provides a redistribution mechanism of kinetic energy between the three different components at a given scale, assuming a scale-dependent relaxation time scale is set. What is to be explored is whether such a Rotta scheme suffices to capture the main redistribution terms across scales when canonical spectra measured in the atmospheric surface layer (ASL) are used across various Ri_f. To guide this inquiry, we ask what is the Rotta constant associated with the scale-by-scale energy redistribution. Is it dependent on Ri_f and scale? Are there "signatures" of more complex processes such as rapid distortion effects across scales that are amplified or dampened with changes in Ri_f?

In section 2, this question is first addressed from a bulk perspective (i.e., integrated over all scales), extending the results presented in Bou-Zeid et al. (2018) that did not focus on the Rotta constant. Section 3 introduces a spectral model of maximum simplicity (following Katul et al., 2013). The model makes use of a stability-dependent spectral budget for the vertical velocity energy and TKE spectra. The terms in these budgets are then determined for idealized canonical spectral shapes reported for the ASL in the literature for modest deviations in $Ri_f \in [-1.2, +0.1]$ from its neutral value (=0). The implications for a "scale-by-scale" Rotta constant are then discussed in section 4. Conclusions are drawn in section 5.

2. A Bulk Analysis

A bulk analysis of the return-to-isotropy problem is first presented so as to introduce notations, concepts, and review the linear Rotta closure scheme. The three instantaneous turbulent velocity components are u', v', and w' in the streamwise (x), cross-stream (y), and vertical (z) directions, respectively, with zero time (or ensemble) averages (i.e., $\overline{u'} = \overline{v'} = \overline{w'} = 0$). Similarly, ρ' is the turbulent density fluctuation around a mean density $\overline{\rho}$. As a logical starting point, a stationary and planar-homogeneous flow at high Reynolds number in the absence of subsidence is considered. The mean velocity in the streamwise direction is denoted by U. Because the focus is on surface layer turbulence, the Coriolis term is ignored. For these idealized flow conditions, the budget equations for the vertical velocity variance $\sigma_w^2 = \overline{w'w'}$ and TKE $e = (1/2)(\overline{u'u'} + \overline{v'v'} + \overline{w'w'})$ reduce to

$$\frac{1}{2}\frac{\partial \sigma_w^2}{\partial t} = 0 = B + R_w - \frac{\epsilon}{3}, \tag{1}$$

$$\frac{\partial e}{\partial t} = 0 = P_m + B - \epsilon. \tag{2}$$

Equation 1 is a balance between buoyancy production or destruction $B = -(g/\overline{\rho})\overline{w'\rho'}$ (g is the gravitational acceleration), the pressure-strain correlation source/sink R_w (discussed below), and viscous dissipation

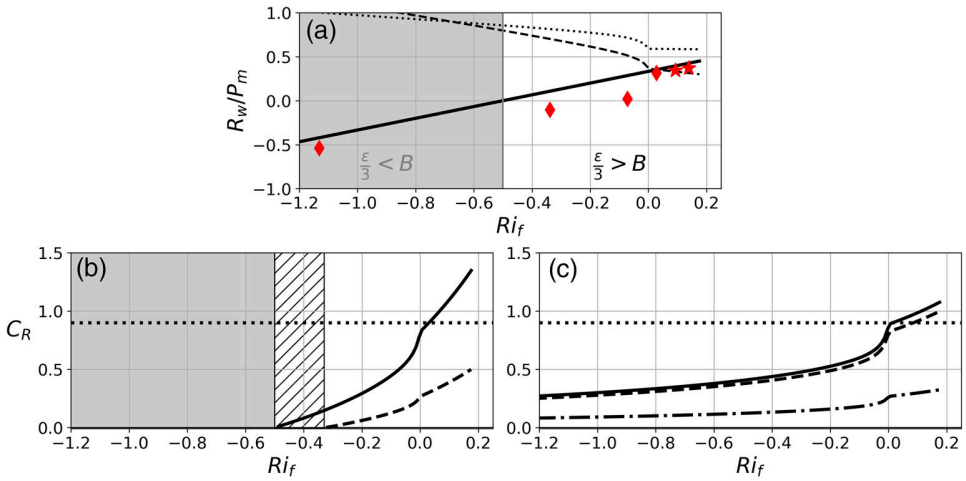

Figure 1. (a) Normalized vertical velocity pressure-strain term R_w/P_m as a function of the flux Richardson number Ri_f. Symbols ⋆ and ◊ are, respectively, DNS and LES results (from Bou-Zeid et al., 2018). Solid line is from Equation 3. Dashed, dotted lines are Rotta model predictions using a standard Rotta constant C_R=0.9 (Equation 5) without rapid-distortion corrections (dashed) and with rapid distortion corrections (dotted lines). (b) Inferred Rotta constant C_R required for a Rotta model to match the expected pressure-strain dependence (solid line in (a)) as a function of the flux Richardson number Ri_f (Equation 6). Solid and dashed lines are the revised Rotta model without rapid-distortion terms ($\alpha_P = \beta_B = 0$) and with rapid-distortion terms ($\alpha_P = 0.225$ and $\beta_B = 1/3$) respectively. The dotted line is the standard value C_R=0.9 used in canonical boundary layer flows. The shaded region is where no positive C_R value is admitted for the first choice of C_R, α_p, and β_p, and hatches represent the increase of the width of the forbidden region when rapid-distortion terms are included. (c) Same as (b) but for the proposed rapid-distortion coefficients, β_B=2/3 and: α_P=−0.026 (solid line), α_P=0 (dashed line), and α_P=0.225 (dashed-dotted line).

rate ϵ. Equation 2 is a balance between mechanical production $P_m = -\overline{u'w'}(dU/dz)$ (always positive in boundary layer flows), buoyancy production or destruction, and TKE viscous dissipation rate. In both budgets, the turbulent transport of $\overline{w'^2}$ and e is ignored. For near neutral conditions, this assumption may be plausible but becomes questionable for dynamic convective, free convective, and strongly stable conditions as discussed elsewhere (Banerjee et al., 2015; Charuchittipan & Wilson, 2009; Ghannam et al., 2017, 2018; Poggi et al., 2004; Raupach, 1981; Salesky et al., 2013). Data and models for the flux transport terms in the ASL, especially for the vertical velocity skewness, remain in demand. The form of dissipation used here ($\epsilon/3$ in Equation 1) assumes that the total viscous dissipation rate is isotropic. For ASL flows, the isobaric approximation yields $\rho \propto T^{-1}$ where T is potential temperature and thus $B = -(g/\overline{T})\overline{w'T'}$. The pressure-strain term only redistributes energy between the different turbulent velocity components (Pope, 2000) and does not produce or dissipate TKE.

Mechanical production enters the TKE budget whereas buoyancy enters through both the TKE and σ_w^2 budgets. This difference in energy sources (or sinks) results in ASL turbulence being anisotropic, conventionally quantified by the so-called anisotropy tensor (Lumley & Newman, 1977). In the following, the diagonal component of the anisotropy tensor for the vertical direction is used and is given by $r = (\sigma_w^2/e) - 2/3$. It is based on the normalized difference (by $e/2$) between the energy of the vertical turbulent motions, $\sigma_w^2/2$, and the mean TKE, $e/3$. The value r=0 is attained only when energy is equi-partitioned among the velocity components so that $\sigma_u^2 = \sigma_v^2 = \sigma_w^2 = 2e/3$. The term "anisotropy" refers to r unless otherwise stated. Hence, the magnitude and sign of r depends on how far σ_w is from the energy equipartition state. The Rotta model, described below, links the pressure-strain correlation R_w to anisotropy r.

Rearranging Equations 1 and 2 yields an expression for a normalized R_w given by (see Bou-Zeid et al., 2018)

$$\frac{R_w}{P_m} = \frac{2}{3}\left(\frac{1}{2} + Ri_f\right). \tag{3}$$

The normalized R_w only depends on the flux Richardson number $Ri_f = -B/P_m$ and is constant at 1/3 for near-neutral conditions (i.e., Ri_f=0). This relation, shown in Figure 1a (solid line), exhibits similar trends

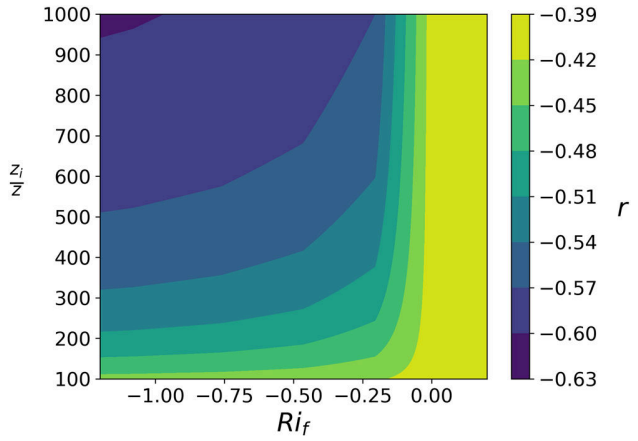

Figure 2. Anisotropy coefficient $r = \sigma_w^2/e - 2/3$ computed from Monin-Obukhov Similarity Theory as a function of the flux Richardson number Ri_f and the ratio between boundary layer height z_i and the measurement height z (see Appendix A for details).

as direct numerical simulations (DNSs) and large eddy simulations (LESs) where the pressure-strain term is computed (stars and diamonds). Figure 1a further shows that R_w should change sign at $Ri_f = -0.5$, that is, be a source (respectively a sink) term in Equation 1 for $Ri_f > -0.5$ (resp. $Ri_f < -0.5$, shaded area), where the buoyancy source B exceeds (resp. is lower than) the dissipation sink $\epsilon/3$. Any model for the pressure-strain term should thus satisfy this Ri_f dependency for the aforementioned idealized flow conditions in the ASL.

In linear return-to-isotropy models for R_w, anisotropic turbulent flows are assumed to be nudged toward isotropy by the pressure-strain correlation term, which is a source or a sink in the σ_w^2 budget depending on whether $r<0$ or $r>0$, respectively. The simplest linear model, the Rotta model, is of the form $R_w \propto (e/\tau) r$ with τ a time scale (Rotta, 1951). In addition to this "slow" component, the Rotta model can be further extended by including rapid-distortion terms (Canuto et al., 2001; Lumley & Khajeh-Nouri, 1975; Pope, 2000). In the case of the vertical velocity component, rapid distortion terms associated with strain and vorticity vanish (Zeman & Tennekes, 1975), and the Rotta model can be written as

$$\frac{R_w}{P_m} = -C_R \frac{(e/\tau)}{P_m} r + \alpha_P + \beta_B Ri_f, \tag{4}$$

where $\tau = e/\epsilon$ is a model for the relaxation time scale to isotropic state, C_R is the Rotta constant for the slow part, and α_P and β_B are rapid-distortion coefficients associated with the rapid part. Thus, the time scale τ/C_R can be interpreted as the time needed for eddies to redistribute energy among the different components so to attain the equi-partition state where $r=0$. The constant C_R is positive, and its optimal value for closure modeling is 0.9 (Pope, 2000). This value also has justification for near-neutral flows (Katul et al., 2013) whereas values for α_p and β_p continue to draw research attention. Here, we chose $\alpha_P = 0.225$ and $\beta_B = 1/3$, as derived from renormalization theory and used in the stratified boundary layer model of Canuto et al. (2001).

It is important to stress the differences between Equations 3 and 4. Unlike Equation 4, Equation 3 should be viewed as a constraint on the numerical value of R_w/P_m (under particular assumptions made about the flow such as ignoring the turbulent transport terms), rather than reflecting the underlying dynamics governing R_w/P_m. For example, it would be incorrect to infer from Equation 3 that the physical processes governing R_w are entirely captured by Ri_f, since we know from the Navier-Stokes equation that R_w is dynamically determined by nonlinear processes associated with correlations between the pressure and strain-rate fields of the flow. An analogy can be made to the inertial range of turbulence where the TKE passing through the energy cascade is on average numerically equal to the kinetic energy dissipation rate (under certain flow conditions). This numerical equality, however, simply reflects an energetic balance; the actual dynamical processes governing the energy cascade in the inertial range differ from the dynamical processes governing the energy dissipation rate at the smallest scales of the flow (see Carbone & Bragg, 2020). Similar to this, Equation 3 simply denotes a numerical constraint on the flow (under particular conditions), but the underlying dynamical processes governing R_w/P_m are not reflected in that constraint equation. In contrast, the right-hand side of Equation 4 does represent, in a phenomenological way, the nonlinear dynamical processes governing R_w/P_m, and in particular the energy redistribution time scale τ/C_R.

A large corpus of data in the ASL (e.g., Kader & Yaglom, 1990; Kaimal & Finnigan, 1994; Sorbjan, 1989) show that (i) r depends only on two factors: Ri_f and the relative boundary layer height z_i/z, (ii) for the range of Ri_f investigated in Figure 1a, r is always negative, and (iii) under near neutral conditions, $r \sim -0.4$. This is illustrated in Figure 2, where the ASL measurements of r are presented (the empirical fits can be found in Appendix A). The question we ask below is whether the linear Rotta model, when constrained by those

measurements (i.e. when r is constrained in Equation 4), is compatible with the constraint described by Equation 3. In other words, we evaluate the ability of the linear Rotta model to represent the nonlinear physical processes governing R_w for a flow satisfying the idealized energy balance (1)–(2). As the focus of the present work is on varying stability conditions, the relative boundary layer height is set to 10^3 in the following discussion. Results are not qualitatively sensitive to changes in this height. Note that the properties of anisotropy are valid for planar-homogeneous flow conditions, predominant for the measurements presented in Figure 2. For realistic flow conditions, other factors induce variations in anisotropy (including flux transport terms).

To understand the compatibility between the constraint in Equation 3 and data on r, the TKE budget (2) is inserted into Equation 4 to arrive at a normalized R_w

$$\left.\frac{R_w}{P_m}\right|_{Rotta} = C_R(Ri_f - 1)r + \alpha_P + \beta_B Ri_f. \tag{5}$$

For neutral conditions and no rapid-distortion corrections, Equation 5 is compatible with Equation 3 for $C_R \sim 0.9$, that is, the optimal value for closure modeling (Pope, 2000). Figure 1a further shows how this ratio varies with stability for the ASL values of r presented above and a Rotta constant fixed at $C_R = 0.9$. With increasing instability (decreasing Ri_f), the Rotta constant increases, due to r being negative. The Rotta model, both without and with rapid distortion corrections (dashed and dotted lines), is not compatible with the expected values of the pressure-strain term (solid line and symbols) except for $Ri_f \in [0,0.2]$.

A compatible variation of normalized R_w can be obtained by allowing C_R to adjust with stability. Upon inserting Equations 2 and 4 in (1) yields

$$C_R(Ri_f, z_i/z) = \frac{1}{3r}\left[\frac{1 - 3\alpha_P + (2 - 3\beta_B)Ri_f}{Ri_f - 1}\right], \tag{6}$$

where r is here to be understood as a function of Ri_f and z_i/z (that is, $r = r(Ri_f, z_i/z)$). This equation shows that an "optimal " C_R must be impacted by two parameters: large-scale anisotropy, r (which, in the ASL, depends on Ri_f and z_i/z; see Appendix A), and the flux Richardson number Ri_f, provided that $\alpha_p \neq 1/3$ and $\beta_p \neq 2/3$ simultaneously. The ratio z_i/z can also be interpreted as a relative distance to the wall, hence showing how wall effects in the surface layer impact C_R.

Solid line in Figure 1b shows the optimal Rotta constant without rapid distortion corrections (i.e., $\alpha_P = \beta_B = 0$ in Equation 6). For near-neutral ASL, as mentioned above, $C_R \sim 0.9$, close to the literature-based value. Its value decreases with increasing instability to match the increase of the buoyancy to dissipation ratio, which requires a decreased R_w in Equation 1. This is consistent with an increase of the average size of eddies as instability increases (see, e.g., Katul et al., 2011), implying an increase in their turnover time, and hence in the isotropization time (τ/C_R). For $Ri_f < -0.5$, the sign change of R_w mentioned above implies a negative Rotta constant C_R, which is not physical. These conditions may also be hinting that other sources, and sinks must be considered such as the turbulent flux transport terms. There is thus a range of stability conditions (gray shading) where the linear Rotta model is simply unable to describe R_w for the idealized flow state considered here. Over the range of allowed Ri_f values, the Rotta constant varies by a factor 4 around its value for near-neutral conditions. Inclusion of rapid distortion terms in the Rotta model (dashed line) even decreases the range over which C_R is positive (hatched area).

A negative Rotta constant originate from the sign of the numerator of the last factor of Equation 6, since r and $Ri_f - 1$ are always negative. Setting $\beta_B = 2/3$ and $\alpha_P < 1/3$ is a sufficient (but not necessary) condition for C_R to be positive for all stability conditions. Targeting a $C_R = 0.9$ for neutral conditions with $r \sim 0.4$ and $\beta_B = 2/3$ requires $\alpha_P = -0.026$. The resulting Rotta constant as a function of stability is shown in Figure 1c (full line), along with results with two other values of α_P: $\alpha_P = 0$ (dashed line) and $\alpha_P = 0.225$ (dotted-dashed line, from Canuto et al., 2001). Results show that these new constraints on the rapid distortion terms allow for the Rotta model to be unconditionally valid. However, those values differ from suggested literature-based values when setting $C_R = 0.9$. For β_p, the proposed value is about a factor of 2 higher whereas for α_P, even the sign differs.

Inclusion of vertical turbulent transport terms in the TKE and vertical velocity variance budgets could also decrease the range of stability conditions over which the Rotta constant is negative. Indeed, several studies have shown that the vertical transport of TKE (T_e) is increasingly important for unstable conditions (e.g., Salesky et al., 2013; Wyngaard & Coté, 1971). For the vertical velocity budget, accounting for vertical turbulent transport results in an additional sink term if $T_e > 3T_w$, where T_w is the vertical transport of vertical velocity variance (see Appendix A of Bou-Zeid et al., 2018). This has been used to explain the increase in critical flux Richardson number over roughness sublayers in stably stratified flow, where this condition is met (Freire et al., 2019). In the present situation, the additional sink in the vertical variance budgets can extend the range of stability conditions over which the Rotta model is physical since the condition $B > \epsilon/3$ will be met for more unstable conditions. Estimates of T_e/T_w are sparse, and both terms are small for near-neutral conditions. We do not discuss this matter quantitatively, but note that including T_e and T_w is expected to increase the range of applicability of the Rotta scheme for a wider range of Ri_f.

The bulk analysis reveals under what conditions a linear Rotta model is compatible with the properties of an idealized ASL flow described by Equations 1 and 2, given ASL measurements of Figure 2. The linear Rotta model (i) should have a Ri_f-dependent Rotta constant and (ii) cannot satisfy mildly unstable ASL anisotropy for the idealized flow conditions considered here when using literature-based rapid-distortion constants. We again stress that these conclusions are valid given the idealized flow conditions considered here, which might not be entirely valid as flow instability increases, and as other terms become important in the TKE and vertical velocity variance budgets. However, maintaining this simplified budget allows performing a scale-by-scale analysis to determine the eddies contributing to the variability in C_R for the restricted range in Ri_f covered here.

3. Spectral Analysis

The R_w analysis and its representation using a Rotta-like closure is now extended scale by scale using a spectral model. The streamwise TKE [$\widetilde{\phi}(k)$] and vertical velocity [$\widetilde{F}_{ww}(k)$] spectra as a function of the streamwise wave number k are considered with normalizing properties $e = \int_0^\infty \widetilde{\phi}(k)dk$ and $\sigma_w^2 = \int_0^\infty \widetilde{F}_{ww}(k)dk$. At very high Reynolds number, a spectral budget for $\widetilde{F}_{ww}(k)$ formulated for eddies in the energy-containing subrange (where anisotropy is large) and inertial subrange (where an isotropic state is approached) is given by Tchen (1953, 1954) and Panchev (1971), as

$$\frac{1}{2}\frac{\partial \widetilde{F}_{ww}(k)}{\partial t} = 0 = \widetilde{B}(k) + \widetilde{R}_w(k) - \widetilde{T}(k). \tag{7}$$

This budget reflects a balance between scalewise buoyancy production/destruction ($\widetilde{B}$, with $\int_0^\infty \widetilde{B}(k)dk = B$), velocity-pressure correlation source/sink ($\widetilde{R}_w$, with $\int_0^\infty \widetilde{R}_w(k)dk = R_w$), and nonlinear transfer of energy across scales ($\widetilde{T}$, with $\int_0^\infty \widetilde{T}(k)dk = 0$), positive over the range of scales considered (i.e., a sink in the above budget). The viscous dissipation term ($\widetilde{\epsilon} = 2\nu k^2 \widetilde{F}_{ww}(k)$ where ν is the kinematic viscosity) is ignored relative to the transfer term in the production-to-inertial eddy sizes. This assumption is likely to hold at very high Reynolds number when $k\eta << 1$, where $\eta = (\nu^3/\epsilon)^{1/4}$ is the Kolmogorov microscale (Pope, 2000). Finally, as in the bulk analysis, vertical turbulent flux transport terms are neglected.

Upon integrating Equation 7 over all scales, which requires including $\widetilde{\epsilon}$ in the budget for small scales (for $k \sim \eta^{-1}$), Equation 1 is recovered (since $\int_0^\infty \widetilde{\epsilon}(k)dk = \epsilon$). For the energy-containing and inertial subrange scales considered here, where $\widetilde{\epsilon}$ is neglected, the nonlinear transfer term $\widetilde{T}$ plays a similar role to the dissipation. The sign of the pressure-strain correlation thus depends on the magnitude of $\widetilde{B}$ relative to $\widetilde{T}$: When the buoyancy term $\widetilde{B}$ exceeds the nonlinear transfer term $\widetilde{T}$ (allowed only for unstable conditions, where $\widetilde{B} > 0$), the pressure-strain correlation should become a sink in the $\widetilde{F}_{ww}$ spectral budget ($\widetilde{R}_w < 0$). We ask now

whether this requirement is compatible with a linear Rotta model for the pressure-strain term in the spectral domain. To answer this question, models for the terms in the spectral budget are required.

3.1. Linear Rotta Model Forced by Idealized ASL Spectra

The state-of-the-science spectral Rotta models (e.g., Besnard et al., 1996; Katul et al., 2013) are conceptually the scale-wise counterparts of the bulk Rotta model (Equation 4). If extended to include rapid-distortion corrections, such spectral Rotta models are given as

$$\begin{aligned}\widetilde{R}_w(k) &= -\frac{\widetilde{C}_R}{\widetilde{\tau}}(k)\left(\widetilde{F}_{ww}(k)-\frac{2}{3}\widetilde{\phi}(k)\right)+\alpha_P\widetilde{P}_m(k)-\beta_B\widetilde{B}(k) \\ &= -\frac{\widetilde{C}_R}{\widetilde{\tau}}(k)\widetilde{\phi}(k)\widetilde{r}+\alpha_P\widetilde{P}_m(k)-\beta_B\widetilde{B}(k),\end{aligned} \tag{8}$$

where $\widetilde{C}_R$ is a (spectral) Rotta coefficient, $\widetilde{r}(k)=\widetilde{F}_{ww}(k)/\widetilde{\phi}(k)-(2/3)$ is the spectral anisotropy, and $\widetilde{\tau}$ is now a scale-dependent turbulence relaxation time scale for which different models have been proposed. To maintain links to prior work (Katul et al., 2013), we selected a $\widetilde{\tau}=\epsilon^{-1/3}k^{-2/3}$ (following Bos et al., 2004). The first rapid distortion correction requires the modeling of a spectral mechanical production $\widetilde{P}_m$ (such that $P_m=\int_0^\infty \widetilde{P}_m(k)dk$). We drop the details about rapid-distortion corrections in the equations within the main text and elaborate on them only in Appendix C and in Figure 5.

Closing the spectral budget requires an analytical expression of spectral anisotropy, which results from choosing idealized expressions for $\widetilde{F}_{ww}$ and $\widetilde{\phi}$ based on measurements. Figures 3a and 3b show measured spectra $\widetilde{\phi}$ and $\widetilde{F}_{ww}$ in an open channel experiment (Katul et al., 2012), over an ice sheet (Cava et al., 2001), grass (Katul et al., 1997), a pine forest (Katul et al., 1999), and a hardwood forest (Katul et al., 1997). Measurements are for near-neutral conditions and for runs where stationary conditions prevailed over extended periods of time.

In agreement with those measurements and earlier work (Banerjee et al., 2015; Grachev et al., 2013; Højstrup, 1982; Kader & Yaglom, 1991; Kaimal, 1978; Kaimal et al., 1972; Katul et al., 2012), only idealized spectral shapes featured in Figure 3c are considered for analytical tractability. These spectra consist of two regimes separated by a transition wave number k_p (vertical line in Figure 3c): (i) the inertial subrange for $k>k_p$, where $\widetilde{\phi}(k)=C_0\epsilon^{2/3}k^{-5/3}$ and $\widetilde{F}_{ww}=C_{ww}\epsilon^{2/3}k^{-5/3}$ (Kolmogorov, 1941), and (ii) the energy-containing range for $k\leq k_p$, where $\widetilde{\phi}(k)=C_0\epsilon^{2/3}k_p^{-2/3}k^{-1}$ and $\widetilde{F}_{ww}(k)=C_{ww}\epsilon^{2/3}k_p^{-5/3}k^0$ (to ensure continuous spectra). The transition wave number is inversely proportional to the measurement height and depends on stability as indicated in Appendix A (Fortuniak & Pawlak, 2015; Kaimal et al., 1972). The spectral constants for boundary layers are taken from Saddoughi and Veeravalli (1994) and are given as $C_0=(33/55)C_K$ and $C_{ww}=(24/55)C_K$, with $C_K=1.55$ being the Kolmogorov constant (used for three-dimensional spectra). For highly unstable or stable conditions (not discussed here), these idealized spectral shapes do not hold. However, as long as these shapes exhibit power laws with negative exponents for $k/k_p<1$, the findings presented below do not qualitatively change (discussed later on).

The resulting turbulent motions are nearly isotropic in the inertial subrange ($\widetilde{r}=0$ for $k>k_p$) and anisotropic in the energy-containing subrange, with vertical motions having less energy than horizontal motions ($\widetilde{r}<0$ for $k<k_p$). Returning to Equation 8, this indicates that in the energy-containing range, the Rotta model predicts a source pressure-strain term ($\widetilde{R}_w>0$). Thus, in the energy-containing range, the ability of the Rotta model to satisfy the spectral budget is conditioned on the relative value of the buoyancy and the nonlinear transfer term, described below. The inertial subrange, where the return-to-isotropy term is almost zero, is not considered.

In the rest of the analysis, the wave number k is normalized by k_p and spectral quantities by powers of ϵ, which leads to an elegant interpretation of the results, independently of variations of k_p and ϵ. Note however that the idealized spectra depend on stability due to the stability-dependence of both k_p (Fortuniak & Pawlak, 2015; Kaimal et al., 1972) and ϵ, which, from Equation 2, can be expressed as $\epsilon=P_m(1-Ri_f)$.

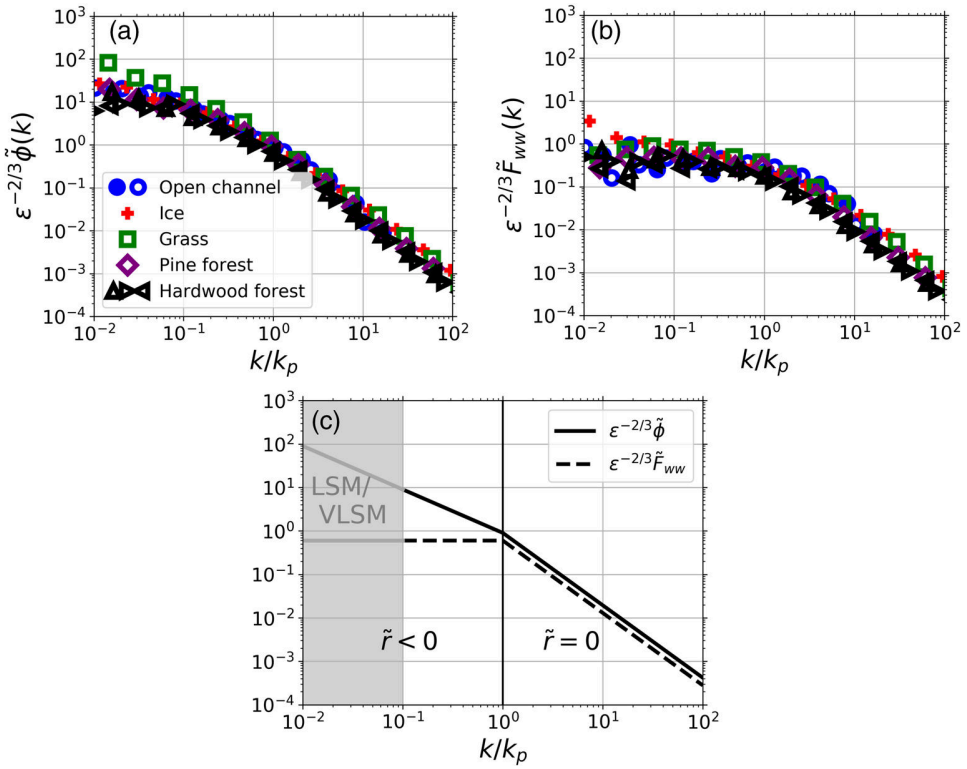

Figure 3. (a, b) Measured streamwise spectra of (a) TKE ($\tilde{\phi}(k)$) (b) vertical velocity ($\tilde{F}_{ww}$) for a near-neutral atmosphere over different terrains, as a function of the relative wave number k/k_p. Spectra have been computed using orthonormal wavelet transforms. (c) Idealized spectra matching measurements, as a function of the relative wave number k/k_p. All spectra are normalized by $\epsilon^{2/3}$. The vertical line in (c) is the threshold below which $\tilde{F}_{ww}(k)$ is smaller than $(2/3)\tilde{\phi}$. The shaded area in (c) is the range of scales where deviations from single-exponent power laws in the measured spectra are evident, presumably due to eddies associated with large or very large scale motion (LSM and VLSM). The simplified canonical shapes considered here do not include them. Note that, when written in dimensional form, those spectra are stability-dependent due both to variations of ϵ and k_p with Ri_f.

3.2. Nonlinear and Buoyancy Terms

In the following, a cospectral model for the buoyancy term $\widetilde{B}$ matching several ASL experiments (Katul et al., 2014; Li et al., 2015) is used. It is expressed as a function of the cospectrum of density-velocity fluctuations. For the nonlinear transfer term $\widetilde{T}$, different models have been proposed (e.g., Heisenberg, 1948; Leith, 1967; Obukhov, 1941). In the following, the Heisenberg model (Heisenberg, 1948) is used for illustration to be consistent with prior work (Katul et al., 2012). It represents $\widetilde{T}$ as resulting from the action of the viscosity of small-scale eddies on large-scale eddies and depends on one constant, the Heisenberg constant C_H. Upon choosing the idealized spectra presented above, $\widetilde{B}$ and $\widetilde{T}$ depend only on the flux Richardson number and the relative wave number k/k_p. Details can be found in Appendix B (Equations B2 and B5 for the buoyancy and nonlinear transfer models, respectively), and the resulting normalized spectral budget is shown in Figure 4 (Equation B11).

Figures 4a–4c show the terms in the spectral $\widetilde{F}_{ww}$ budget (Equation 7) as a function of the relative scale for different stability conditions. The buoyancy term $\widetilde{B}$ (dashed line) is a scale-independent sink for stable conditions (Figure 4a) and source for increasing unstable conditions (Figures 4b and 4c). The nonlinear transfer term $\widetilde{T}$ (dashed line) increases with increasing k/k_p in the energy containing range and is independent of stability when normalized and plotted as a function of k/k_p. So is the pressure-strain correlation term $\widetilde{R}_{ww}$ with a Rotta constant $\widetilde{C}_R = 0.9$, which decreases with increasing k/k_p, consistent with a decreasing anisotropy as the isotropic inertial subrange is approached. As mentioned earlier, rapid distortion corrections are not considered here.

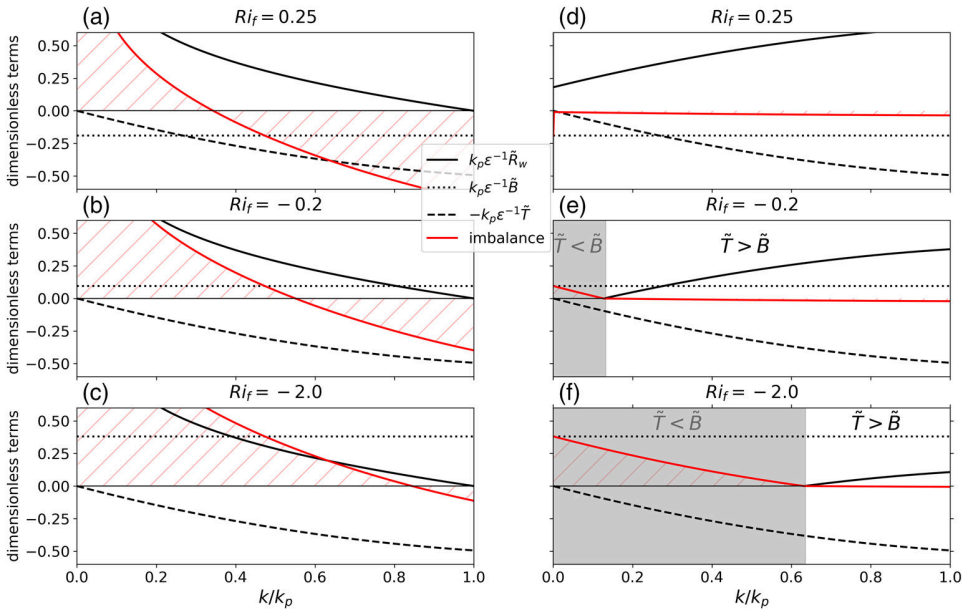

Figure 4. Normalized terms (black) in the spectral budget (7) and residual imbalance (red) as a function of k/k_p for different values of the flux Richardson number Ri_f. In (a)–(c) the Rotta constant in the pressure-strain correlation term is fixed at a constant value of 0.9. In (d)–(f) the Rotta constant evolves with stratification and scale, following Equation 9. The shaded area is where no positive Rotta constant is admitted since the buoyancy source term exceeds the nonlinear transfer sink term. The details of the budget can be found in Appendix B. In this figure, rapid-distortion corrections to the Rotta model are not included (α_P=β_B=0).

The imbalance in the $\widetilde{F}_{ww}$ spectral budget cannot be canceled at all scales with such a scale-independent choice of Rotta constant (red line in Figures 4a–4c). The scale-by-scale analysis is now further extended by allowing the Rotta constant to be scale and stratification dependent so as to satisfy the spectral budget.

4. Scale-Dependent Rotta Constant

As with the bulk analysis, we asked the question of whether or not a linear Rotta model is compatible with the spectral budget (7), given the idealized spectral model presented in section 3.1 (based on observations for mildly stable and unstable conditions). As found above, a linear Rotta model cannot satisfy the spectral balance (7) over the entire energy-containing wave number range when $\widetilde{C}_R$ is scale independent. However, it can be satisfied in a limited range of wave numbers if $\widetilde{C}_R$ is allowed to depend on scale and stability. From Equations 7 and 8, and using idealized spectra described in section 3.1, a scale- and stability-dependent Rotta constant needed to maintain the spectral balance can be derived and is given as

$$\widetilde{C}_R(k/k_p,\, Ri_f) = \left[\widetilde{r}(k/k_p)\right]^{-1}\left\{\frac{1+[\widetilde{\mathscr{A}}_1(k/k_p)-1]Ri_f}{Ri_f-1}\right\}\widetilde{\mathscr{A}}_2(k/k_p). \tag{9}$$

Functions $\tilde{A}_1$ and $\tilde{A}_2$ depend on the normalized nonlinear transfer term $k_p\widetilde{T}/\epsilon$ and on the time scale $\tilde{\tau}$. For the Rotta time scale selected here, they are given as

$$\widetilde{\mathscr{A}}_1(k/k_p) = \frac{4}{7}\left[\frac{k_p\widetilde{T}}{\epsilon}(k/k_p)\right]^{-1}, \quad \widetilde{\mathscr{A}}_2(k/k_p) = C_0^{-1}\left(\frac{k}{k_p}\right)^{1/3}\frac{k_p\widetilde{T}}{\epsilon}(k/k_p), \tag{10}$$

where the normalized nonlinear transfer term reads, when modeled with the Heisenberg model,

$$\frac{k_p\widetilde{T}}{\epsilon}(k/k_p) = 2C_H C_0^{1/2} C_{ww}\left[\frac{2}{3}\frac{k}{k_p} - \frac{1}{4}\left(\frac{k}{k_p}\right)^2\right]. \tag{11}$$

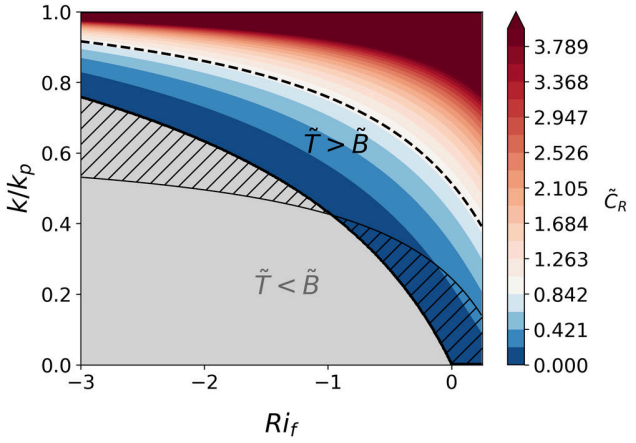

Figure 5. Scalewise Rotta constant $\tilde{C}_R$ as a function of the relative wave number $k/k_p<1$ (in the energy-containing subrange) and the flux Richardson number Ri_f, following Equation 9. Dashed line is the level where $\tilde{C}_R$ matches its standard value of 0.9. The shaded region is where no positive $\tilde{C}_R$ is admitted. The area varies when rapid-distortion terms are included in the Rotta model (hatches), as described in Appendix C.

The Heisenberg constant C_H is set to $(8/9)C_0^{-3/2}$ to recover the TKE spectral properties under neutral conditions (Banerjee & Katul, 2013). Details about the derivation of Equations 9–11 are in Appendix C, which also contains a general expression of $\widetilde{C}_R$ when rapid-distortion terms are included in the spectral Rotta model (Equation C14). Note that, in the above expressions, the scale parameter is implicitly stability-dependent through the stability dependence of k_p.

Figures 4d–4f show the terms of the $\widetilde{F}_{ww}$ spectral balance with the pressure-strain term parametrized by means of a scale- and stability-dependent Rotta constant (Equation 9). For stable stratification (Figure 4d), the balance is satisfied at all scales (the red line is uniformly zero). With increased instability (Figures 4e and 4f), the dynamic $\widetilde{C}_R(k)$ model cannot guarantee a positive Rotta constant at large scales (or small k/k_p) because the redistribution model can no longer predict the sign of the energy exchanges: for scales large enough (shaded area), the buoyancy source term exceeds the nonlinear transfer sink term, and hence, the pressure-strain term is expected to change sign to maintain a scalewise balance. From Equation 8, this implies a negative Rotta constant given that the sign of the anisotropy factor is constant (and negative) in the energy-containing range. The range of scales over which the Rotta constant is negative increases with increasing instability (i.e., for $k/k_p<0.1$ and $k/k_p<0.4$ in Figures 4c and 4d, respectively). Similar to the bulk analysis, the spectral model reveals that, for the idealized flow conditions described in Figure 3c (and based on measurements), (i) a scale- and stability-dependent Rotta constant is required to close the spectral budget and that (ii) below a critical wave number, a linear Rotta model fails to predict the correct sign of the pressure-strain correlation term.

The scale-by-scale picture is however more refined. It reveals that for stability conditions over which the bulk Rotta model fails to predict the correct sign of the pressure-strain correlation term (for $Ri_f<-0.5$, see Figure 1b), its spectral counterpart is still valid, but over a limited range of scales. This behavior is summarized in Figure 5, which shows the increase of the region over which Rotta constant is negative as a function of stability and scale (shaded area, where $\widetilde{C}_R<0$). The figure also reveals that as the scale increases, the range of stability conditions over which the Rotta model is not physical increases. This finding indicates that for larger and more anisotropic eddies, the classical linear Rotta model becomes physically unrealistic.

Accounting for rapid-distortion terms in the Rotta model (as described in Appendix C1) changes the area where the Rotta constant is not physical (hatches in Figure 5). However, unlike the bulk case, the area increases for $k/k_p<0.4$ and decreases for $k/k_p>0.4$. This is a consequence of the antagonist behavior of the two rapid-distortion terms, respectively, $\alpha_P\widetilde{P}_m$ and $-\beta_B\widetilde{B}$ (see Equation 8). When the rapid distortion terms are included in the $\widetilde{F}_{ww}$ budget as part of the Rotta model, the first term is an additional source in the budget (since $\widetilde{P}_m$ is a source, as in the bulk model), and the second term acts as an additional sink for unstable conditions (since $\widetilde{B}>0$ and $\beta_B>0$). Hence, at a given scale k/k_p, the (negative) threshold Ri_f below which the buoyancy source exceeds the nonlinear transfer sink (and hence the slow Rotta term must change sign) is displaced due to these two additional terms. Whether the threshold Ri_f increases or decreases depends on the relative magnitude of $\alpha_P\widetilde{P}_m$ with respect to $-\beta_B\widetilde{B}$, that is, whether the two additional terms add up as an additional source or a sink in the budget. This further depends on the relative scale k/k_p, since $\widetilde{P}_m$ and $\widetilde{B}$ are both scale dependent. The finding here shows that the spectral behavior of the rapid-distortion terms is nontrivial as compared to the bulk case. Choosing rapid-distortion constants that result in a unconditionally positive Rotta constant (as in the bulk case; Figure 1b), although feasible, is nontrivial and is outside of the scope of the present work. It would require choosing and validating scale-dependent models for α_P and β_B.

Figure 5 also summarizes the variations of the "optimal" Rotta constant as a function of scale and stability, in the region where it is positive. Consistent with the bulk analysis, the Rotta constant decreases with

increasing instability at a fixed large scale. As the inertial subrange is approached ($k/k_p \to 1$), the observed increase in $\widetilde{C}_R$ results from anisotropy decreasing to zero, and hence the expression for the Rotta constant losing physical meaning (i.e., the solution becomes degenerate). However, far enough from this limit (e.g., on the left of the dashed line for which $\widetilde{C}_R = 0.9$), the behavior of $\widetilde{C}_R$ is physically sound. Figure 5 shows that $\widetilde{C}_R$ decreases with increasing scale. This dependence is identical to the nonlinear transfer term variation with k/k_p, which is predicted to decrease down to zero as large scales are approached (dashed lines in Figure 4). It can be traced back to function $\tilde{A}_2$ (Equation 10), proportional to the nonlinear transfer term. From a physical perspective, this link implies that the efficiency of eddies at redistributing energy between the different components (C_R^{-1}) is related to their efficiency at transporting energy toward small scales ($\widetilde{T}$). Choosing other models for the nonlinear transfer term does not alter this finding, but it affects variations of $\widetilde{C}_R$ with k/k_p.

The above analysis relies on turbulence satisfying idealized spectral budgets with a prescribed form of the spectra and their variation with stability (through ϵ and k_p). Those spectra are limited by several factors. At large scales ($k < 10^{-1}k_p$), the measured spectra start deviating from the idealized -1 or 0 power laws (Figures 3a and 3b). For simplicity, this effect is neglected, but its inclusion does not qualitatively change the findings here. In the energy-containing range, the -1 power law of the TKE spectra has been a subject of debate due to differences and uncertainties in the measurements at this range of scales and possible influence of stability and the use of Taylor's frozen turbulence hypothesis (Banerjee et al., 2015; Drobinski et al., 2007; Katul & Chu, 1998; Marusic et al., 2010; Morrison et al., 2002; Nickels et al., 2005; Nikora, 1999). Again, the results here are not significantly dependent on the choice of the power law for $\widetilde{\phi}$ as long as it is smaller than 0. The general expression of $\widetilde{C}_R$ presented in Appendix C is also independent of the choice of the power law. As instability increases, the -1 power law describing the large-scale TKE spectrum begins to migrate toward a $-5/3$ exponent as evidenced by a number of ASL experiments (Banerjee et al., 2015; Kader & Yaglom, 1991). In fact, for strongly unstable (near convective) cases (not considered here), measurements (Kader & Yaglom, 1991) further suggest that the spectra of TKE and w can be almost discontinuous at the transition wave number k_p. These spectra exhibit a $-5/3$ law at large scales with a discontinuity, followed by another $-5/3$ regime associated with Kolmogorov scaling. Hence, in those situations anisotropy $\widetilde{r}$ changes sign, with more energy in the vertical than in the horizontal turbulent components. Finally, additional terms could partly explain the inconsistency of the spectral Rotta model revealed by the above analysis. As for the bulk case, inclusion of vertical transport of turbulence in the $\widetilde{F}_{ww}$ spectral budget can act as an additional sink. Given that the bulk transport terms are small for the mildly unstable conditions considered here, inclusion of their effect will not qualitatively change the above analysis, except perhaps above roughness sublayers (Freire et al., 2019).

5. Conclusion

This work analyzed the implications of using linear return-to-isotropy models of the pressure-strain correlation (or simply Rotta models) to describe planar-homogeneous and stationary boundary layer turbulence for mildly stable to mildly unstable conditions. The flow was analyzed by combining TKE and vertical velocity variance budgets representing the bulk and scale-by-scale properties of turbulence. The analysis required estimates of turbulence anisotropy as well as spectral shapes. Those were externally supplied from measurements in the ASL for which a rich literature on both velocity spectral shapes and bulk anisotropy variations, along with their dependence with flow instability, is available. The analysis revealed two inconsistencies when using a linear Rotta model to describe return to isotropy for the idealized flow conditions described by those measurements. The first is that for some stability conditions and eddy sizes, the Rotta model is not physical. It should thus be amended by other processes beyond a linear return to isotropy such as quadratic dependencies on anisotropy. The second is that, to satisfy the two aforementioned budgets outside of the nonphysical range, the Rotta constant should depend on stability and scale. Both results are sensitive to the balance considered. In particular, the relative importance of the vertical flux transport by turbulence terms, which were neglected in the present study, cannot be overlooked for stratified ASL flow conditions. The work here has also remained "silent" on another anisotropy-producing mechanism, which is likely to be of significance in the sublayers below the ASL. This mechanism is labeled "wall-blocking" effect because the presence of an impervious boundary dampens w', which, in turn, is sensed everywhere in the domain by

p', the pressure perturbation. Classical closure theories accommodate this effect as a new term in the Rotta return-to-isotropy scheme (or its spectral version) as discussed elsewhere (McColl et al., 2016). In smooth-wall boundary layers, wall blocking appeared to be minor in the absence of stratification for the log region. However, the interplay between wall blocking and density stratification has not been explicitly considered and remains a research topic better kept for the future.

Appendix A: Anisotropy According to Monin-Obukhov Similarity Functions

In the ASL, stability dependence of bulk flow statistics and spectral properties are routinely analyzed in the context of Monin-Obukhov Similarity Theory (MOST Foken, 2006; Monin & Obukhov, 1954). From dimensional arguments, dimensionless turbulent fluctuations and shear should depend only on a dimensionless stability parameter $\zeta = z/L$ (negative for unstable and positive for stable stratification), where z is the distance from the boundary (or displacement height) and L is the Obukhov length, and on the boundary layer height, z_i.

Numerous ASL measurements (e.g., Sorbjan, 1989, Table 4.2) have provided the following expressions for dimensionless shear

$$\phi_m(\zeta) = \frac{\kappa z}{(-\overline{u'w'})^{1/2}} \frac{dU}{dz} = \begin{cases} 1 + 4.7\zeta & \text{if } \zeta \geq 0 \\ (1 - 15\zeta)^{-1/4} & \text{if } \zeta < 0 \end{cases}, \tag{A1}$$

dimensionless vertical velocity standard deviation

$$\phi_w(\zeta) = \frac{\sigma_w}{(-\overline{u'w'})^{1/2}} = \begin{cases} 1.25 & \text{if } \zeta \geq 0 \\ 1.25(1 - 3\zeta)^{1/3} & \text{if } \zeta < 0 \end{cases}, \tag{A2}$$

and dimensionless horizontal velocity standard deviation

$$\phi_{u_h}\left(\zeta, \frac{z_i}{z}\right) = \left(\frac{\overline{u_h'u_h'}}{-\overline{u'w'}}\right)^{1/2} = \begin{cases} 2.28 & \text{if } \zeta \geq 0 \\ \left[12 - 0.5\frac{z_i}{z}\zeta\right]^{1/3} & \text{if } \zeta < 0 \end{cases}, \tag{A3}$$

where $\kappa = 0.4$ is the von Kármán constant and u_h is either u or v. Finally, the flux Richardson number and the stability parameter are linked through $Ri_f = \zeta/\phi_m(\zeta)$.

Figure 2 shows anisotropy

$$r = \frac{\phi_w^2}{(1/2)(\phi_w^2 + \phi_u^2 + \phi_v^2)} - \frac{2}{3} \tag{A4}$$

computed for the aforementioned dimensionless functions as a function of the flux Richardson number and the relative boundary layer height. For the range of stability conditions investigated in the present work ($Ri_f > -5$), which exclude the free convection limit, Figure 2 shows that the anisotropy ratio is always negative. This indicates that more energy is concentrated in the horizontal than in the vertical turbulent components. In the main text, the boundary layer height is set to be 10^3 times higher than the measurement height. The sign of the anisotropy ratio is not sensitive to the choice of the boundary layer height (not shown).

Finally, as an illustration, we show below an example of a model of k_p from the Kansas experiment (Kaimal & Finnigan, 1994):

$$zk_p^k(\zeta) = \begin{cases} \zeta, & \zeta > 2 \\ 1.1 + 0.45\zeta, & 1 < \zeta \le 2 \\ 0.55 + \zeta, & 0 \le \zeta \le 1 \\ 0.55 + 0.38\zeta, & -1 \le \zeta < 0 \\ 0.17, & \zeta < -1 \end{cases}. \tag{A5}$$

Note however that the results of the main text are all expressed as a function of k/k_p and are hence independent of a particular model of k_p.

Appendix B: Details on the Spectral Budget

At very high Reynolds number, a spectral budget for $\widetilde{F}_{ww}(k)$ formulated for large and inertial subrange eddies follows from Tchen (1953, 1954) and Panchev (1971) and is given by

$$\frac{1}{2}\frac{\partial \widetilde{F}_{ww}(k)}{\partial t} = 0 = \widetilde{B}(k) + \widetilde{R}_w(k) - \widetilde{T}(k). \tag{B1}$$

Details on the different terms of this budget are now provided. The model for the pressure-strain term $\widetilde{R}$ is presented in Equation 8.

For the ASL with an isobaric approximation, the buoyancy source/sink term $\widetilde{B}$ is related to the cospectrum of temperature fluctuations $\widetilde{F}_{wT}$ as

$$\widetilde{B}(k) = -\frac{g}{T}\widetilde{F}_{wT}(k), \tag{B2}$$

where the cospectrum has the normalizing property $\overline{w'T'} = \int_0^\infty \widetilde{F}_{wT}(k)dk$. Katul et al. (2014) and Li et al. (2015) proposed a cospectrum matching both a theoretical spectral budget and ASL measurements, of the form $\widetilde{F}_{wT}(k) = C_{wT}\epsilon^{1/3}\frac{dT}{dz}k^{-7/3}$ for $k \ge k_p$ and $\widetilde{F}_{wT}(k) = C_{wT}\epsilon^{1/3}\frac{dT}{dz}k_p^{-7/3}$ for $k \le k_p$. The transition wave number k_p between the energy-containing and the inertial subranges is proportional to the measurement height and changes slightly with stratification (Fortuniak & Pawlak, 2015; Kaimal et al., 1972). The spectral constant reads $C_{wT} = C_{uw}Q(\zeta)$ with

$$Q(\zeta) = 1 - \frac{C_T\zeta}{(1 - C_{1T})C_0(\phi_m - \zeta)}, \tag{B3}$$

C_0=0.9, C_T=0.8, C_{1T}=3/5 (Katul et al., 2014), and ζ the stability parameter defined in Appendix A.

The nonlinear transfer term $\widetilde{T}$ is represented using the Heisenberg model (Heisenberg, 1948), to be consistent with the models of the buoyancy and Rotta terms (as explained in the main text). Within this spectral approach of turbulence, developed by Heisenberg (1948) and Tchen (1953, 1954) (and summarized in Panchev, 1971, pp. 203–224), what is described is an integrated spectral budget, obtained by integration of Equation B1 over streamwise wave numbers between k and ∞. This results in an equation describing the spectral balance for a particular wavelength k, the lower limit of the integral. What is then modeled is $\widetilde{W}$, the integral of the nonlinear transfer term,

$$\widetilde{W}(k) = \int_k^\infty \widetilde{T}(p)dp, \tag{B4}$$

and hence $\widetilde{T}(k) = -\frac{d}{dk}\widetilde{W}(k)$. Following Heisenberg (1948), $\widetilde{W}$ is modeled as resulting from the action of viscosity generated by eddies of wavelength greater than k on eddies of wavelength smaller than k

$$\widetilde{W}(k) = -2C_H \int_k^\infty \left(\frac{\widetilde{\phi}(p)}{p^3}\right)^{1/2} dp \int_0^k p^2 \widetilde{F}_{ww}(p) dp, \tag{B5}$$

where $C_H = (8/9)C_0^{-3/2}$ for consistency with Kolmogorov scaling in the inertial range (Banerjee & Katul, 2013; Schumann, 1994). Since $\widetilde{W}$ models the nonlinear energy transfer in the vertical component of turbulence, enstrophy (the second factor) is here computed from $\widetilde{F}_{ww}$ (and not from the TKE spectrum $\widetilde{\phi}$ as in Panchev, 1971, where the transfer term was computed for the TKE spectral budget).

Expressions of the terms of the spectral budget in the energy-containing range ($k \leq k_p$) are presented for idealized spectra $\widetilde{\phi}(k)$ and $\widetilde{F}_{ww}(k)$ presented in the main text (and drawn in Figure 3c). First, the nonlinear transfer term reads, from derivation of (B5) with respect to k,

$$\widetilde{T}(k) = 2C_H C_0^{1/2} C_{ww} k_p^{-1} \epsilon \left[\frac{2}{3}\frac{k}{k_p} - \frac{1}{4}\left(\frac{k}{k_p}\right)^2\right]. \tag{B6}$$

Second, the pressure-strain term following the Rotta model without rapid-distortion corrections (Equation 8, with $\alpha_P = \beta_B = 0$) reads

$$\widetilde{R}_w = -C_0^{1/2} C_R \epsilon k_p^{-1} \left(\frac{k}{k_p}\right)^{2/3} \left[C_{ww} - \frac{2}{3} C_0 \frac{k_p}{k}\right]. \tag{B7}$$

Finally, using the idealized $\widetilde{F}_{wT}$ cospectra presented above, the spectral buoyancy term can be rewritten as a function of the flux Richardson number. This results from the bulk buoyancy B being expressed as a function of (i) the spectral buoyancy term

$$\begin{aligned} B &= -\frac{g}{T}\int_0^\infty \widetilde{F}_{wT}(p) dp \\ &= -\frac{7}{4}\epsilon^{1/3} C_{wT} \frac{g}{T}\frac{dT}{dz} k_p^{-4/3}(k), \quad k \leq k_p, \\ &= \frac{7}{4} k_p \widetilde{B} \end{aligned} \tag{B8}$$

and (ii) TKE dissipation, using the bulk TKE budget (Equation 2)

$$B = \epsilon \frac{Ri_f}{1 - Ri_f}. \tag{B9}$$

This yields

$$\widetilde{B} = \frac{4}{7}\epsilon k_p^{-1} \frac{Ri_f}{Ri_f - 1}, \quad k \leq k_p. \tag{B10}$$

The spectral budget (B1) (or Equation 7) normalized by ϵk_p^{-1} thus reads

$$\frac{4}{7}\frac{Ri_f}{Ri_f - 1} - C_0^{1/2} C_R \left[C_{ww}\frac{k}{k_p} - \frac{2}{3} C_0\right] - 2C_H C_0^{1/2} C_{ww} \left[\frac{2}{3}\frac{k}{k_p} - \frac{1}{4}\left(\frac{k}{k_p}\right)^2\right] = 0, \tag{B11}$$

a balance between (from left to right) dimensionless buoyancy, energy redistribution, and nonlinear transfer of energy across scales. The terms have been normalized by ϵk_p^{-1} and are plotted in Figure 4. As already mentioned above, we again stress that, in this budget, rapid-distortion corrections have not been included in the Rotta model of the energy redistribution term.

Appendix C: General Derivation of the Scale- and Stratification-Dependent Rotta Constant

This section presents the steps leading to a generalized form of Equation 9, valid for different choices of time scales and nonlinear transfer models, and including rapid-distortion corrections to the Rotta model.

The spectral Rotta models considered in the literature (Bos et al., 2004; Katul et al., 2013) only contain a slow component. In this work, the spectral Rotta model is generalized by adding rapid distortion terms on the basis of the bulk model of Canuto et al. (2001), such that

$$\widetilde{R}_w = -\frac{\widetilde{C}_R}{\widetilde{\tau}}\left(\widetilde{F}_{ww} - \frac{2}{3}\widetilde{\phi}\right) + \alpha_P \widetilde{P}_m - \beta_B \widetilde{B}, \tag{C1}$$

where α_P and β_B are set to their bulk values of 0.225 and 0.35, respectively.

The scalewise production term $\widetilde{P}_m$ is obtained from a spectral balance for TKE (e.g., Tchen, 1953), which for stationary and planar-homogeneous flow at high Reynolds number in the absence of subsidence reads

$$\frac{\partial \widetilde{\phi}}{\partial t} = 0 = \widetilde{P}_m + \widetilde{B} - \widetilde{T}_\phi. \tag{C2}$$

Hence, the nonlinear Rotta scheme model reads

$$\widetilde{R}_w = -\frac{\widetilde{C}_R}{\widetilde{\tau}}\left(\widetilde{F}_{ww} - \frac{2}{3}\widetilde{\phi}\right) + \alpha_P(\widetilde{T}_\phi - \widetilde{B}) - \beta_B \widetilde{B}. \tag{C3}$$

The nonlinear transfer term $\widetilde{T}_\phi$ is computed using a Heisenberg viscosity approach (see Appendix B for its application to the vertical velocity spectral budget; Heisenberg, 1948). Heisenberg (1948) and Tchen (1953,1954) model the terms of an integrated spectral budget, derived by integrating Equation C2 between k and ∞. The nonlinear transfer term in the resulting equation

$$\widetilde{W}_\phi(k) = \int_k^\infty \widetilde{T}_\phi(p)dp \tag{C4}$$

is then modeled as resulting from the action of viscosity of eddies of wavelength greater than k on eddies of wavelength smaller than k, that is,

$$\tilde{W}_\phi(k) = -2C_H \int_k^\infty \frac{\tilde{\phi}(p)}{p^3}^{1/2} dp \int_0^k p^2 \tilde{\phi}(p)dp, \tag{C5}$$

where $C_H = (8/9)C_0^{-3/2}$. The idealized TKE spectrum presented in Figure 3 yields the following form of the nonlinear transfer term $\widetilde{T}_\phi(k) = -\frac{d}{dk}\widetilde{W}_\phi(k)$ for $k \le k_p$,

$$\widetilde{T}_\phi(k, \eta) = 2C_H C_0^{3/2}\left[\frac{2}{4} - \frac{1}{4}\frac{k}{k_p}\right]\epsilon k_p^{-1}. \tag{C6}$$

The time scale $\widetilde{\tau}$ is usually assumed to be k dependent and to depend only on inertial range variables (ϵ, conserved across the cascade, k and k_p) in conventional spectral models (e.g., Besnard et al., 1996; Katul et al., 2013; Panchev, 1971). From dimensional considerations, its general form in the energy-containing range ($k \le k_p$) is

$$\widetilde{\tau}(k) \propto \epsilon^{-1/3} k_p^{-2/3}\left(\frac{k}{k_p}\right)^m = \widetilde{\phi}(k)\mathscr{A}_\tau \epsilon^{-1} k_p \left(\frac{k}{k_p}\right)^{m-a} \tag{C7}$$

with $\widetilde{\phi}(k) = C_0 \epsilon^{2/3} k_p^{-5/3-a} k^a$ the TKE spectrum of slope a, C_0 is the Kolmogorov constant, and m and $\mathscr{A}_\tau$ depend on the model used for the time scale. For a TKE spectrum with $a = -1$, the time scale $\widetilde{\tau} = \epsilon^{-1/3}$

$k^{-2/3}$ (used in the following Bos et al., 2004; Katul et al., 2013) corresponds to $m=-2/3$ and $A_\tau = C_0^{-1}$, while other estimates of the time scale, for example, $\widetilde{\tau} = k^{-3/2}\widetilde{\phi}^{-1/2}$ (Besnard et al., 1996), correspond to $m=-1$ and $A_\tau = C_0^{-3/2}$.

Using the Rotta model (C3) and the time scale (C7), the $\widetilde{F}_{ww}$ spectral budget can be solved for $\widetilde{C}_R$, yielding

$$\widetilde{C}_R = \widetilde{r}^{-1}\left\{-1 + [(1-\beta_B)-\alpha_P]\frac{\widetilde{B}}{\widetilde{T}} + \alpha_P\frac{\widetilde{T}_\phi}{\widetilde{T}}\right\}\frac{\widetilde{T}}{\epsilon}\mathscr{A}_\tau k_p^{1-m+a}k^{m-a}. \tag{C8}$$

Evaluation of Equation C8 requires an expression for the ratio $\widetilde{B}/\widetilde{T}$. We now show that, regardless of the choosen model for the nonlinear transfer of energy across scales ($\widetilde{T}$), this ratio reads

$$\frac{\widetilde{B}}{\widetilde{T}} = \widetilde{\mathscr{A}}_1\frac{Ri_f}{Ri_f - 1}. \tag{C9}$$

The constant $\widetilde{\mathscr{A}}_1$ depends on the model and is given below. Different models for the nonlinear transfer term (Heisenberg, 1948; Leith, 1967; Obukhov, 1941) all assume that it depends on the TKE spectrum and hence should depend only on k, k_p, and ϵ. Dimensional considerations then yield that

$$\widetilde{T} = \widetilde{\mathscr{B}}_{NL}\epsilon k_p^{-1}, \tag{C10}$$

where $\widetilde{\mathcal{B}}_{NL}$ depends only on k/k_p. For the Heisenberg (1948) model (Equation B6), used in the following, it reads

$$\widetilde{\mathscr{B}}_{NL} = 2C_H C_0^{1/2} C_{ww}\left[\frac{2}{3}\frac{k}{k_p} - \frac{1}{4}\left(\frac{k}{k_p}\right)^2\right]. \tag{C11}$$

In the general case, dividing the expression of the buoyancy term derived in Appendix B (Equation B10)

$$\widetilde{B} = \frac{4}{7}\epsilon k_p^{-1}\frac{Ri_f}{Ri_f - 1}, \quad k \le k_p, \tag{C12}$$

by Equation C10, yields Equation C9 with

$$\widetilde{\mathscr{A}}_1 = \frac{4}{7}\epsilon\widetilde{T}^{-1}k_p^{-1} = \frac{4}{7}\widetilde{\mathscr{B}}_{NL}^{-1}. \tag{C13}$$

By using (C9) in Equation C8, we obtain the generalized expression of the Rotta constant

$$\widetilde{C}_R = \widetilde{r}^{-1}\left\{\frac{1 + [(1-\beta_B-\alpha_P)\widetilde{\mathscr{A}}_1 - 1]Ri_f}{Ri_f - 1} + \alpha_P\frac{\widetilde{T}_\phi}{\widetilde{T}}\right\}\widetilde{\mathscr{A}}_2, \tag{C14}$$

where, using (C13),

$$\tilde{A}_2 = \mathscr{A}_\tau k_p^{1-m+a}k^{m-a}\frac{\widetilde{T}}{\epsilon} = \mathscr{A}_\tau k_p^{-m+a}k^{m-a}\widetilde{B}_{NL}. \tag{C15}$$

If the Heisenberg model is used for $\widetilde{T}$ and $\widetilde{T}_\phi$ (Equations B6 and C6), their ratio reads

$$\frac{\widetilde{T}_\phi}{\widetilde{T}} = C_0 C_{ww}^{-1}\frac{\left[\frac{2}{4} - \frac{1}{4}\frac{k}{k_p}\right]}{\left[\frac{2}{3}\frac{k}{k_p} - \frac{1}{4}\left(\frac{k}{k_p}\right)^2\right]}. \tag{C16}$$

Equation C14 reduces to Equation 9 when rapid-distortion terms are dropped ($\alpha_P=\beta_B=0$) and when, in the evaluation of $\widetilde{\mathscr{A}}_1$ and $\widetilde{\mathscr{A}}_2$, the Heisenberg (1948) and Katul et al. (2013) models are used for the nonlinear transfer term and the Rotta time scale, respectively, which yields

$$\tilde{A}_1\left(\frac{k}{k_p}\right)=\frac{2}{7}C_H^{-1}C_0^{-1/2}C_{ww}^{-1}\left[\frac{2}{3}\frac{k}{k_p}-\frac{1}{4}\left(\frac{k}{k_p}\right)^2\right]^{-1}$$
$$\tilde{A}_2\left(\frac{k}{k_p}\right)=2C_HC_0^{-1/2}C_{ww}\left[\frac{2}{3}\frac{k}{k_p}-\frac{1}{4}\left(\frac{k}{k_p}\right)^2\right]\left(\frac{k}{k_p}\right)^{1/3}. \quad \text{(C17)}$$

Acknowledgments

Data were not created for this research. A. A. was supported by DGA Grant No. D0456JE075, the French Brittany Regional Council, ANR Caravel, and ISblue project, Interdisciplinary graduate school for the blue planet (ANR-17-EURE-0015), cofunded by a grant from the French Government under the program "Investissements d'Avenir". G. K. was supported by the National Science Foundation (NSF-AGS-1644382 and NSF-IOS-1754893).

References

Abid, R., & Speziale, C. G. (1993). Predicting equilibrium states with Reynolds stress closures in channel flow and homogeneous shear flow. *Physics of Fluids A: Fluid Dynamics*, *5*(7), 1776–1782. https://doi.org/10.1063/1.858852

Banerjee, T., & Katul, G. G. (2013). Logarithmic scaling in the longitudinal velocity variance explained by a spectral budget. *Physics of Fluids*, *25*(12), 125106. https://doi.org/10.1063/1.4837876

Banerjee, T., Katul, G. G., Salesky, S. T., & Chamecki, M. (2015). Revisiting the formulations for the longitudinal velocity variance in the unstable atmospheric surface layer. *Quarterly Journal of the Royal Meteorological Society*, *141*(690), 1699–1711. https://doi.org/10.1002/qj.2472

Besnard, D. C., Harlow, F. H., Rauenzahn, R. M., & Zemach, C. (1996). Spectral transport model for turbulence. *Theoretical and Computational Fluid Dynamics*, *8*(1), 1–35. https://doi.org/10.1007/BF00312400

Bos, W. J. T., Touil, H., Shao, L., & Bertoglio, J.-P. (2004). On the behavior of the velocity-scalar cross correlation spectrum in the inertial range. *Physics of Fluids*, *16*(10), 3818–3823. https://doi.org/10.1063/1.1779229

Bou-Zeid, E., Gao, X., Ansorge, C., & Katul, G. G. (2018). On the role of return to isotropy in wall-bounded turbulent flows with buoyancy. *Journal of Fluid Mechanics*, *856*, 61–78. https://doi.org/10.1017/jfm.2018.693

Brugger, P., Katul, G. G., DeRoo, F., Kröniger, K., Rotenberg, E., Rohatyn, S., & Mauder, M. (2018). Scalewise invariant analysis of the anisotropic Reynolds stress tensor for atmospheric surface layer and canopy sublayer turbulent flows. *Physical Review Fluids*, *3*(5), 054608. https://doi.org/10.1103/PhysRevFluids.3.054608

Canuto, V. M., Howard, A., Cheng, Y., & Dubovikov, M. S. (2001). Ocean turbulence. Part I: One-point closure model-momentum and heat vertical diffusivities. *Journal of Physical Oceanography*, *31*(6), 1413–1426. https://doi.org/10.1175/1520-0485(2001)031<1413:OTPIOP>2.0.CO;2

Carbone, M., & Bragg, A. D. (2020). Is vortex stretching the main cause of the turbulent energy cascade? *Journal of Fluid Mechanics*, *883*, R2. https://doi.org/10.1017/jfm.2019.923

Cava, D., Giostra, U., & Tagliazucca, M. (2001). Spectral maxima in a perturbed stable boundary layer. *Boundary-Layer Meteorology*, *100*(3), 421–437. https://doi.org/10.1023/A:1019219117439

Charuchittipan, D., & Wilson, J. D. (2009). Turbulent kinetic energy dissipation in the surface layer. *Boundary-Layer Meteorology*, *132*(2), 193–204. https://doi.org/10.1007/s10546-009-9399-x

Cuxart, J., Bougeault, P., & Redelsperger, J.-L. (2000). A turbulence scheme allowing for mesoscale and large-eddy simulations. *Quarterly Journal of the Royal Meteorological Society*, *126*, 1–30. https://doi.org/10.1002/qj.49712656202

Drobinski, P., Carlotti, P., Redelsperger, J.-L., Masson, V., Banta, R. M., & Newsom, R. K. (2007). Numerical and experimental investigation of the neutral atmospheric surface layer. *Journal of the Atmospheric Sciences*, *64*(1), 137–156. https://doi.org/10.1175/JAS3831.1

Foken, T. (2006). 50 years of the Monin-Obukhov similarity theory. *Boundary-Layer Meteorology*, *119*(3), 431–447. https://doi.org/10.1007/s10546-006-9048-6

Fortuniak, K., & Pawlak, W. (2015). Selected spectral characteristics of turbulence over an urbanized area in the centre of Łódź, Poland. *Boundary-Layer Meteorology*, *154*(1), 137–156. https://doi.org/10.1007/s10546-014-9966-7

Freire, L. S., Chamecki, M., Bou-Zeid, E., & Dias, N. L. (2019). Critical flux Richardson number for Kolmogorov turbulence enabled by TKE transport. *Quarterly Journal of the Royal Meteorological Society*, *145*, 1551–1558. https://doi.org/10.1002/qj.3511

Ghannam, K., Duman, T., Salesky, S. T., Chamecki, M., & Katul, G. (2017). The non-local character of turbulence asymmetry in the convective atmospheric boundary layer. *Quarterly Journal of the Royal Meteorological Society*, *143*(702), 494–507. https://doi.org/10.1002/qj.2937

Ghannam, K., Katul, G. G., Bou-Zeid, E., Gerken, T., & Chamecki, M. (2018). Scaling and similarity of the anisotropic coherent eddies in near-surface atmospheric turbulence. *Journal of the Atmospheric Sciences*, *75*(3), 943–964. https://doi.org/10.1175/JAS-D-17-0246.1

Grachev, A. A., Andreas, E. L., Fairall, C. W., Guest, P. S., & Persson, P. G. (2013). The critical Richardson number and limits of applicability of local similarity theory in the stable boundary layer. *Boundary-Layer Meteorology*, *147*(1), 51–82. https://doi.org/10.1007/s10546-012-9771-0

Heisenberg, W. (1948). On the theory of statistical and isotropic turbulence. *Proceedings of the Royal Society of London. Series A. Mathematical and Physical Sciences*, *195*(1042), 402–406. https://doi.org/10.1098/rspa.1948.0127

Højstrup, J. (1982). Velocity spectra in the unstable planetary boundary layer. *Journal of the Atmospheric Sciences*, *39*(10), 2239–2248.

Kader, B. A., & Yaglom, A. M. (1990). Mean fields and fluctuation moments in unstably stratified turbulent boundary layers. *Journal of Fluid Mechanics*, *212*, 637–662. https://doi.org/10.1017/S0022112090002129

Kader, B. A., & Yaglom, A. M. (1991). Spectra and correlation functions of surface layer atmospheric turbulence in unstable thermal stratification. *Turbulence and Coherent Structures* (pp. 387–412): Springer. https://doi.org/10.1007/978-94-015-7904-9_24

Kaimal, J. C. (1978). Horizontal velocity spectra in an unstable surface layer. *Journal of the Atmospheric Sciences*, *35*(1), 18–24. https://doi.org/10.1175/1520-0469(1978)035<0018:HVSIAU>2.0.CO;2

Kaimal, J. C., & Finnigan, J. J. (1994). *Atmospheric boundary layer flows: Their structure and measurement*: Oxford University Press.

Kaimal, J. C., Wyngaard, J., Izumi, Y., & Coté, O. R. (1972). Spectral characteristics of surface-layer turbulence. *Quarterly Journal of the Royal Meteorological Society*, *98*(417), 563–589. https://doi.org/10.1002/qj.49709841707

Katul, G., & Chu, C.-R. (1998). A theoretical and experimental investigation of energy-containing scales in the dynamic sublayer of boundary-layer flows. *Boundary-Layer Meteorology*, *86*(2), 279–312. https://doi.org/10.1023/A:1000657014845

Katul, G., Hsieh, C.-I., Bowling, D., Clark, K., Shurpali, N., Turnipseed, A., et al. (1999). Spatial variability of turbulent fluxes in the roughness sublayer of an even-aged pine forest. *Boundary-Layer Meteorology*, *93*(1), 1–28. https://doi.org/10.1023/A:1002079602069

Katul, G., Hsieh, C.-I., Kuhn, G., Ellsworth, D., & Nie, D. (1997). Turbulent eddy motion at the forest-atmosphere interface. *Journal of Geophysical Research*, *102*(D12), 13,409–13,421. https://doi.org/10.1029/97JD00777

Katul, G., Hsieh, C.-I., & Sigmon, J. (1997). Energy-inertial scale interactions for velocity and temperature in the unstable atmospheric surface layer. *Boundary-Layer Meteorology*, *82*(1), 49–80. https://doi.org/10.1023/A:1000178707511

Katul, G. G., Konings, A. G., & Porporato, A. (2011). Mean velocity profile in a sheared and thermally stratified atmospheric boundary layer. *Physical Review Letters*, *107*(26), 268,502. https://doi.org/10.1103/PhysRevLett.107.268502

Katul, G. G., Porporato, A., Manes, C., & Meneveau, C. (2013). Co-spectrum and mean velocity in turbulent boundary layers. *Physics of Fluids*, *25*(9), 091702. https://doi.org/10.1063/1.4821997

Katul, G. G., Porporato, A., & Nikora, V. (2012). Existence of k^{-1} power-law scaling in the equilibrium regions of wall-bounded turbulence explained by Heisenberg's eddy viscosity. *Physical Review E*, *86*(6), 066311. https://doi.org/10.1103/PhysRevE.86.066311

Katul, G. G., Porporato, A., Shah, S., & Bou-Zeid, E. (2014). Two phenomenological constants explain similarity laws in stably stratified turbulence. *Physical Review E*, *89*(2), 023007. https://doi.org/10.1103/PhysRevE.89.023007

Kolmogorov, A. N. (1941). The local structure of turbulence in incompressible viscous fluid for very large Reynolds numbers. *Cr Acad. Sci. URSS*, *30*, 301–305.

Lane, T. P., & Sharman, R. D. (2014). Intensity of thunderstorm-generated turbulence revealed by large-eddy simulation. *Geophysical Research Letters*, *41*, 2221–2227. https://doi.org/10.1002/2014GL059299

Launder, B. E., Reece, G. J., & Rodi, W. (1975). Progress in the development of a Reynolds-stress turbulence closure. *Journal of Fluid Mechanics*, *68*(3), 537–566.

Leith, C. E. (1967). Diffusion approximation to inertial energy transfer in isotropic turbulence. *The Physics of Fluids*, *10*(7), 1409–1416. https://doi.org/10.1063/1.1762300

Li, D., Katul, G. G., & Bou-Zeid, E. (2015). Turbulent energy spectra and cospectra of momentum and heat fluxes in the stable atmospheric surface layer. *Boundary-Layer Meteorology*, *157*(1), 1–21. https://doi.org/10.1007/s10546-015-0048-2

Li, D., Katul, G. G., & Zilitinkevich, S. S. (2015). Revisiting the turbulent Prandtl number in an idealized atmospheric surface layer. *Journal of the Atmospheric Sciences*, *72*(6), 2394–2410. https://doi.org/10.1175/JAS-D-14-0335.1

Lovejoy, S., Tuck, A. F., Hovde, S. J., & Schertzer, D. (2007). Is isotropic turbulence relevant in the atmosphere? *Geophysical Research Letters*, *34*, L15802. https://doi.org/10.1029/2007GL029359

Lumley, J. L., & Khajeh-Nouri, B. (1975). Computational modeling of turbulent transport. *Advances in Geophysics*(Vol. 18, pp. 169–192): Elsevier. https://doi.org/10.1016/S0065-2687(08)60460-4

Lumley, J. L., & Newman, G. R. (1977). The return to isotropy of homogeneous turbulence. *Journal of Fluid Mechanics*, *82*(1), 161–178. https://doi.org/10.1017/S0022112077000585

Marusic, I., McKeon, B. J., Monkewitz, P. A., Nagib, H. M., Smits, A. J., & Sreenivasan, K. R. (2010). Wall-bounded turbulent flows at high Reynolds numbers: Recent advances and key issues. *Physics of Fluids*, *22*(6), 065103. https://doi.org/10.1063/1.3453711

McColl, K. A., Katul, G. G., Gentine, P., & Entekhabi, D. (2016). Mean-velocity profile of smooth channel flow explained by a cospectral budget model with wall-blockage. *Physics of Fluids*, *28*(3), 035107. https://doi.org/10.1063/1.4943599

Mellor, G. L., & Yamada, T. (1982). Development of a turbulence closure model for geophysical fluid problems. *Reviews of Geophysics*, *20*(4), 851–875.

Monin, A., & Obukhov, A. (1954). Basic laws of turbulent mixing in the surface layer of the atmosphere. *Geophysical Center of the Russian Academy of Sciences*, *151*(163), e187.

Morrison, J. F., Jiang, W., McKeon, B. J., & Smits, A. J. (2002). Reynolds number dependence of streamwise velocity spectra in turbulent pipe flow. *Physical Review Letters*, *88*(21), 214501. https://doi.org/10.1103/PhysRevLett.88.214501

Nickels, T. B., Marusic, I., Hafez, S., & Chong, M. S. (2005). Evidence of the k_1^{-1} law in a high-Reynolds-number turbulent boundary layer. *Physical Review Letters*, *95*(7), 074501.

Nikora, V. (1999). Origin of the "−1" spectral law in wall-bounded turbulence. *Physical Review Letters*, *83*(4), 734. https://doi.org/10.1103/PhysRevLett.83.734

Obukhov, A. M. (1941). On the spectral distribution of energy in turbulent flow. *Izv. Acad. Sci. U.S.S.R., Geogr. a,d Geophys. Ser.*, *4*(5).

Panchev, S. (1971). *Random functions and turbulence* (Vol. 32). Elsevier.

Poggi, D., Katul, G. G., & Albertson, J. D. (2004). Momentum transfer and turbulent kinetic energy budgets within a dense model canopy. *Boundary-Layer Meteorology*, *111*(3), 589–614. https://doi.org/10.1023/B:BOUN.0000016502.52590.af

Pope, S. B. (2000). *Turbulent flows*: Cambridge University Press. https://doi.org/10.1017/CBO9780511840531

Raupach, M. R. (1981). Conditional statistics of Reynolds stress in rough-wall and smooth-wall turbulent boundary layers. *Journal of Fluid Mechanics*, *108*, 363–382. https://doi.org/10.1017/S0022112081002164

Rotta, J. C. (1951). Statistische theorie nichthomogener turbulenz. *Zeitschrift für Physik*, *129*(6), 547–572.

Saddoughi, S. G., & Veeravalli, S. V. (1994). Local isotropy in turbulent boundary layers at high Reynolds number. *Journal of Fluid Mechanics*, *268*, 333–372. https://doi.org/10.1017/S0022112094001370

Salesky, S. T., Katul, G. G., & Chamecki, M. (2013). Buoyancy effects on the integral lengthscales and mean velocity profile in atmospheric surface layer flows. *Physics of Fluids*, *25*(10), 105101. https://doi.org/10.1063/1.4823747

Schumann, U. (1994). On relations between constants in homogeneous turbulence models and Heisenberg's spectral model. *Beiträge zur Physik der Atmosphäre*, *2*, 141–147.

Sorbjan, Z. (1989). *Structure of the atmospheric boundary layer*. Englewood Cliffs, NJ: Prentice Hall.

Tchen, C. M. (1953). On the spectrum of energy in turbulent shear flow. https://doi.org/10.6028/jres.050.009

Tchen, C. M. (1954). Transport processes as foundations of the Heisenberg and Obukhoff theories of turbulence. *Physical Review*, *93*(4). https://doi.org/10.1103/PhysRev.93.4

Wyngaard, J. C., & Coté, O. R. (1971). The budgets of turbulent kinetic energy and temperature variance in the atmospheric surface layer. *Journal of the Atmospheric Sciences*, *28*(2), 190–201. https://doi.org/10.1175/1520-0469(1971)028<0190:TBOTKE>2.0.CO;2

Zeman, O., & Tennekes, H. (1975). A self-contained model for the pressure terms in the turbulent stress equations of the neutral atmospheric boundary layer. *Journal of the Atmospheric Sciences*, *32*(9), 1808–1813. https://doi.org/10.1175/1520-0469(1975)032<1808:ASCMFT>2.0.CO;2

2.3 Article: "Scaling laws for the Length Scale of Energy-containing Eddies in a Sheared and Thermally Stratified Atmospheric Surface Layer"

Manuscript submitted to *Geophysical Research Letters* on 01/08/2020.

Scaling Laws for the Length Scale of Energy-Containing Eddies in a Sheared and Thermally Stratified Atmospheric Surface Layer

A. Ayet[1,2] **and G. G. Katul**[3]

[1]Ifremer, CNRS, IRD, Univ. Brest/ Laboratoire d'Océanographie Physique et Spatiale (LOPS), IUEM, Brest, France
[2]LMD/IPSL, CNRS, École Normale Supérieure, PSL Research University, Paris, France
[3]Nicholas School of the Environment, Box 90328, Duke University, Durham, NC 27708-0328, USA

Key Points:

- Numerical Weather Prediction models use a master turbulence length scale linked to the characteristic wavelength of energy-containing eddies
- A relation predicting variations of this wavelength with atmospheric stability is derived
- Predictions agree with experiments and offer a new perspective on return-to-isotropy approaches

Corresponding author: Alex Ayet, `alex.ayet@normalesup.org`

Abstract
In the atmospheric surface layer (ASL), a characteristic wavelength marking the limit between energy-containing and inertial subrange scales can be defined from the vertical velocity spectrum. This wavelength is related to the integral length scale of turbulence, used in turbulence closure approaches for the ASL. The scaling laws describing the displacement of this wavelength with changes in atmospheric stability have eluded theoretical treatment and are considered here. Two derivations are proposed for mildly unstable to mildly stable ASL flows - one that only makes use of normalizing constraints on the vertical velocity variance along with idealized spectral shapes featuring production to inertial subrange regimes, while another utilizes a co-spectral budget with a return-to-isotropy closure. The expressions agree with field experiments and permit inference of the variations of the wavelength with atmospheric stability. This methodology offers a new perspective for numerical and theoretical modelling of ASL flows and for experimental design.

Plain Language Summary

Turbulent flows in the atmosphere are composed of a large number of eddies whose sizes vary from kilometers to fractions of millimeters. The energy content in the vertical direction associated with each eddy size dictates the overall ability of turbulent motion to mix and transport particles (such as seeds, pollen, or spores), gases (such as carbon dioxide, ozone, methane, isoprene, etc...), energy (such as latent and sensible heat) and momentum from or to the underlying surface. Despite this multiplicity of eddy sizes, numerous experiments and simulation studies have shown that an effective or dominant eddy size may be sufficient to represent the overall mixing and transport properties of turbulent flows. This finding is a corner-stone to representing the effects of turbulence on transport in Numerical Weather Prediction models. The work here explores how surface heating or cooling (i.e. near-surface atmospheric stability) regulates this dominant or effective eddy size. The derivation makes use of well-established constraints on the overall turbulent kinetic energy in the vertical direction, and highlights the parameters dictating this regulation.

1 Introduction

Close to the ground, in the so-called Atmospheric Surface Layer (ASL), shear and buoyancy forces impact many flow statistics including the distribution of turbulent kinetic energy among eddy sizes (Kaimal & Finnigan, 1994). This is apparent in the spectrum of the vertical velocity $E_{ww}(k)$ (k is the streamwise wavenumber related to an inverse eddy size) which exhibits a two-regime behaviour, valid for a mildly stable to unstable atmosphere (Kaimal & Finnigan, 1994; Wyngaard, 2010, pages 42 and 216 respectively, and references therein). This behaviour is exemplified in Figure 1a for flows above several surfaces and a near-neutral stratification. At large k (small scales), $E_{ww}(k)$ follows an approximate $k^{-5/3}$ law predicted by Kolmogorov's theory (Kolmogorov, 1941) for locally homogeneous and isotropic turbulence (the inertial subrange). For low k (in the so-called production subrange), $E_{ww}(k)$ follows an approximate k^0 law, presumed to occur because the surface leads to 'splashing' (redistribution) of energy across scales (see, e.g., Hoxey & Richards, 1992; Hunt & Carlotti, 2001; Ayet, Katul, et al., 2020).

A key variable in the description of this two-regime behavior, and hence of the near-surface $E_{ww}(k)$, is the wavenumber k_p of the transition between production and inertial subranges. In fact, k_p^{-1} is proportional to the characteristic scale of energy-containing eddies close to the surface, and to the integral length scale of turbulence (Townsend, 1980; Katul et al., 2007). As such, its value is needed in closure schemes such as the Mellor-Yamada scheme (Mellor & Yamada, 1982) used in numerical weather prediction models and for Large Eddy Simulations. In both cases, an integral length scale (also called

master length scale) is required (e.g. Mellor & Yamada, 1982; Redelsperger et al., 2001; Rodier et al., 2017). Furthermore, knowledge of the physics upon which k_p depends provides insights into the energy redistribution mechanisms in the ASL. Indeed k_p separates (small scale) isotropic and (large scale) anisotropic motions, and the difference between those motions is grounded, among others, in how energy is redistributed among the different turbulent components. In the above-mentioned numerical models, these mechanisms are modelled through return to isotropy closure schemes (Launder et al., 1975; Lumley & Newman, 1977; Abid & Speziale, 1993; Mellor & Yamada, 1982; Cuxart et al., 2000; Canuto et al., 2001; Drobinski et al., 2007), whose validity has been recently questioned for a sheared and stratified ASL (Ayet, Katul, et al., 2020).

Finally, knowledge of the transition wavenumber is also essential for other geophysical applications involving $E_{ww}(k)$. Two examples are singled out: the first is the determination of the effectiveness of the vertical dispersion of scalars, or Lagrangian stochastic modelling of turbulence, which both rely on the vertical velocity variance $\sigma_w^2 = \int_0^\infty E_{ww}(k)dk$ (e.g. Taylor, 1922) along with a characteristic length or time scale. The second example are co-spectral budgets and related phenomenological models describing turbulent momentum transport in the ASL (Gioia et al., 2010; Katul et al., 2011, 2014). In those models, the vertical velocity spectrum is prescribed under an idealized form, and the value of the transition wavenumber is key to recover the flow statistics over a flat wall (Katul et al., 2011, 2013, 2014), a rough channel (Bonetti et al., 2017) or ocean surface waves (Ayet, Chapron, et al., 2020).

For the neutral conditions of Figure 1, the transition wavenumber k_p is expected to scale as $1/z$, where z is the distance from the surface, due to energy-containing eddies being attached to the latter (Townsend, 1980). This is exemplified in Figure 1b, in which k_p can be determined as the wavenumber of the peak of the so-called "premultiplied spectrum" $kE(k)$. The decade of values spanned by the neutral k_p (grey shadings in Figure 1b) shows that there remains uncertainties about the exact value of the proportionality coefficient. The exact value depends, among others, on the geometrical properties of the surface.

In this contribution, this uncertainty is not the main focus. What is sought are variations of the transition wavenumber with shear and buoyancy forces, whose ratio is related to the atmospheric stability parameter. Indeed, starting from the historical Kansas and Minnesota experiments, measurements have revealed robust variations of k_p with atmospheric stability (see e.g. Figure 4 of Kaimal et al., 1972). Those *relative* variations of k_p with respect to its neutral value are key for the applications cited above, since they determine how the various ASL turbulent processes are influenced by the presence of buoyancy (e.g. the energy redistribution mechanisms, see Bou-Zeid et al., 2018; Ayet, Katul, et al., 2020). This is also a first step towards understanding the variations of those processes due to other external parameters, e.g. fixed roughness elements (Bonetti et al., 2017) or ocean surface waves (Ayet, Chapron, et al., 2020). In addition to the aforementioned applications, the relative variations of k_p with stability have been recently used to explain the shape of the stability correction functions to the log-law mean velocity profile in stratified atmospheric flows (Katul et al., 2011) with caveats partly associated with the assumed variations of k_p with stability (Li et al., 2016; Salesky et al., 2013). Undoubtedly, there is a need for expressions that predict the displacement of k_p with changes in atmospheric stability. To date, no theoretical expression explaining this displacement exists, and this knowledge gap frames the scope of this work.

Two links between the spectral and bulk properties of turbulence are used to provide a constraint on k_p and its variation with the dimensionless stability parameter for mildly stable and unstable conditions (those exclude free convective and very stable conditions where turbulence may be patchy). The expressions derived provide means of estimating the transition wavenumber from bulk quantities of the flow in the ASL. These are then tested with published data sets collected in the ASL (including the weighty Kansas

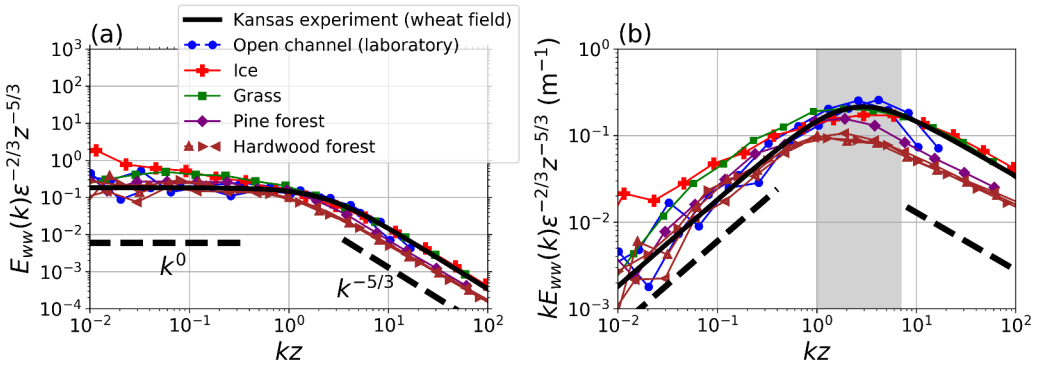

Figure 1. Illustrative figure showing the existence of a transition wavenumber in the *near-neutral ASL*. (a) Normalized vertical velocity spectra and (b) its premultiplied version (i.e. multiplied by k) as a function of the normalized wavenumber. In the normalization factor $\epsilon^{2/3}z^{5/3}$, ϵ is the TKE dissipation rate and z is the measurement height. In (a) dashed lines show the existence of two regimes, separated by a transition wavenumber k_p, apparent in (b) where it spans one decade around $1/z$ (grey shadings) for the data shown here. The experiments and data sources span forests, grassland, ice sheets, and canonical smooth-walls. The post-processing and data sources are described elsewhere (Kaimal et al., 1972; Katul, Hsieh, & Sigmon, 1997; Katul, Hsieh, Kuhn, et al., 1997; Katul & Chu, 1998; Katul et al., 2012, 2016) and are not repeated here. Only the Kansas data are used in the rest of the analysis since the other data here are available for near-neutral conditions only, and are only used to illustrate near-neutral conditions above various types of surfaces.

and Minnesota experiments). The expressions also explicitly account for the filtering properties of the instruments, should they be needed.

2 Theory

2.1 Definitions and Nomenclature

A turbulent flow within the ASL is considered with u', v', w', and T' defining the three instantaneous turbulent velocity components in the streamwise (x), cross-stream (y) and vertical (z) directions and the turbulent air temperature fluctuations. These fluctuations have zero-mean so that $\overline{u'} = \overline{v'} = \overline{w'} = \overline{T'} = 0$, where overline indicates time (or ensemble) averaging. Stability dependence of bulk flow statistics and spectral properties of the ASL are routinely expressed in the context of Monin-Obukhov Similarity Theory (MOST, Monin & Obukhov, 1954; Foken, 2006). This similarity theory considers a stationary and planar homogeneous flow without subsidence and turbulent flux transport so that the turbulent kinetic energy (TKE) budget is given by

$$\epsilon = u_*^2 \frac{dU}{dz} + \frac{g}{T_a}\overline{w'T'}, \tag{1}$$

where ϵ is, again, the mean TKE dissipation rate, $-u_*^2 = \overline{u'w'}$ is the turbulent momentum flux (u_* is the friction velocity), $\overline{w'T'}$ is the turbulent sensible heat flux, U is the mean velocity, T_a is the mean air temperature, and g is the gravitational acceleration. Equation (1) can also be re-arranged to introduce MOST dimensionless quantities:

$$\epsilon = \frac{u_*^3}{\kappa z}\left[\phi_m(\zeta) - \zeta\right], \tag{2}$$

where $\zeta = z/L$ is the stability parameter, $L = -u_*^3(\kappa g\overline{w'T'}/T_a)^{-1}$ is the Obukhov length, $\kappa = 0.4$ is the von Kármán constant, and $\phi_m(\zeta)$ is the so-called stability correction function for the mean velocity profile, defined below. The ASL is labelled as moderately unstable when $-2 < \zeta < -0.1$, near neutral when $|\zeta| \leq 0.1$, and stable when $0.1 < \zeta < 1$. Conditions where the ASL is in forced ($-5 < \zeta < 2$) to free ($\zeta > -5$) convection (Kader & Yaglom, 1990) or very stable conditions ($\zeta \geq 1$, where the flux Richardson number reaches a maximum, see Grachev et al., 2013; Katul et al., 2014; Li et al., 2016) are outside the scope of the present work.

Within MOST, $\phi_m(\zeta)$ and the dimensionless vertical velocity variances are

$$\phi_m(\zeta) = \frac{\kappa z}{u_*}\frac{dU}{dz}, \quad \phi_w(\zeta) = \frac{\sigma_w^2}{u_*^2}, \tag{3a, b}$$

where $\sigma_w^2 = \overline{w'^2}$. In the following, the analysis is restricted to $-2 < \zeta < 1$. The balance in Equation (1), as well as the validity of the scaling used for MOST stability correction functions (ϕ_m and ϕ_w) are expected to hold for the range of ζ corresponding to mildly stable to unstable conditions, as demonstrated by a number of ASL experiments (Charuchittipan & Wilson, 2009; Hsieh & Katul, 1997; Salesky et al., 2013).

2.2 A Spectral Link Approach

In this Letter, the normalization condition for the one-dimensional spectrum of vertical velocity $E_{ww}(k)$ is exploited to arrive at expressions for $k_p z$. The measured σ_w^2 is linked to $E_{ww}(k)$ using

$$\sigma_w^2 = \int_{2\pi a_i/z_i}^{2\pi a_s/d_s} E_{ww}(k)dk, \tag{4}$$

where σ_w^2 is routinely measured using sonic or acoustic Doppler anemometers. Because scales in the flow are finite in any experiment, the spectrum is integrated between two wavelengths (grey shading in Figure 2a): (i) a fraction a_i of the wavelength of the largest energetic scale $2\pi/z_i$, where z_i is the height of the boundary layer: (ii) a fraction of a_s of the wavelength sampled by the measuring device $2\pi/d_s$. In the case of sonic anemometery common to ASL field experiments, d_s is the path length between transducers (of the order of 0.1 m for many commercial anemometers). For a given measurement height z, it is assumed that $d_s < z < z_i$. The proportionality constant a_i accounts for the fact that, due to a finite sampling period, not all the large scales of the flow might be sampled. In contrast, the proportionality constant a_s reflects the effect of instrument averaging on the measured small-scale spectrum of turbulence (Moore, 1986). The quantities $2\pi a_i/z_i$ and $2\pi a_s/d_s$ are hence the *effective* wavelengths in between which the spectrum is effectively sampled.

To extract information about k_p, an idealized spectral shape for $E_{ww}(k)$ is considered and is given under its normalized form by

$$\frac{E_{ww}(k)}{\epsilon^{2/3}z^{5/3}} = \begin{cases} C_{ww}(zk_p)^{-5/3}k^0, & k \leq k_p \\ C_{ww}(zk)^{-5/3} & k > k_p \end{cases}, \tag{5}$$

where $C_{ww} = 0.65$ is the Kolmogorov constant for the vertical velocity energy spectrum (Saddoughi & Veeravalli, 1994). This spectrum consists of the two regimes mentioned in the Introduction (dashed lines in Figure 1a, and solid line in Figure 2a): (i) the inertial subrange for $k > k_p$ (Kolmogorov, 1941); (ii) the production range for $k \leq k_p$, whose spectral constant is determined by requiring continuity (but not smoothness) with regime (i). Under neutral conditions, the transition wavenumber is inversely proportional to the measurement height so that $k_p z = C_1$ (Townsend, 1980). As mentioned in the introduction, the focus of the Letter is on the displacement of k_p with ζ from its neutral value, labelled $k_p(0)$ (for $\zeta = 0$).

The idealized spectral shapes defined in Equation (5) agree with numerous measurements published in the literature (Kader & Yaglom, 1991; Kaimal & Finnigan, 1994; Katul et al., 2012) and only few examples are shown in Figure 1 to illustrate their existence and general features for different surface covers. The measurements reported here are for different types of ASL experiments: flow over an ice sheet (Katul et al., 2016), grass (Katul, Hsieh, & Sigmon, 1997), a pine forest (canopy height 14 m) and a hardwood forest (canopy height 28 m) (Katul, Hsieh, Kuhn, et al., 1997). For reference, results for an open channel flow above a smooth stainless steel surface at two differing bulk Reynolds numbers are also featured (Katul & Chu, 1998). The spectra in the ASL presented here have been selected for near-neutral conditions and for runs where stationary conditions prevailed over extended periods of time (>3600 s). For $-2 < \zeta < 1$, the idealized spectral shapes for vertical velocity spectra roughly hold but with a displaced k_p (e.g. Figure 4 of Kaimal et al., 1972). Note that this is not the case for highly unstable or very stable stability conditions (not considered here), as shown by several long-term experiments (Kader & Yaglom, 1991; Grachev et al., 2013). With respect to more sophisticated models of the spectra (see e.g. Tchen, 1953; Panchev, 1971), the idealized spectral shapes of Equation (5) retain the essential feature needed in the present work: the existence of two regimes separated by the transition wavenumber k_p.

To obtain an expression for zk_p, Equation (5) is inserted into Equation (4), yielding

$$\Sigma_* = (zk_p)^{-2/3}\left\{\left[1 - \frac{2\pi a_i z}{z_i}(zk_p)^{-1}\right] + \frac{3}{2}\left[1 - \left(\frac{d_s}{2\pi a_s z}\right)^{2/3}(zk_p)^{2/3}\right]\right\}, \tag{6}$$

where z has been introduced to normalize length scales (as in Equation (5)), and $\Sigma_* = \sigma_w^2(C_{ww}z^{2/3}\epsilon^{2/3})^{-1}$ is a dimensionless vertical velocity variance that depends on the bulk characteristics of the turbulent flow, and hence only on atmospheric stability (discussed in section 2.4). Equation (6) has two terms balancing Σ_* on the right-hand side (RHS): (i) contributions from the production subrange (first term) and from the inertial subrange (second term). Solving this expression for externally supplied z_i, d_s, and Σ_* as well as estimates of a_i and a_s determines zk_p.

2.3 A Co-spectral Budget Approach

An alternative model for determining $k_p z$ is now proposed based on a different set of assumptions. It relies on the normalization condition of the co-spectrum of vertical and horizontal velocity fluctuations $F_{uw}(k)$

$$-\overline{u'w'} = \int_{2\pi a_i/z_i}^{2\pi a_s/d_s} F_{uw}(k)dk. \tag{7}$$

Using the same idealized flow conditions than those of Equation (1), $F_{uw}(k)$ follows a co-spectral budget given as (Panchev, 1971; Bos et al., 2004; Katul et al., 2013)

$$\frac{\partial F_{uw}(k)}{\partial t} = 0 = \frac{dU}{dz}E_{ww}(k) - \frac{C_R}{\tau(k)}F_{uw}(k) - C_l\frac{dU}{dz}E_{ww}(k). \tag{8}$$

This budget is a balance between mechanical production (first term on the RHS) and energy redistribution through pressure-strain correlations (second and third terms on the RHS). The pressure-strain correlations are modeled with a standard spectral Rotta scheme. Its first component is a linear return-to-isotropy term with a Rotta constant $C_R \sim 1.8$ (slow part), and a characteristic timescale $\tau(k) = \epsilon^{-1/3}k^{-2/3}$ for $k \geq k_p$ and $\tau(k) = \epsilon^{-1/3}k_p^{-2/3}$ for $k < k_p$ (Katul et al., 2013). The second component is a non-linear correction (Zeman & Tennekes, 1975) with characteristic constant $C_l = 3/5$ (called isotropization of the production). Note that the constant C_R used in the Rotta scheme is the same than for return-to-isotropy models used for the vertical velocity variance budget (see, e.g. Ayet, Katul, et al., 2020).

This budget has been successfully used (Katul et al., 2013) to model the observed co-spectrum in a neutral ASL. In this budget, the buoyancy source/sink term is neglected. This assumption follows from ASL measurements (the Kansas measurements, see Wyngaard et al., 1971; Wyngaard, 2010, page 233), scaling analysis in the inertial subrange, as well as direct numerical simulations (Katul et al., 2014).

From Equation (8), the co-spectrum $F_{uw}(k)$ can be expressed as a function of the spectrum E_{ww}, and hence the normalization condition (Equation (7)) reads

$$K = \frac{(1-C_l)}{C_R}\int_{2\pi a_i/z_i}^{2\pi a_s/d_s} \tau(k) E_{ww}(k) dk, \tag{9}$$

where $K = -\overline{u'w'}/(dU/dz)$ is the bulk turbulent viscosity. Using the idealized spectrum for $E_{ww}(k)$ presented in Equation (5), the previous expression becomes

$$K_* = (zk_p)^{-4/3}\left\{\left[1 - \frac{2\pi a_i z}{z_i}(zk_p)^{-1}\right] + \frac{3}{4}\left[1 - \left(\frac{d_s}{2\pi a_s z}\right)^{4/3}(zk_p)^{4/3}\right]\right\}, \tag{10}$$

with $K_* = K\left(C_{ww}\epsilon^{1/3}z^{4/3}(1-C_l)/C_R\right)^{-1}$ a dimensionless turbulent viscosity that varies with atmospheric stability. This equation links zk_p to the bulk properties of the flow. It is comparable but not identical to Equation (6), relying on a spectral budget (Equation (8)).

2.4 Dimensionless variance and stability dependence

The dimensionless transition wavenumber zk_p has been linked to bulk properties of the flow: the dimensionless variance $\Sigma_* = \sigma_w^2(C_{ww}z^{2/3}\epsilon^{2/3})^{-1}$ and turbulent viscosity $K_* = K\left(C_{ww}\epsilon^{1/3}z^{4/3}(1-C_l)/C_R\right)^{-1}$. Those two bulk quantities are now expressed as a function of the stability parameter ζ using conventional MOST dimensionless functions (Equation (3)) and estimates of TKE dissipation rate from Equation (2).

The dimensionless variance Σ_* is given as

$$\Sigma_*(\zeta) = \frac{\kappa^{2/3}\phi_w(\zeta)}{C_{ww}(\phi_m - \zeta)^{2/3}}. \tag{11}$$

Accepted MOST dimensionless functions from the Kansas experiment (Kaimal & Finnigan, 1994; Sorbjan, 1989, see Supporting Information) are used to evaluate Σ_*. As shown in Figure 2b (solid line), the resulting Σ_* increase (resp. decrease) for unstable (resp. stable) conditions. The neutral value of Σ_* is 1.3, following the fact that $\phi_w(0) \sim 1.56$.

Similarly, the dimensionless turbulent viscosity can be expressed as a function of ζ and is given by

$$K_* = \frac{\kappa^{4/3}C_K}{C_{ww}\phi_m(\phi_m - \zeta)^{1/3}}, \tag{12}$$

where $C_K = C_R/(1-C_l)$. Its behavior (dashed line) is similar to Σ_*, even though its neutral value is of about 2.

3 Discussion

Equation (6) provides values of zk_p given the stability parameter ζ (that sets Σ_* through Equation (11)), and the two cutoff lengths d_s/a_s and z_i/a_i. In the following, it is assumed that the measurement height is small relative to the boundary layer height (i.e. $z/z_i \ll 1$) which, from Equation (6), yields the following expression of zk_p

$$zk_p(\zeta) = \left(\frac{5}{2}\right)^{3/2}\left[\Sigma_*(\zeta) + \frac{3}{2}\left(\frac{d_s}{2\pi a_s z}\right)^{2/3}\right]^{-3/2}. \tag{13}$$

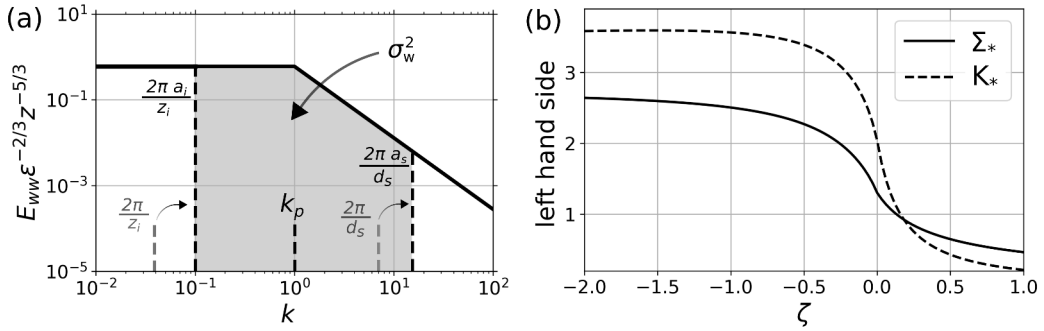

Figure 2. (a) Idealized $E_{ww}(k)$ spectrum (solid line), and key wavenumbers used in the derivation (dashed lines), for $z = 1$ m and $k_p = 1/z$. In the spectral link (Equations (4) and (9)), the spectrum is integrated between two finite bounds and the integration area, corresponding to the measured σ_w^2, is shown as a grey shading. (b) Left hand side of Equation (6) (dimensionless variance Σ_*, solid line) and Equation (10) (dimensionless turbulent viscosity K_*, dashed line) as a function of stability.

While this approximation is valid in the ASL for a measurement height close to the surface, it can fail for measurements higher up in the atmospheric boundary layer, or for very stable conditions (not considered here).

In this simplified model, the only remaining parameter that requires specification is $d_s/(a_s z)$. This parameter depends on the measuring properties of the instrument: the smallest wavelength sampled by the measuring device ($2\pi/d_s$) and its averaging and spectral filtering properties (a_s). An estimate of $d_s/(a_s z)$ may be obtained for neutral conditions by specifying a value of $zk_p(0)$ in Equation (13). As discussed in the introduction and in Figure 1b, there is uncertainty in the value of zk_p for neutral conditions, which we use here to provide a range of values for $d_s/(a_s z)$.

Two limiting cases are considered: $k_p(0)z = 1$, as assumed in prior models (Katul et al., 2011), and a larger value $k_p(0)z = 1/\kappa \sim 1/0.4$ close to the estimates from the Kansas measurements (Kaimal et al., 1972, see the Supporting Information). Using Equation (13), and the fact that $\Sigma_*(0) = 1.3$ (see Figure 2b) yields $d_s/(2\pi a_s z) = 0.71$ and $d_s/(2\pi a_s z) = 0.017$ for the first and second cases respectively. Note that, assuming a typical measurement height $z = 5$m and an anemometer path length $d_s = 0.1$m, implies $a_s = 0.003$ and $a_s = 0.19$ respectively. In the first case (i.e. for $k_p(0)z = 1$), this corresponds to an effective cutoff wavenumber $2\pi a_s/d_s$ (i.e. including the spatial filtering properties of the instrument) three orders of magnitude larger than original instrument cutoff $2\pi/d_s$. This is a significant modulation, which questions the physical relevance of assuming $k_p(0)z = 1$ when using MOST dimensionless functions from the Kansas experiments to constrain Σ_*.

The modeled k_p *deviations* from the neutral value are now compared to reported measurements and estimates of k_p from several published ASL experiments. The estimates of this deviation, $k_p(\zeta)/k_p(0)$, are shown in Figure 3a and summarized in the Supporting Information. First, the widely-used estimate of k_p from the Kansas experiment (Kaimal et al., 1972, measurements form 5 to 22 m on top of wheat stubble) is shown as a black line. This estimate results from a direct determination of k_p as the wavenumber of the peak of the premultiplied vertical velocity spectra (as in Figure 1b). Second, the Advection Horizontal Array Turbulence Study (AHATS, z from 1 to 7 m on top of grass) provided an estimate of the streamwise integral lengthscale of the vertical veloc-

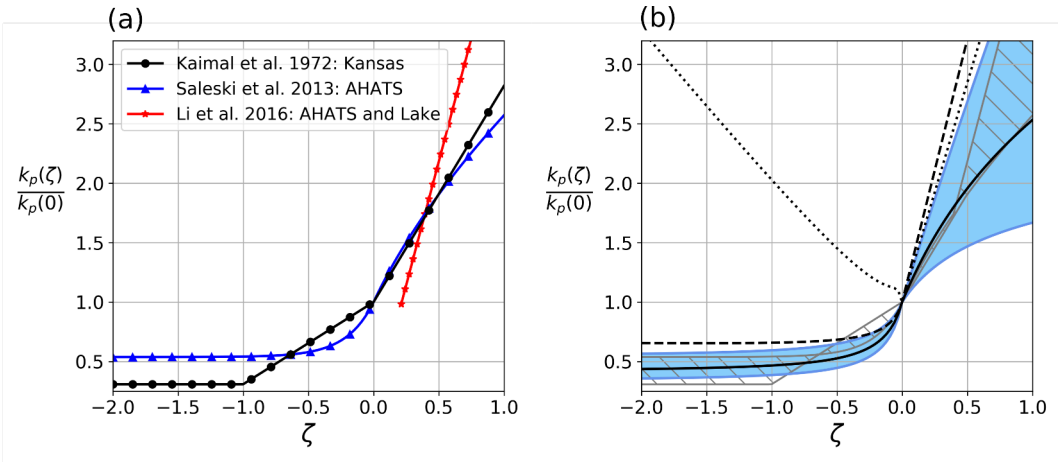

Figure 3. Relative transition wavenumber versus stability. (a) Experiments: spectral measurements from the Kansas experiment, two different estimates of the integral length scale from Salesky et al. (2013), and estimates of the Ozmidov length scale from Li et al. (2016). (b) Model predictions: matching between vertical variance and spectra (equation (13)) for $k_p(0) = 1.6/z$ (solid black line) and for a range of values from $k_p(0) = 1/(\kappa z) = 2.5/z$ (upper blue line) to $k_p(0) = 1/z$ (lower blue line); matching between turbulent viscosity and co-spectra (equation (14)) with a fixed return-to-isotropy set of constants (dashed line) and with a stability-dependent Rotta constant from Ayet, Katul, et al. (2020) (dotted line); envelope covering the data estimates of panel (a) (grey dashed area).

ity, which is inversely proportional to k_p (Salesky et al., 2013, blue lines). Finally, for moderately stable conditions ($0.3 < \zeta < 1$), Li et al. (2016) argued that the Ozmidov length scale should be the dominant scale for the turbulence spectra. The authors showed that replacing other estimates of k_p by the Ozmidov length scale in phenomenological models allowed explaining some of their caveats for mildly stable conditions. Being an additional estimate of the wavenumber of energy-containing eddies k_p, we show the Ozmidov length scale proposed by the authors on the basis of the AHATS data and of additional data above a lake in red.

The modelled variation of zk_p from Equation (13) is shown in Figure 3b for the two limit values of $d_s/(a_s z)$ mentioned above (blue lines and shading). The trends are consistent with the expected increase (resp. decrease) of zk_p for stable (resp. unstable) conditions, which reflects the change, due to buoyancy, in the shape of the dominant eddies driving the vertical momentum flux (e.g. Katul et al., 2011). Variations of $d_s/(a_s z)$ allow testing the sensitivity of zk_p to changes in the large wavenumber cutoff, and hence to changes in the neutral value $zk_p(0)$ (as seen in Figure 1b). As expected, the sensitivity is higher for stable than for unstable conditions. This results from σ_w^2 being lower for stable than for unstable conditions (and hence also Σ_*, see Figure 2). A change of $d_s/(a_s z)$ in Equation (13) is thus larger relative to Σ_* for stable than for unstable conditions, causing a higher relative change in zk_p. In stable conditions, where the bulk variance is lower, the transition wavenumber is difficult to estimate, being sensitive to such measurement issues (as expected). Note that z/z_i was also varied over a reasonable range for the ASL ($z/z_i \leq 0.3$, not shown). The resulting variations of zk_p (from Equation (6)) were found significantly smaller than the variations induced by a change of $d_s/(a_s z)$.

Overall, the range of values obtained by varying $zk_p(0)$ (blue shadings) is larger than the range of values spanned by the data for stable conditions and similar to it for

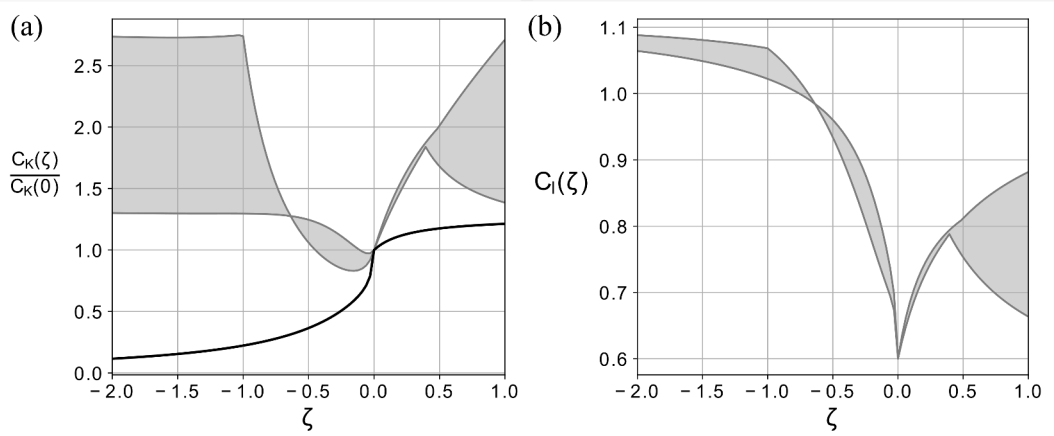

Figure 4. Return-to-isotropy constants versus stability. (a) Relative variation of $C_K = C_R/(1 - C_l)$ (i) required to match the data from Figure 3 (grey shadings) and (ii) by keeping C_l fixed and a stability-dependent C_R from Ayet, Katul, et al. (2020) (solid line); (b) Grey shadings show the absolute variations of C_l required to match the data from Figure 3 if C_R is assumed to follow the stability-dependent variations presented in (a), solid line.

unstable conditions (grey hatches). For stable conditions, choosing $zk_p(0) \sim 1$ results in a poor estimate of the trend of zk_p, with respect to choosing $zk_p(0) \sim 1/\kappa$, closer to the Kansas data. This again hints towards the latter value of $zk_p(0)$ being more physical to describe ASL turbulence above a flat terrain. Nonetheless, the choice $zk_p(0) \sim 1/\kappa = 2.5$ (which is within the bounds of $zk_p(0)$ of Figure 1b, grey shadings) results in a relative deviation of k_p outside the envelope of the data (grey hatches in Figure 3b). Hence, the best match to the measurements was determined, and is shown in black line in Figure 3b. It corresponds to $zk_p(0) = 1.6/z$ (and to $d_s/(2\pi a_s z) = 0.2$). The model falls close (for $-0.8 < \zeta < 0.5$) or within (for $\zeta \leq -0.8$ and $\zeta \geq 0.5$) the envelope of the data. More precisely, comparison between the AHATS estimates (blue line in Figure 3a) and the model (black line in Figure 3b) shows that it is correct up to a multiplicative factor of order one.

The matching between the spectra and the vertical velocity variance offers an acceptable constraint to predict the relative variations of the transition wavenumber with ζ. This is ensured partly from the universality of the Kolmogorov constant C_{ww}. Instead, the matching between the co-spectra and the turbulent viscosity (Equation (10)) relies on two return-to-isotropy "constants", C_R and C_l whose universality for different conditions has been recently questioned. As mentioned earlier, C_R is also the return-to-isotropy constant used in the vertical velocity variance budget. In Ayet, Katul, et al. (2020) we have shown, using such a budget, that the value of the Rotta constant C_R should be revised to include stability-dependent effects. In the following, we extend this analysis to C_l, using the matching between the co-spectra and the turbulent viscosity and comparing it to the data of the transition wavenumber.

The transition wavenumber predicted from the matching between the co-spectra and the turbulent viscosity is obtained by setting $z/z_i \ll 1$ in Equation (10):

$$zk_p(\zeta) = \left(\frac{7}{4}\right)^{3/4} \left[K_*(\zeta) + \frac{3}{4}\left(\frac{d_s}{2\pi a_s z}\right)^{2/3}\right]^{-3/4}, \tag{14}$$

where K_* depends, among others, on the ratio of the return-to-isotropy constant $C_K = C_R/(1 - C_l)$ which, for a neutral atmosphere has a value of 4.5 (with $C_R = 1.8$ and

$C_l = 3/5$). For a neutral atmosphere, we further assume, following Katul et al. (2013), that $d_s/(a_s z) = 0$. This results, using $K_*(0) \sim 2$ (see Figure 2), in $zk_p = (8/7)^{-3/4} = 0.9$, close to the expected unity value put forth in Townsend (1980). Katul et al. (2013) showed that this choice of d_s/a_s was required for the co-spectral model to recover the spectral properties of the ASL for neutral conditions.

As shown in Figure 3b (dashed line), the modeled transition wavenumber trend from Equation (14) is in worse agreement with the data than Equation (13). Since this matching depends on the value of C_K, this comparison suggests that C_K should be adjusted with respect to its neutral value of 4.5 to match zk_p. As a first adjustment, the stability dependence of C_R discussed in Ayet, Katul, et al. (2020) is added while maintaining $C_l = 3/5$ fixed (dotted line in Figure 3b). Even though for stable conditions the agreement with the data is improved, for unstable conditions the predicted behavior of zk_p is not consistent with its expected (and measured) decrease.

In fact, the variations of C_K needed to match the data of Figure 3a are an increase of C_K for mildly unstable and stable conditions (grey shadings in Figure 4a), which is inconsistent with the predicted decrease of C_R from Ayet, Katul, et al. (2020) (solid line in Figure 4a). Assuming that the stability dependence of C_R from Ayet, Katul, et al. (2020) also applies to the co-spectral budget (in Ayet, Katul, et al. (2020), it was derived for the budget of the vertical velocity), the only alternative left is that C_l should be stability-dependent. The values of C_l needed to match the data of Figure 3a are shown as grey shadings in Figure 4b.

This co-spectral analysis shows that the timescales associated with the Rotta and non-linear return-to-isotropy constants can be linked to the characteristic wavelength of the energy-containing spectrum (k_p), which is a physical result *per-se*. They also hint for revising the value of those constants for non-neutral conditions. Since the constant C_R is also used for return-to-isotropy modelling in the vertical variance budget, this analysis also gives insights into the return-to-isotropy terms in such budgets, which are essential for numerical modelling (e.g. Mellor & Yamada, 1982; Canuto et al., 2001), and have been discussed in details in Bou-Zeid et al. (2018) and Ayet, Katul, et al. (2020).

4 Conclusion

An equation linking the bulk and spectral properties of the the vertical turbulent motions in the ASL was derived to predict the displacement of the transition wavenumber in the pre-multiplied vertical velocity spectrum. The derived expression weakly depends on the atmospheric boundary layer height and instrument cutoff scale (d_s/a_s). The expression compared reasonably against multiple ASL measurements in a simplified framework where the effects of a finite boundary layer height were neglected. Besides improving the theoretical understanding of the ASL, this result also opens the path for several applications: (i) it can be used to diagnose the transition wavenumber from datasets measuring the bulk properties of the flow, and hence help designing experiments where only large scale information or estimates about the flow are available; (ii) it can assist in building turbulent closure in numerical simulations by linking the bulk properties of the flow to that of energy-containing eddies (whose size is proportional to k_p, see e.g. Townsend, 1980; Gioia et al., 2010; Katul et al., 2011).

To gain further insight on the physics controlling the transition wavenumber, an alternative link was studied, based on a co-spectral budget of turbulence. This second link involves constants controlling the timescale of return-to-isotropy of the flow. In accordance with the results of Ayet, Katul, et al. (2020), those constants should depend on stability to ensure a matching between the predicted transition wavenumber from the co-spectral framework and the data. A fair critique to the method used here is the choice of $\tau(k)$ (that only varies with ϵ) and the determination of ϵ from an equilibrated TKE

budget. Not withstanding this critique, this second analysis establishes a physical link between the return-to-isotropy timescales and the transition wavenumber, which could lead to important insights on how external parameters (buoyancy, surface geometry, large-scale forcings) can influence near-surface turbulence isotropy. This link will be elaborated upon in the future.

Acknowledgements

The data used for Figure 1 can be found in Kaimal et al. (1972), Katul, Hsieh, and Sigmon (1997), Katul, Hsieh, Kuhn, et al. (1997), Katul and Chu (1998) and Katul et al. (2016). The data used for Figures 2, 3 and 4 is described in the Supporting Information and in Kaimal et al. (1972), Salesky et al. (2013) and Li et al. (2016). The code used to generate the figures is available freely on Github [link will be provided upon acceptance]. AA was supported by DGA grant No D0456JE075, the French Brittany Regional Council, ANR Caravel, and ISblue project, Interdisciplinary graduate school for the blue planet (ANR-17-EURE-0015), co-funded by a grant from the French government under the program "Investissements d'Avenir". GGK was supported by the US National Science Foundation (Grants NSF-AGS-164438, NSF-IOS-175489, and NSF-AGS-2028633).

References

Abid, R., & Speziale, C. (1993). Predicting equilibrium states with Reynolds stress closures in channel flow and homogeneous shear flow. *Physics of Fluids A: Fluid Dynamics*, *5*(7), 1776–1782.

Ayet, A., Chapron, B., Redelsperger, J.-L., Lapeyre, G., & Marié, L. (2020). On the impact of long wind-waves on near-surface turbulence and momentum fluxes. *Boundary-Layer Meteorology*, *174*(3), 465–491. doi: 10.1007/s10546-019-00492-x

Ayet, A., Katul, G., Bragg, A., & Redelsperger, J. (2020). Scalewise return-to-isotropy in stratified boundary layer flows. *Journal of Geophysical Research: Atmospheres*, *125*(16). doi: 10.1029/2020JD032732

Bonetti, S., Manoli, G., Manes, C., Porporato, A., & Katul, G. (2017). Mannings formula and Stricklers scaling explained by a co-spectral budget model. *Journal of Fluid Mechanics*, *812*, 1189–1212.

Bos, W., Touil, H., Shao, L., & Bertoglio, J.-P. (2004). On the behavior of the velocity-scalar cross correlation spectrum in the inertial range. *Physics of Fluids*, *16*(10), 3818–3823. doi: 10.1063/1.1779229

Bou-Zeid, E., Gao, X., Ansorge, C., & Katul, G. (2018). On the role of return to isotropy in wall-bounded turbulent flows with buoyancy. *Journal of Fluid Mechanics*, *856*, 61–78.

Canuto, V. M., Howard, A., Cheng, Y., & Dubovikov, M. (2001). Ocean turbulence. Part I: One-point closure model – momentum and heat vertical diffusivities. *Journal of Physical Oceanography*, *31*(6), 1413–1426. doi: 10.1175/1520-0485(2001)031⟨1413:OTPIOP⟩2.0.CO;2

Charuchittipan, D., & Wilson, J. (2009). Turbulent kinetic energy dissipation in the surface layer. *Boundary-Layer Meteorology*, *132*(2), 193–204.

Cuxart, J., Bougeault, P., & Redelsperger, J.-L. (2000). A turbulence scheme allowing for mesoscale and large-eddy simulations. *Quarterly Journal of the Royal Meteorological Society*, *126*, 1–30. doi: 10.1002/qj.49712656202

Drobinski, P., Carlotti, P., Redelsperger, J.-L., Masson, V., Banta, R. M., & Newsom, R. K. (2007). Numerical and experimental investigation of the neutral atmospheric surface layer. *Journal of the Atmospheric Sciences*, *64*(1), 137–156. doi: 10.1175/JAS3831.1

Foken, T. (2006). 50 years of the Monin–Obukhov similarity theory. *Boundary-Layer Meteorology*, *119*(3), 431–447.

Gioia, G., Guttenberg, N., Goldenfeld, N., & Chakraborty, P. (2010). Spectral theory of the turbulent mean-velocity profile. *Physical Review Letters*, *105*(18), 184501. doi: 10.1103/PhysRevLett.105.184501

Grachev, A., Andreas, E., Fairall, C., Guest, P., & Persson, P. (2013). The critical Richardson number and limits of applicability of local similarity theory in the stable boundary layer. *Boundary-Layer Meteorology*, *147*(1), 51–82.

Hoxey, R., & Richards, P. (1992). Spectral characteristics of the atmospheric boundary layer near the ground. In *First uk wind engineering conference, engineering department, university of cambridge, uk, september.*

Hsieh, C.-I., & Katul, G. G. (1997). Dissipation methods, Taylor's hypothesis, and stability correction functions in the atmospheric surface layer. *Journal of Geophysical Research: Atmospheres*, *102*(D14), 16391–16405.

Hunt, J., & Carlotti, P. (2001). Statistical structure at the wall of the high Reynolds number turbulent boundary layer. *Flow, Turbulence and Combustion*, *66*(4), 453–475.

Kader, B., & Yaglom, A. (1990). Mean fields and fluctuation moments in unstably stratified turbulent boundary layers. *Journal of Fluid Mechanics*, *212*, 637–662.

Kader, B., & Yaglom, A. (1991). Spectra and correlation functions of surface layer atmospheric turbulence in unstable thermal stratification. In *Turbulence and Coherent Structures* (pp. 387–412). Springer.

Kaimal, J., & Finnigan, J. (1994). *Atmospheric Boundary Layer Flows: Their Structure and Measurement*. Oxford university press.

Kaimal, J., Wyngaard, J., Izumi, Y., & Coté, O. (1972). Spectral characteristics of surface-layer turbulence. *Quarterly Journal of the Royal Meteorological Society*, *98*(417), 563–589.

Katul, G., Banerjee, T., Cava, D., Germano, M., & Porporato, A. (2016). Generalized logarithmic scaling for high-order moments of the longitudinal velocity component explained by the random sweeping decorrelation hypothesis. *Physics of Fluids*, *28*(9), 095104.

Katul, G., & Chu, C.-R. (1998). A theoretical and experimental investigation of energy-containing scales in the dynamic sublayer of boundary-layer flows. *Boundary-Layer Meteorology*, *86*(2), 279–312.

Katul, G., Hsieh, C.-I., Kuhn, G., Ellsworth, D., & Nie, D. (1997). Turbulent eddy motion at the forest-atmosphere interface. *Journal of Geophysical Research: Atmospheres*, *102*(D12), 13409–13421. doi: 10.1029/97JD00777

Katul, G., Hsieh, C.-I., & Sigmon, J. (1997). Energy-inertial scale interactions for velocity and temperature in the unstable atmospheric surface layer. *Boundary-Layer Meteorology*, *82*(1), 49–80. doi: 10.1023/A:1000178707511

Katul, G., Konings, A., & Porporato, A. (2011). Mean velocity profile in a sheared and thermally stratified atmospheric boundary layer. *Physical Review Letters*, *107*(26), 268502.

Katul, G., Porporato, A., Daly, E., Oishi, A., Kim, H.-S., Stoy, P., ... Siqueira, M. (2007). On the spectrum of soil moisture from hourly to interannual scales. *Water Resources Research*, *43*(5).

Katul, G., Porporato, A., Manes, C., & Meneveau, C. (2013). Co-spectrum and mean velocity in turbulent boundary layers. *Physics of Fluids*, *25*(9), 091702. doi: 10.1063/1.4821997

Katul, G., Porporato, A., & Nikora, V. (2012). Existence of k^{-1} power-law scaling in the equilibrium regions of wall-bounded turbulence explained by Heisenberg's eddy viscosity. *Physical Review E*, *86*(6), 066311.

Katul, G., Porporato, A., Shah, S., & Bou-Zeid, E. (2014). Two phenomenological constants explain similarity laws in stably stratified turbulence. *Physical Review E*, *89*(2), 023007.

Kolmogorov, A. (1941). The local structure of turbulence in incompressible viscous

fluid for very large Reynolds numbers. *Cr Acad. Sci. URSS*, *30*, 301–305.

Launder, B., Reece, G. J., & Rodi, W. (1975). Progress in the development of a Reynolds-stress turbulence closure. *Journal of Fluid Mechanics*, *68*(3), 537–566.

Li, D., Salesky, S., & Banerjee, T. (2016). Connections between the Ozmidov scale and mean velocity profile in stably stratified atmospheric surface layers. *Journal of Fluid Mechanics*, *797*.

Lumley, J., & Newman, G. (1977). The return to isotropy of homogeneous turbulence. *Journal of Fluid Mechanics*, *82*(1), 161–178.

Mellor, G., & Yamada, T. (1982). Development of a turbulence closure model for geophysical fluid problems. *Reviews of Geophysics*, *20*(4), 851–875.

Monin, A., & Obukhov, A. (1954). Basic laws of turbulent mixing in the surface layer of the atmosphere. *Geophys. Inst. Acad. Sci. USSR*, *151*(163), e187.

Moore, C. J. (1986). Frequency response corrections for eddy correlation systems. *Boundary-Layer Meteorology*, *37*(1-2), 17–35. doi: 10.1007/BF00122754

Panchev, S. (1971). *Random Functions and Turbulence* (Vol. 32). Elsevier. doi: 10.1016/C2013-0-02360-2

Redelsperger, J.-L., Mahé, F., & Carlotti, P. (2001). A simple and general subgrid model suitable both for surface layer and free-stream turbulence. *Boundary-Layer Meteorology*, *101*(3), 375–408. doi: 10.1023/A:1019206001292

Rodier, Q., Masson, V., Couvreux, F., & Paci, A. (2017). Evaluation of a buoyancy and shear based mixing length for a turbulence scheme. *Frontiers in Earth Science*, *5*, 65. doi: 10.3389/feart.2017.00065

Saddoughi, S., & Veeravalli, S. (1994). Local isotropy in turbulent boundary layers at high Reynolds number. *Journal of Fluid Mechanics*, *268*, 333–372. doi: 10.1017/S0022112094001370

Salesky, S., Katul, G., & Chamecki, M. (2013). Buoyancy effects on the integral length scales and mean velocity profile in atmospheric surface layer flows. *Physics of Fluids*, *25*(10), 105101.

Sorbjan, Z. (1989). *Structure of the Atmospheric Boundary Layer* (No. 551.51 SOR). Prentice Hall.

Taylor, G. (1922). Diffusion by continuous movements. *Proceedings of the London mathematical society*, *2*(1), 196–212.

Tchen, C. (1953). On the spectrum of energy in turbulent shear flow. doi: 10.6028/jres.050.009

Townsend, A. (1980). *The Structure of Turbulent Shear Flow*. Cambridge university press.

Wyngaard, J. (2010). *Turbulence in the Atmosphere*. Cambridge University Press.

Wyngaard, J., Coté, O., & Izumi, Y. (1971). Local free convection, similarity, and the budgets of shear stress and heat flux. *Journal of the Atmospheric Sciences*, *28*(7), 1171–1182. doi: 10.1175/1520-0469(1971)028⟨1171:LFCSAT⟩2.0.CO;2

Zeman, O., & Tennekes, H. (1975). A self-contained model for the pressure terms in the turbulent stress equations of the neutral atmospheric boundary layer. *Journal of the Atmospheric Sciences*, *32*(9), 1808–1813.

Supporting Information for "Scaling Laws for the Length Scale of Energy-Containing Eddies in a Sheared and Thermally Stratified Atmospheric Surface Layer"

A. Ayet[1,2*], **G. G. Katul**[3]

[1]Ifremer, CNRS, IRD, Univ. Brest/ Laboratoire d'Océanographie Physique et Spatiale (LOPS), IUEM, Brest, France
[2]LMD/IPSL, CNRS, École Normale Supérieure, PSL Research University, Paris, France
[3]Nicholas School of the Environment, Box 90328, Duke University, Durham, NC 27708-0328, USA
[4]Department of Civil and Environmental Engineering, Duke University, Durham, NC 27708, USA

Contents

Introduction

The Supporting Information provides the expressions for the data used in the main text.

Text S1

The MOST dimensionless functions as well as several estimates of the spectral peaks as a function of atmospheric stability are listed. From the Kansas experiment, Kaimal and Finnigan (1994) give the following MOST dimensionless functions

$$\phi_m(\zeta) = \begin{cases} 1 + 4.7\zeta, & \zeta \geq 0 \\ (1 - 15\zeta)^{-1/4}, & \zeta < 0 \end{cases}, \quad \phi_w(\zeta) = \begin{cases} 1.56, & \zeta \geq 0 \\ 1.56(1 - 3\zeta)^{2/3}, & \zeta < 0 \end{cases} \qquad (1a, b)$$

and values of the spectral peak

$$zk_p^K(\zeta) = \begin{cases} 2\pi\zeta, & \zeta > 2 \\ 2\pi(1.1 + 0.45\zeta), & 1 < \zeta \leq 2 \\ 2\pi(0.55 + \zeta), & 0 \leq \zeta \leq 1 \\ 2\pi(0.55 + 0.38\zeta), & -1 \leq \zeta < 0 \\ 2\pi 0.17, & \zeta < -1 \end{cases}. \qquad (2)$$

From the AHATS experiment data, Salesky et al. (2013) provided an estimate of the streamwise integral length scale of the vertical velocity

$$\Lambda(z) = \int \frac{\overline{w'(0,z)w'(x,z)}}{\sigma_w^2(z)} dx \qquad (3)$$

which is inversely proportional to the transition wavenumber. The resulting relative variations of k_p are

$$\frac{k_p^s(\zeta)}{k_p^s(0)} = \begin{cases} (1 + 4.01\zeta)^{0.586}, & \zeta \geq 0 \\ 1 - 0.462(1 - e^{4.82\zeta}), & \zeta < 0 \end{cases} \qquad (4)$$

Li et al. (2016) presents the following expression for the Ozmidov length scale in accordance with the AHATS experiment and lake data

$$zL_{oz} = (1/0.4)[\zeta\phi_m(\zeta)]^{3/4}[\phi_m(\zeta) - \zeta]^{-1/2}, \quad \zeta > 0.2. \qquad (5)$$

*Current address, Ifremer, Technopôle Brest Iroise, 29280 Plouzané, France

Corresponding author: A. Ayet, alex.ayet@normalesup.org

References

Kaimal, J., & Finnigan, J. (1994). *Atmospheric boundary layer flows: their structure and measurement*. Oxford university press.

Li, D., Salesky, S., & Banerjee, T. (2016). Connections between the ozmidov scale and mean velocity profile in stably stratified atmospheric surface layers. *Journal of Fluid Mechanics*, *797*.

Salesky, S., Katul, G., & Chamecki, M. (2013). Buoyancy effects on the integral lengthscales and mean velocity profile in atmospheric surface layer flows. *Physics of Fluids*, *25*(10), 105101.

2.4 Conclusion

Starting from the evident limitations of the standard spectral budgets in predicting the value of the spectral peak wavenumber k_p (Sec. 2.1), we have shown evidence of several flaws in the Rotta closure for the vertical velocity (Sec. 2.2). This revealed that the time-scale of energy redistribution by energy-containing eddies should probably be stability and scale dependent. Besides giving interesting insights on the processes governing anisotropic turbulence in the ASL, this result is of interest for the numerical modeling community, since numerous subgrid turbulence schemes used in atmospheric and ocean models, are built on this closure [e.g. Mellor and Yamada, 1982, Cuxart et al., 2000, Canuto et al., 2001]

In Sec. 2.3, we have evaluated under which conditions k_p can be recovered from bulk turbulence measurements. Using Monin-Obukhov similarity functions as a constraint, we have derived variations of the spectral properties of the flow. We found that accurate prediction of k_p was subject to properly including, in the spectral link, the high frequency cutoff of the measuring device. The approach of these two works is inverse to the one pursued by phenomenological models presented in the literature [e.g. Katul and Manes, 2014, Li et al., 2016]. They can hence be seen as a necessary (but not sufficient) first step to assess the validity of many phenomenological models and their underlying assumptions.

As a side remark, it should be noted that, in Sec. 2.2 we have focused on correcting the model for the return-to-isotropy. Indeed, it seems reasonable to adjust this model to match measured anisotropy ratios, since it plays a key role in setting their value. Nonetheless, the scaling (2.3) on page 78 suggests that we could have equivalently focused on adjusting the inter-scale energy transfer model. In fact, both are related by equation (9) of Sec. 2.2.

To summarize, this Chapter has demonstrated the sensitivity of the spectral link to several of its ingredients, and in particular to the pressure-strain correlation. On top of sea waves, it is to be expected that these mechanisms should be strongly modified, as the directionality of waves certainly induces additional anisotropy in the overlying flow. It is out of the scope of this thesis to explore these modifications starting from the spectral budget. In the following chapters, we hence use the bulk formulation of the phenomenological model (i.e. in terms of the geometry of energy-containing eddies) to explore turbulence on top of waves.

CHAPTER 3

GEOMETRICAL IMPACT OF WIND-WAVES ON ENERGY-CONTAINING EDDIES

"Le vent pousse la mer", Zao Wou-Ki (2004).
Private collection © ADAGP, Paris, 2018. Photography : Dennis Bouchard.

3.1 INTRODUCTION

In Chapter 1 (Sec. 1.2) we have introduced a phenomenological model, which relates the geometrical properties of energy-containing eddies $s_h(z)$ and $s_v(z)$, at a given height z, to ϵ, the dissipation of Turbulent Kinetic Energy (TKE)

$$\epsilon(z) \propto u_*^6 \left(\frac{dU}{dz}\right)^{-3} s_v(z)^{-3} s_h(z)^{-1}, \tag{3.1}$$

where u_* is the friction velocity and U the mean wind speed, and s_h and s_v are the streamwise and vertical scales of the energy-containing eddy, respectively. Above a windy sea, it is natural to ask what would be the relation between the geometry of the sea surface and the geometry of energy-containing eddies. If such a geometrical link exists, we can already guess that it should involve relatively long and fast wind-waves. Such waves should be capable of producing geometrical patterns which, in the reference frame of the moving eddy, should persist long enough to impact the eddy properties. Below we use a simple model to quantify this effect, and we term these waves as being "long" wind-waves, as opposed to short wind-waves which, in standard theories, are the main sea-surface components coupled to the wind (see Sec. 1.3).

To evaluate the consequences of this effect on open-ocean momentum fluxes, we further use a wind-over-waves model, which allows inclusion of this new process in a wind and waves equilibrium describing open-ocean measurements (see Sec. 1.3.3.1 on page 62). In fact, long wind-waves are sensitive to environmental conditions (such as fetch and currents). If existing, the geometrical link could hence introduce a dependency of momentum fluxes to environmental parameters, which could help explaining the scatter observed in the measurements (as discussed in the Introduction, page 20).

3.2 ARTICLE: "ON THE IMPACT OF LONG WIND-WAVES ON NEAR-SURFACE TURBULENCE AND MOMENTUM FLUXES"

Boundary-Layer Meteorology (2020) 174:465–491
https://doi.org/10.1007/s10546-019-00492-x

RESEARCH ARTICLE

On the Impact of Long Wind-Waves on Near-Surface Turbulence and Momentum Fluxes

A. Ayet[1,2] · B. Chapron[1] · J. L. Redelsperger[1] · G. Lapeyre[2] · L. Marié[1]

Received: 15 May 2019 / Accepted: 27 November 2019 / Published online: 19 December 2019

Abstract
We propose a new phenomenological model to represent the impact of wind-waves on the dissipation of turbulence kinetic energy near the sea surface. In this model, the momentum flux at a given height results from the averaged contribution of eddies attached to the sea surface whose sizes are related to the surface geometry. This yields a coupling between long wind-waves and turbulence at heights of about 10 m. This new wind-and-waves coupling is thus not exclusively confined to the short wave range and heights below 5 m, where most of the momentum transfer to the waves is known to occur. The proposed framework clarifies the impact of wind-waves on Monin–Obukhov similarity theory, and the role of long wind-waves on the observed wind-wave variability of momentum fluxes. This work reveals which state variables related to the wind–wave coupling require more accurate measurements to further improve wind-over-waves models and parametrizations.

Keywords Air–sea fluxes · Wall-bounded turbulence · Wave boundary layer · Wind stress · Wind-waves

1 Introduction

Observing a windy sea immediately reveals that wind and waves are strongly coupled. Yet, consistent physical mechanisms explaining this two-way coupling are still elusive both to theory and observations (e.g. Soloviev and Kudryavtsev 2010; Hristov 2018; Villas Boas et al. 2019). Of particular interest is the link between near-surface momentum fluxes and waves, due to its importance in atmospheric models, from the synoptic to the climate scale (e.g. Janssen and Viterbo 1996; Shimura et al. 2017; Pineau-Guillou et al. 2018; Villas Boas et al. 2019). For a given near-surface mean wind speed, a large source of variability in turbulent fluxes is atmospheric stability (e.g. Geernaert 1990; Fairall et al. 2003), consistently described by Monin–Obukhov similarity theory (MOST, see the review by Foken 2006). However, for

A. Ayet
alex.ayet@normalesup.org

1 Univ. Brest, CNRS, IRD, Ifremer, Laboratoire d'Océanographie Physique et Spatiale (LOPS), IUEM, Brest, France

2 LMD/IPSL, CNRS, École Normale Supérieure, PSL Research University, Paris, France

neutral atmospheric conditions, open-ocean observations exhibit a variability around their mean value for a given mean wind speed, which has been attributed to waves (see e.g. Edson et al. 2013). The mean value results from a local equilibrium between short wind-waves and atmospheric turbulence. For low wind speeds, swell and non-stationary wind conditions have been suggested as possible reasons of its variability (Drennan et al. 1999), whereas at moderate to high wind speeds, the physical processes are still not clearly determined.

Close to the surface, wave impact on atmospheric turbulence has been accounted for through the so-called wave-induced stress. Assuming that wind fluctuations can be described as a linear superposition of a turbulent and an ocean-wave induced component, wave-induced stress results, for growing seas, from the transfer of mean flow energy to the wave-induced component (Janssen 1989). This energy is then transfered to turbulent motions, which support the growth of wind-waves (Plant 1982). In an equilibrium wind-and-waves situation, i.e. for waves that have equilibrated with a local stationary airflow, wave-induced stress induces an enhancement of turbulent motions compared to flow over a smooth surface (Makin and Mastenbroek 1996). This net enhancement occurs up to a height that defines the wave boundary layer (WBL), above which wave-induced stress vanishes. Wave-induced stress is mostly correlated to the presence of short wind-waves, which are thus strongly coupled to the low-level wind field and receive most of the wind energy input. Conceptual models including this physical process were able to successfully predict measured open-ocean fluxes (Makin and Kudryavtsev 1999; Hara and Belcher 2002; Kudryavtsev et al. 2014). These single-column models (called wind-over-waves models in the following) couple a turbulence kinetic energy (TKE) equation to a spectral wave model through wave-induced stress, and predict the equilibrated turbulent momentum flux and wind-wave spectrum given a reference-height mean wind speed. Following experimental and numerical studies, Kudryavtsev et al. (2014) included wave-breaking effects (i.e. the effect of discontinuities in the surface slope) as an additional source of wave-induced stress, and showed that this effect could be significant in explaining the observed momentum fluxes. Being mostly supported by short waves (with wavelength of the order of 0.01 to 1 m), both processes act on a shallow atmospheric layer, of height one order of magnitude smaller than their wavelength. This results in a height of the WBL of at most 5 m in the absence of swell.

While wave-induced contributions to atmospheric variables are often reported as being particularly difficult to detect at higher altitudes from single-point measurements (Soloviev and Kudryavtsev 2010), Edson et al. (2004) mention that "field campaigns have shown that some turbulent statistics, e.g., the pressure transport term in the kinetic energy budget equation, are influenced by waves up to heights z where $k_p z \approx 2$, where k_p is the peak wavenumber of the dominant waves. The latter findings suggest a thicker WBL for some characteristics of the flow". Hence the coupling between atmospheric turbulence and wind-waves could possibly extend on vertical scales much above 5 m, suggesting the existence of other processes beyond wave-induced stress. Similarly to wave-induced stress, those processes result from spatial correlations between atmospheric quantities on the scale of wind-waves, and should thus be more easily observed if spatial statistics of the atmospheric field (e.g., multiple-point measurements) were available. In the absence of such measurements, a method extracting those spatial correlations from single-point measurements is necessary (as developed for wave-induced stress in Hristov et al. 1998, 2003). The present study is a first step towards such a method by revealing state variables in which those processes might be buried.

More generally, the understanding of the local wind-and-waves equilibrium is related to the longstanding question of the influence of a structured boundary (both in terms of geometry and of velocity) on the properties of turbulence at a certain distance from the boundary (see the review by Belcher and Hunt 1998). Wave-induced stress only accounts

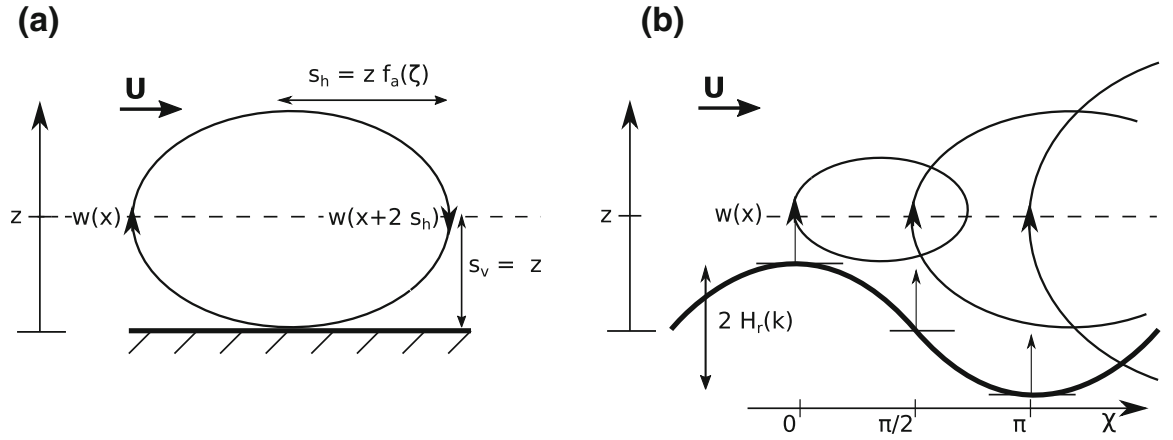

Fig. 1 **a** State-of-the-art and **b** proposed attached-eddy model describing vertical turbulent fluxes through a surface at a height z (dashed lines). **a** For wall-bounded turbulence (Gioia et al. 2010), the most energetic structure (i.e. inducing most of the fluxes) has a vertical length scale $2s_v$ equal to twice the considered height z. Its horizontal length scale $2s_h$ varies with stratification (Katul et al. 2011). The difference between the upward and downward vertical velocity of the structure w yields the mean vertical turbulent motion. The structure can be notionally represented by an attached eddy (thin solid line). **b** In the presence of a surface wave (thick solid line), depending on the relative phase between the eddy and the wave (denoted χ), the height of the surface and thus the size of the attached eddy varies. We propose that multiple attached eddies contribute to the flux (only three examples are drawn)

for the interaction of the turbulent field with additional, wave-induced, fluctuations. It does not represent the possible reorganization of the turbulent fluctuations due to the presence of a structured boundary (e.g. the formation of rolls presented by Phillips et al. 1996). This reorganization has been shown to occur due to stratification effects for a flat and non-moving boundary (in experiments, theory, and numerical simulations respectively: Kaimal et al. 1972; Elperin et al. 2002; Li et al. 2018).

A phenomenological model enabling the inclusion of organized turbulent structures near a wall has been recently described in Gioia et al. (2010). The model assumes that the turbulent fluxes at a given height are driven by surface-attached eddies representing cross-wind atmospheric turbulent structures in a convected frame of reference (invariant in the spanwise direction), and whose horizontal and vertical length scales are related to the height at which the flux is computed (dashed line in Fig. 1). The reorganization of these attached eddies due to stratification was then included in this model by Katul et al. (2011) and Li et al. (2012). These authors introduced an "eddy anisotropy" coefficient f_a (related to the eddies horizontal to vertical aspect ratio), accounting for the deformation of attached eddies due to buoyancy forces (Fig. 1a). As this deformation can be linked to properties of the turbulence spectra (as explained in Katul and Manes 2014), the authors calibrated eddy anisotropy based on measurements from Kaimal et al. (1972). One of the main outcomes of Katul et al. (2011) is to recover MOST universal functions, which were obtained through measurements, using a theoretical model based on a TKE balance. In this balance, the deformation of attached eddies translated into a change in TKE dissipation.

In the presence of surface waves, the link between the shape and spatial organization of the turbulent structures and the geometry of the surface is still an open question. Hence, we (i) propose that wind-waves deform attached eddies, inducing a change in TKE dissipation; (ii) model this effect within the Katul et al. (2011) framework; and (iii) evaluate the impact of this deformation on turbulent momentum fluxes, and its ability to explain the observed variability at moderate wind speeds. The model assumes that the deformed surface allows attached eddies of different sizes to contribute to the momentum flux at a given height (Fig. 1b). The proposed

physical mechanism is mainly supported by long wind-waves (wavelengths of the order of 10 m), and results in a modification of TKE dissipation at heights above 5 m. It introduces a dependency of the wind-wave local equilibrium to the local spectral characteristics of long wind-waves and to the intensity of the mechanism modulating the size of the eddies. This variability is then used to explain open-ocean measurements using the wind-over-waves model of Kudryavtsev et al. (2014) to obtain the mean observed wind-and-waves equilibrium.

The paper is organized as follows: the wall-bounded model and the new physical mechanism are presented in Sects. 2 (for a single wind wave) and 3 (for a realistic sea surface). The wind-over-waves model is briefly summarized in Sect. 4. Section 5 focuses on the resulting impact of the coupling mechanism on near-surface momentum fluxes for neutral conditions, allowing explanation of their variability for a given wind in open ocean measurements. Section 6 then studies the effect of stability on near-surface turbulence, by linking the model with MOST and comparing it to measurements. Conclusions are presented in Sect. 7.

2 A Wall-Bounded Turbulence Model over a Monochromatic Wave

In this section, we propose a new mechanism to model the impact of a wave with a specific wavenumber on TKE dissipation. To this end, starting from a model developed to describe wall-bounded stratified turbulence (recalled in Sect. 2.1), an extension is proposed in order to account for a periodic and undulating surface (Sect. 2.2).

2.1 A Model for Wall-Bounded Stratified Turbulence

We first recall the framework presented in Gioia et al. (2010), Katul et al. (2011) and Li et al. (2012) to describe a stratified surface boundary layer (SBL). The framework models the SBL by means of a TKE balance equation. The mean wind shear and stratification are specified, and the model predicts turbulent fluxes. The key result of the framework is to derive a closure for TKE dissipation by considering the shape of eddies attached to the surface.

The SBL is defined as the lowest part of the surface atmospheric boundary layer (adjacent to the surface) where the flow is horizontally homogeneous and stationary, and with no subsidence. In what follows, the dominant wind-waves are assumed to be aligned with the mean wind direction (and the horizontal coordinate x), so that we only consider perturbations in the (x, z) directions (where z is the vertical coordinate). The turbulent momentum flux normalized by air density $(u_*^l)^2 = -\overline{u'w'}$ is constant within the layer due to horizontal homogeneity. Anticipating Sect. 4, u_*^l is called the *local* friction velocity.

The TKE balance equation within this layer is assumed to be a balance between mechanical (or shear) production, buoyancy production/destruction, and TKE dissipation ϵ

$$-\overline{u'w'}\frac{\partial U}{\partial z} + \frac{g}{\theta_h}\overline{w'\theta'} = \epsilon, \tag{1}$$

where U is the mean wind speed and $(\cdot)'$ denotes turbulent fluctuations. In the following, water vapour effects are omitted for the sake of simplicity. Defining H, the sensible heat flux within the SBL, as

$$H = -\rho C_p \overline{w'\theta'},$$

and using the definition of u_*^l, the TKE balance can been written as

$$(u_*^l)^2 \frac{\partial U}{\partial z} - \frac{gH}{\rho C_p \theta_h} = \epsilon, \tag{2}$$

where g is the acceleration due to gravity, ρ is air density, and C_p is the heat capacity of dry air.

We also introduce the Obukhov length,

$$L = \frac{\rho C_p \theta_h (u_*^l)^3}{\kappa g H}, \tag{3}$$

where $\kappa = 0.4$ is the von Kármán constant and θ_h is a reference potential temperature. With this definition, the stability parameter $\zeta = z/L$, is negative for an unstable boundary layer and positive in the stable case.

The TKE balance equation can then be rewritten in dimensionless form from Eqs. 2 and 3, and the definition of ζ (see e.g. Hogstrom 1996)

$$-\frac{\kappa z}{u_*^l}\frac{\partial U}{\partial z} + \zeta + \frac{\kappa z}{(u_*^l)^3}\epsilon = 0. \tag{4}$$

Following Katul et al. (2011), we further include the first-order effect of the turbulent flux-transport and pressure redistribution terms (which are neglected in Eq. 1, and were shown to be significant for non-neutral conditions) as a constant correction β_2 to the buoyancy term, yielding

$$-\frac{\kappa z}{u_*^l}\frac{\partial U}{\partial z} + (1+\beta_2)\zeta + \frac{\kappa z}{(u_*^l)^3}\epsilon = 0, \tag{5}$$

where $\beta_2 = 1$ (Katul et al. 2011).

To solve this equation (i.e. to obtain u_*^l from given values of $\partial U/\partial z$, z, and ζ), a closure for TKE dissipation ϵ is necessary. To this end, Gioia et al. (2010) and Katul et al. (2011) proposed that turbulent fluxes at a height z are determined by the mean difference between vertical velocities w at x and $x + 2s_h$ (at the same height z) corresponding to the edges of a turbulent structure with given horizontal ($2s_h$) and vertical ($2s_v$) length scales. In such a situation, the momentum flux is estimated as

$$\begin{aligned}(u_*^l)^2(z) &= \kappa_T |w(x+2s_h) - w(x)|[U(z+s_v) - U(z-s_v)] \\ &\sim \kappa_T |w(x+2s_h) - w(x)| \frac{\partial U}{\partial z} 2s_v,\end{aligned} \tag{6}$$

i.e., as the product between the turbulent structure mean vertical velocity and the horizontal momentum perturbation, assuming that momentum is transported across the entire vertical extension of the structure (Gioia et al. 2010). In the above expression, κ_T is a dimensionless proportionality coefficient.

The vertical velocity differences were then estimated using the Kolmogorov 4/5 law for the third-order velocity structure function (e.g. Monin and Yaglom 1975),

$$|w(x+2s_h) - w(x)| = (\kappa_\epsilon \epsilon s_h)^{1/3}, \tag{7}$$

where κ_ϵ is a dimensionless proportionality coefficient. Inserting (7) into (6), and after some algebra, the following expression results for dissipation,

$$\epsilon = \kappa^{-4}(u_*^l)^6 \left(\frac{\partial U}{\partial z}\right)^{-3} s_v^{-3} s_h^{-1}, \tag{8}$$

where $\kappa = 2^{3/4}\kappa_T^{3/4}\kappa_\epsilon^{1/4}$ is the von Kármán constant (this matching is required to recover the law-of-the-wall under neutral conditions).

In Eqs. 6– 8 only the most energetic structure at a height z is considered, i.e. corresponding to the leading order contribution to the third-order structure function and hence to the vertical momentum flux. It is the structure whose half vertical length scales as the height at which the turbulent flux is computed, i.e. $s_v = z$. In the absence of stratification, the horizontal length scale is further assumed to be equal to the vertical length scale (Gioia et al. 2010). Katul et al. (2011) showed that stratification introduces an eddy anisotropy factor f_a in the horizontal length scale, such that

$$s_h = f_a(\zeta)s_v, \tag{9}$$

where $f_a = 1$ for neutral conditions (i.e. $\zeta = 0$).

Figure 1a shows a conceptual representation of the most energetic turbulent structure for a height z as an ensemble-mean eddy in a convected frame of reference (following Gioia et al. 2010; Katul et al. 2011). The shape of the eddy depends on the horizontal and vertical length scales of the turbulent structure. This conceptual representation does not entail any velocity field associated with the eddy, apart from the vertical velocities at its upward and downward branches (black arrows), corresponding to $w(x)$ and $w(x + 2s_h)$ respectively.

The condition $s_v = z$ then yields that the eddies associated with the most energetic turbulent structures (termed energy-containing eddies) are eddies attached to the surface, reminiscent of the attached-eddy model of turbulence introduced by Townsend (1980) (see also the review by Marusic and Monty 2019). The spatial aspect ratio of the energy-containing eddies, fixed by relation (9), reflects their reorganization due to buoyancy forces (through the stability parameter ζ).

2.2 Inclusion of a Single Wave Within the Wall-Bounded Model

We now propose an extension of the wall-bounded model to include the reorganization of energy-containing eddies due to a boundary with a spatial structure. Let us first consider the impact of a wave of wavenumber k and of height $H_r(k)$ on an attached eddy driving the momentum flux at a height z. In the following, we derive the horizontal extent of the eddy $2\tilde{s}_h$ in the presence of the monochromatic wave. More generally, we use the notation $\widetilde{(\cdot)}$ throughout to denote the contribution a single wave of wavelength k to turbulent quantities.

The sea-surface height h varies around its reference value depending on the position along the wave, measured by the relative phase (denoted χ) between the wave and the eddy. The height variations follow $h(k, \chi) = H_r(k)\cos\chi$. Within the wall-bounded model presented in Sect. 2.1, the vertical extent of the most efficient eddy is twice the distance between the surface and the height z (Fig. 1a). In the presence of a surface wave, the now phase-dependent vertical extent of the attached eddy driving the momentum flux $\tilde{s}_v$ varies around its reference value z. Figure 1b shows the configurations corresponding to $\chi = 0, \pi/2$, and π.

Using (9), the horizontal length scale of the eddy varies as a function of phase χ as

$$\begin{aligned}\tilde{s}_h(z, \zeta, k, \chi) &= f_a(\zeta)(z - h(k, \chi))) \\ &= z f_a(\zeta)[1 - (H_r(k)/z)\cos\chi].\end{aligned} \tag{10}$$

For a given wave, we further consider only the "outer region" of the SBL (as defined in Belcher and Hunt 1993, 1998). Within this region, (i) the mean flow speed is larger than the phase speed of the wave, and (ii) eddies have a turnover time longer than the advection time above the considered wave. Thus, during the eddy lifetime and its advection above a wave,

different configurations (depending on χ, and shown in Fig. 1b) can occur, which can all potentially contribute to the resulting upward transport of momentum (Eq. 6) and to TKE dissipation (Eq. 8).

We consider the most general form accounting for the contribution of all possible configurations to the eddy horizontal length scale, a weighted average over all configurations

$$\langle \tilde{s}_h \rangle(z, \zeta, k) = \int_0^{\pi} p(\chi) \tilde{s}_h(z, \zeta, k, \chi) \mathrm{d}\chi, \tag{11}$$

where $p(\chi)$ is a weight, or the (normalized) probability density function (p.d.f.) of the configurations, and $\langle \cdot \rangle$ denotes the average over all configurations labeled by χ. The average vertical extent of the attached eddy is assumed to be unchanged by the presence of waves (i.e. $\langle \tilde{s}_v \rangle = s_v = z$). From Eq. 6 (see also Gioia et al. 2010), the vertical extent results from the Taylor expansion of vertical wind variations (i.e. $U(z + s_v) - U(z - s_v) \sim (\partial U / \partial z) 2 s_v$) and denotes the height over which the eddy mixes momentum. The horizontal extent denotes the size and energy of the structure (through Kolmogorov's law, Eq. 7). We thus consider that, on average, the presence of waves only affects the energy of the horizontal structure.

If the p.d.f. $p(\chi)$ is not symmetric around $\chi = \pi/2$, then the wave-induced sea-surface height variation leads on average to a variation of the eddy aspect ratio, affecting TKE dissipation (Eq. 8). In particular, a compression (respectively a stretching) occurs for a distribution where configurations around $\chi = 0$ (resp. $\chi = \pi$) are dominant.

The different configurations in χ can also be interpreted as representing TKE bursts. From Kolmogorov's law (Eq. 7), a change in s_h is related to a change in the vertical velocity difference of the turbulent structure. Increase or decrease in s_h due to a change in the phase χ can thus be interpreted as an increase or decrease in the vertical velocity at the edges of the turbulent structure, and those velocity variations can be associated with bursts. The average horizontal length scale computed in Eq. 11 can thus be interpreted as accounting for the contribution of bursts to TKE dissipation in the SBL due to the presence of waves. Bursts were suggested as possibly supporting a large fraction of open-ocean surface momentum fluxes (Dorman and Mollo-Christensen 1973). Laboratory measurements revealed that such events could have an asymmetric p.d.f. (see Fig. 26 of Kawamura and Toba 1988).

3 The Impact of Wind-Waves on Near-Surface Turbulent Structures

Section 2 presented a wall-bounded turbulence model where the effects of a single wave were included in TKE dissipation through the stretching or the compression of an attached eddy, i.e. the change in its horizontal to vertical aspect ratio. We now generalize the model to the case of a wave field (Sect. 3.1), while Sect. 3.2 then discusses the physical quantities modulating the proposed mechanism.

3.1 Generalization of the Eddy-Stretching Process to a Wind-Wave Sea

So far we discussed how a monochromatic wave could affect a given turbulent structure. In the case of a wave field composed of the sum of monochromatic waves of different wavelengths and directions the question is to determine which waves can potentially stretch or compress an attached eddy contributing to the momentum flux at a height z (in the sense of changing its aspect ratio). In the following, we make the assumption that the deformation occurs mainly

when wave and attached eddy sizes are close, i.e. for a wave of wavelength k scaling as the inverse of the height $1/z$, with z roughly the horizontal extent of the eddy (defined in Eq. 10).

The assumption can be made more precise by considering the physical mechanisms likely to cause eddy deformation. The geometry of short wind-waves is modulated by the supporting longer waves. Hence, the resulting surface roughness (due to wave-induced stress from short wind-waves) varies horizontally following the longer waves, on lengths of half the modulating wave horizontal length scale (e.g. Kudryavtsev and Chapron 2016). This modulation has been shown to significantly affect the near-surface atmospheric flow (Gent and Taylor 1976; Kudryavtsev and Chapron 2016) and could also impact attached eddies by inducing a roughness variation on a scale resonant with that of the eddy. The average deformation of an attached eddy by a wave, described in Sect. 2.2, is thus assumed to be due to these modulated shorter waves. Within this picture, modulating waves whose half horizontal length scale is shorter than the horizontal eddy size are not capable of interacting with both the upward and the downward branch of the attached eddy. Moreover, among these longer modulating wind-waves, we only consider the one experiencing the longest interaction time with the eddy advected above, i.e. the shortest (slowest) wind-wave. It is thus assumed that eddy stretching or compression occurs for a resonant wave whose half-horizontal extent (π/k_r) is equal to the horizontal length scale of the wall-bounded attached eddy prior to deformation ($2zf_a$)

$$k_r(z) = \frac{\pi}{2zf_a(\zeta)}. \tag{12}$$

The horizontal extent of an energy-containing eddy at a height z over a wave field, $2\langle s_h\rangle$, is then expressed from the individual contribution of monochromatic waves as

$$\langle s_h\rangle(z,\zeta) = \langle \tilde{s}_h\rangle[z,\zeta,k_r(z)]. \tag{13}$$

Using Eqs. 10 and Eq. 11, it further reads

$$\langle s_h\rangle(z,\zeta) = zf_a(\zeta)g_e(z,\zeta), \tag{14}$$

where we defined the eddy-stretching factor g_e as

$$g_e(z,\zeta) = \int_0^\pi \left\{1 - \frac{H_r}{z}\cos\chi\right\} p(\chi)\mathrm{d}\chi, \tag{15}$$

where H_r is the height of the resonant wave.

For a sea surface described by a wave spectrum $S(k)$ (as a function of the isotropic wavenumber k), H_r can be computed from contributions of a narrow wave-packet around k_r, of width Δk as

$$H_r^2(k_r) = \int_{k_r-\Delta k/2}^{k_r+\Delta k/2} S(p)\mathrm{d}p \approx S(k_r)\Delta k. \tag{16}$$

Note that for the physical picture of Fig. 1 to hold, the resonant wave height must be lower than the height z at which fluxes are computed, restricting the physical process to cases where $H_r(k_r) < z$.

The width of the wave-packet Δk is related to the accuracy of the resonance condition (Eq. 12), since it quantifies to what extent waves that are not exactly of wavelength k_r contribute to eddy stretching. It can also be related to the magnitude of the physical mechanism causing eddy stretching, i.e. the modulation of short wind-waves by long wind-waves, which is highly variable (e.g. due to slicks, sea-surface temperature, and jointly varying surface currents and stability conditions, see Vandemark et al. 1997; Grodsky et al. 2012; Kudryavtsev et al. 2012). The wave-packet width is thus considered as a model parameter, called Δ_k. The

resulting form for the wave-packet width, including the physical condition mentioned above is

$$\Delta k = \begin{cases} \Delta_k & \text{for } H_r(k_r) < z \\ 0 & \text{for } H_r(k_r) \geq z \end{cases}. \tag{17}$$

For $H_r(k_r) \geq z$, or for no waves (i.e. $S(k) = 0$), Eq. 14 is reduced to the expression proposed by Katul et al. (2011) (Eq. 9).

Eddy stretching accounts for the change in the shape of an energy-containing eddy by interaction with a surface wave of a size resonant with the size of the eddy. Using Eq. 14 in Eq. 8, TKE dissipation including eddy stretching reads

$$\frac{\kappa z}{(u_*^l)^3}\epsilon = \frac{(u_*^l)^3}{(\kappa z)^3}\left(\frac{\partial U}{\partial z}\right)^{-3} f_a(\zeta)^{-1} g_e(z,\zeta)^{-1}. \tag{18}$$

Due to the resonance condition between the wave and the eddy (Eq. 12), the change in TKE dissipation due to eddy stretching only occurs at heights $h_e = \pi/[2 f_a(\zeta) k] \sim 1/k$, matching the heights suggested in Edson et al. (2004) and also discussed in the introduction.

For g_e and f_a equal to one (i.e. neutral conditions and a flat boundary), we recover the expression of TKE dissipation obtained for homogeneous and isotropic turbulence (and used in the wind-over-waves model of Kudryavtsev et al. 2014, see Sect. 4).

3.2 Sources of Variability of Eddy Stretching

Eddy stretching is a new coupling mechanism between the wave and the wind fields, whose magnitude can vary for a given mean wind speed. In order to understand the sources of this variability, the expression of eddy stretching presented in Eq. 15 is rewritten in wavenumber space, i.e. by defining $\tilde{g}_e$ such that

$$g_e(z,\zeta) = \tilde{g}_e(k_r,\zeta). \tag{19}$$

By using Eq. 15 together with the resonance condition (Eq. 12) and the height of the resonant wave (Eq. 16), $\tilde{g}_e$ can be expressed as

$$\tilde{g}_e(k_r,\zeta) = 1 - 2\Delta k^{1/2}\frac{f_a(\zeta)}{\pi}[k_r^2 S(k_r)]^{1/2}\int_0^{\pi} p(\chi)\cos\chi \,\mathrm{d}\chi. \tag{20}$$

In addition to stability, $\tilde{g}_e$ depends on the wavenumber of the resonant wave (k_r) through the spectrum of the wave slopes ($k_r^2 S(k_r)$). Typical wind-wave slope spectra exhibit a peak depending on the degree of sea-state development (e.g. spatial fetch, as modelled in Donelan et al. 1985; Elfouhaily et al. 1997), and almost vanish for waves below 1 m (corresponding to $k_r \sim 10\,\mathrm{m}^{-1}$). For waves larger than the spectral peak (e.g. 60 m for a fetch of 100 km in the Donelan et al. 1985, model), $k_r^2 S(k_r)$ quickly vanishes. Eddy stretching thus reflects the impact of intermediate to long wind-waves (of the order of tenths of metres) on atmospheric turbulence, through the increase of the air–sea interface area (related to the sea surface mean slope). This is consistent with remote sensing measurements indicating a sensitivity of air–sea fluxes to the air–sea interface area (similar to radar backscatter, e.g. Kitaigorodskii 1973; Brown 1979; Vandemark et al. 1997). The range of the spectrum contributing the most to sea-surface slope (long wind-waves) can be highly variable for a given 10-m mean wind speed, sensitive to fetch, rising/decaying winds, surface currents, modulating longer swells, thus introducing variability into the wind-wave equilibrium (e.g. see Zhang et al. 2009, where

surface currents caused long wind-waves to deviate from the mean wind direction, impacting surface stress).

Eddy stretching also depends on the probability distribution of the different events $p(\chi)$ and the bandwidth coefficient Δ_k. Variations of $p(\chi)$ can induce an eddy stretching smaller or greater than one. As shown in Fig. 1b, for probability distributions where predominant configurations are for phases smaller than $\pi/2$, the horizontal extent of the eddy is reduced with respect to the wall bounded case, and hence eddy stretching is smaller than one (see Eq. 14). Conversely, when predominant configurations are for phases greater than $\pi/2$, eddy stretching is larger than one. Both quantities $p(\chi)$ and Δ_k are related to the physical process inducing eddy stretching (the modulation of short wind-wave stress by long wind-waves) whose magnitude can vary for a given 10-m mean wind speed (Gent and Taylor 1976; Dulov et al. 2013; Kudryavtsev and Chapron 2016).

For a given 10-m mean wind speed, eddy stretching can thus vary due to, (i) variations of the wave-slope spectrum, and (ii) variation of the magnitude of the physical process causing eddy stretching. However, as described in Sect. 4, in order to obtain a realistic wind-wave spectrum and the associated wind-over-waves equilibrium (i.e. matching observations), we use the wind-over-waves model of Kudryavtsev et al. (2014). Within this particular model, the only parameter controlling the long wind-wave spectrum is spatial fetch, following the parametrization of Donelan et al. (1985). To simply account for deviations from this parametrization, as well as for the sources of variability mentioned above, Eq. 20 is rewritten as

$$\tilde{g}_e(k_r,\zeta) = \begin{cases} 1-\gamma\dfrac{f_a(\zeta)}{\pi}[k_r^2 S(k_r)]^{1/2} & \text{for } H_r(k_r) < z \\ 1 & \text{for } H_r(k_r) \geq z \end{cases}, \tag{21}$$

where

$$\gamma = 2{\Delta_k}^{1/2}\int_0^{\pi} p(\chi)\cos\chi\,\mathrm{d}\chi. \tag{22}$$

The new parameter γ contains all the dependencies to $p(\chi)$ and Δ_k. Implicitly, it also contains variations in the wind-wave slope spectrum not described by the wind-over-waves model (e.g. non-stationary winds, surface currents, etc.).

Variations of spatial fetch in the Donelan et al. (1985) parametrization only change the spectrum of wind-waves greater than about 60 m (by causing a shift of the peak of the wind-wave slope spectra towards larger waves). From Eq. 21, this induces a change in eddy stretching at heights h_e (proportional to the wave size) too large to impact the surface momentum flux u_* (not shown). On the other hand, variations of γ in Eq. 21 induce a global change in the eddy-stretching magnitude. This includes a change in the eddy-stretching magnitude corresponding to 10-m waves, describing a change in the wave energy not described by the Donelan et al. (1985) parametrization. This corresponds to changes in eddy stretching at heights around 10 m having a significant impact on momentum fluxes, as will be shown numerically in Sect. 5.

The condition $H_r(k_r) < z$ in Eq. 21 sets upper and lower bounds on $\tilde{g}_e$: since $H_r(k_r)$ is related to $k_r^2 S(k_r)$, this condition sets an upper bound on $k_r^2 S(k_r)$, implying that $\tilde{g}_e$ cannot be too large or too small relative to one for $\gamma < 0$ or $\gamma \geq 0$ respectively. In practice, evaluating this condition would require evaluating $H_r(k_r)$ through Eq. 16, and hence choosing a value for Δ_k. This is not compatible with the choice, made in this work, to use only one free parameter in the description of eddy stretching (the parameter γ). Hence, in the following, the condition $H_r(k_r) < z$ is replaced by setting bounds on g_e, i.e. by the condition that

$\tilde{g}_e < 10^2$ or $\tilde{g}_e > 10^{-2}$ for $\gamma < 0$ or $\gamma \geq 0$, respectively. This choice of bounds covers two orders of magnitude of $\tilde{g}_e$ around one. It also ensures that $\tilde{g}_e$ is positive, and hence that the TKE dissipation is positive.

4 Wind-Over-Waves Model

In the previous sections, we proposed a mechanism accounting for the impact of long wind-waves on TKE dissipation within an SBL model where a wave spectrum was prescribed. We now briefly describe the wind-over-waves model introduced in Kudryavtsev et al. (2014), predicting the generation of wind-waves by turbulent motions within a wind-and-waves equilibrium. This wind-over-waves model is then used in the following sections to explore the sensitivity of the wind-and-waves equilibrium to the proposed mechanism.

The wind-over-waves model couples an atmospheric TKE equation with an equation describing a wind-wave field. Low-level turbulent motions lose energy to short wind-waves, which in turn generate atmospheric fluctuations enhancing TKE by extracting energy from the mean flow. Wave-wave non-linear interactions then result in an equilibrium wind-and-waves state, where TKE is enhanced with respect to flow over a smooth surface, reproducing the mean observed momentum flux in open-ocean measurements for a given mean wind under neutral conditions. At the core of this coupling is thus the transfer of energy between atmospheric turbulent motions and atmospheric wave-induced motions, the latter being coupled to the wind-wave field (e.g. Makin and Kudryavtsev 1999; Hara and Belcher 2002; Kudryavtsev et al. 2014). The atmospheric flow is thus decomposed into a mean component, a turbulent component and a wave-induced component which decays with height.

The first implication of this triple decomposition is that, as opposed to a standard SBL, the turbulent momentum flux $-\overline{u'w'} = (u_*^l)^2$ is no longer constant with height, due to the presence of wave-induced stress $\tau^w = \rho(u_*^w)^2$ associated to wave-induced motions. The sum of both wave-induced and turbulent contributions is however constant and equal to u_*^2, defined as the normalized turbulent momentum flux on top of the WBL (defined as the SBL sub-layer where wave-induced stress is non-zero, e.g. Makin and Mastenbroek 1996)

$$(u_*^l)^2(z) + (u_*^w)^2(z) = u_*^2. \tag{23}$$

From this equation, we introduce the coupling coefficient

$$\alpha_c(z) = \left[\frac{u_*^w(z)}{u_*}\right]^2, \tag{24}$$

which quantifies the relative impact of wave-induced stress in the SBL. Equation 23 can then be rewritten as

$$u_*^l = (1 - \alpha_c)^{1/2} u_*. \tag{25}$$

The second implication of the triple decomposition is that the TKE balance in the presence of wave-induced stress reads

$$[(u_*^w)^2 + (u_*^l)^2]\frac{\partial U}{\partial z} - (1 + \beta_2)\frac{gH}{\rho C_p \theta_h} = \epsilon. \tag{26}$$

With respect to the wall-bounded case (Eq. 2), the TKE balance now contains an additional term $(u_*^w)^2 \partial U/\partial z$, describing the extraction of energy from the mean flow by its interaction with wave-induced stress. Equation 26 is a straightforward generalization of the Kudryavtsev

et al. (2014) balance (derived in, e.g., Kudryavtsev and Makin 2004; Hara and Sullivan 2015) where stratification has been included (through the term $gH/C_p\theta_h$). In this balance, the presence of waves enhances TKE through the so-called wake production term, as found in numerical simulations over idealized sinusoidal waves (Hara and Sullivan 2015) and over a breaking-wave field (Suzuki et al. 2013).

Note that other balances could be considered. In particular, Janssen (1999) and Cifuentes-Lorenzen et al. (2018) consider that $(u_*^w)^2 \partial U/\partial z$ acts directly as a source of wave energy (and hence does not appear in Eq. 26), leading to a decrease in TKE in the presence of wind-waves. This balance describes TKE decrease observed very close to the surface in numerical simulations (Hara and Sullivan 2015). This region is not described by the Kudryavtsev et al. (2014) model, which is written in Cartesian coordinates, hence losing validity when approaching wave crests.

Using Eqs. 3 and 25 in Eq. 26, the TKE balance in dimensionless form reads

$$-(1-\alpha_c)^{-1}\frac{\kappa z}{u_*^l}\frac{\partial U}{\partial z}+(1+\beta_2)\zeta+\frac{\kappa z}{(u_*^l)^3}\epsilon=0. \tag{27}$$

The atmospheric component of the Kudryavtsev et al. (2014) wind-over-waves model is recovered for a neutral stratification (i.e. $\zeta \neq 0$). The standard TKE equation describing stratified turbulence in absence of waves is recovered in its dimensionless form (Eq. 5) for $\alpha_c = 0$.

Using the expression for TKE dissipation Eq. 18 in Eq. 27 further yields

$$-(1-\alpha_c)^{-1}\frac{\kappa z}{u_*^l}\frac{\partial U}{\partial z}+(1+\beta_2)\zeta+\frac{(u_*^l)^3}{(\kappa z)^3}\left(\frac{\partial U}{\partial z}\right)^{-3} f_a^{-1} g_e^{-1}=0, \tag{28}$$

where eddy anisotropy f_a depends on stratification ζ, and eddy stretching g_e depends on γ, height z, and the wave spectrum (through Eqs. 19 and 21). Equation 28 can thus be solved for the dimensionless shear $[(\kappa z)/u_*^l]\partial U/\partial z$, given ζ, α_c, f_a, and g_e.

The wave-induced stress τ^w, and thus α_c, is required to solve Eq. 28. As presented in Kudryavtsev et al. (2014), the coupling parameter α_c describes not only the wave-induced stress in the WBL resulting from the smooth deformation of the airflow above waves (losely called "form drag" in the following), but also the stress induced by airflow separation events on top of breaking waves (Reul et al. 1999; Husain et al. 2019). For a given wave of wavelength k, both these effects act over a shallow atmospheric layer, up to heights $h(k) \sim 0.1k^{-1}$ and $h_a(k) \sim 0.3k^{-1}$ respectively. Note that this is at variance with eddy stretching, acting at greater heights (i.e. $h_e \sim 1/k$, see Sect. 3).

Furthermore, both form drag and airflow separation are, unlike eddy stretching, mostly confined to the short wind-wave range (waves of the order of 1 m, following Plant 1982) and thus couple Eq. 28 to a stationary short wind-wave spectrum (described by Eq. 34 in Appendix 1). The full wind-wave spectrum is described, in the Kudryavtsev et al. (2014) model, as a superposition of the aforementioned short wind-wave part and a prescribed long-wave part, mostly governed by the degree of sea-state development (i.e. fetch and wave age, following Donelan et al. 1985; Elfouhaily et al. 1997, and discussed in Sect. 3.2). Details on both the wind-wave spectrum and the parametrization of the coupling coefficient can be found in Appendix 1.

The resulting wind-and-waves equilibrium matches atmospheric measurements (see Sect. 5.2) and wave measurements (Yurovskaya et al. 2013). It is not sensitive to variations in the long wind-wave spectrum (i.e. variations in fetch), since it does not contribute to form drag nor airflow separation.

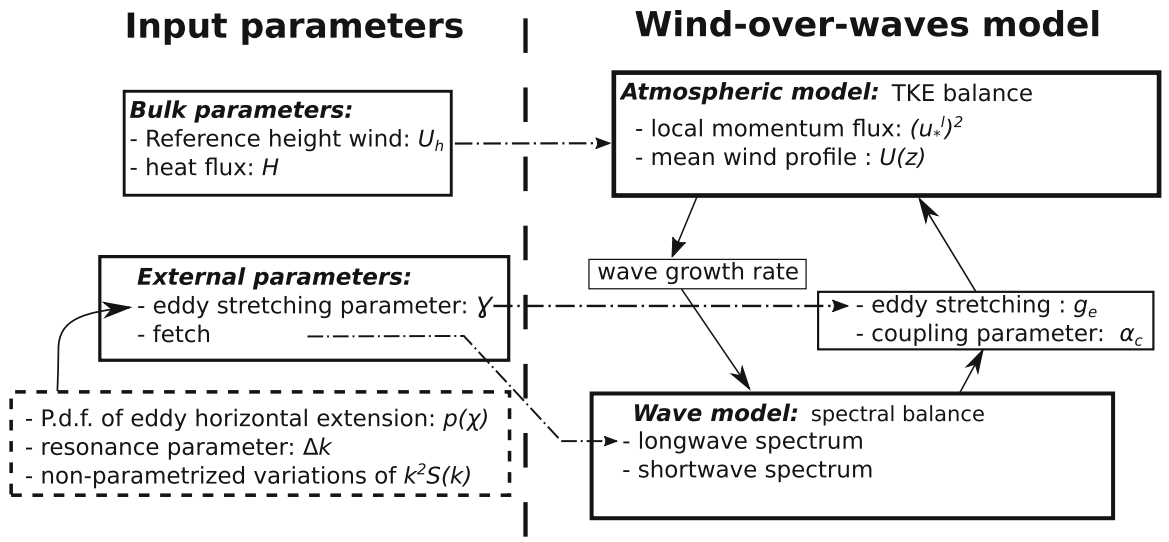

Fig. 2 Flow chart of the wind-over-waves model. The left panel shows the input parameters of the model and how they impact the different steps of model (dotted-dashed arrows). The parameters used in standard bulk formulae are called "bulk parameters", as opposed to the "external parameters". Note in particular the different quantities impacting the proxy eddy-stretching parameter γ (dashed box, Eq. 21). Right panel shows the structure of the wind-over-waves model. The equilibrium solution is obtained by iteratively solving the two model components (the atmospheric model, Eq. 28 and the wave model, Eq. 34), using a bulk formula as a first guess for the momentum flux

5 Momentum Fluxes Variability Under Moderate Wind Speeds

In this section, we first describe how the new physical mechanism (described in Sects. 2 and 3) can be incorporated in the wind-over-waves model described in Sect. 4 (Sect. 5.1). The resulting new wind-and-waves equilibrium is then compared to open-ocean measurements (Sect. 5.2).

5.1 The Coupled Model

As summarized in Fig. 2, the coupled wind-over-waves model solves the TKE balance (28). The equation depends on the short wind-wave spectrum (through α_c) obtained by solving a budget equation (Eq. 34 in Appendix 1). It also depends on the parameter γ through g_e, introduced in Eq. 21. The coupled system is solved by iterations, given a 10-m wind speed U_{10}, a heat flux H, fetch (for the prescribed long wind-wave spectrum), and the parameter γ. It returns a friction velocity on top of the WBL (u_*), a mean wind profile $U(z)$, and a wind-wave spectrum $S(k)$, characterizing the wind-and-waves equilibrium. The inclusion of eddy stretching introduces a sensitivity of the wind-and-waves equilibrium to long wind-waves, absent in the Kudryavtsev et al. (2014) model and discussed below.

Note that even though Eq. 28 is valid for any stability condition, only unstable stratification conditions can be simulated by the coupled model (i.e. when α_c is determined recursively by solving Eq. 34 in Appendix 1). When the atmosphere is stably stratified, the TKE model yields unrealistically weak turbulence. It is out of the scope of the present paper to describe the coupled stably-stratified case, that would require the introduction of other physical processes such as gravity waves or a total kinetic energy balance (e.g. Zilitinkevich et al. 2008).

5.2 Comparison to Experiments

Near-surface momentum fluxes (u_*^2) from the wind-over-waves model and its extension presented above were compared to measurements presented in Edson et al. (2013), compiling data obtained from different field campaigns in open sea. The data were collected 50 km off the southern Californian coast (Hristov et al. 2003), 10 km off the coast of Denmark (Mahrt et al. 1996), south of Martha's Vineyard (Edson et al. 2007), and on the northern wall of the Gulf Stream (Marshall et al. 2009), and were filtered to retain only young seas (i.e. with presumably no swell). This dataset covers a wide range of winds speeds (up to 25 m s^{-1}) and stability conditions (stability parameter from -1.2 to 0.8). These observations are of particular relevance since they were used to calibrate the COARE parametrization (e.g. Fairall et al. 2003).

Figure 3a shows the observed bin-averaged values of momentum fluxes as a function of the neutral 10-m wind speed (U_{10N}, black dots). In the observations, the neutral wind speed is obtained by applying a MOST stability correction to the wind speed extrapolated from direct measurements. It corresponds to the expected wind speed at equilibrium with the measured momentum flux in neutral stability conditions (e.g. Liu and Tang 1996). In the following, measurements will be compared with the wind-over-waves model in neutral conditions ($\zeta = 0$) leading to an eddy anisotropy factor $f_a = 1$.

The solid line in Fig. 3a shows the equilibrium solution of the coupled model including wave-induced stress and without eddy stretching (i.e. $\gamma = 0$), for a fetch of 100 km. As expected from Kudryavtsev et al. (2014), the solution is in good agreement with observations. On the contrary, without wave-induced stress (i.e. $u_*^w = 0$ or $\alpha_c = 0$), the modelled momentum fluxes are smaller than those observed for wind speeds greater than about 10 m s^{-1} (dashed line in Fig. 3a). The effect of short waves on the SBL (through form drag and airflow separation, which increase TKE) is thus an essential physical process to explain the mean dependency of wind stress on U_{10N}. In fact, for the considered range of wind speeds, the coupling coefficient α_c varies between 0 and 0.6, and increases with wind speed (solid line in Fig. 3b, which shows the maximal coupling coefficient for a given wind speed, located very near the surface). For wind speeds above 15 m s^{-1}, wave-induced stress is larger than the turbulent momentum stress (i.e. $\alpha_c > 0.5$).

In the wind-over-waves model, to each value of U_{10N} corresponds a short wind-wave spectrum. Long wind-waves depend on fetch and on wave age (u_*/c_p, with c_p the phase speed of the spectral-peak wave component), following the parametrization of Donelan et al. (1985). The correspondence between U_{10N} and wave age in the model is shown in Fig. 3b (dashed line). The modelled range (between 0.6 and 1.2) is consistent with the range of observed values in Edson et al. (2013), which are interpreted as young seas. Note that even though there is a one-to-one correspondence between U_{10N} and wave age, there is no reason for such a relation between wave age and the near-surface momentum flux, which is discussed below by showing other sources of variability of momentum flux independent of wave age.

The momentum fluxes measurements exhibit a significant scatter (black error bars in Fig. 3a), which may be attributed to the influence of local processes on the wind-and-waves equilibrium (Edson et al. 2013). In the present work we investigate the possibility that this variability is caused by eddy stretching, through a change in the long wind-wave spectrum (and particularly 10-m waves), or through a change in the intensity of the modulation of short wind-waves by long wind-waves. To this end, we use the simplified expression of eddy stretching (Eq. 21) in which a single parameter, γ, is varied as a proxy for these two effects. Variation of γ between -20 and 8 yields the grey shading in Fig. 3a. This corresponds to values of eddy stretching between 10^{-2} and 10^{1}, as shown in Fig. 4. The range of variation

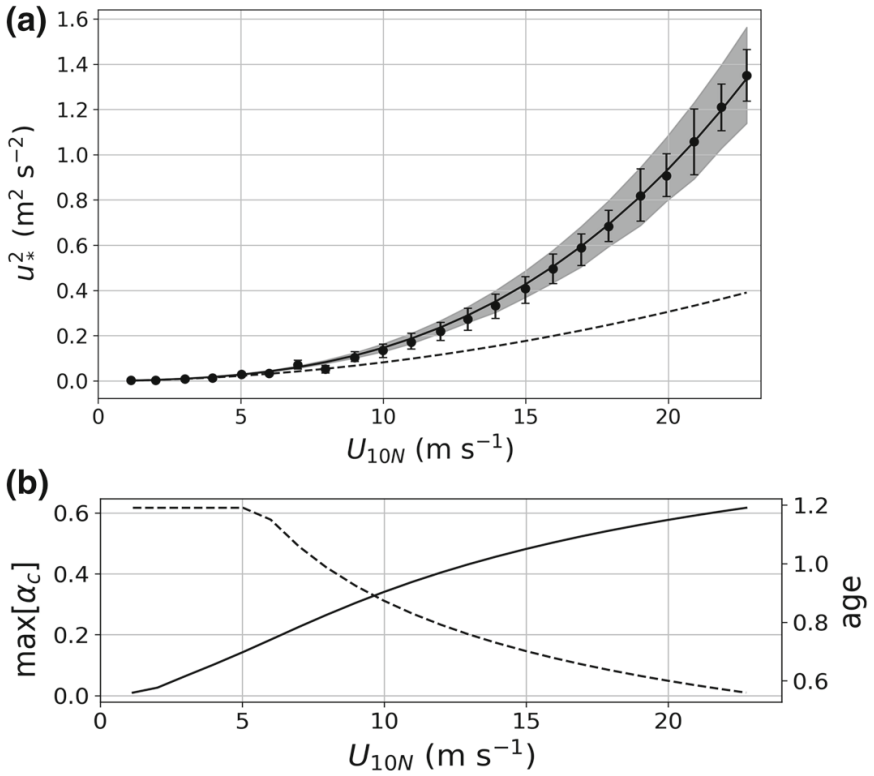

Fig. 3 **a** Surface momentum fluxes (divided by air density) vs neutral 10-m wind speed. Dots indicate bin-averaged measurements from Edson et al. (2013), vertical error bars are the associated standard deviations, the dashed line is the model result without accounting for the impact of waves on the SBL, and the solid line is the model result with wave-induced stress. Grey shading is the range of values obtained varying eddy stretching around its neutral value of one (corresponding to $\gamma = 0$). **b** Maximal (i.e. surface) coupling parameter α_c (solid line), and wave age (dashed line) vs 10-m neutral wind speed. For the range of observed wind speeds, the coupling parameter varies between 0 and 0.6

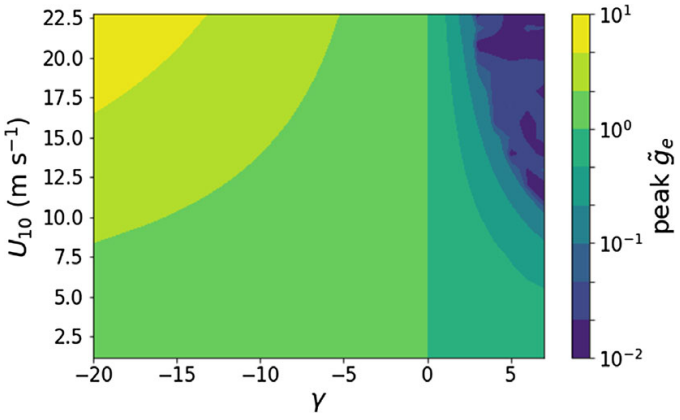

Fig. 4 Magnitude of eddy stretching g_e at its spectral peak (from Eq. 21) as function of the coefficient γ and 10-m wind

in momentum flux resulting from the variation of eddy stretching covers the scatter that is observed in the data (compare shadings and error bars in Fig. 3a). Note that the lower part of the grey shading in Fig. 3 corresponds to values of g_e greater than one, and conversely. Other factors could be invoked to explain the scatter in the measurements, in particular fetch. To this end, fetch was varied in the coupled model between 10 and 1000 km, with fixed γ in Eq. 21. The resulting variability was not sufficient to explain the observed scatter (not shown). This is consistent with the fact that fetch variations induce a change in eddy stretching at heights which do not significantly affect the surface momentum flux (as discussed in Sect. 3.2).

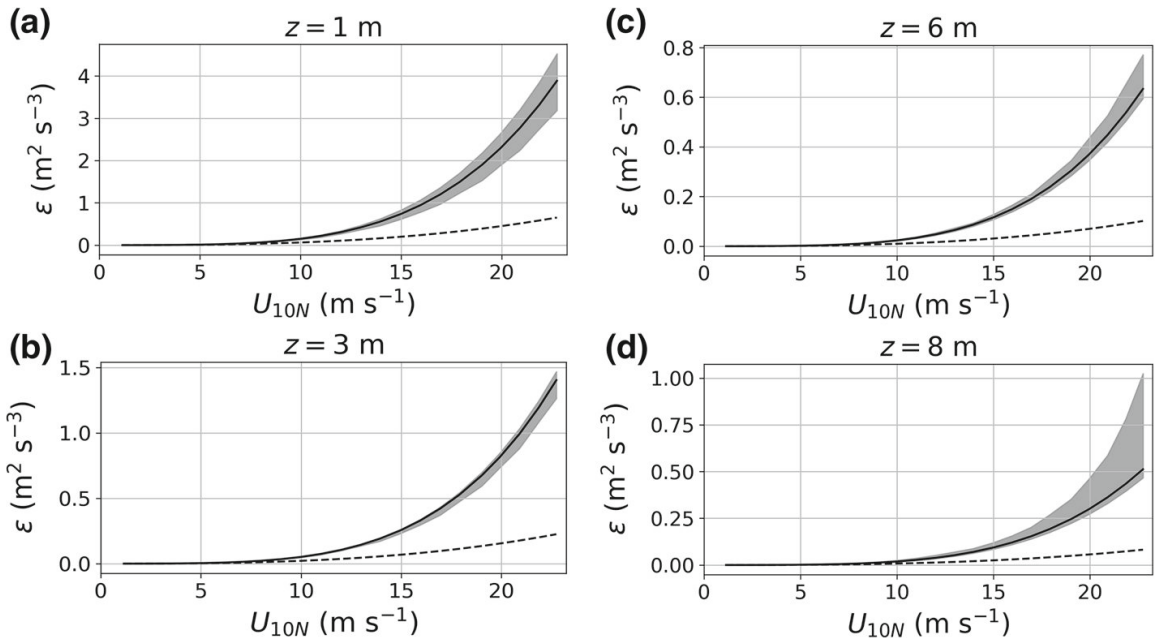

Fig. 5 TKE dissipation versus 10-m wind speed at different heights. Note the differences in vertical-axis ranges. The dashed line is the model result without accounting for the impact of waves on the SBL and the solid line is the model result with wave-induced stress. Grey shading is the range of values obtained varying eddy stretching around its neutral value of one (corresponding to $\gamma = 0$)

Wave-induced stress and eddy stretching were shown above to have a significant impact on surface momentum fluxes. Figure 5 further shows how both processes change TKE dissipation (Eq. 18) at different heights. As expected from the wind-over-waves model, TKE dissipation is enhanced when waves are included in the model (compare the dashed and the solid lines): the additional TKE production arising from wave-induced stress is locally balanced by an enhanced TKE dissipation. It is then interesting to focus on the sensitivity of TKE dissipation to variations of eddy stretching (grey shadings). The sensitivity of TKE dissipation to eddy stretching first decreases with height for heights below 5 m (compare grey shadings between Figs. 5a and b), and then increases with height above 5 m (compare grey shadings between Figs. 5c and d). This highlights two different causes of the sensitivity of TKE dissipation to changes in eddy stretching. Let us first recall that eddy stretching magnitude at a height z ($\tilde{g}_e$) depends on the slope of waves whose wavenumber k_r is such that $k_r \propto 1/z$, called "resonant waves". This follows from Eqs. 12 and 21, where the resonant waves slope is $k_r^2 S(k_r)$. Furthermore, the slope of wind-waves decreases with their wavenumber, since $S(k) \propto k^{-3}$ (in the "saturation range" of wind-waves, see, e.g. Phillips 1977, p. 148). Hence, near the surface (below 5 m), the resonant waves (which are small) are not steep, and hence $\tilde{g}_e$ is close to one. At those heights, the observed sensitivity of TKE dissipation to eddy stretching thus results from the changes in the turbulent momentum flux u_*^l (first factor in Eq. 18), caused by changes in TKE dissipation over the whole atmospheric column. As height increases, so does the slope of the resonant waves, and hence for heights above 5 m, the sensitivity of TKE to eddy stretching results from g_e being significantly different from one. Those two mechanisms show that the impact of long wind-waves on TKE dissipation can both directly and indirectly affect the whole atmospheric column.

Coming back to momentum fluxes, two effects can be invoked to explain their sensitivity to eddy stretching. First, as discussed above, stretching g_e could directly affect atmospheric turbulence through its (direct or indirect) effect on TKE dissipation ϵ (Eq. 18). Second, as the wave growth rate depends on atmospheric turbulence through u_*^l (Eq. 35 in Appendix 1), the

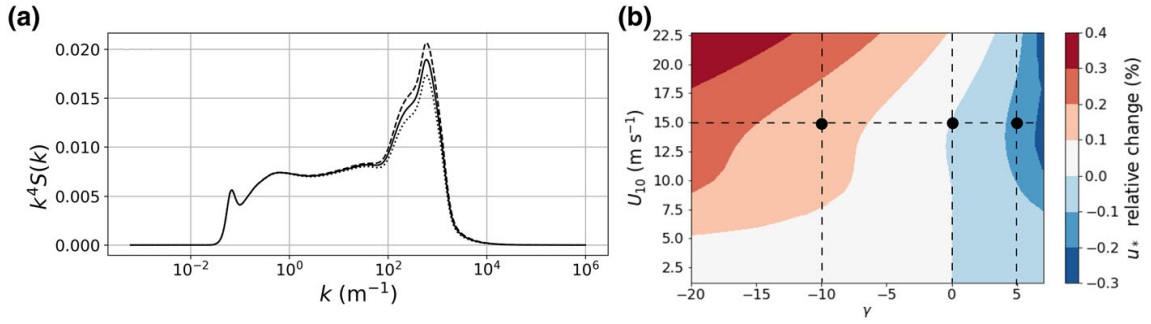

Fig. 6 **a** Modelled saturation spectrum ($k^4 S(k)$) for a 10-m wind speed of 15 m s^{-1} and an eddy stretching parameter γ of -10 (dashed line), 0 (solid line), and 5 (dotted line); **b** Relative impact on momentum fluxes of a change in the wind-wave spectrum due to eddy stretching change represented as function of the coefficient γ and 10-m wind. Black dots indicate the three values of U_{10} and γ presented in (**a**)

aforementioned modification, through a change in the wind-wave spectrum $S(k)$, could affect wave-induced stress τ^w, ultimately leading to a change in atmospheric turbulence. Figure 6a shows three examples of modelled wind-wave spectra for the same value of 10-m wind and different values of γ. It reveals that the short wind-wave spectrum on which wave-induced stress depends (i.e. k of the order of 10^3 m^{-1}) is not significantly sensitive to variations in eddy stretching. To further assess if these variations are significant, we quantified their impact on atmospheric turbulence. Runs of an uncoupled version of the wind-over-waves model were performed and compared to coupled runs. A set of wave spectra were first computed by running a coupled wind-over-waves model with no eddy stretching ($\gamma = 0$) and different values of U_{10N}. The uncoupled model was then run, meaning that the wind-wave dependent coupling variables α_c and g_e in Eq. 28 were derived from the previous coupled runs at the same wind. The resulting momentum flux was then compared to the result of a coupled run with the same values of γ and U_{10N}. Over all the ranges of U_{10N} and γ, the relative difference between the momentum fluxes obtained from the coupled and uncoupled runs is lower than 0.4 %, as shown on Fig. 6b, indicating that the variations in wind-wave spectrum due to eddy stretching do not significantly affect atmospheric turbulence. Thus, variations in eddy stretching do not significantly impact the short wind-wave spectrum, which was calibrated in Kudryavtsev et al. (2014) to fit observations (Yurovskaya et al. 2013). The short wind-wave spectrum is indeed determined by the coupling between low-level flow and short waves, occurring at heights where eddy stretching is negligible (i.e. at around 1 m).

6 Effects of Stability on the Surface Boundary Layer

As discussed in Sect. 4, Kudryavtsev et al. (2014) did not include atmospheric stratification in their wind-over-waves model. However, the atmospheric turbulence model presented in Sect. 2.1 includes atmospheric stratification effects in the TKE balance. In Katul et al. (2011) it was further compared to Monin–Obukhov similarity theory (MOST). Based on dimensional arguments, MOST represents the impact of stratification on near surface momentum fluxes by means of a universal function (called the MOST momentum function), determined from measurements. Katul et al. (2011) computed an analytical form of the MOST momentum function matching measurements. In this section we discuss how inclusion of waves into the Katul et al. (2011) framework changes the analytical MOST momentum function (Sect. 6.1), and how this compares to measurements (Sect. 6.2).

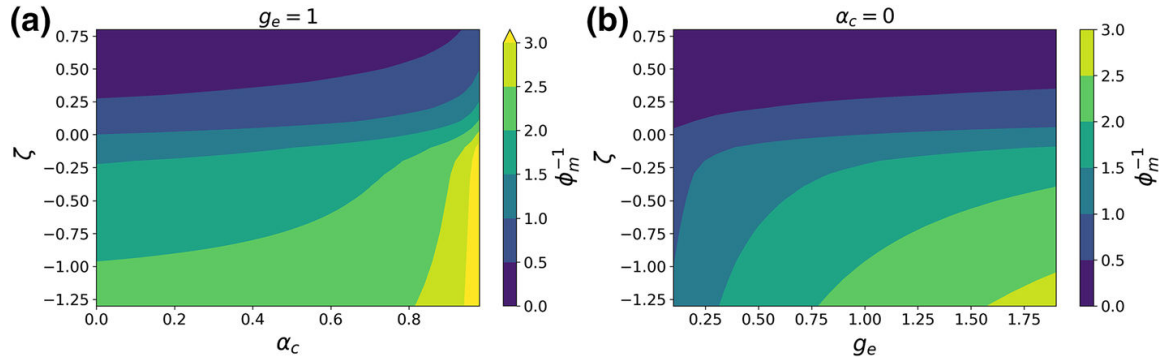

Fig. 7 Inverse universal momentum function ϕ_m^{-1} (proportional to turbulent diffusion) as a function of **a** stability and the coupling coefficient for eddy stretching set to one, **b** stability and eddy stretching for a coupling coefficient set to zero

6.1 Dependence of the Monin–Obukhov Similarity Theory Momentum Function on Wind-Waves

One of the main outcomes of the Katul et al. (2011) work was to recover the MOST universal momentum function from the TKE budget (Eq. 5) and eddy anisotropy (f_a). The authors recovered the O'KEYPS equation (Panofsky 1963; Businger 1988), which was originally derived based on heuristic and dimensional arguments to recover the empirical MOST momentum function over land (see Foken 2006), such as the Businger–Dyer function (Businger 1988, Eq. 39 in Appendix 2).

Defining the MOST momentum universal function (or dimensionless shear) as

$$\phi_m = \frac{\kappa z}{u_*^l} \frac{\partial U}{\partial z}, \tag{29}$$

Eq. 28 can be rewritten as

$$(1 - \alpha_c)^{-1} \phi_m^4 - (1 + \beta_2) \zeta \phi_m^3 = f_a^{-1} g_e^{-1}, \tag{30}$$

assuming that $(1 - \alpha_c) u_*^4 \neq 0$.

The resulting equation reveals that ϕ_m depends on the wind-wave spectrum through α_c and g_e, unlike standard MOST which assumes that the universal momentum function only depends on ζ. Furthermore, it extends the O'KEYPS equation and the results of Katul et al. (2011) who considered the case of a flat boundary (i.e. $\alpha_c = 0$ and $g_e = 1$).

Equation 30 can be solved analytically (solutions, presented in the supporting information of Katul et al. 2011, can be easily extended to the present case), yielding the MOST momentum function ϕ_m. Note that in the following, we take α_c and g_e as parameters of the model, unlike the coupled case where they are determined recursively by the wave model (Sect. 5.1). This allows exploration of all the range of stability conditions (in particular stable conditions $\zeta > 0$).

The inverse of the solution of Eq. 30 as a function of ζ, α_c, and g_e is shown in Fig. 7. The inverse of the MOST momentum function is of particular interest since ϕ_m^{-2} proportional to the turbulent diffusion coefficient (K, defined as $(u_*^l)^2 = K \partial_z U$). Note first that the expected dependence of the turbulent diffusion coefficient with atmospheric stability is observed: turbulent diffusion is higher for an unstable atmosphere ($z/L < 0$) than for a stable atmosphere ($z/L > 0$). Second, an increase in wave-induced stress (i.e. in α_c in Fig. 7a) for a fixed stability induces an increase in turbulent diffusion. This is consistent with enhanced turbulent motions due to enhanced wake production. Third, eddy stretching greater (respectively

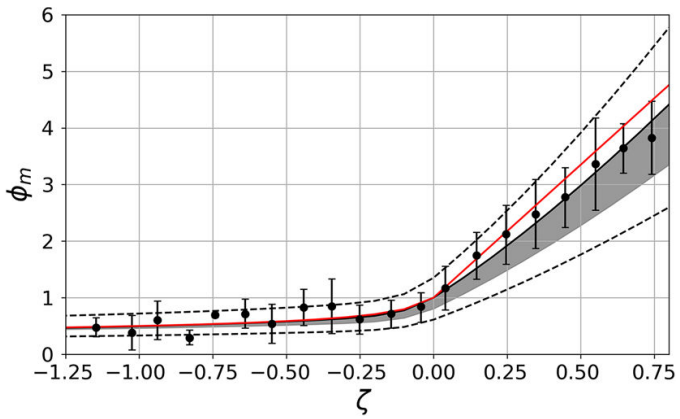

Fig. 8 Monin–Obukhov universal momentum function as a function of stability. Dots indicate bin-averaged measurements from Edson et al. (2013) and vertical error bars are the associated standard deviations. Red and black lines are the Businger–Dyer function (Businger 1988) and the present model result, respectively. Grey shading and dashed lines are the range of values obtained varying the wave coupling parameter and eddy stretching respectively

lower) than one causes an increase (respectively a decrease) in turbulent diffusion, for a given stability (Fig. 7b). Since eddy stretching larger than one implies reduced TKE dissipation, the observed increase in turbulent energy is consistent with an increase in the production term in the TKE equation, balanced by a constant energy-transfer term from wave motions and buoyancy, and a decreasing dissipation.

Figures 7a, b show how the sensitivity of atmospheric turbulence (i.e. the diffusion coefficient) to stability is modulated by wave-induced stress and eddy stretching. Figure 7a reveals that increasing wave-induced stress causes an increase in this sensitivity. This is also the case for $g_e < 1$, while eddy stretching larger than one causes a decrease in this sensitivity (Fig. 7b). The sensitivity of atmospheric turbulence to stability is an important feature since, as mentioned in the introduction, the first source of variability of turbulent momentum fluxes is atmospheric stability. These results indicate that short and long wind-waves play an important role in this variability.

6.2 Comparison to Measurements

Figure 8 shows the bin-averaged MOST momentum function as a function of stability for the measurements over open ocean from Edson et al. (2013) described in Sect. 5.2 (black dots). The measurements were performed above or close to the expected height of the WBL (of the order of 5 m) where MOST is expected to work (since wave-induced stress vanishes).

The solid black line in Fig. 8 represents the solution of Eq. 30 excluding the effect of waves (i.e. $\alpha_c = 0$ and $g_e = 1$) using the expression of eddy anisotropy f_a from Katul et al. (2011) (Eq. 40 in Appendix 2). The values of f_a are based on observed turbulent statistics over land (Kaimal et al. 1972). There is a good qualitative agreement between the model solution and the data, consistent with the measurements being at the expected height of the WBL. The Businger–Dyer function (red line) is also shown in Fig. 8 and fits similarly to the measurements, even though it differs from the Katul et al. (2011) solution in the stable case.

The scatter observed in the measurements (black error bars) contains contributions from both eddy-covariance sampling uncertainties and variations in surface wave conditions. To investigate the contribution of the second effect on the scatter, Eq. 30 was solved for different values of the coupling coefficient α_c and eddy stretching g_e.

We first varied the coupling coefficient α_c to test the importance of wave-induced stress on atmospheric turbulence (through its effect on MOST) at heights above 5 m. Even though it is usually assumed that this is not the case, airflow separation events on top of breaking waves could, for instance, extend higher in the SBL (see e.g. the numerical simulations of Suzuki et al. 2013). The range of variation of α_c (between 0 and 0.6) is inferred from the range obtained with the coupled wind-over-waves model in Sect. 5.2, and shown in Fig. 3b. It captures the range of observed short wind-wave conditions, neglecting atmospheric stratification effects. The resulting variation in modelled MOST functions (grey shading) shows that α_c might explain some scatter in the data, but the scatter is smaller than that found in observations. In particular, the data scatter in the stable case ($z/L > 0$) is not explained. Provided that waves are significant in explaining the measured scatter, this result indicates that sources of variability of ϕ_m other than short wind-wave variability should be investigated, such as eddy stretching.

Eddy stretching impacts TKE dissipation at heights above 5 m (being supported by 10-m waves, see Sect. 3.2), and can thus impact MOST momentum function (from Eq. 30). Variation of eddy stretching g_e between 0.3 and 3 (dashed lines) covers the data scatter. This variation range is consistent with the one used in Sect. 5 (and shown in Fig. 4), showing that eddy stretching, and thus long wind-wave variability, seems to be able to explain the variability of MOST momentum function. Note however that the variation range required to explain the observed scatter is smaller than the one required to explain the scatter of momentum fluxes under neutral conditions, and that this range could be even smaller if eddy covariance sampling uncertainties are deduced from the observed scatter.

Comparison of the wind-over-waves model with measurements thus shows that (i) observed stratification effects on MOST momentum function are consistent with the theoretical SBL model; (ii) Monin–Obukhov similarity theory quantities are less sensitive to the presence of wind-waves than momentum fluxes, as found in Hristov and Ruiz-Plancarte (2014) by only considering wave-induced motions within the momentum WBL.

6.3 Dimensionless Dissipation

Similarly to Fig. 5, we now investigate the sensitivity of TKE dissipation ϵ to stability. Following MOST, we define dimensionless dissipation ϕ_ϵ as

$$\phi_\epsilon = \frac{\kappa z \epsilon}{(u_*^l)^3}, \tag{31}$$

which can be computed from Eqs. 28 and 29 as

$$\phi_\epsilon = \phi_m - (1 + \beta_2)\zeta. \tag{32}$$

The solid black line in Fig. 9 is the dimensionless dissipation computed with ϕ_m from Eqs. 30, excluding the effect of waves (i.e. $\alpha_c = 0$ and $g_e = 1$). As expected, there is a good agreement between this value and the Businger–Dyer function (red line). Values of g_e larger (resp. smaller) than one cause a decrease (resp. an increase) in ϕ_ϵ, consistent with Eq. 18 (dashed lines, which correspond to $g_e = 0.3$ and 3 respectively). Finally, as also shown in Fig. 5 for neutral conditions, an increase of wave-induced stress causes an increase of TKE dissipation (grey shading), consistent with the additional production term in the TKE balance equation. Overall, waves have a significant impact on the dimensionless TKE dissipation, consistent with previous studies (e.g. Cifuentes-Lorenzen et al. 2018).

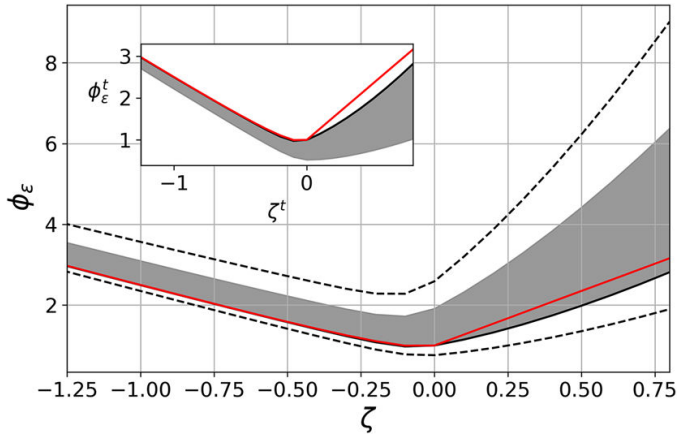

Fig. 9 Dimensionless TKE dissipation as a function of stability. Red line is the Businger–Dyer function (Businger 1988) and black line is the model result. Grey shading and dashed lines are the range of values obtained varying the wave coupling parameter or eddy stretching respectively. The inset shows the same quantities, but for a different choice of normalization velocity

In deriving the dimensionless equations (30) and (32), u_*^l has been chosen as the normalizing velocity in the definition of ϕ_m, ϕ_ϵ, and ζ. This choice is physically sound, since in this case ϕ_m^{-2} is proportional to the turbulent diffusion. In measurements, however, it is difficult to disentangle wave-induced stresses from turbulent stresses (see e.g. Hristov et al. 2003), and the only measurable quantity could then be u_*, the total momentum flux. Hence, we must discuss the differences between choosing u_* instead of u_*^l as a normalizing velocity in MOST, i.e. by considering the following alternative forms of the universal momentum function, dimensionless dissipation, and stability parameter

$$\phi_m^t = \frac{\kappa z}{u_*}\frac{\partial U}{\partial z}, \quad \phi_\epsilon^t = \frac{\kappa z \epsilon}{u_*^3}, \quad \zeta^t = \frac{\kappa z g H}{\rho C_p \theta_h u_*^3}. \tag{33}$$

First, there is no qualitative difference in the behaviour of ϕ_m^t with respect to ϕ_m (not shown). However, the behaviour of ϕ_ϵ^t, is qualitatively different from ϕ_ϵ. As shown in the inset of Fig. 9, an increase in wave-induced stress now causes a decrease in dimensionless dissipation (the grey shading is below the solid black line in the inset), inconsistent with the conclusions drawn earlier (in the main figure, the grey shading as above the black curve). This shows that MOST is sensitive to the choice of the normalization in the presence of waves. This could have important implications for the interpretation of measurements.

7 Conclusion

We investigated the role of wind-waves and atmospheric stratification on atmospheric turbulence and momentum fluxes. The geometry of the ocean surface, resulting from the superposition of (periodic) surface wind-waves, is assumed to change the shape of energy-containing turbulent structures (conceptually viewed as attached eddies). Extending a wall-bounded turbulence model proposed by Katul et al. (2011) allowed to model the impact of this deformation on TKE dissipation, for a surface whose height follows a wind-wave spectrum.

It was further argued that for an attached eddy of a given horizontal length scale, most of the deformation of its shape is due to surface waves with a similar horizontal extension. This was based on the assumption that the eddy deformation is caused by the surface wave periodically modulating the surface roughness induced by shorter waves, on a length scale resonant with that of the attached eddy. The overall result is a modification of TKE dissipation by long wind-waves (of the order of 10 m), at heights above 5 m, where the impact of wind-waves on atmospheric turbulence has been observed but was unexplained by wind-over-waves models.

The impact of the new mechanism on surface momentum fluxes was quantified by its inclusion in a wind-over-waves model (Kudryavtsev et al. 2014), which predicts a wind-and-waves equilibrium by coupling a TKE budget to a wind-wave energy budget. The wind-and-waves equilibrium, normally defined solely by 10-m wind speed and atmospheric stability, is now also dependent on a single parameter linked to the long wind-wave spectrum and to the intensity of the modulation of short wind-wave roughness by long wind-waves (i.e. related to the deformation of attached eddies by wind-waves). The variability observed over open ocean for both momentum flux (for a given 10-m wind speed) and MOST momentum function (for a given stability), was explained by variation of this parameter. If existent, the distortion of atmospheric eddies by the geometry of 10-m wind-waves is thus an important process in the determination of surface momentum fluxes. This analysis also revealed that the sensitivity of MOST momentum functions to stability is impacted by the presence of both short and long wind-waves. Both processes should be included in momentum flux parametrizations.

Wind-waves longer than 10 m were found to modify TKE dissipation at a height too high to impact surface momentum fluxes. However, if the assumptions of stationarity and horizontal homogeneity were relaxed (i.e. the SBL is no longer a constant-stress layer, which can occur, e.g., when the boundary-layer height decreases significantly), their impact on TKE could significantly affect momentum fluxes in the whole surface layer. This process could then play an important role in the coupling of wind-waves with large scale atmospheric structures.

This theoretical work is based on the idea that surface waves are able to distort atmospheric eddies. However it does not rely on experimental evidence, and the expression of the distortion includes a free parameter. Katul and Manes (2014) linked the shape of the attached eddies to properties of the vertical turbulent velocity spectra. This link could be further investigated within open-ocean measurements in order to test the present theory. The proposed framework thus opens new paths for numerical and experimental investigations of turbulence on top a realistic sea surface. Those would require the joint analysis of atmospheric vertical velocity and sea surface elevation/slope signals to infer the expected changes in turbulence spectral properties.

More generally, our study is a step towards a more precise description of multi-scale interactions within the WBL, linking the shape of large atmospheric structures with macroscopic properties of the surface wave field. By showing the importance of atmospheric eddy distortions for air–sea fluxes, we emphasize that this description is essential in order to advance our understanding of the wind-and-waves coupled system and to improve air–sea flux parametrizations.

Acknowledgements The code used to generate the figures is available upon request to the corresponding author. The authors thank the anonymous reviewers for the comments that helped improve the original manuscript. The authors wish to acknowledge V.N. Kudryavtsev for sharing the code and for the insightful help, and M.N. Bouin and S. Brumer for interesting discussions. AA was supported by DGA Grant No. D0456JE075 and French Brittany Regional Council. Finally, the authors also wish to acknowledge the support from ANR Caravele.

Appendix 1: Coupling Between Short Wind-Waves and Atmospheric Turbulence

Details are provided on the coupling between short wind-waves and atmospheric turbulence, following the wind-over-waves model presented in Kudryavtsev et al. (2014) and references therein. The short wind-wave model is first described, and expressions for wave-induced stress are then presented.

Waves are described by their wavenumber k, frequency ω, phase speed c, and direction of propagation ψ, and follow the dispersion relation $\omega^2 = gk + T_{sw}k^3$ where T_{sw} is the dynamical surface water tension. The wave field is specified by means of the directional spectrum $S^d(k, \psi)$. We also introduce the saturation spectrum $B(k, \psi) = k^4 S^d(k, \psi)$, which will be used in the following.

As proposed by Kudryavtsev et al. (2014), the full wave spectrum can be defined as a composition of a short-wave spectrum B_{sw} and a long-wave spectrum B_{lw} (in this study, the fetch-dependent spectrum of Donelan et al. 1985, is used). The weighted sum between B_{lw} and B_{sw} represents a wind-driven sea spectrum, without the presence of non-local waves (swell). It is in a one-to-one relation with the local atmospheric state. The short-wave spectrum is coupled to atmospheric turbulence through form drag, and further affects the momentum WBL through airflow separation stresses. The long-wave part is prescribed given some parameters (here spatial fetch).

The short-wave component B_{sw} describes both gravity waves and parasitic capillary waves. The latter are generated on the forward face of shorter gravity waves (in the wavelength range 0.03–0.3 m), as they approach their maximum steepness, which, for longer gravity waves, would lead to breaking (Longuet-Higgins 1963).

The gravity short wind-wave spectrum results from a balance between wind forcing (β), non-linear energy losses due to wave breaking (or generation of parasitic capillary waves for shorter waves), and generation of short waves by large breakers (or of parasitic capillary waves by steep and shorter waves, Q_b). The balance equation reads

$$\beta_v(k, \psi)B(k, \psi) - B(k, \psi)\left(\frac{B(k, \psi)}{a}\right)^{n_g} + Q_b(k, \psi) = 0, \tag{34}$$

with $\beta_v(k, \psi) = \beta(k, \psi) - 4\nu k^2/\omega$ the effective growth rate (with ν air viscosity), and $a = 2.2 \times 10^{-3}$ and $n_g = 10$ two tuning constants fitted to observations (from Yurovskaya et al. 2013). Expression for the source term Q_b can be found in Appendix A of Kudryavtsev et al. (2014).

The short parasitic capillary waves, corresponding to waves of wavelengths of 3×10^{-4} m or less, follow the balance Eq. 34 without the wind input term, and with modified constants a and n_g. For this range of waves for which wave breaking does not occur, the non-linear term is associated to a non-linear saturation of the wave spectrum.

Both equations are solved by iterations, given a wind forcing resulting from the WBL model (Eq. 28), and expressed as

$$\beta(k, \psi) = \begin{cases} c_\beta \left\{\dfrac{u_*^l[h(k)]}{c}\right\}^2 \cos\psi|\cos\psi| & \text{for } U[h(k)] > c \\ 0 & \text{for } U[h(k)] < c \end{cases} \tag{35}$$

where $c_\beta = 3 \times 10^{-2}$ is Plant's constant and $h(k) = 0.1\,k^{-1}$ is the inner region height. Note that since wind input depends on the ratio between friction velocity and wave phase speed, it is supported mostly by slow (and short) waves (Plant 1982).

To solve Eq. 28, the wave-induced stress must be specified. Let $\tilde{T}$ and $\tilde{T}_a$ be the intensity of form drag and airflow separation induced by a wave component of wavenumber k. Both these effects act over a shallow atmospheric layer, up to heights $h(k) \sim 0.1k^{-1}$ and $h_a(k) \sim 0.3k^{-1}$, respectively (Kudryavtsev et al. 2014). We further assume, for simplicity, that form drag (respectively airflow separation) is constant up to h (resp. h_a) and cancels for $z > h$ (resp. $z > h_a$). This yields the following expression for the total wave-induced stress

$$(u_*^w)^2(z) = \int \tilde{T}(k)\mathrm{He}[h(k) - z]\mathrm{d}k + \int \tilde{T}_a(k)\mathrm{He}[h_a(k) - z]\mathrm{d}k \tag{36}$$

where $\mathrm{He}(x)$ is the Heaviside step function ($\mathrm{He}(x) = 1$ for $x > 0$ and 0 otherwise). This expression couples the short wind-wave model (Eq. 34) to the SBL model (Eq. 28).

Form drag describes the impact of the wind-to-waves energy transfer on atmospheric turbulence, and is expressed as

$$\tilde{T}(k) = \begin{cases} \frac{c_\beta}{k}\frac{\rho_w}{\rho_a}\{u_*^l[h(k)]\}^2 \int B(k,\psi)\,(\cos\psi)^3\,\mathrm{d}\psi & \text{for } U[h(k)] > c \\ 0 & \text{for } U[h(k)] < c \end{cases}, \tag{37}$$

where ρ_w and ρ_a are the density of water and air respectively.

Waves of wavelength greater than 0.3 m generate an additional stress due to airflow separation on top of breaking waves (Reul et al. 1999). The expression for airflow separation stress for a given wavenumber depends on wave-breaking statistics. However, following Phillips (1985), wave-breaking statistics can be related to wave energy dissipation (the second term from the left in Eq. 34). For waves in the equilibrium range, on top of which most of airflow separation events occur, the spectral balance (Eq. 34) is further assumed to be reduced only to a balance between wind input and dissipation. This results in the following expression for airflow separation for $U[h_a(k)] > c$

$$T_a(k) = \frac{2c_{db}c_\beta}{a}h_a(k)kf_g(k)\left(\frac{U[h_a(k)]}{c} - 1\right)^2 \int B(k,\psi)(\cos\psi)^5\,\mathrm{d}\psi \tag{38}$$

where $f_g(k)$ is a cut-off function restricting airflow separation in the equilibrium range, and c_{db} is the local roughness on top of breaking crests, which has a mean value of 0.35 (see Kudryavtsev and Makin 2001). For $U[h_a(k)] < c$, airflow separation is assumed to vanish (i.e. $T_a = 0$) which limits airflow separation to slow (short) waves (similar to form drag).

Appendix 2: Expressions for the Eddy Anisotropy and the Businger–Dyer Momentum Function

The Businger–Dyer universal momentum function (Businger 1988), derived from the Kansas measurements, reads

$$\phi_m^B(\zeta) = \begin{cases} 1 + 4.7\zeta & \text{for } \zeta > 0 \\ (1 - 15\zeta)^{-1/4} & \text{for } \zeta < 0 \end{cases}. \tag{39}$$

This empirical function was recovered by Katul et al. (2011), by considering an eddy anisotropy of the form

$$f_a(\zeta) = \begin{cases} \left(1 - \frac{0.38}{0.55}[1 - \exp(15\zeta)]\right)^{-1} & \text{for } \zeta \le 0 \\ \left(1 + \frac{1}{0.55}\zeta\right)^{-6} & \text{for } \zeta > 0 \end{cases}. \tag{40}$$

This expression was obtained from measurements of turbulent vertical velocity spectra (from Kaimal et al. 1972).

References

Belcher S, Hunt J (1993) Turbulent shear flow over slowly moving waves. J Fluid Mech 251:109–148. https://doi.org/10.1017/S0022112093003350

Belcher S, Hunt J (1998) Turbulent flow over hills and waves. Annu Rev Fluid Mech 30(1):507–538. https://doi.org/10.1146/annurev.fluid.30.1.507

Brown GS (1979) Estimation of surface wind speeds using satellite-borne radar measurements at normal incidence. J Geophys Res Sol Earth 84(B8):3974–3978. https://doi.org/10.1029/JB084iB08p03974

Businger J (1988) A note on the businger-dyer profiles. Boundary-Layer Meteorol 42(1–2):145–151. https://doi.org/10.1007/BF00119880

Cifuentes-Lorenzen A, Edson JB, Zappa CJ (2018) Air-sea interaction in the southern ocean: exploring the height of the wave boundary layer at the air–sea interface. Boundary-Layer Meteorol 169(3):461–482. https://doi.org/10.1007/s10546-018-0376-0

Donelan MA, Hamilton J, Hui W (1985) Directional spectra of wind-generated ocean waves. Philos Trans R Soc A 315(1534):509–562. https://doi.org/10.1098/rsta.1985.0054

Dorman GE, Mollo-Christensen E (1973) Observation of the structure on moving gust patterns over a water surface ("cat's paws"). J Phys Oceanogr 3(1):120–132. https://doi.org/10.1175/1520-0485(1973)003<0120:OOTSOM>2.0.CO;2

Drennan WM, Graber HC, Donelan MA (1999) Evidence for the effects of swell and unsteady winds on marine wind stress. J Phys Oceanogr 29(8):1853–1864. https://doi.org/10.1175/1520-0485(1999)029<1853:EFTEOS>2.0.CO;2

Dulov V, Kudryavtsev V, Bol'Shakov A (2013) A field study of whitecap coverage and its modulations by energy containing surface waves. In: Donelan MA, Drennan WM, Saltzman ES, Wanninkhof R (eds) Gas transfer at water surfaces. American Geophysical Union, Washington, DC, pp 187–192. https://doi.org/10.1029/gm127p0187

Edson JB, Zappa CJ, Ware J, McGillis WR, Hare JE (2004) Scalar flux profile relationships over the open ocean. J Geophys Res Oceans. https://doi.org/10.1029/2003JC001960

Edson J, Crawford T, Crescenti J, Farrar T, Frew N, Gerbi G, Helmis C, Hristov T, Khelif D, Jessup A, Jonsson H, Li M, Mahrt L, McGillis W, Plueddemann A, Shen L, Skyllingstad E, Stanton T, Sullivan P, Sun J, Trowbridge J, Vickers D, Wang S, Wang Q, Weller R, Wilkin J, Williams AJ, Yue DKP, Zappa C (2007) The coupled boundary layers and air-sea transfer experiment in low winds. Bull Am Meteorol Soc 88(3):341–356. https://doi.org/10.1175/BAMS-88-3-341

Edson JB, Jampana V, Weller RA, Bigorre SP, Plueddemann AJ, Fairall CW, Miller SD, Mahrt L, Vickers D, Hersbach H (2013) On the exchange of momentum over the open ocean. J Phys Oceanogr 43(8):1589–1610. https://doi.org/10.1175/JPO-D-12-0173.1

Elfouhaily T, Chapron B, Katsaros K, Vandemark D (1997) A unified directional spectrum for long and short wind-driven waves. J Geophys Res Oceans 102(C7):15,781–15,796. https://doi.org/10.1029/97JC00467

Elperin T, Kleeorin N, Rogachevskii I, Zilitinkevich S (2002) Formation of large-scale semiorganized structures in turbulent convection. Phys Rev E 66(6):66,305–66,320. https://doi.org/10.1103/PhysRevE.66.066305

Fairall C, Bradley EF, Hare J, Grachev A, Edson J (2003) Bulk parameterization of air–sea fluxes: updates and verification for the coare algorithm. J Clim 16(4):571–591. https://doi.org/10.1175/1520-0442(2003)016<0571:BPOASF>2.0.CO;2

Foken T (2006) 50 years of the Monin–Obukhov similarity theory. Boundary-Layer Meteorol 119(3):431–447. https://doi.org/10.1007/s10546-006-9048-6

Geernaert G (1990) Bulk parameterizations for the wind stress and heat fluxes. In: Geernaert GL, Plant WL (eds) Surface waves and fluxes. Springer, pp 91–172. https://doi.org/10.1007/978-94-009-2069-9_5

Gent P, Taylor P (1976) A numerical model of the air flow above water waves. J Fluid Mech 77(1):105–128. https://doi.org/10.1017/S0022112076001158

Gioia G, Guttenberg N, Goldenfeld N, Chakraborty P (2010) Spectral theory of the turbulent mean-velocity profile. Phys Rev Lett 105(18):184,501. https://doi.org/10.1103/PhysRevLett.105.184501

Grodsky SA, Kudryavtsev VN, Bentamy A, Carton JA, Chapron B (2012) Does direct impact of SST on short wind waves matter for scatterometry? Geophys Res Lett 39:L12602. https://doi.org/10.1029/2012gl052091

Hara T, Belcher SE (2002) Wind forcing in the equilibrium range of wind–wave spectra. J Fluid Mech 470:223–245. https://doi.org/10.1017/S0022112002001945

Hara T, Sullivan PP (2015) Wave boundary layer turbulence over surface waves in a strongly forced condition. J Phys Oceanogr 45(3):868–883

Hogstrom ULF (1996) Review of some basic characteristics of the atmospheric surface layer. Boundary-Layer Meteorol 78(2):215–246. https://doi.org/10.1007/BF00120937

Hristov T (2018) Mechanistic, empirical and numerical perspectives on wind-waves interaction. In: Procedia IUTAM, vol 26. Elsevier B.V., pp 102–111. https://doi.org/10.1016/j.piutam.2018.03.010
Hristov T, Ruiz-Plancarte J (2014) Dynamic balances in a wavy boundary layer. J Phys Oceanogr 44(12):3185–3194. https://doi.org/10.1175/JPO-D-13-0209.1
Hristov T, Friehe C, Miller S (1998) Wave-coherent fields in air flow over ocean waves: identification of cooperative behavior buried in turbulence. Phys Rev Lett 81(23):5245. https://doi.org/10.1103/PhysRevLett.81.5245
Hristov T, Miller S, Friehe C (2003) Dynamical coupling of wind and ocean waves through wave-induced air flow. Nature 422(6927):55. https://doi.org/10.1038/nature01382
Husain N, Hara T, Buckley M, Yousefi K, Veron F, Sullivan P (2019) Boundary layer turbulence over surface waves in a strongly forced condition: LES and observation. J Phys Oceanogr. https://doi.org/10.1175/JPO-D-19-0070.1
Janssen PA (1999) On the effect of ocean waves on the kinetic energy balance and consequences for the inertial dissipation technique. J Phys Oceanogr 29(3):530–534. https://doi.org/10.1175/1520-0485(1999)029<0530:OTEOOW>2.0.CO;2
Janssen PA, Viterbo P (1996) Ocean waves and the atmospheric climate. J Clim 9(6):1269–1287. https://doi.org/10.1175/1520-0442(1996)009<1269:OWATAC>2.0.CO;2
Janssen PaEM (1989) Wave-induced stress and the drag of air flow over sea waves. J Phys Oceanogr 19(6):745–754. https://doi.org/10.1175/1520-0485(1989)019<0745:WISATD>2.0.CO;2
Kaimal JC, Wyngaard J, Izumi Y, Coté O (1972) Spectral characteristics of surface-layer turbulence. Q J R Meteorol Soc 98(417):563–589. https://doi.org/10.1002/qj.49709841707
Katul GG, Manes C (2014) Cospectral budget of turbulence explains the bulk properties of smooth pipe flow. Phys Rev E 90(6):063,008. https://doi.org/10.1103/PhysRevE.90.063008
Katul GG, Konings AG, Porporato A (2011) Mean velocity profile in a sheared and thermally stratified atmospheric boundary layer. Phys Rev Lett 107(26):268,502. https://doi.org/10.1103/PhysRevLett.107.268502
Kawamura H, Toba Y (1988) Ordered motion in the turbulent boundary layer over wind waves. J Fluid Mech 197:105–138. https://doi.org/10.1017/S0022112088003192
Kitaigorodskii S (1973) Physics of air–sea interactions. Israël Program for scientific translations
Kudryavtsev V, Chapron B (2016) On growth rate of wind waves: impact of short-scale breaking modulations. J Phys Oceanogr 46(1):349–360. https://doi.org/10.1175/JPO-D-14-0216.1
Kudryavtsev V, Makin V (2001) The impact of air-flow separation on the drag of the sea surface. Boundary-Layer Meteorol 98(1):155–171. https://doi.org/10.1023/A:1018719917275
Kudryavtsev VN, Makin VK (2004) Impact of swell on the marine atmospheric boundary layer. J Phys Oceanogr 34(4):934–949. https://doi.org/10.1175/1520-0485(2004)034<0934:IOSOTM>2.0.CO;2
Kudryavtsev V, Myasoedov A, Chapron B, Johannessen JA, Collard F (2012) Imaging mesoscale upper ocean dynamics using synthetic aperture radar and optical data. J Geophys Res Oceans. https://doi.org/10.1029/2011jc007492
Kudryavtsev V, Chapron B, Makin V (2014) Impact of wind waves on the air–sea fluxes: a coupled model. J Geophys Res Oceans 46(2):1022–1037. https://doi.org/10.1002/2013JC009412
Li D, Katul GG, Bou-Zeid E (2012) Mean velocity and temperature profiles in a sheared diabatic turbulent boundary layer. Phys Fluids 24(10):105,105. https://doi.org/10.1063/1.4757660
Li Q, Gentine P, Mellado JP, McColl KA (2018) Implications of nonlocal transport and conditionally averaged statistics on Monin–Obukhov similarity theory and townsend's attached eddy hypothesis. J Atmos Sci 75(10):3403–3431. https://doi.org/10.1175/JAS-D-17-0301.1
Liu WT, Tang W (1996) Equivalent neutral wind. Jet Propulsion Laboratory, Technical Report
Longuet-Higgins MS (1963) The generation of capillary waves by steep gravity waves. J Fluid Mech 16(1):138–159. https://doi.org/10.1017/S0022112063000641
Mahrt L, Vickers D, Howell J, Højstrup J, Wilczak JM, Edson J, Hare J (1996) Sea surface drag coefficients in the risø air sea experiment. J Geophys Res Oceans 101(C6):14,327–14,335. https://doi.org/10.1029/96JC00748
Makin V, Kudryavtsev V (1999) Coupled sea surface-atmosphere model: 1. Wind over waves coupling. J Geophys Res Oceans 104(C4):7613–7623. https://doi.org/10.1029/1999JC900006
Makin VK, Mastenbroek C (1996) Impact of waves on air–sea exchange of sensible heat and momentum. Boundary-Layer Meteorol 79(3):279–300. https://doi.org/10.1007/BF00119442
Marshall J, Ferrari R, Forget G, Maze G, Andersson A, Bates N, Dewar W, Doney S, Fratantoni D, Joyce T et al (2009) The climode field campaign: observing the cycle of convection and restratification over the gulf stream. Bull Am Meteorl Soc 90(9):1337–1350. https://doi.org/10.1175/2009BAMS2706.1
Marusic I, Monty JP (2019) Attached eddy model of wall turbulence. Annu Rev Fluid Mech 51:49–74. https://doi.org/10.1146/annurev-fluid-010518-040427

Monin A, Yaglom A (1975) Statistical fluid mechanics. Translated from original Russian 1967 version. MIT press, Cambridge, MA

Panofsky HA (1963) Determination of stress from wind and temperature measurements. Q J R Meteorol Soc 89(379):85–94. https://doi.org/10.1002/qj.49708937906

Phillips OM (1977) The dynamics of the upper ocean. Cambridge University Press, Cambridge

Phillips OM (1985) Spectral and statistical properties of the equilibrium range in wind-generated gravity waves. J Fluid Mech 156:505–531. https://doi.org/10.1017/S0022112085002221

Phillips W, Wu Z, Lumley J (1996) On the formation of longitudinal vortices in a turbulent boundary layer over wavy terrain. J Fluid Mech 326:321–341. https://doi.org/10.1017/S0022112096008336

Pineau-Guillou L, Ardhuin F, Bouin MN, Redelsperger JL, Chapron B, Bidlot JR, Quilfen Y (2018) Strong winds in a coupled wave-atmosphere model during a north atlantic storm event: evaluation against observations. Q J R Meteorol Soc 144(711):317–332. https://doi.org/10.1002/qj.3205

Plant WJ (1982) A relationship between wind stress and wave slope. J Geophys Res Oceans 87(C3):1961–1967. https://doi.org/10.1029/JC087iC03p01961

Reul N, Branger H, Giovanangeli JP (1999) Air flow separation over unsteady breaking waves. Phys Fluids 11(7):1959–1961. https://doi.org/10.1063/1.870058

Shimura T, Mori N, Takemi T, Mizuta R (2017) Long-term impacts of ocean wave-dependent roughness on global climate systems. J Geophys Res Oceans 122(3):1995–2011. https://doi.org/10.1002/2016jc012621

Soloviev YP, Kudryavtsev V (2010) Wind-speed undulations over swell: field experiment and interpretation. Boundary-Layer Meteorol 136(3):341–363. https://doi.org/10.1007/s10546-010-9506-z

Suzuki N, Hara T, Sullivan PP (2013) Impact of breaking wave form drag on near-surface turbulence and drag coefficient over young seas at high winds. J Phys Oceanogr 43(2):324–343. https://doi.org/10.1175/jpo-d-12-0127.1

Townsend AA (1980) The structure of turbulent shear flow. Cambridge University Press, Cambridge

Vandemark D, Edson JB, Chapron B (1997) Altimeter estimation of sea surface wind stress for light to moderate winds. J Atmos Ocean Technol 14(3):716–722. https://doi.org/10.1175/1520-0426(1997)014<0716:AEOSSW>2.0.CO;2

Villas Boas AB, Ardhuin F, Ayet A, Bourassa MA, Chapron B, Brandt P, Cornuelle BD, Farrar JT, Fewings MR, Fox-Kemper B et al (2019) Integrated observations of global surface winds, currents, and waves: requirements and challenges for the next decade. Front Mar Sci 6:425. https://doi.org/10.3389/fmars.2019.00425

Yurovskaya M, Dulov V, Chapron B, Kudryavtsev V (2013) Directional short wind wave spectra derived from the sea surface photography. J Geophys Res Oceans 118(9):4380–4394. https://doi.org/10.1002/jgrc.20296

Zhang FW, Drennan WM, Haus BK, Graber HC (2009) On wind-wave-current interactions during the shoaling waves experiment. J Geophys Res Oceans 114(C1):2. https://doi.org/10.1029/2008JC004998

Zilitinkevich S, Elperin T, Kleeorin N, Rogachevskii I, Esau I, Mauritsen T, Miles M (2008) Turbulence energetics in stably stratified geophysical flows: strong and weak mixing regimes. Q J R Meteorol Soc 134(633):793–799. https://doi.org/10.1002/qj.264

3.3 CONCLUSION

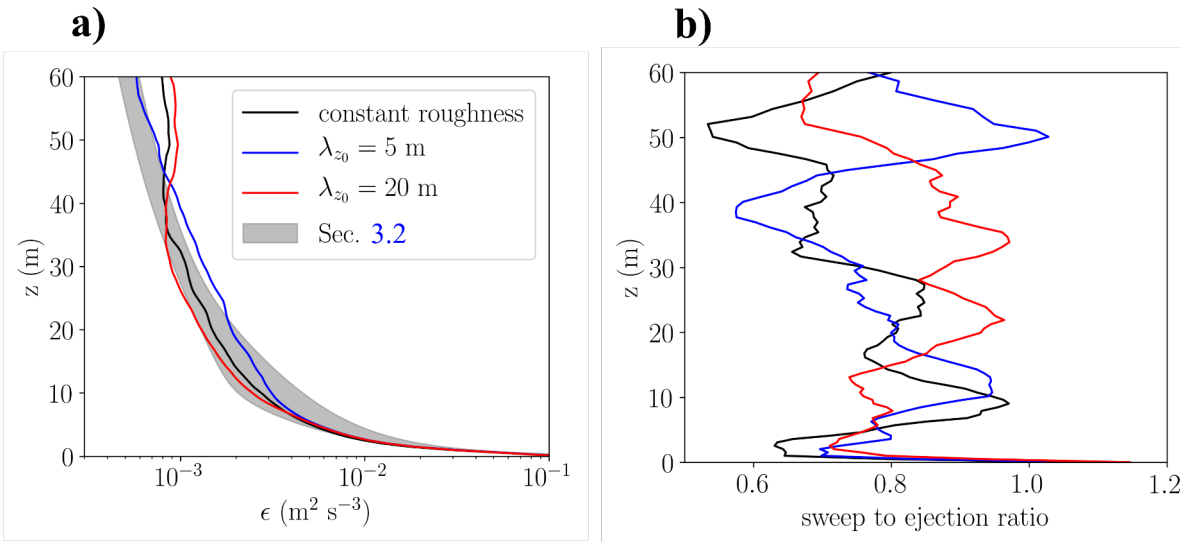

Figure 3.1: Preliminary results from an LES over periodic roughness patterns in the streamwise direction (blue and red lines), and from a reference LES with constant roughness (black lines), for $u_* \sim 0.22$ m s^{-1}. (a) TKE dissipation as a function of height, with grey shading indicating the range of values obtained from the coupled model of Sec. 3.2. (b) Ratio between the contributions of sweeps (Q4) and ejection (Q2) events to the vertical momentum flux $\overline{u'w'}$ (computed using conditional averages).

In this Chapter we have proposed a relation between the geometry of long wind-waves and TKE dissipation in the WBL. A candidate mechanism for this relation is the modulation of short wind-waves by long wind-waves, which results in the emergence of patterns in the sea-surface roughness field, whose characteristic scale can leave an imprint on the scale of the overlying energy-containing eddies. More precisely, the imprint changes the "anisotropy factor" of energy-containing eddies, an effect similar to that of buoyancy (see page 40 of Chapter 1).

The resulting modification in TKE dissipation could not be estimated from the theory, and would require e.g. Large Eddy Simulations (LES) over periodic roughness patterns in order to be quantified. In Fig. 3.1 we show some preliminary spatially-averaged statistics of such an LES, where we imposed a roughness length z_0 varying periodically in the streamwise direction around an averaged Charnock value by ±75% (see Annex C for details on the simulation). [1] The variations had a wavelength λ_{z_0} of 5m and 10m (blue and red lines respectively). Figure 3.1a shows the averaged TKE dissipation, computed from the LES subgrid model. Differences between the various cases (solid lines) seem to be similar to the spread investigated with the theoretical model (grey shading), even though no clear trend is observed with respect to variations of λ_{z_0}. The same holds for a measure of the instantaneous properties of turbulence, the sweep to ejection ratio (Fig. 3.1b), for which no clear trend is observed. The sweep to

[1] The variations of ±75% are an upper bound for the modulation of short wind-waves by long wind-waves [Gent and Taylor, 1976].

ejection ratio is the ratio between the contribution of sweeps and that of ejections to the vertical momentum flux, which is e.g. close to two in the roughness sublayer of canopies, where sweeps dominate with respect to ejections (see the discussion page 33).

These results are preliminary and, in particular, are sensitive to the choice of the spatial averaging box. This indicates the need for more simulations to test the convergence of the averaging procedure and to understand its effects on the resulting statistics. Other statistics also need to be explored, e.g. statistics conditional to the relative phase with respect to the roughness patterns. Finally, this simulation aims at isolating the effect of roughness variations on the overlying flow, i.e. without considering the geometrical effect of the surface-height variations induced by long wind-waves. The latter could be important in the process described in Sec. 3.2, requiring the need for more sophisticated LES, over a wavy boundary [e.g. Husain et al., 2019]. Overall, these results again show the difficulty of extracting signatures of wind-wave interactions from the wind field [Soloviev and Kudryavtsev, 2010, Hristov, 2018, Villas Boas et al., 2019].

Close to the surface (below a height of 1 m), it is fair to state that the interaction between energy-containing eddies and wind-waves should follow different rules. Indeed, for the scale of waves that should be considered at those heights, wave-breaking is much more frequent and intense. Hence the geometrical elements interacting with energy-containing eddies are intermittent, both in space and time. This is explored in the next Chapter.

CHAPTER 4

DYNAMICAL IMPACT OF WIND-WAVES ON ENERGY-CONTAINING EDDIES

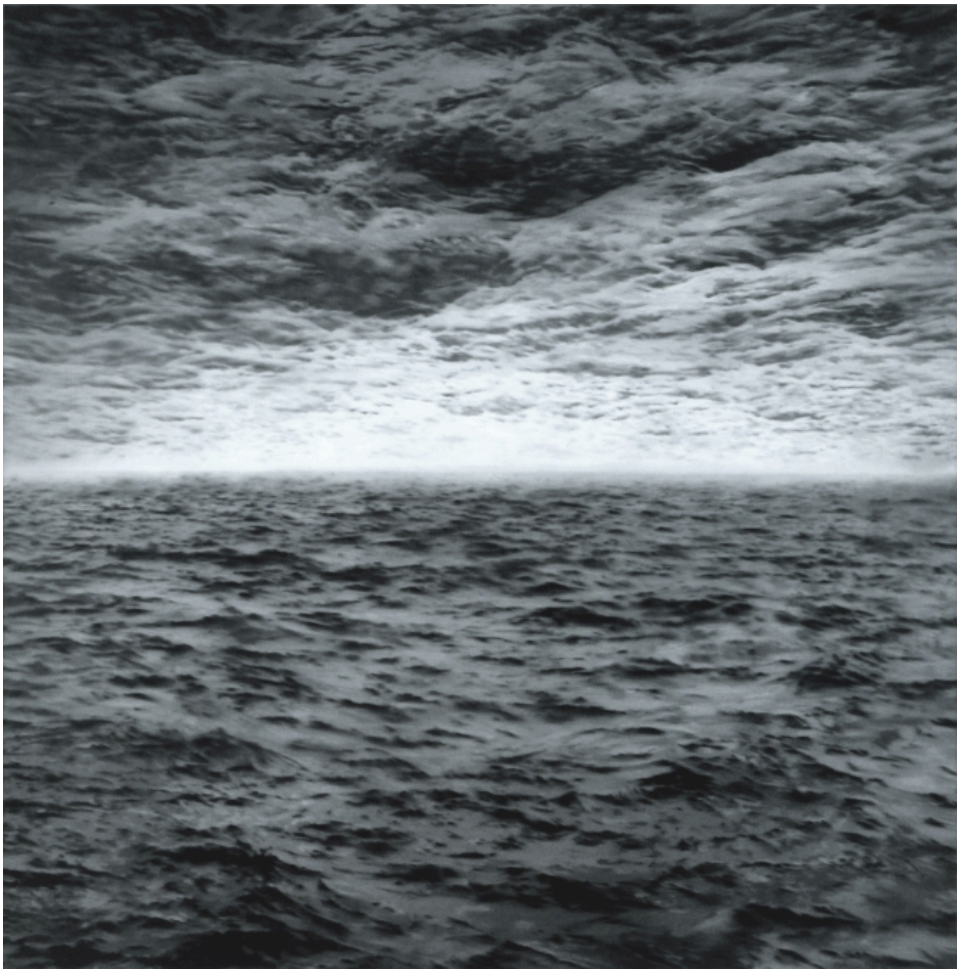

" Seestück (See-See)"/"Seascape (Sea-Sea)", Gerhard Richter (1970)
Nationalgalerie, Staatliche Museen zu Berlin, Berlin, Germany © 2020 Gerhard Richter

4.1 INTRODUCTION

In the previous Chapter, we have discussed how the geometry of energy-containing eddies can be modified by long wind-waves, at heights above 1 m. This involved an interaction between waves and eddies of similar horizontal extension, proportional to the height z. However, as the surface gets closer, the waves that could possibly interact with energy-containing eddies are steeper and more prone to breaking. At these heights, the geometrical elements affecting energy-containing eddies are hence closer to being organized in intense and intermittent patches [as envisioned by Melville, 1996] than in smooth undulations (as considered in the previous Chapter).

It could then be argued that these events trigger instabilities in the overlying flow, generating vortices at their top in a similar way to the coherent vortices described on top of canopies by Raupach et al. [1996] (see page 34). This criterion can be used to define the roughness sublayer associated to these geometrical elements, where the instabilities constrain the size of energy-containing eddies to the scale of the wind shear $u_*/(dU/dz)$ [what Harman and Finnigan, 2007, call the vorticity thickness, with u_* the friction velocity and dU/dz the mean wind shear].

In this Chapter we pursue this analogy by defining an effective roughness height associated to these instabilities above a windy sea. The roughness height is estimated from measurements of momentum fluxes, using the phenomenological model of Bonetti et al. [2017] (an extension of the model presented in Sec. 1.2 to rough surfaces). This height is intended to characterize in a compact form the complex interplay between turbulent structures, and breaking and non-breaking waves close to the surface (as described in Sec. 1.3).

4.2 ARTICLE: "REVISITING BEAUFORT SCALE: THE DYNAMICAL COUPLING BETWEEN TURBULENCE AND BREAKING WAVES"

Manuscript to be submitted to the *Proceedings of the National Academy of Sciences*.

4.2.1 MAIN TEXT

Revisiting the Beaufort scale: the dynamical coupling between turbulence and breaking waves

Alex Ayet[a,b,1], **Bertrand Chapron**[a], **Peter Sutherland**[a], **and Gabriel G. Katul**[c]

[a]Ifremer, CNRS, IRD, Univ. Brest/ Laboratoire d'Océanographie Physique et Spatiale (LOPS), IUEM, Brest, France; [b]LMD/IPSL, CNRS, École Normale Supérieure, PSL Research University, Paris, France; [c]Nicholas School of the Environment, Box 90328, Duke University, Durham, NC 27708-0328, USA

This manuscript was compiled on October 15, 2020

The coupling between wind–waves and atmospheric surface layer turbulence is usually represented through a roughness length. Originally suggested on purely dimensional grounds, this roughness length does not directly correspond to a measurable physical quantity of the wind-and-wave system. Here, ideas underlying the Beaufort scale are formalized by quantifying the interaction between turbulent velocities and roughness elements that contribute most to momentum transport. A length associated with the velocity and size of breaking short waves is identified. This length scale represents the effects of breaking waves which efficiently impede turbulent structures, and which are strongly coupled to the wind field. Scales of the eddies contributing to momentum fluxes are then constrained inside a so-called roughness sub-layer. Unlike previous theoretical developments, the dynamical coupling thus becomes directly measurable.

air-sea coupling | momentum flux | wind wave interactions | wave breaking

When at sea, an experienced seafarer can estimate the wind velocity just by looking at the local sea surface. A windy sea indeed demonstrates an apparent visual organization associated with the occurrence and intensity of breaking waves. This led George Simpson, in 1906, to derive a scale for the surface wind speed, labelled the Beaufort scale after the original classification of the sea surface by Frances Beaufort in 1831 (red text in Fig. 1). While under duration- and fetch-limited conditions, the wind speed can be linked, in a remarkably concise form, to the evolution of the wind-wave peak energy and period (1–3), the Beaufort scale relies partly on the visual properties of short-scale breaking waves. Those small-scale properties must hence contain the imprint of the wind aloft and of its direct coupling with wind-waves, no matter the history of the system. In this work, a first step towards quantifying this wind-dependent imprint is taken in the form of two summarizing scales: a vertical scale for near surface turbulence, and a horizontal scale for the breaking wave field (Fig. 1). This is the first instance of such a mathematical quantification of the Beaufort scale.

The Beaufort scale partly relies on wind-wave coupling being independent of the peak wind-wave energy "provided short wave scales are well established" (4). More precisely, the mean-squared slope of the surface, largely governed by short wave scales, is linked to surface roughness statistics and hence to wind stress (5). The slope distribution of the short waves is further related to wave breaking and formation of whitecaps. Hence wave breaking statistics are related to the wind-wave coupling (6–8). Yet, the impact of wind-waves on turbulence in the atmospheric surface layer is, to date, usually represented through a roughness length (9–11), which does not directly correspond to measurable turbulence or surface wave physical quantities (12). This is largely due to the challenges associated with modelling a surface that is no longer connected due to wave breaking, and for which the governing equations of motion are not fully known (13).

The goal of this article is to demonstrate that this complex process can be summarized through a horizontal wave length scale, associated with the velocity of short-scale breaking fronts. The wave properties associated with the predicted length scale (italic text in Fig. 1, from Ref. 7) correspond to the Beaufort scale. A key result is that this length scale is derived independently from (i) recent high-resolution measurements of wave-breaking statistics (14, 15) and (ii) a phenomenological model of turbulence that does not presume wave statistical properties (16–19). Unlike previous theoretical developments, this is a directly measurable trace of the dynamical wind-wave coupling. Furthermore, the turbulence model allows the definition of a vertical length associated with the typical scales of energy-containing eddies within the air-side roughness sublayer.

Analysis of wave-breaking measurements

Data. Open-ocean measurements of wave-breaking statistics (14, 15) were obtained during three field campaigns on-board R/V *FLIP*: the RaDyO experiment, which took place 120 km south of the Island of Hawai'i in 2009 (20), and the HiRes and SoCal experiments, which took place 25km off the coast of Northern California and in the Southern California Bight, respectively. As shown in Fig. 2 (red diamonds), the 10-meter mean wind U_{10} (averaged over 20-minute intervals) ranged

Significance Statement

Wind drag on the ocean surface is a key control and uncertainty on many geophysical phenomena, from global circulation to hurricanes. It results from the complex interplay between waves and turbulence, which has been modeled using a turbulent roughness length. Yet, its physical interpretation has remained elusive. This work overcomes that obstacle by relating the structure of atmospheric turbulence directly to the **velocity** of breaking waves. Consequently, by measuring the distribution of breaker velocities - possible via remote sensing - ocean surface wind drag can be determined. This opens the path towards new parameterizations. It also provides a physical model for something seafarers have been doing for centuries; estimating wind velocity by simply "looking at the sea" (the Beaufort scale).

Author contributions: A.A., B.C. and G.G.K. designed research; A.A. and B.C. performed research; P.S. collected data; A.A., B.C. and P.S. analysed data; A.A., B.C., P.S. and G.G.K. wrote the paper

The authors declare no conflict of interest.

[1]To whom correspondence should be addressed. E-mail: alex.ayet@normalesup.org

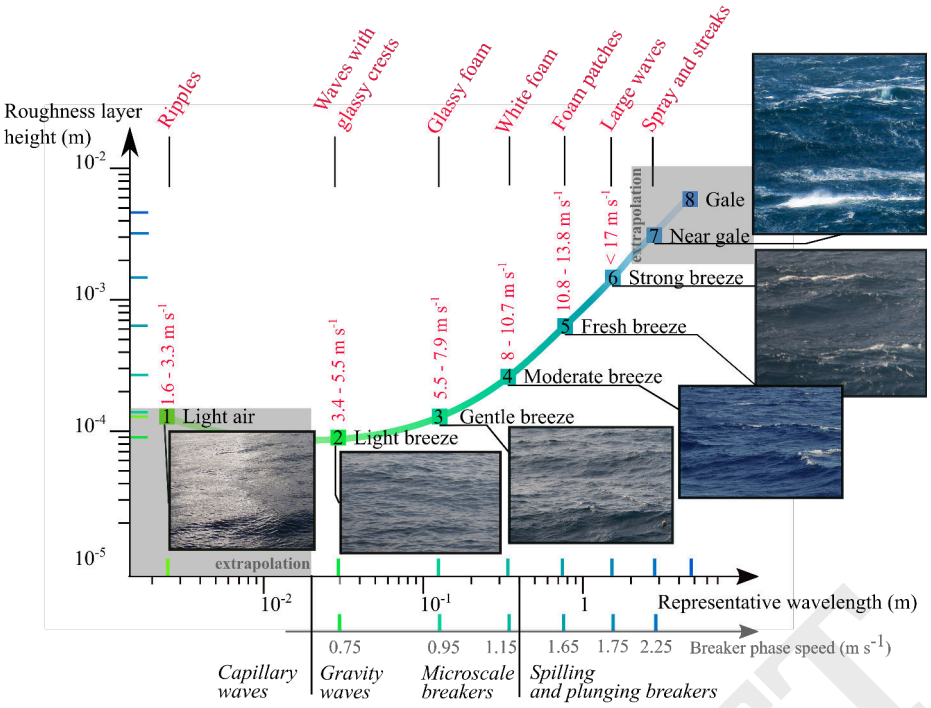

Fig. 1. Beaufort scale (red text) and its quantification using two wind-dependent length scales: a representative wavelength of breaking fronts (horizontal axis) and height of the roughness sublayer, equivalent to the smallest size of energy-containing eddies (the vertical axis). Classification of breaker types on the horizontal axis is from (7).

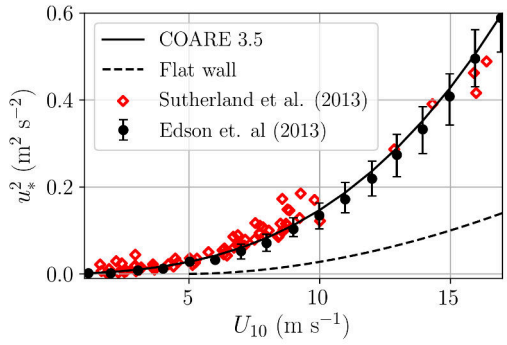

Fig. 2. Momentum flux u_*^2 versus U_{10} from the COARE 3.5 parameterization (solid line) and the corresponding open-ocean measurements (11, dots and bins). The flat-wall dependence is included for reference (dashed line). The open-ocean measurements used in this study (14, 15) are shown as diamonds. The COARE 3.5 parameterization is used to obtain $h_r(U_{10})$ from the phenomenological turbulence model.

from 2 to 16 m s^{-1} with few measurements for $U_{10} > 10$ m s^{-1}. Fig. 2 also shows the measured friction velocity u_* defined as $u_*^2 = \tau/\rho_a$, where τ is the directly-measured turbulent wind stress at 10-m height and ρ_a is the mean air density. These measurements are consistent with other experiments (11) (dots and bins) used to calibrate the COARE parameterization (solid line). The presence of wind-waves at equilibrium results in a bulk drag coefficient $C_d = u_*^2/U_{10}^2$ that is higher than a C_d associated with a flat surface (dashed line, and see also e.g. Ref. 21, their Fig. 3). Except for very low winds, atmospheric stability was almost neutral during the measurements (*SI Supplementary*). For this reason, atmospheric stability effects are not discussed further and low U_{10} runs are filtered out so as to only maintain near-neutral atmospheric stability conditions. In the measurements, no strong correlation was found between variations in atmospheric stability conditions for low winds and variations in u_* for a given U_{10}.

To each point in Fig. 2 corresponds a 20-minute averaged spectrum of wave-breaking statistics, measured using a stereo pair of long-wave infrared cameras. In contrast to measurements in the visible range (22), the use of infrared cameras allows the measurement of non-air-entraining microbreakers with crest speeds as slow as the gravity-capillary phase speed minimum.

Results. The statistics of the breaker front length $\Lambda(c)$ per unit area of sea surface per unit increment of breaking front velocity c are now analyzed (defined in Ref. 6). Near breaking crests, local energy fluxes, proportional to c^3, become too large for the ocean surface to stay smooth (13). The associated roughness elements modify near-surface turbulent stress (8), and the intensity of the modification depends on $c^3\Lambda(c)$ (Fig. 3a). Further, as the Beaufort scale relies on the changes of the visual characteristics of breaking waves, the *gradient* of $c^3\Lambda(c)$ with respect to changes in U_{10} must be used (Fig. 3b). The choice of $c^3\Lambda(c)$ is also justified by the turbulence model (see below).

The physical arguments presented in this work depend on the breaker crest speed and not on wavelength. However, the intuitive interpretation of the results is facilitated by following Ref. (6) in assuming that the breaker crest speed is equal to the phase speed, c, of a linear deep water wave whose length, λ, is related to that phase speed by the dispersion relation, $\lambda = 2\pi c^2/g$, where g is gravitational acceleration.

Data were first binned for U_{10} intervals corresponding to Beaufort numbers (see Fig. 1 for the intervals). Dots and error bars in Fig. 3c show the average and standard deviation of $c^3\Lambda(c)$ for each Beaufort number bin, normalized by the wavenumber-dependent maximum it reaches in the range of measured U_{10}. Examples of the dependence of $c^3\Lambda(c)$ with

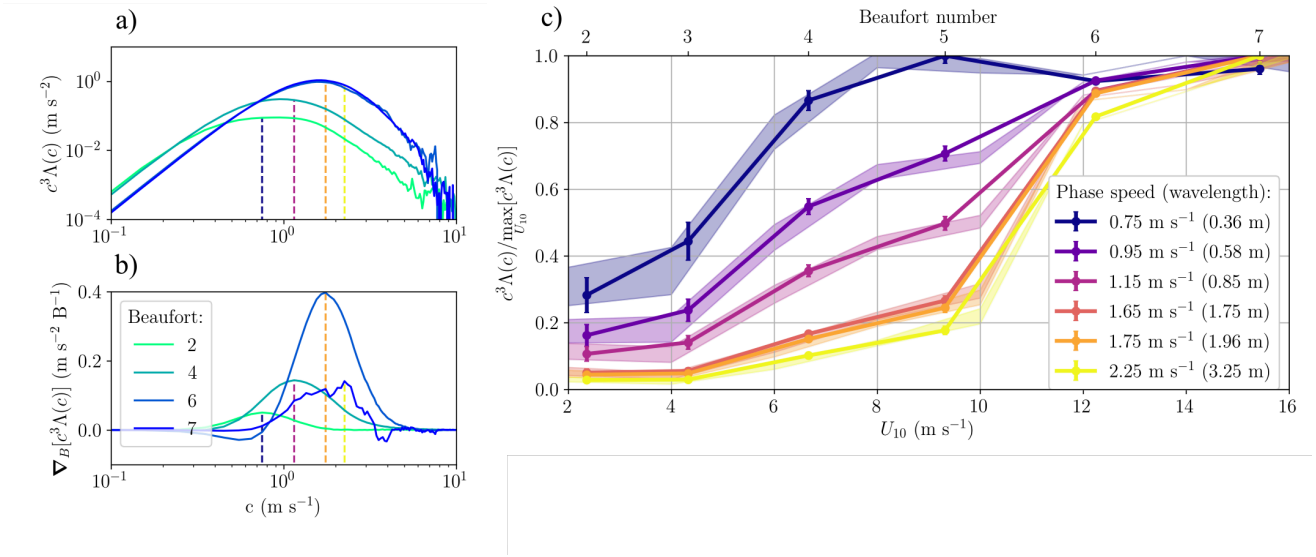

Fig. 3. Analysis of the wave breaking measurements. The data was binned in U_{10} intervals corresponding to Beaufort numbers. (a) Binned $c^3\Lambda(c)$ vs breaker speed for different Beaufort numbers. (b) Gradient of the binned $c^3\Lambda(c)$ with respect to changes in Beaufort number vs breaker speed, for different Beaufort numbers. The vertical dashed lines correspond, for each Beaufort number, to the speed whose gradient $\partial[c^3\Lambda(c)]/\partial B$ is the largest. (c) Average and standard deviation of binned $c^3\Lambda(c)$ for different breaker speeds vs U_{10} and Beaufort number. Dots and error bars correspond to data binned in U_{10} intervals corresponding to Beaufort numbers, and shadings to intervals of 1 m s^{-1}. The wavelengths $\lambda_w = 2\pi c^2/g$ correspond to those of deep-water linear waves travelling with phase speed c, and have been included for reference. The colors in (c) correspond to the to the phase speeds of the vertical lines in (a) and (b).

c are shown in Fig. 3a. For a fixed breaker speed c, the increase in $c^3\Lambda(c)$ with Beaufort number (B) is not constant, but is maximal around a particular wind speed before $c^3\Lambda(c)$ reaches its maximal value (see the solid lines in Fig. 3c). For a given B, the increase is found strongest around a speed c_r, termed representative wave speed in the following (see Fig. 3b). This speed increases with Beaufort number: for $B = 2$, it is $c_r = 0.75$ m s^{-1} (blue vertical line in Fig. 3b) while for $B = 6$, it is $c_r = 1.75$ m s^{-1} (orange vertical line in Fig. 3b). Note that, even though for $B = 7$ such a wave speed can still be defined ($c_r = 2.25$ m s^{-1}, yellow line in Fig. 3b), the low number of measurement points used for binning induces noise in the gradient of $c^3\Lambda(c)$.

Hence, for each Beaufort number B, a representative velocity (and associated wavelength) can be defined, corresponding to the short scale waves whose breaking statistics are the most sensitive to changes in mean wind speed (red line in Fig. 4). Sensitivity to the bin size was tested by using 10-m wind speed binning intervals of a width of 1 and 2 m s^{-1}. The resulting variability of the average value of $c^3\Lambda(c)$ in each bin is shown as shadings in Fig. 1a, and as dashed and dotted lines in Fig. 4. The outcomes are qualitatively consistent with the analysis above.

A measurable kinematic relation. A key property of the representative velocity c_r is its kinematic link with the friction velocity

$$c_r = 2.5u_*. \qquad [1]$$

While an approximate form of this relation can be obtained from a best fit to the data (in Fig. 4), the turbulence model presented in the next section provides an exact derivation of Eq. 1. It results from a kinematic condition on the motion of turbulent eddies near the surface

Such a relation was discussed in Ref. (4) (p. 141) when considering the interaction between small scale waves and surface drift induced by viscous wind stress. The magnitude of the surface drift was indeed reported to be $q = 0.55u_*$ m s^{-1} (23), and (4) argued that small waves with phase speeds "smaller by a factor of at least five than" the surface drift would be strongly impacted. Hence, wave scales such that $c = 5 \times 0.55u_* \sim 2.5u_*$ are the smallest waves that do not significantly interact with surface drift. Interactions with surface drift tends to reduce the critical steepness needed for wave breaking. This leads to (i) a reduction of the amplitude of drift-affected waves with respect to a no-drift situation, and hence to (ii) a reduction of the strength of the breaking event, i.e. its capacity to be visually detected.

Consequence (ii) can explain the existence of a maximum in the gradient of $c^3\Lambda(c)$ with respect to Beaufort number in Fig. 3b. With increasing winds, short wave-breaking occurrence is expected to increase. However, this increase is truncated for drift-affected waves. This leads to the Bell-shaped curves of Fig. 3b, i.e. to the fact that a representative surface wave characteristic can be visually defined for a given wind. As for consequence (i), it implies that amplitudes of drift-affected waves are reduced, and so is their contribution to "effective roughness elements" for atmospheric turbulence, such as discussed in the next section.

To summarize, breaker data analysis suggests that it is possible to relate a change in U_{10} to a change in the energetic properties of breaking crests of a particular wave front velocity. This reflects both local wind stress variations and changes in wind-induced surface drift.

A roughness sublayer from a phenomenological turbulence model

In this section, a phenomenological model of turbulence above fixed roughness elements (16, 19) is now applied to a windy

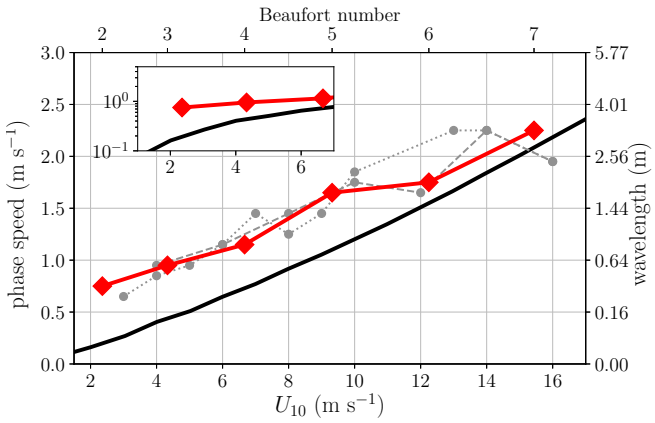

Fig. 4. Representative wave speed of the wind-wave local coupling as a function of 10-m wind speed and Beaufort number. Solid red line is the result from analysis of wave-breaking statistics $c^3\Lambda(c)$, binned in Beaufort number intervals or, dotted and dashed lines, in intervals of 1 and 2 m s^{-1} respectively. Solid black line is the result from the phenomenological model of turbulence. The conversion between Beaufort number and wind speed is $U_{10} = 0.836B^{3/2}$ m s^{-1} (25). The wavelengths $\lambda_w = 2\pi c^2/g$ correspond to those of deep-water linear waves travelling with phase speed c, and have been included for reference.

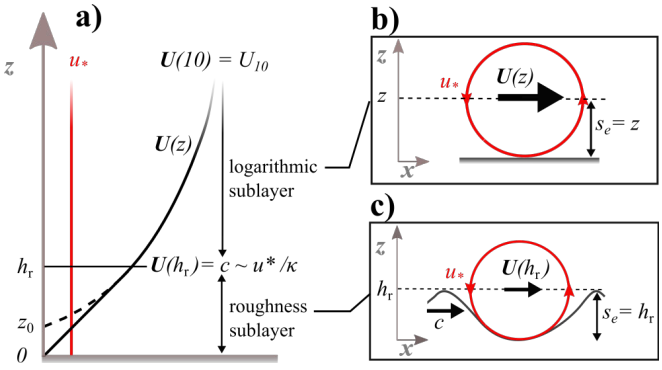

Fig. 5. Phenomenological model describing the SBL in the presence of an effective roughness element of height h_r. (a) The SBL is divided into two sublayers: (b) the logarithmic sublayer, where energy-containing eddies scale with z; (c) the roughness sublayer, where their size is independent of height and is equal to h_r, yielding a linear wind profile.

sea.

The model. The phenomenological model describes turbulence in the Surface Boundary Layer (SBL), where the flow is horizontally homogeneous and stationary with no subsidence, and hence u_* is height-independent. Turbulence is modelled through a turbulence kinetic energy balance and so-called energy-containing eddies (red in Figs. 5b,c), which are leading order contributors to the vertical momentum flux at a given height (dashed lines in Figs. 5b,c).

Those eddies are defined by their streamwise extension or height s_e and their turnover velocity, proportional to u_* (consistent with other models of turbulence, e.g. Ref. 24). For neutral conditions, the mean wind shear is then expressed as

$$\frac{\partial U}{\partial z}(z) = \frac{u_*}{\kappa s_e(z)}, \qquad [2]$$

where U is the mean wind speed in the streamwise (x) direction, and z is height, whose origin is the mean sea surface height, and $\kappa \sim 0.4$ is the Von Kármán constant. Details on the derivation of Eq. 2 from the model hypotheses (18, 19, 21) are in the *SI Appendix*. It is to be noted that this model is also compatible with (though not explicitly derived from) the Maximum Entropy Production (MEP) principle (see also *SI Appendix*).

The phenomenological model defined in Eq. 2 thus links the mean wind shear to the friction velocity and the size of the energy-containing eddies. For flow past a rough wall, Refs. (16, 19) proposed that the surface boundary can be decomposed into two sublayers, depicted in Fig. 5a. The highest sublayer is a logarithmic layer, in which the size of the energy-containing eddies scales with distance from the wall ($s_e(z) = z$), corresponding to attached eddies (as proposed in Ref. 26, and depicted in Fig. 5b). From Eq. 2, the mean wind profile is hence logarithmic

$$U_{\log}(z) = \frac{u_*}{\kappa}\log(z/z_0), \quad \text{for } z \geq h_r, \qquad [3]$$

where z_0 is the roughness height. Below the logarithmic sublayer lies the roughness sublayer of height h_r. In this layer, the size of the energy-containing eddies is constant with height and scales with the height of the roughness elements, equal to h_r. To ensure continuity of the mean wind shear at the interface between both layers, the scaling constant is considered to be equal to one, i.e. $s_e(z) = h_r$ for $z \leq h_r$ (see Fig. 5c and Ref. 19). Equation (2) then yields a linear wind profile

$$U_{\text{lin}}(z) = \frac{u_*}{\kappa}\frac{z}{h_r}, \quad \text{for } 0 \leq z \leq h_r. \qquad [4]$$

The height of the roughness elements h_r is in general different from the roughness height z_0 (which is an extrapolation of the logarithmic profile) and, by definition, $h_r \geq z_0$ (27).

In the present case, this relation can be made more precise by requiring continuity of the wind profile at h_r. This yields

$$z_0 = h_r \exp(-1). \qquad [5]$$

This equation defines the height of roughness elements given z_0. We term these roughness elements as being *effective*, since the height h_r models the bulk effect of intermittent wind-wave breaking events on the SBL, but not the height of measurable monochromatic wind-waves. Instead, only their speed c_r can be readily interpreted, and we define it below as equal to the phase speed of wind-waves contributing the most to shape roughness-sublayer energy-containing eddies.

In the aerodynamically smooth regime, h_r matches the height of the viscous sublayer $\exp(1)z_0^v$, where $z_0^v = \gamma\nu/u_*$ is the viscous roughness height (and ν and $\gamma \sim 0.11$ are the kinematic viscosity of the air and the roughness Reynolds number of smooth flows, respectively). The resulting relation between u_*^2 and U_{10} is plotted in Fig. 2 (dashed line).

Model extension to an ocean surface. Using open-ocean measurements of u_* and U_{10} and their COARE fit (solid line in Fig. 2), a wind-dependent z_0 can be inferred and a corresponding h_r can be computed from Eq. 5. As shown in Fig. 1, h_r ranges from 10^{-4} m to 10^{-2}m. For winds below 3 m s^{-1}, h_r decreases with increasing U_{10} as expected for an aerodynamically smooth surface (28). For higher winds, the effect of wind-waves becomes predominant and h_r increases with increasing U_{10}. These two regimes are reminiscent of the

Charnock parameterization of the roughness height z_0 (see Refs. 9, 11, and *SI Appendix*).

The height of the effective roughness elements h_r can be further projected into a horizontal speed or length scale using the physical interpretation of the roughness sublayer. Unlike z_0, which is defined as the extrapolated height where the wind speed is zero for a logarithmic wind profile, the wind speed at h_r is such that

$$U(h_r) = \frac{u_*}{\kappa}, \qquad [6]$$

and we argue below that it corresponds to the phase speed c_r of the waves most coupled to atmospheric turbulence (which defines the velocity of the effective roughness elements).

The argument relies on the dynamical interpretation of $U(h_r)$ as setting the properties of energy-containing eddies in the roughness sublayer. Energy-containing eddies can be seen as resulting from the interaction between mean wind shear and turbulence: rearranging Eq. 2, the streamwise extension of energy-containing eddies (which defines their properties) can be expressed as $s_e \propto w_e T_e$, i.e. as a product of an the eddy turnover velocity $w_e \propto u_*$ and time $T_e \propto (dU/dz)^{-1}$. For roughness-sublayer eddies, the turnover velocity further reads $T_e = (U(h_r)/h_r)^{-1}$, indicating that those are controlled by the *bulk* mean wind shear over the sublayer, whose essential parameters are its scale h_r and magnitude $U(h_r)$. Roughness-sublayer eddies can thus be viewed as originating from an instability of a similar form to those above canopies (29), triggered by the wind shear whose scale, also labelled vorticity thickness (30), matches the eddy size ($s_e \propto h_r$). The scale is already set by the continuity of the wind profile at h_r (Eq. 5). Now, if the wind shear in the roughness sublayer is set by intermittent, yet intense wave breaking events, fluid is entrained at the speed c_r of the breaker fronts (31). Hence the magnitude of the bulk wind shear $U(h_r)$ should be equal to the wave speed

$$U(h_r) = c_r. \qquad [7]$$

Note that this kinematic condition, together with Eq. 6, readily yields Eq. 1.

The above discussion shows that the linear mean wind profile in the roughness sublayer is not essential for the description of energy-containing eddies. What is instead essential is the bulk mean wind shear across the sublayer (see also MEP arguments in the *SI appendix*). In fact, the mean wind speed in the roughness sublayer does not have a well-defined physical interpretation. In the logarithmic sublayer, it is the convection velocity of energy-containing eddies (see e.g. Ref. 32). But, in the roughness sublayer, the convection velocity could be ill-defined due to transient roughness elements (12). Certainly, it is more reasonable to assume that the convection velocity of eddies at all heights $z_0^v \leq z \leq h_r$ is $U(h_r)$, is the convection velocity of the roughness-sublayer eddies of size h_r.

Equation 7 could at first glance lead to an interpretation of the roughness height as (i) the lowest height at which waves of phase speed c_r can induce airflow separation events (12, 31), or (ii) the height at which inviscid instabilities above a free surface are generated (33). While both mechanisms certainly play a role in the generation of roughness-sublayer eddies, they are associated with wind-wave generation, which is not what we aim to describe through the kinematic condition Eq. 1 and roughness-sublayer eddies. The latter should instead be viewed as wave-coherent motions (as defined in 34), which are an indirect imprint of wind-wave growth. Indeed, wind-wave growth occurs at smaller wave scales and greater heights (8), and it is through its role in setting the properties of the wave breaking field (6) that it affects roughness-sublayer eddies.

At those greater heights, wind-wave growth is also characterized by the presence of wave-induced motions, which cause a deviation of the mean wind from a logarithmic profile (35). In the *SI Appendix*, the phenomenological model is extended to account for these motions above the roughness sublayer (following Ref. 21). In this case, Eq. 5 is more complex, but the resulting h_r are only slightly different than results reported in Fig. 1. More interestingly, with increasing wind, wave-induced motions become more energetic, and the ratio s_e/h_r is found to increase (up to 2.2 for 16 m s^{-1}). This finding is consistent with detailed laboratory experiments on flow over granular roughness elements that reported (i) attainment of spatially uniformity in flow statistics and (ii) a log region commencing at approximately 1.6 times the mean grain height (36). It also supports the interpretation of the effective roughness elements as being intermittent, with an average size smaller than the scale of the eddies they generate. Finally, it reveals the existence of a direct interaction between wave growth and roughness-sublayer eddies, through the presence of wave-induced motions.

The phenomenological model used here does not contain *any* a priori spectral information on the wave field, and solely requires specification of the bulk information contained in open-ocean measurements of u_* and U_{10}. Yet, the resulting wave velocity is similar to the one obtained from analysis of wave-breaking statistics. This is shown in Fig. 4, where the wave velocity c_r corresponding to the velocity obtained from Eq. 7 (black line) is of the same order of magnitude than that of obtained from data (red line), with a similar trend as a function of U_{10}. For very low winds, model and data trends disagree (see inset of Fig. 4), but suggested scales are close to the capillary-gravity transition, and hence also to the measurement limit of the wave-breaking data.

This analysis shows the that there is a correspondence between the properties of the wave breaking field and those of the energy-containing eddies. This positive result is used below to propose a three-dimensional interpretation of the phenomenological model in the presence of roughness elements associated to wave breaking.

A three-dimensional view of wave-breaking-constrained turbulence

In the previous section, a roughness height was found, related to the streamwise scale of energy-containing eddies s_e. Theoretical (37, 38), experimental (39) and numerical (40) work further revealed that the interaction between breaking waves and turbulence is a three-dimensional processes in which the spanwise length of the breaking crests plays an essential role. In the following, the phenomenological model of turbulence is extended so as to bridge this spanwise length to the streamwise scale of energy-containing eddies. The model is sketched in Fig. 6a, and described below. The spanwise direction is labelled as y.

Let l_Λ be a spanwise extension of surface roughness elements, proportional to the individual crest length associated with breaking fronts of speed c (whose sum per unit area of ocean surface is $\Lambda(c)dc$). Roughness elements are assumed to trigger spanwise atmospheric eddies of similar extension

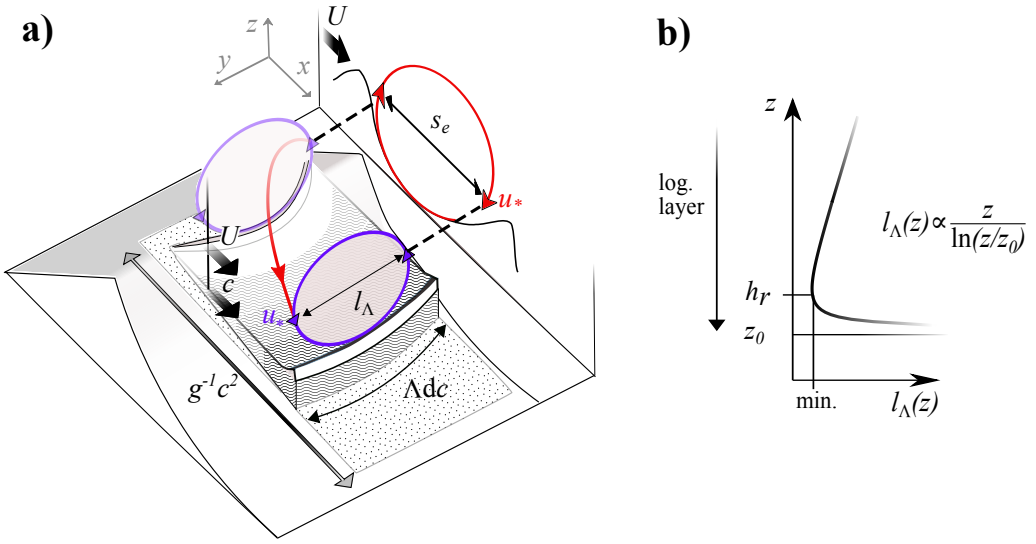

Fig. 6. Three-dimensional interpretation of the phenomenological model (Fig. 5) over a rough sea surface. (a) Breaker fronts of speed c and spanwise extension Λdc constrain the spanwise extension l_Λ of vortices advected at a speed $U = c$ (blue circles). The streamwise scale of energy-containing eddies s_e (red circle) results from the spiraling motion of a fluid parcel (red line) due to advection at mean wind speed and rotation at a turnover velocity u_*. Over their liftetime (longer than the eddie lifetime), breaker fronts cover an approximate streamwise distance $g^{-1}c^2$ and hence the dotted area. Note the difference in the geometry of the individual breaker front and of the effective roughness element (black line in the (x, z) transect). (b) Required l_Λ for logarithmic-layer energy-containing eddies, i.e. for $s_e = z$ and $U \propto u_* \ln(z/z_0)$.

with a turnover velocity proportional to u_*. These eddies are also advected at the mean wind at a speed U (blue circle in Fig. 6a). The turnover time of the eddies is $T_\Lambda \propto l_\Lambda/u_*$, and the streamwise distance, s_e, travelled by a representative fluid parcel during a turnover time $s_e = UT_\lambda$, is

$$s_e(z) \propto U(z) l_\Lambda(z)/u_*. \quad [8]$$

As sketched in Fig. 6a (red line), the distance s_e can be represented as the streamwise Lagrangian distance separating the ascending and descending branches of the eddy, in between which a representative fluid parcel would undergo a spiraling motion. It is hence also the streamwise extension of the energy-containing eddies defined in the phenomenological turbulence model (red circle). As for the phenomenological model, this representation is to be understood in an ensemble mean sense, unlike similar but instantaneous representations of turbulence over flat walls (41, 42) and waves (37, 38) which would result from conditional sampling of the flow.

This three-dimensional interpretation relates, through Eq. 8, the streamwise extension of the energy-containing eddy s_e to the spanwise extension of the roughness elements constraining its size, l_Λ. For a logarithmic layer, $s_e = z$ and $U \propto u_* \ln(z/z_0)$, and Eq. 8 then yields the $l_\Lambda(z)$ required to obtain attached energy-containing eddies at each height z satisfying the law of the wall. As shown in Fig. 6b, after some algebra, $l_\Lambda(z)$ has a minimum, reached at a height corresponding to the roughness sublayer height h_r defined in Eq. 5. For a wavy surface, an increase of l_Λ with decreasing height is not physical. This would indeed imply an increase of the spanwise extension of breaking fronts (proportional to l_Λ) as height decreases. Further, for decreasing heights, the speed and wavelength of the representative waves decrease (Eq. 7). This result would hence imply an increase of the breaking front average length with decreasing wavelength, which is not realistic (see Refs. 43, 44, which, among others, highlight the self-similarity of breaking fronts). Hence, breaking fronts can only imprint their spanwise scale on energy-containing eddies for $z \geq h_r$.

Subsequently, h_r represents the smallest height at which roughness elements associated with breaking fronts can set the spanwise and streamwise extension of energy-containing eddies. Below this height, the scale of energy-containing eddies is h_r. This interpretation offers an alternative argument for the importance of h_r in the characterization of the wind-over-waves coupling.

From the wave-breaking data, this scale emerged from the variations of $c^3\Lambda(c)dc$ with U_{10}. Assuming foam patches to have a lifetime proportional to the underlying wave period (44), $g^{-1}c^2\Lambda(c)dc$ is related to the the fraction of sea-surface turned over by breaking fronts, weighted by their lifetime. Hence $c^3\Lambda(c)dc$ also contains information about both the lifetime of roughness elements and their momentum (proportional to c). The fact that a change in the properties of roughness-sublayer energy containing eddies is coupled to a change in $c_r^3\Lambda(c_r)dc$ thus indicates that not only the size of the breaking fronts ($\propto l_\Lambda$) but also their momentum ($\propto c_r$) and lifetime ($\propto c_r/g$) are essential for the description of near-surface turbulence properties.

Conclusions

The Beaufort scale analysis was revisited by identifying a wave speed corresponding to small scale breakers that are most coupled to the atmosphere. Infrared measurements of wave breaking statistics have indeed revealed that variations of $c^3\Lambda(c)dc$ with wind (or Beaufort number) are significant only for a particular breaker speed, which increases with friction velocity. We consistently interpreted this measurable kinematic relation as a macroscopic property of the turbulent flow, resulting from the existence of a minimal scale for energy-containing eddies related to the spanwise extension of breaking

fronts (Fig. 6). An important feature of this description is that it does not require specification of the spectrum of waves or roughness elements through form drag and air-flow separation (as in e.g. Refs. 8, 45, 46). It instead describes an overall modification of near surface turbulence over a moving windy sea.

The turbulence model used herein relies on the existence of a roughness sublayer, sensing the waves, at the bottom of the logarithmic sublayer. While the existence of a roughness sublayer over a windy sea has already been suggested elsewhere (e.g. Refs. 10, 12, 37), the properties of roughness-sublayer eddies proposed herein are not supported by empirical evidence, but based on an analogy with other types of surfaces (19, 47). These energy-containing eddies have been related to spectral properties of turbulence in prior work (19, 48, 49). The present work hence enables new hypotheses of wind-wave interactions to be formulated and tested using direct numerical simulations (50) or in situ measurements of turbulence spectral properties (51).

Finally, the representative wave speed was converted to a wave scale associated with the visual description of a rough windy sea by the Beaufort scale (Fig. 1). The scale results from the selective attenuation of the amplitude of short waves by surface drift. The amplitude of those waves is generally described by a wave action budget balancing wind input, breaking wave dissipation and non-linear wave-wave interactions (6). On the other hand, the size of energy-containing eddies was found to be dependent on the presence of wave-induced motions (*SI Supplementary*). Hence, the dynamical wind-wave coupling expressed by those two scales should be sensitive to modifications of these different processes by environmental conditions, e.g. the presence of slicks, surface currents and modulating longer waves that can alter surface drift (52), the wave action budget (53) and wave-induced motions (21). Additionally, atmospheric stability effects, not considered in the present work, can be integrated into the proposed dynamical framework, as modifying the scale of energy-containing eddies (18, 54).

This measurable breaker scale is a promising candidate for the characterization of air-sea interactions and their modulation by changes in environmental conditions, both by in situ or remote sensing methods. It can guide methods for the interpretation of remote sensing observations, sensitive to breakers and foam-coverage properties, as well as help design future satellite-borne instruments, especially to directly retrieve sea surface Doppler estimates.

ACKNOWLEDGMENTS. The code used to generate the figures is available freely on [....]. AA was supported by DGA grant No D0456JE075, the French Brittany Regional Council and ANR grant ANR-10-IEED-0006-26. PS was supported by funding from the European Research Council (ERC) under the European Union's Horizon 2020 research and innovation programme (grant agreement No 805186). GGK was supported by the US National Science Foundation (Grants NSF-AGS-164438 and NSF-IOS-175489).

1. S KITAIGORODSKII, Applications of the theory of similarity to the analysis of wind-generated wave motion as a stochastic process. *Izv., Geophys. Ser. Acad. Sci., USSR* **1**, 105–117 (1962).
2. Y Toba, Local balance in the air-sea boundary processes. *J. Oceanogr.* **28**, 109–120 (1972).
3. VE Zakharov, SI Badulin, PA Hwang, G Caulliez, Universality of sea wave growth and its physical roots. *J. Fluid Mech.* **780**, 503–535 (2015).
4. OM Phillips, *The dynamics of the upper ocean.* (Cambridge University Press), (1977).
5. W Munk, Wind stress on water: An hypothesis. *Q. J. Royal Meteorol. Soc.* **81**, 320–332 (1955).
6. O Phillips, Spectral and statistical properties of the equilibrium range in wind-generated gravity waves. *J. Fluid Mech.* **156**, 505–531 (1985).
7. KB Katsaros, SS Ataktürk, Dependence of wave-breaking statistics on wind stress and wave development in *Breaking Waves.* (Springer), pp. 119–132 (1992).
8. V Kudryavtsev, B Chapron, V Makin, Impact of wind waves on the air-sea fluxes: A coupled model. *J Geophys. Res Ocean.* **46**, 1022–1037 (2014).
9. H Charnock, Wind stress on a water surface. *Q J R Meteorol Soc* **81**, 639–640 (1955).
10. SA Kitaigorodskii, *The physics of air-sea interaction.* (Israel Program for Scientific Translations Jerusalem), (1973).
11. JB Edson, et al., On the exchange of momentum over the open ocean. *J Phys Ocean.* **43**, 1589–1610 (2013).
12. E Kraus, Wind stress along the sea surface. *Adv. Geophys.* **12**, 213–255 (1967).
13. AC Newell, VE Zakharov, Rough sea foam. *Phys. Rev. Lett.* **69**, 1149 (1992).
14. P Sutherland, WK Melville, Field measurements and scaling of ocean surface wave-breaking statistics. *Geophys. Res Lett* **40**, 3074–3079 (2013).
15. P Sutherland, WK Melville, Field measurements of surface and near-surface turbulence in the presence of breaking waves. *J. Phys. Oceanogr.* **45**, 943–965 (2015).
16. G Gioia, F Bombardelli, Scaling and similarity in rough channel flows. *Phys. review letters* **88**, 014501 (2001).
17. G Gioia, N Guttenberg, N Goldenfeld, P Chakraborty, Spectral theory of the turbulent mean-velocity profile. *Phys Rev Lett* **105**, 184501 (2010).
18. GG Katul, AG Konings, A Porporato, Mean velocity profile in a sheared and thermally stratified atmospheric boundary layer. *Phys Rev Lett* **107**, 268502 (2011).
19. S Bonetti, G Manoli, C Manes, A Porporato, GG Katul, Manning's formula and strickler's scaling explained by a co-spectral budget model. *J Fluid Mech* **812**, 1189–1212 (2017).
20. T Dickey, et al., Introduction to special section on recent advances in the study of optical variability in the near-surface and upper ocean. *J. Geophys. Res. Ocean.* **117** (2012).
21. A Ayet, B Chapron, JL Redelsperger, G Lapeyre, L Marié, On the impact of long wind-waves on near-surface turbulence and momentum fluxes. *Boundary-Layer Meteorol.* **174**, 465–491 (2020).
22. JM Kleiss, WK Melville, Observations of wave breaking kinematics in fetch-limited seas. *J. Phys. Ocean.* **40**, 2575–2604 (2010).
23. J Wu, Wind-induced drift currents. *J. Fluid Mech.* **68**, 49–70 (1975).
24. J Hunt, S Leibovich, K Richards, Turbulent shear flows over low hills. *Q J R Meteorol Soc* **114**, 1435–1470 (1988).
25. WMO, *The Beaufort Scale of Wind Force: Technical and Operational Aspects.* (World Meteorological Organization) No. 3, (1970).
26. AA Townsend, *The structure of turbulent shear flow, Vol. 2.* (Cambridge university press), (1976).
27. MR Raupach, RA Antonia, S Rajagopalan, Rough-Wall Turbulent Boundary Layers. *Appl. Mech. Rev.* **44**, 1–25 (1991).
28. S Kitaigorodskii, MA Donelan, Wind-wave effects on gas transfer in *Gas transfer at water surfaces.* (Springer), pp. 147–170 (1984).
29. M Raupach, J Finnigan, Y Brunet, Coherent eddies and turbulence in vegetation canopies: the mixing-layer analogy in *Boundary-layer meteorology 25th anniversary volume, 1970–1995.* (Springer), pp. 351–382 (1996).
30. IN Harman, JJ Finnigan, A simple unified theory for flow in the canopy and roughness sublayer. *Boundary-Layer Meteorol* **123**, 339–363 (2007).
31. WK Melville, Wind stress and roughness length over breaking waves. *J. Phys. Oceanogr.* **7**, 702–710 (1977).
32. OM Phillips, On the generation of waves by turbulent wind. *J. fluid mechanics* **2**, 417–445 (1957).
33. JW Miles, On the generation of surface waves by shear flows. *J. Fluid Mech.* **3**, 185–204 (1957).
34. R Stewart, The wave drag of wind over water. *J. fluid mechanics* **10**, 189–194 (1961).
35. JW Miles, A note on the interaction between surface waves and wind profiles. *J. Fluid Mech.* **22**, 823–827 (1965).
36. C Manes, D Pokrajac, I McEwan, Double-averaged open-channel flows with small relative submergence. *J. Hydraul. Eng.* **133**, 896–904 (2007).
37. G Csanady, Air-sea momentum transfer by means of short-crested wavelets. *J Phys Ocean.* **15**, 1486–1501 (1985).
38. W Eifler, A hypothesis on momentum and heat transfer near the sea-atmosphere interface and a related simple model. *J. marine systems* **4**, 133–153 (1993).
39. N Reul, H Branger, JP Giovanangeli, Air flow separation over unsteady breaking waves. *Phys Fluids* **11**, 1959–1961 (1999).
40. N Suzuki, T Hara, PP Sullivan, Turbulent airflow at young sea states with frequent wave breaking events: Large-eddy simulation. *J. atmospheric sciences* **68**, 1290–1305 (2011).
41. SJ Kline, WC Reynolds, F Schraub, P Runstadler, The structure of turbulent boundary layers. *J Fluid Mech* **30**, 741–773 (1967).
42. RF Blackwelder, H Eckelmann, Streamwise vortices associated with the bursting phenomenon. *J Fluid Mech* **94**, 577–594 (1979).
43. S Belcher, J Vassilicos, Breaking waves and the equilibrium range of wind-wave spectra. *J Fluid Mech* **342**, 377–401 (1997).
44. N Reul, B Chapron, A model of sea-foam thickness distribution for passive microwave remote sensing applications. *J. Geophys. Res. Ocean.* **108** (2003).
45. T Hara, SE Belcher, Wind profile and drag coefficient over mature ocean surface wave spectra. *J Phys Ocean.* **34**, 2345–2358 (2004).
46. T Kukulka, T Hara, SE Belcher, A model of the air–sea momentum flux and breaking-wave distribution for strongly forced wind waves. *J Phys Ocean.* **37**, 1811–1828 (2007).
47. M Raupach, Canopy transport processes in *Flow and transport in the natural environment: advances and applications.* (Springer), pp. 95–127 (1988).
48. GG Katul, C Manes, Cospectral budget of turbulence explains the bulk properties of smooth pipe flow. *Phys. Rev. E* **90**, 063008 (2014).
49. A Ayet, G Katul, Scaling laws for spectral peaks in a sheared and thermally stratified surface

4.2.2 SUPPLEMENTARY MATERIAL

Supporting Information Text

Phenomenological model of turbulence. The derivation of Eq. 2 in the main text is offered starting from a phenomenological model of wall-bounded turbulence (1, 2). The calculations follow closely Ref. (3).

An idealized SBL is defined as the lowest part of the atmospheric boundary layer (adjacent to the surface) where the flow is high Reynolds number, horizontally homogeneous and stationary, with no subsidence. All averaged atmospheric quantities are invariant with respect to the streamwise and spanwise directions, and depend only on height (z) from the surface. The Turbulence Kinetic Energy (TKE) equation is then a balance between mechanical production and dissipation

$$u_*^2 \frac{\partial U}{\partial z} = \epsilon, \qquad [1]$$

where U is the mean wind speed (in the streamwise direction), u_* is the friction velocity, and ϵ is the TKE dissipation rate.

To obtain a link between the mean wind speed and friction velocity, a closure for ϵ is needed. To this end, it was hypothesized (1, 2) that turbulent structures of half streamwise and vertical extension s_e are attached to the surface (red circles in Fig. 5b,c). The turnover velocity of these structures was related to ϵ using the Kolmogorov 4/5 law for the third-order velocity structure function (4),

$$w_e(s_e) \propto (\epsilon s_e)^{1/3}. \qquad [2]$$

The momentum flux u_*^2 through a given surface at a height z (dashed lines in Fig. 5b,c of the main text) then relates to the vertical transport of mean wind momentum by the turbulent structures as

$$u_*^2(z) \propto w_e(s_e)[U(z+s_e) - U(z-s_e)] \propto w_e(s_e)\ \frac{\partial U}{\partial z}\ 2s_e. \qquad [3]$$

The TKE dissipation is obtained by using Eq. 3 in Eq. 2. Using this result in Eq. 1, Eq. 2 of the main text is obtained

$$\frac{\partial U}{\partial z} = \frac{u_*}{\kappa s_e}, \qquad [4]$$

as well as the scaling $w_e \propto u_*$.

In Eq. 3, wave-induced fluctuations were not separated from turbulent fluctuations, as done in Ref. (3). Rather, we consider u_*^2 to be the average over contributions for different wavelengths $\tilde{u}_*^2(k)$ weighted by a PDF $p(k)$, i.e.

$$u_*^2 = \int \tilde{u}^2(k)p(k)dk = \kappa\epsilon^{1/3}2\partial_z U\overline{s_e}^{4/3}, \qquad [5]$$

where the mean scale $\overline{s_e}$ reads

$$\overline{s_e} = \left[\int p(k)s_e^{4/3}(k))dk\right]^{3/4}. \qquad [6]$$

Using this approach, which does not rely on the triple decomposition of atmospheric quantities (5), allows representation of the *bulk* effect of waves on atmospheric turbulence without having to distinguish between (i) the energy exchange between wave-induced components and turbulent components (6, 7) (ii) the direct modulation of turbulence by the wavy surface (3, 8).

An MEP consistency argument for dU/dz. To illustrate the connection between Eq. 4 and the Maximum Entropy Production (MEP) principle, consider a gradient-diffusion closure for $\overline{u'w'}(z)$ given by

$$\overline{u'w'} = -K_t\frac{dU}{dz} = -\left(l_m(z)\frac{dU}{dz}\right)^2, \qquad [7]$$

where K_t is the eddy-diffusivity and $l_m(z)$ is an unknown mixing length set by boundary conditions on the flow. The turbulent kinetic energy production, assumed to be roughly balancing ϵ (or simply proportional to it), as in Eq. 1, is given by

$$\epsilon = -\overline{u'w'}\frac{dU}{dz} = -\left(l_m(z)\frac{dU}{dz}\right)^2\frac{dU}{dz}. \qquad [8]$$

As discussed in the main text on page 5, in the roughness sublayer only bulk quantities are assumed to be physical. For what follows and to be applicable to the logarithmic layer and to the roughness sublayer, the bulk dissipation rate, i.e. the depth-integrated $\epsilon(z)$ up to a height h is considered and is given as

$$\epsilon_b(h) = -\int_0^h \left(l_m(z)\frac{dU}{dz}\right)^2\frac{dU}{dz}dz. \qquad [9]$$

Maximizing the magnitude of ϵ_b is equivalent to maximizing entropy production as discussed in Ref. (9). This maximization can be solved by setting the Lagrangian of the system as $L_a = l_m(z)^2\dot{U}^3$ where $\dot{U} = dU/dz$ (used for notation consistency with Hamiltonian mechanics). The Euler-Lagrange equation then reduces to

$$\frac{\partial L_a}{\partial U} - \frac{d}{dz}\left(\frac{\partial L_a}{\partial \dot{U}}\right) = 0 - 3\frac{d}{dz}l_m(z)^2\dot{U}^2 = 0. \qquad [10]$$

Integrating with respect to z yields

$$l_m(z)^2\dot{U}^2 = c_1, \quad \frac{dU}{dz} = \frac{\sqrt{c_1}}{l_m(z)}. \tag{11}$$

A constant $\overline{u'w'} = u_*^2$ sets $c_1 \sim u_*^2$. And $l_m(z) = s_e$ recovers Eq. 4. In short, the resulting velocity profile satisfies Eq. 11 when boundary conditions force the shape of $l_m(z)$ to also satisfy the MEP principle (at least within the confines of gradient-diffusion arguments). These assumptions and the MEP approach taken here are not identical to those invoked in the phenomenological model (e.g. local isotropy required when employing Eq. 2) thereby adding robustness to Eq. 4.

Height of the roughness sublayer. The wind-dependent roughness sub-layer height h_r discussed in the main text (Fig. 1) is here compared to other heights in Fig. S2a. As shown in the log-log inset, h_r (black solid line) and z_0 (dashed line) follow a power law whose exponent is negative for winds lower than 3 m s^{-1}, and tends towards $u_*^{2.5}$ for wind speeds larger than 8 m s^{-1}. These two regimes are reminiscent, of the dependence of z_0 with u_*, which is usually parameterized as (10)

$$z_0 = z_0^v + \alpha_c \frac{u_*^2}{g}. \tag{12}$$

where α_c is the Charnock coefficient, which depends on U_{10} or u_* (see e.g. Ref. 11). Through Eq. 5 of the main text, this dependence is hence similar to that of h_r.

In wind-over-waves models (e.g. 7, 12–14), the impact of waves on the SBL can encompass the contribution from breaking waves through air-flow separation (15), and the contribution of waves with low steepness through wave-induced stress (16, 17). For a given wind-wave field, both mechanisms decay exponentially with height, and dashed-dotted and dotted lines correspond to their vertical integral length scales divided by 100. When scaled, the integral length scales of both mechanisms seems to have the same order of magnitude of h_r, but do not exhibit the correct power-law exponent (as shown in the log-log inset). Characterizing as a whole the wind-over-wave coupling, h_r thus encompasses both wave-induced stress and air-flow separation mechanisms, and corresponds to the height of an *effective roughness element*, representing the bulk effect of individual wind-waves on the energy-containing eddies in the SBL.

Coupling with wave-induced motions. It is however well known that above the roughness sublayer, wave-induced motions and wave-induced stress induce a deviation in the wind profile from its logarithmic form (e.g 5–7). This in turn affects the wind speed at the bottom of logarithmic layer and hence the properties of the roughness sublayer.

In the presence of wave-induced stress, the TKE dissipation is modified (see Ref. 3), leading to a wind gradient of the form (see also Ref. 18)

$$\frac{dU}{dz}(z) = \frac{u_*[1-\alpha_c(z)]^{3/4}}{\kappa s_e(z)}, \quad \text{for } z \geq h_r \tag{13}$$

where $\alpha_c = (u_*^2 - \overline{u'w'})/u_*^2 < 1$ is the coupling coefficient that accounts for attenuation of the turbulent momentum flux $\overline{u'w'}$ as height decreases, due to motions being increasingly coherent with the waves (i.e. the presence of wave-induced stress, see Refs. 5, 19). In the roughness sublayer, as mentioned above, it is assumed that turbulent motions are indistinguishable from wave-induced motions, and hence

$$\frac{dU}{dz}(z) = \frac{u_*}{\kappa s_e}, \quad \text{for } z \leq h_r \tag{14}$$

The continuity of the mean wind shear at the top of the roughness sublayer leads to a relation between the size of roughness-sublayer energy-containing eddies and the height of the roughness sublayer that depends on wave-induced stress at the bottom of the roughness sublayer

$$s_e = h_r[1-\alpha_c(h_r)]^{-3/4}. \tag{15}$$

As discussed in the main text, this interesting relation reveals that the properties of roughness-sublayer energy-containing eddies are coupled with wave-induced motions aloft.

In general, the dependence of α_c with height is non trivial and analytical calculations of h_r are not possible. In Fig. S2a we show (red line) h_r using a wind-dependent profile of α_c from the wind-over-waves model of Ref. (7). In this model, α_c includes both airflow separation events and wave-induced stress to yield a momentum flux and short wind-wave spectrum consistent with measurements and the COARE parameterization. The power-law dependence of h_r discussed above is affected by the presence of wave-induced motions the logarithmic sublayer (see inset). However, the order of magnitude of h_r is similar to that when wave-induced motions are neglected (compare black and red lines). In Fig. S2b, we further show the values of the coupling coefficient at the top of the roughness sublayer (dashed line) and the resulting ratio between s_e and h_r (solid line). The latter is discussed in the main text (page 5).

For completeness, a simplified case for which the roughness sublayer height can be computed explicitly is illustrated. To that end, a simplified height dependence of wave-induced stress is assumed (20) and given as

$$\alpha_c(z) = \alpha_c^0 \mathcal{H}(h_w - z), \tag{16}$$

where $\mathcal{H}$ is the Heaviside step function, and h_w is the height at which the effect of waves on momentum flux becomes negligible. This expression assumes that the coupling coefficient is constant and equal to α_c^0 below a height h_w, and zero above.

Equation (13) reveals that wave-coherent motions induce a deviation from the logarithmic profile. Nevertheless, by extrapolating a logarithmic profile, a roughness height z_0 can still be defined from the wind at an arbitrary height z, $U(z) = (u_*/\kappa)\log(z/z_0)$. Upon using this expression, the simplified height dependence of α_c, and integrating Eq. 13 from an arbitrary height z down to h_r, the mean wind speed at the roughness sublayer height reads

$$U(h_r) = \frac{u_*}{\kappa}\log\left(\frac{h_r^{(1-\alpha_c^0)^{3/4}}}{z_0} h_w^{1-(1-\alpha_c^0)^{3/4}}\right) \qquad [17]$$

By further using Eq. 15, the mean wind speed and the roughness sublayer height can be expressed as

$$U(h_r) = (u_*/\kappa)(1-\alpha_c(h_r))^{-3/4}, \quad h_r = z_0^{(1-\alpha_c^0)^{-3/4}} h_w^{1-(1-\alpha_c^0)^{-3/4}} e^{(1-\alpha_c^0)^{-3/4}}. \qquad (18a, b)$$

The above expressions show that, as α_c increases, the roughness sublayer height increases from $z_0\exp(1)$, and so does the mean wind speed on top of the roughness sublayer. The limit $\alpha_c \to 1$ is out of the range of the model, since the mean wind shear can no longer be continuous in this regime.

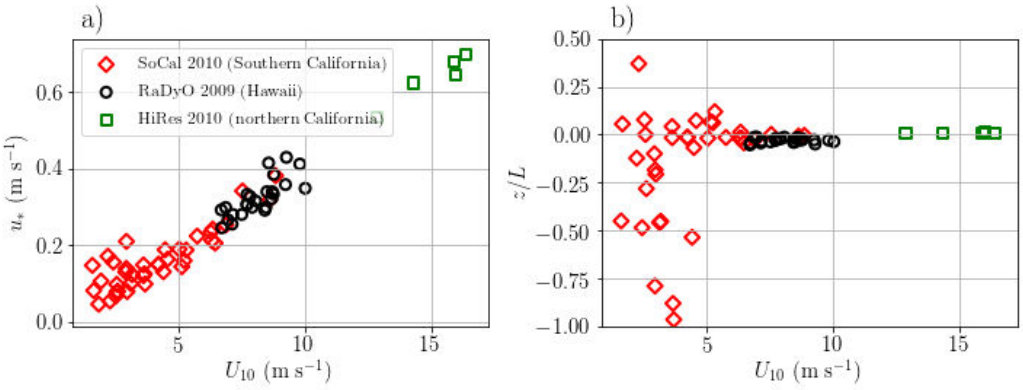

Fig. S1. Environmental variables of the measurements of wave-breaking statistics used in this study, grouped by campaign. (a) Friction velocity and (b) atmospheric stability versus 10-m wind speed. Atmospheric stability was quantified by the dimensionless stability parameter z/L, where z is the height of the measurement, and L the Obukhov length. In the analysis of the main text, only measurements for which $-0.2 \leq z/L \leq 0.2$ have been used.

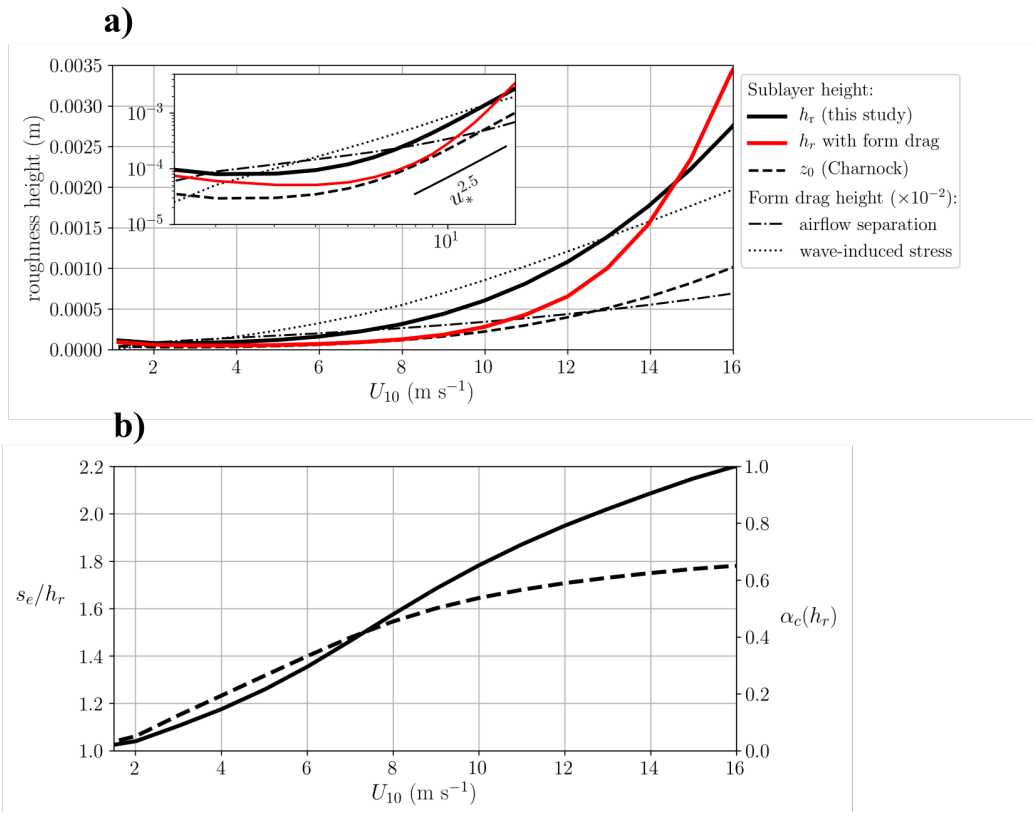

Fig. S2. Properties of the roughness sublayer. (a) Different sublayer heights are compared: the roughness sublayer height (solid line) from this study, the roughness height z_0 using the Charnock parameterization. Also shown are the vertical integral length scales of airflow separation (dotted-dashed line) and wave-induced stress (dotted line) from the wind-over-wave model of Ref. (7). (b) The ratio of the size of roughness-sublayer eddies and the height of the roughness sublayer when wave-induced motions are included in the logarithmic sublayer (solid line, left axis). This ratio has been computed from Eq. 15, using a coupling coefficient at the top of the roughness sublayer (dashed line, right axis) from the wind-over-wave model of Ref. (7).

4.3 Conclusion

In this Chapter we have described the dynamical impact of wind-waves on energy-containing eddies. By entraining fluid during the wave-breaking process, short and steep waves maintain a mean wind gradient in the roughness sublayer, whose length scale and intensity control the size of energy-containing eddies. It was further found that this length scale could be related to a particular wave breaker speed, corresponding to the smallest scale of waves whose breaking properties are not significantly affected by wind-induced drift. The intensity (or speed) of this particular breaker has been used to summarize the overall effect of the complex wind-wave interactions occurring close to the surface without relying on standard theories.

Hence, compared to Chapter 3, this analysis does not rely on a specific wind-over-waves model, and results in a characterization of open-ocean momentum fluxes by means of a measurable quantity, the speed of the breakers, unlike usual parameterizations that rely on the roughness length (see e.g. page 45).

An interesting consequence of this work is to highlight the sensitivity of the near-surface coupling process to the presence of ocean currents. Let us assume that, to first order, the effect of a surface ocean current of streamwise speed U_o is to induce a Doppler shift in the phase speed of waves. Then, the speed c of the smallest waves which are not affected by surface drift (Eq. 1 in the main text of Sec. 4.2) changes such that

$$c + U_o = 2.5 u_*. \tag{4.1}$$

As a consequence, wind stress, and surface drift, must adjust to satisfy this kinematic relation, and also because the energy of attached eddies in the roughness sublayer will be affected by the change of c. Hence the variations of u_* with respect to a situation with no currents are of the order of $U_o/2.5$.

This estimate is not realistic, since a current of 1 m s^{-1} would induce a change in u_* of 0.4 m s^{-1}. Indeed, this exploratory analysis relies on a number of assumptions. First, it is assumed that the kinematic relation (Eq. 1 in the main text of Sec. 4.2) is a general property of the wind-and-waves system, which can be extrapolated beyond the data used in Sec. 4.2. Second, currents certainly have other effects on the wind-and-waves system than just inducing a Doppler shift of the wave speed. As an example, the presence of currents changes the relative wind felt by waves, affecting their growth. It is also associated to the presence of sea-surface temperature fronts, which affect the properties of turbulence aloft [Ayet and Redelsperger, 2019]. Hence, the adjusted equilibrium in the presence of currents is certainly more complex than the simple relation (4.1). Field experiments should be used to understand these processes further.

CONCLUSION

In this thesis we have addressed, from a theoretical perspective, questions related to the organization of near-surface turbulence by wind-waves. As mentioned in Chapter 1, this is a key element of the wind-and-waves coupling, whose understanding would allow going beyond standard parameterizations in use in numerical models, by assessing their limiting assumptions and their sensitivity to environmental parameters. Presently, these parameterizations rely on a description of wind-and-wave interactions through the interaction of turbulent motions with wave-induced motions, coherent with the wave phase. This flow decomposition has proven to be useful for the description of the generation of low-steepness wind-waves [e.g. Miles, 1957, Hara and Belcher, 2002, Kudryavtsev et al., 2014], even though it generally fails at recovering the infamous "inconvenient sea truth", i.e. the linear link between wind speed and the mean squared slope parameter, "to be too fundamental to be ignored, too incomplete to be understood" [Munk, 2009]. Hence, the ability of such a theoretical framework to accurately describe the mechanisms at stake for a realistic multiscale and coupled sea-surface, with, among others, local changes in topology due to wave breaking [Newell and Zakharov, 1992], and a coupling between waves and currents, can be questioned.

In fact, even in the uncoupled case, several numerical studies have revealed the effect of the sea surface on the instantaneous properties of turbulence, beyond the presence of wave-induced motions [Sullivan et al., 2000, 2014, Yang and Shen, 2009, 2010, Suzuki et al., 2011, 2013]. This suggests that turbulent eddies above the sea surface might behave differently than above a flat surface [see e.g. Srinath et al., 2018], e.g. as observed for flow above canopies [Raupach et al., 1996]. In an effort to bridge the gap between these ideas, we have proposed an alternative theoretical framework, based on a phenomenological representation of turbulence, which relates a spectral property of the flow to two of its bulk properties: the vertical momentum flux and TKE dissipation. The spectral property is the wavenumber of the peak of the premultiplied vertical velocity spectrum, equivalently interpreted as the size of energy-containing eddies at a given height (defined on page 30).

The link between the peak wavenumber and the bulk properties of the flow was explored in Chapter 2. This link relies on so-called spectral budgets, which are obtained as a Fourier transform of the Kármán-Howart-Monin equation (for the two-point correlations of the flow). These budgets describe the energy balances at a given wavenumber, and rely on a certain

number of simplifying assumptions. The first assumption is to use a standard Rotta model for the modeling of the energy redistribution between turbulent components, and we showed that such a model was unable to close the spectral budget for a canonical ASL. Instead, we proposed that the timescale of energy redistribution between turbulent components, which is usually a (Rotta) constant, should depend both on stability and on the eddy scale. The second assumption is to use a limited number of parameters to describe the turbulent spectra (what we called "canonical spectra"). We showed that the relation between the spectral peak wavenumber and the variance of vertical velocities is very sensitive to one of these parameters, the high-wavenumber spectral cutoff in the vertical velocity spectrum due to the measuring instrument resolution.

Chapters 3 and 4 then presented two extensions of the phenomenological model to the wind-and-waves coupled system. Those are exemplified in Fig. 4.1 where they are compared to the properties of a logarithmic sublayer (solid black lines).

First, the geometrical imprint of wind-waves on energy-containing eddies was investigated in Chapter 3. We showed that this imprint was effective mainly for long wind-waves, of the order of 10m, which could change the size of energy-containing eddies at similar heights. Using the phenomenological model, we then showed that this resulted in a change of TKE dissipation which propagates at all heights (blue shadings in Fig. 4.1a). Going one step further, we then proposed that this geometrical imprint could be related to long wind-waves modulating the steepness of shorter waves, which results in organized patches of roughness on the scale of the long waves. Hence the geometrical imprint was proposed to be sensitive to external parameters upon which this modulation depends (currents, slicks, etc.). The exact link between the changes in TKE dissipation and the modulation couldn't be derived, and hence a sensitivity test was carried, resulting in TKE dissipation varying over the range of values shown as blue shadings in Fig. 4.1a. Preliminary results from numerical simulations were presented, aiming at quantifying those variations. Note that, besides these variations, the mean value of TKE dissipation and the mean wind profile deviate from their logarithmic layer counterparts below 0.1 m, due to the presence of wave-induced motions which follow from standard theories (compare the middle of the blue shadings and the black lines).

In Chapter 4 we then investigated the dynamical coupling between wave-breaking events and the geometry of energy-containing eddies. Using the phenomenological model, we defined the so-called roughness sublayer, in which the properties of energy-containing eddies are set by the bulk mean wind shear across the layer (horizontal dashed line in Fig. 4.1). Using wave breaking measurements, the bulk wind shear was related to the phase speed of the most actively breaking waves. These waves were further interpreted as the smallest waves on which wind-induced surface drift has not effect. Smaller waves have a reduced steepness due to wind-induced drift, and hence the intensity of their coupling with the atmosphere through wave breaking is weakened. This work allows a description of the coupled wind-and-waves system through a measurable speed, that of the most actively breaking waves. It does not rely on a theoretical paradigm, such as the coupling of turbulence with wave-induced motions, and hence allows a description of the complex zoology of wind-and-wave motions close to surface by means of very few parameters. It also allows inclusion of external parameters (currents, fronts) in the wind-over-waves coupled system through the modulation of three-way coupling between turbulence, wave breaking events, and surface drift, even though this would require additional

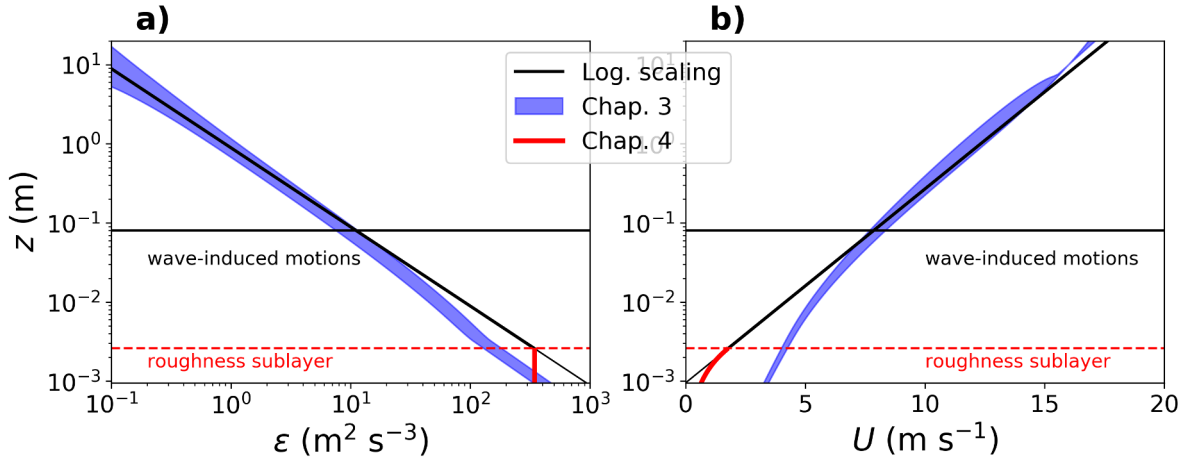

Figure 4.1: Example of the implications of the processes proposed in Chapters 3 and 4 on (a) TKE dissipation and (b) mean wind speed. The ASL if forced with a 10-m mean wind of 16 m s^{-1}, corresponding to $u_* = 0.7$ m s^{-1} on top of wind-waves. Solid line is to logarithmic-layer scaling of TKE dissipation $\epsilon = u_*^3/(\kappa z)$ and mean wind $U = (u_*/\kappa)\log(z/z_0)$, where z_0 follows the Charnock parameterization. The blue shadings are computed from the wind-over-waves model presented in Sec. 3.2, and the scatter corresponds to variations of the anisotropy factor of energy-containing eddies as in Figs. 3a and 5 of Sec. 3.2. The red lines are the TKE dissipation and mean wind profiles in the roughness sublayer, whose height and properties follow the derivation in Sec. 4.2.

observations, given its complexity (see page 167 and below).

One consequence of this last work is that the size of energy-containing eddies, and hence TKE dissipation, should be constant with height in this sublayer (red line in Fig. 4.1a). Similarly, the mean wind is linear in this sublayer (red line in Fig. 4.1b). It should be stressed that both roughness-sublayer profiles, even though they are a *consequence* of the model, are not one of its *necessary* features: their evaluation from data, which is a difficult task, can yield different results depending on the averaging method. Only the bulk (i.e. vertically-averaged) quantities over the roughness sublayer are important for the properties of energy-containing eddies.

One of the main limitations of the theoretical framework presented in this thesis is the fact that the spectral link and subsequent phenomenological model disregard, by definition, the phase of the turbulent motions. Hence it does not enable an instantaneous description of their modulation by wind-waves, which would require e.g. using a wavelet-transformed Kármán-Howart-Monin equation [see, recently, Dubrulle, 2019]. This description would allow including effects more directly related to the instantaneous modulation of coherent structures described in Chapter 1.

This thesis opens several promising avenues, which shall guide future work. First the analysis carried in Chapter 2 revealed that the standard models of the energy-redistribution term in use in numerical models (the Rotta model) might fail in closing the ASL turbulent budget

for non-neutral conditions. A possible alternative model would rely on a spectral analysis to compute a spectrum- and stability-dependent energy-redistribution term. This should be tested in Large Eddy Simulations and compared with Direct Numerical Simulations. This failure of the Rotta model also highlights that, in the presence of wind-waves which introduce additional (coupled) forcings in the system, the need to reconsider the energy-redistribution term is even more pregnant. This could guide the analysis of direct numerical simulations over moving waves [e.g. Sullivan et al., 2000, Yang and Shen, 2010], but should also be addressed from a theoretical perspective (along the lines of Sec. 2.2).

The analysis of Chapters 3 and 4 set a first step towards the understanding of the relation between turbulent fluctuations and bulk variables (TKE dissipation and, more importantly, the turbulent momentum flux), in the presence of a multiscale and coupled sea surface. From a theoretical standpoint, an important next step would be to understand how the averaging operation, which filters some of these scales, affects the bulk variables, in order to assess the scale-dependence and limitations of parameterizations in use in numerical weather prediction models [a similar approach than Bachman et al., 2017].

As stressed in Chapter 4, the complexity of the relation between turbulence and bulk variables arises not only from the direct coupling between wind and waves, but also from the surface drift induced by the wind, which sets the scale of the most actively breaking waves [this is a similar argument than Csanady, 1985]. This invites going beyond the traditional thinking of wind-and-wave interaction, in which the governing parameters are the relative wave age and stability, by explicitly including surface drift in the wind-and-waves system. This would allow a better understanding of how the wind-and-waves equilibrium adjusts to variations in environmental parameters: the presence of swell, ocean currents and associated sea-surface temperature fronts, slicks, and also changes in boundary-layer scale turbulence conditions. These processes all have identifiable signatures on the short wind-waves roughness [Wang et al., 2019], and should hence affect the wind-and-waves system. Besides theoretical approaches, along the line of this thesis or of Ayet and Redelsperger [2019], advances should be driven by targeted field or remote sensing experiments. Those experiments should aim at capturing the simultaneous spatio-temporal features of near-surface wind, waves and currents, using multiple-point measurements [e.g. Buckley and Horstmann, 2020], and should span a variety of environmental conditions (e.g. the upcoming SWOT mission and associated field experiments).

To guide those experiments, the spectral link needs to be better understood, along the lines of Sec. 2.3. In fact, in Chapters 3 and 4 only the bulk formulation of the phenomenological model has been used, and the spectral link has not been exploited. However, as mentioned in Chapter 1, the presence of roughness elements can have an imprint on the spectral properties of turbulence, besides affecting energy-containing eddies. In particular, the associated form drag can result in a shortcutting of the inertial turbulent cascade, leading to enhanced TKE dissipation in the roughness sublayer. Hence, linking the proposed modifications of TKE dissipation (Fig. 4.1a) to spectral properties of turbulence other than the peak wavenumber seems a promising research avenue, which could support the design of experiments [see, recently, Ortiz-Suslow and Wang, 2019].

APPENDICES

ANNEX A: SOME STEPS FOR THE DERIVATION OF THE SPECTRAL BUDGET

In this Annex we give some details on the steps needed to derive the spectral budget presented in Sec. 2.1. We start from a Reynolds decomposition of the flow

$$u = \overline{u} + u'. \tag{4.2}$$

Within this decomposition, the Kármán-Howarth-Monin equation for the spatial correlation tensor

$$B_{ij}(\boldsymbol{r}) = \overline{u_i'(\boldsymbol{0})u_j'(\boldsymbol{r})} \tag{4.3}$$

is readily obtained from the equation for the fluctuations, yielding

$$\begin{aligned}\partial_t B_{il} + \overline{u}_j\partial_j B_{il} + B_{jl}\partial_j\overline{u_i} + B_{ij}\partial_j\overline{u_l} + \overline{u_l'(\boldsymbol{r})\partial_j(u_j'u_i') + u_i'\partial_j(u_j'(\boldsymbol{r})u_l'(\boldsymbol{r}))} \\ = -\overline{u_l'(\boldsymbol{r})\partial_i p' + u_i'\partial_l p'(\boldsymbol{r})} + \mathrm{B} + \mathrm{DS}\end{aligned} \tag{4.4}$$

where $\boldsymbol{r}$ is the three-dimensional coordinate vector, u denotes $u(\boldsymbol{0})$ and B and DS are the buoyancy and dissipation terms respectively. Their expressions can be found in Panchev [1971]. The dependence of the turbulent field with time has been dropped.

For a horizontally homogeneous, stationary ASL with no subsidence, the equation for the vertical covariance tensor B_{33} reads

$$\overline{u_3'(\boldsymbol{r})\partial_j(u_j'u_3') + u_3'\partial_j(u_j'(\boldsymbol{r})u_3'(\boldsymbol{r}))} = -\overline{u_3'(\boldsymbol{r})\partial_3 p' + u_3'\partial_3 p'(\boldsymbol{r})} + \mathrm{B} + \mathrm{DS} \tag{4.5}$$

The spectrum can then be computed by Fourier transform of the correlation tensor

$$\tilde{F}_{u_iu_j}(k) = \int B_{ij}(x)e^{ikx}dx, \tag{4.6}$$

yielding the spectral budget for the vertical velocity spectrum $\tilde{F}_{ww}$

$$\tilde{T}(k) + \frac{g}{T}\tilde{F}_{wT}(k) - 2\nu k^2 \tilde{F}_{ww}(k) = 0. \tag{4.7}$$

Studies such as Heisenberg [1948], Tchen [1954], Panchev [1971] and more recently Katul et al. [2012] use an integrated form of the above budget. More precisely, if the previous budget is integrated between k and ∞, we get

$$\int_k^\infty \tilde{T}(s)ds + \frac{g}{T}\int_k^\infty \tilde{F}_{wT}(s)ds + 2\nu \int_0^k s^2 \tilde{F}_{ww}(s)ds = 2\nu \int_0^\infty s^2 \tilde{F}_{ww}(s)ds \tag{4.8}$$

where $\int_0^\infty s^2 \tilde{F}_{ww}(s)ds$ is the total dissipation for the vertical fluctuations denoted by $\epsilon/3$.

ANNEX B: COMPARISON OF SEVERAL ROTTA CONSTANTS

Due to the variety of notations in the turbulence literature, in this Annex we compare the bulk budget considered in Sections 2.1 and 2.2, with the budgets considered in other works, and compute the associated Rotta constants in our notations.

We are considering a budget of the form

$$\frac{1}{2}\frac{\partial \sigma_w^2}{\partial t} = 0 = B + R_w - \frac{\epsilon}{3} \tag{4.9}$$

with

$$R_w = -\frac{C_R}{\tau}(\sigma_w^2 - \frac{2}{3}e) + \alpha_P P_m - \frac{2}{3}(1-\beta_B)B, \tag{4.10}$$

and $\tau = e/\epsilon$, and a spectral budget of the form

$$\frac{1}{2}\frac{\partial \tilde{F}_{ww}(k)}{\partial t} = 0 = \tilde{B}(k) + \tilde{R}_w(k) - \tilde{T}(k), \tag{4.11}$$

with

$$\tilde{R}_w(k) = -\frac{\tilde{C}_R}{\tilde{\tau}(k)}\left(\tilde{F}_{ww}(k) - \frac{2}{3}\tilde{\phi}(k)\right). \tag{4.12}$$

Taking the example of the bulk budget, the notation differences with the literature can be separated into two categories.

1. a difference in the considered budget, i.e instead of a half-variance budget, a budget of the form
$$\frac{\alpha}{2}\frac{\partial \sigma_w^2}{\partial t} = 0 = \alpha B + R_w^\alpha - \alpha\frac{\epsilon}{3} \tag{4.13}$$
with $\alpha \neq 1$, and involving R_w^α which we would like to link to R_w of our notations. The half variance budget then reads
$$\frac{1}{2}\frac{\partial \sigma_w^2}{\partial t} = 0 = B + \frac{1}{\alpha}R_w^\alpha - \frac{\epsilon}{3} \tag{4.14}$$

and hence $R_w = \frac{1}{\alpha} R_w^\alpha$. In the case of a spectral budget [Besnard et al., 1996], the correction should also apply to the non-linear transfer term.

2. A difference in the definition of the quantities considered in the return-to-isotropy term (or the non-linear term in the case of the spectral budget), for example

$$R = \frac{C_R^\alpha}{\tau}(\alpha\sigma_w^2 - \frac{2}{3}\alpha e), \tag{4.15}$$

with $\alpha \neq 1$ and C_R^α the Rotta constant we want to link to our notations. In this case, factoring α out leads to $C_R = \alpha C_R^\alpha$. This also works in the case of the coefficient for the non-linear term.

BOU-ZEID ET AL. Bou-Zeid et al. [2018] follow closely the notations used in the present work, by also considering half variance (bulk) budgets. In their work, the mean value of C_r is 0.9, with some variations (0.7 to 1.1) based on DNS results. Theoretical bounds for C_r are also derived to ensure a physically-sound critical Richardson number.

CANUTO ET AL. Canuto et al. [2001] consider a full variance budget, i.e. a budget on σ_w^2 (instead of $0.5\sigma_w^2$). Hence, in this budget, the buoyancy term is equal to $2B$ and the return-to-isotropy term to $2R_w$ (case 1 above, with $\alpha = 2$).. Their model for the return-to-isotropy term is (their Equation (7a))

$$2R_w = -2\tau_{\rho v}^{-1}(\sigma_w^2 - \frac{2}{3}e) + \frac{4}{5}eS_{33} - \frac{4}{3}(1-\beta_B)B - \mathrm{RD}, \tag{4.16}$$

where S_{ij} is the strain tensor (defined below).

The last (rapid-distortion) term RD, reads

$$\mathrm{RD} = -\alpha_1\Sigma_{33} - \alpha_2 Z_{33}. \tag{4.17}$$

The two quantities, Σ_{33} and Z_{33} depend on the strain tensor

$$S_{ij} = \frac{1}{2}(\delta_{13} + \delta_{31})\frac{dU}{dz}$$

and on the vorticity tensor

$$V_{ij} = \frac{1}{2}(\delta_{13} - \delta_{31})\frac{dU}{dz} \tag{4.18}$$

where δ_{ij} the Kronecker Delta. Those two expressions are written for a horizontally homogeneous flow in the absence of subsidence, and with the x direction aligned with the mean wind U.

The two quantities, Σ_{33} and Z_{33}, then read

$$\Sigma_{33} = S_{31}b_{13} + S_{31}b_{31} - \frac{2}{3}[S_{13}b_{13} + S_{31}b_{31}] = \frac{1}{3}\overline{u'w'}\frac{dU}{dz} \tag{4.19}$$

$$Z_{33} = V_{31}b_{13} + V_{31}b_{31} = -\overline{u'w'}\frac{dU}{dz} \tag{4.20}$$

where $b_{ij} = \tau_{ij} - \frac{2}{3}\delta_{ij}e$ is the anisotropy tensor. This leads to the following expression of return-to-isotropy term

$$R_w = -\tau_{\rho v}^{-1}(\sigma_w^2 - \frac{2}{3}e) - \frac{2}{3}(1-\beta_B)B + \frac{1}{2}(\alpha_2 - \frac{\alpha_1}{3})P_m \tag{4.21}$$

where $P_m = -\overline{u'w'}dU/dz$ is the production term in the TKE equation.

Following the notations of Canuto et al. [2001], the constant $\tau_{\rho v}^{-1}$ is linked to a turbulence timescale τ^C by defining a constant λ (their equation (12))

$$\lambda = \tau_{\rho v}(\tau^C)^{-1} \tag{4.22}$$

with $\tau^C = 2e/\epsilon$ (notice the factor 2, unlike the definition of τ in the present work). By identifying this expression with Equation (4.10), we get the following expression for the Rotta constant

$$C_R = (2\lambda)^{-1} \tag{4.23}$$

Two models are proposed for λ (their equations (20b) and (22c) respectively): $\lambda = 2/5$ which leads to $C_R = 1.25$, and $\lambda = (15/4)0.127$, leading to $C_R = 1.05$.

The two constants α_1 and α_2 are linked to other constants λ_2 and λ_3 (in the Canuto et al. [2001] notation, their equation (12)) as

$$\alpha_1 = 1 - \frac{2\lambda_2}{\lambda}, \quad \alpha_2 = 1 - \frac{2\lambda_3}{\lambda} \tag{4.24}$$

For the two models mentioned above, the final constant for the rapid distortion term is

$$\frac{1}{2}(\alpha_2 - \frac{\alpha_1}{3}) = \alpha_P = \begin{cases} 0.225 \\ 0.15 \end{cases} \tag{4.25}$$

The buoyancy correction coefficient β_B is equal to 1/2 for model 1 and to 0.48 for model 2. Those values are summarize in Table 4.1

ZEMAN AND TENNEKES Zeman and Tennekes [1975] consider full variance budgets as in the previous example. The notations are slightly different, and the return-to-isotropy term reads (their equation (17))

$$2R_w = -\frac{C_1}{\tau^Z}(\sigma_w^2 - \frac{2}{3}e) + 2\alpha_0 q^2 S_{33} + \alpha_1 q^2 A_{33}^s + \gamma_1 q^2 A_{33}^r \tag{4.26}$$

where C_1/τ^Z, α_0, α_1 and γ_1 are constants defined in Zeman and Tennekes [1975], and $q^2 = 2e$. The terms A^s_{33} and A^r_{33} are, as in the Canuto et al. [2001] model, expressed as a function of the strain and vorticity tensors, and read

$$q^2 A^s_{33} = \frac{2}{3}\overline{u_1' u_3'}\frac{dU}{dz} \tag{4.27}$$

$$q^2 A^r_{33} = -2\overline{u_1' u_3'}\frac{dU}{dz}. \tag{4.28}$$

This yields the following return-to-isotropy

$$R_w = -\frac{C_1}{2\tau^Z}(\sigma_w^2 - \frac{2}{3}e) + (\gamma_1 - \frac{1}{3}\alpha_1)P_m \tag{4.29}$$

where $P_m = -\overline{u'w'}dU/dz$ and $\tau^Z = 2e\beta/\epsilon$, and hence

$$C_r = C_1/4\beta. \tag{4.30}$$

Using simplified bulk budgets, Zeman and Tennekes [1975] further evaluate the constants C_1/β, α_1 and γ_1 for different experimental data, based on measured turbulent variances. The resulting Rotta and rapid distortion constants are presented in Table 4.1. Case numbers are the same than in Zeman and Tennekes [1975].

Note that in Equation (20) of Zeman and Tennekes [1975], the σ_w^2 bulk budget is normalized by $\overline{\epsilon}$, where $\overline{\epsilon} = P_m$, and reads

$$2\left[-\frac{C_1}{2\beta}\frac{1}{2e}\left(\sigma_w^2 - \frac{2}{3}e\right) + \gamma_1 - \frac{1}{3}\alpha_1 - \frac{1}{3}\right] = 0. \tag{4.31}$$

BESNARD AND COWORKERS Besnard et al. [1996] derive a spectral budget for the half three-dimensional spectra of vertical velocity E_{33} and TKE E. If we assume isotropic turbulence and Kolmogorov inertial range scaling, those are linked to the streamwise spectra as $E_{33} = \frac{1}{2}\frac{55}{24}\tilde{F}_{ww}$ and $E = \frac{55}{33}\tilde{\phi}$ [see, e.g. Banerjee et al., 2016] (E_{33} and E are the notations in Besnard et al. [1996], Clark and Zemach [1995], while $\tilde{F}_{ww}$ and $\tilde{\phi}$ are the spectra used in the present work).

We are thus in a situation where case 1 and case 2, defined above, are combined. The following return-to-isotropy for the vertical component is considered in Besnard et al. [1996]

$$\frac{24}{55}\tilde{R}_w = -c_m k\sqrt{kE}(E_{33} - \frac{1}{3}E) \tag{4.32}$$

which, in the present notations, reads, assuming that the norm of the three-dimensional wavenumber (considered in Besnard et al. [1996]) and the streamwise cut (denoted by k),

	C_R	α_P	β_B
Pope [2000]	0.9	N/A	N/A
Zeman and Tennekes [1975] cases			
1	0.81	0.18	N/A
2 (atmospheric surface layer)	0.95	0.05	N/A
3	0.49	0.15	N/A
4 (atmospheric surface layer)	0.87	0.12	N/A
5	0.67	0.15	N/A
6	0.44	0.14	N/A
7	0.48	0.10	N/A
Canuto et al. [2001]			
model 1 (renormalization group method)	1.25	0.225	1/2
model 2 (surface layer scaling)	1.05	0.15	0.48

Table 4.1: Values of the Rotta constant C_r and the rapid-distortion correction constants for several works.

are the same

$$\tilde{R}_w = -\frac{55}{24}\frac{c_m}{2}k\sqrt{\frac{55}{33}k\tilde{\phi}}\left(\frac{55}{24}F_{ww} - \frac{2}{3}\frac{55}{33}\tilde{\phi}\right) \tag{4.33}$$

$$\sim -\frac{55}{24}\frac{1}{2}\left(\frac{55}{24}+\frac{55}{33}\right)\left(\frac{55}{33}\right)^{1/2}\frac{c_m}{2}k\sqrt{k\tilde{\phi}}\left(F_{ww} - \frac{2}{3}\tilde{\phi}\right) \tag{4.34}$$

$$\sim -2.93c_m k\sqrt{k\tilde{\phi}}\left(F_{ww} - \frac{2}{3}\tilde{\phi}\right) \tag{4.35}$$

And c_m is determined from

$$c_m \sim \frac{26}{9}c_2 \tag{4.36}$$

with $c_2 = 0.148$ a constant associated to the Leith [1967] non-linear transfer model. This leads to $c_m = 0.42$, and in our notations, to $\tilde{c}_r \sim 2.93c_m = 1.2$. We should again stress that this expression is valid if we assume isotropy, and we do an approximation of the coefficients (Eq. (4.34)).

The value of c_m was chosen to match experiments Clark [1992], but as mentioned in Clark and Zemach [1995]: "There is some experimental evidence, admittedly inconclusive, that this is the proper behavior for the anisotropic spectral components of stress. [...] More decisive experiments would be needed to discriminate between Eq. (4.36) and other choices for c_m, and to test the general adequacy of [the spectral budget] to describe the decay of the deviatoric components of the spectral tensor."

KATUL ET AL. Katul et al. [2013] consider co-spectral budgets, and hence the Rotta constant to be considered is equal to twice the constant considered in the present work. Their value is consistent with Pope [2000] and Bou-Zeid et al. [2018] value.

ANNEX C: DETAILS ON THE PRELIMINARY NUMERICAL SIMULATION

The numerical simulations presented in Sec. 3.3 were performed using the Meso-NH code [Lafore et al., 1997, Lac et al., 2018], in a configuration similar to Stevens et al. [2014]. As shown in Fig. 3.2a, the simulation was carried in a doubly-periodic box, with a resolution of 0.5 m. The flow was forced by a constant pressure gradient at all levels and an initial uniform wind of 10 m s^{-1} which, at equilibrium, results in a friction velocity $u_* \sim 0.22$ m s^{-1}. The roughness pattern was set to vary sinusoidally around a mean value by ±75% (red and blue stripes in Fig. 3.2a). This mean value is was computed from the Charnock parameterization which, as discussed on page 45, is such that $z_0 = \alpha_c u_*^2/g$ where g is the gravity acceleration, u_* the friction velocity, and α_c a wind-dependent Charnock constant [see e.g. the COARE parameterization, Edson et al., 2013]. Here, $u_* \sim 0.22$, yielding $z_0 \sim 2\times10^{-4}$. The box extends up to 300 m, and here we only show the first 60 m. Figure 3.2b shows the resulting mean wind speed, with, in particular, $U_{10} \sim 6$ m s^{-1}. The differences between the different cases are sensitive to the averaging procedure, and it is hence out of the scope of this preliminary study to discuss them.

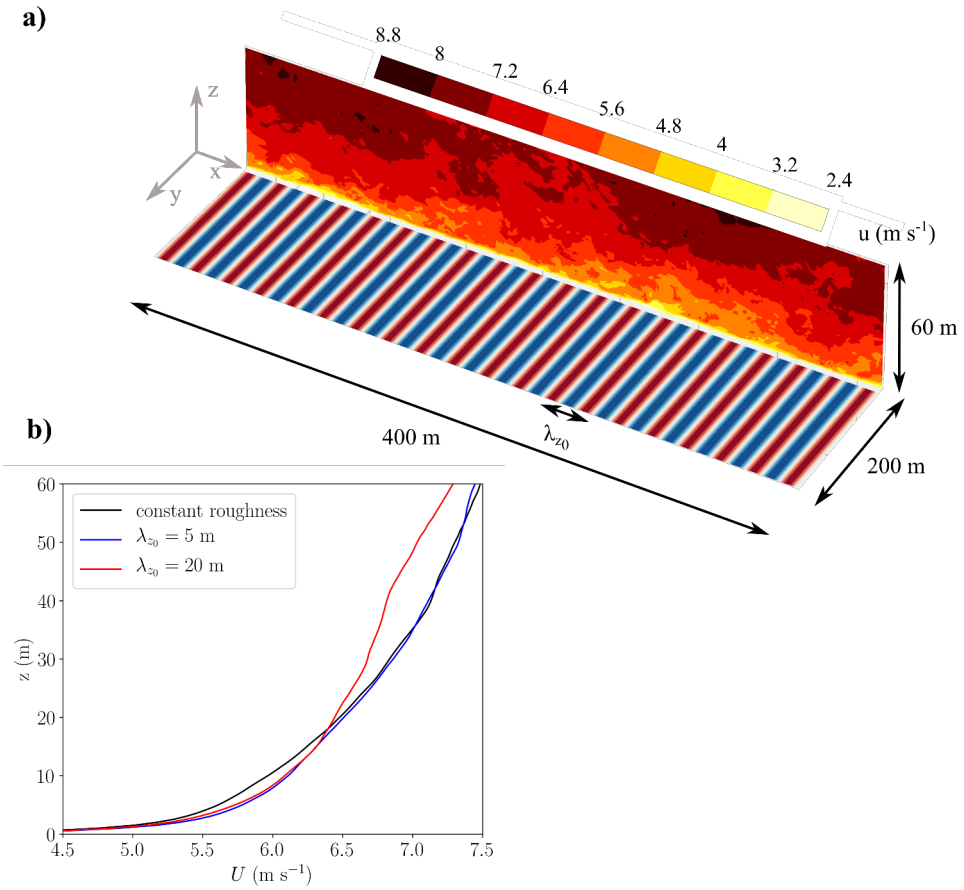

Figure 4.2: (a) Configuration of the LES, showing in particular a snapshot of streamwise velocity at the center of the simulation after 8h (corresponding to a statistically equilibrated turbulent regime, (x,z) panel), and the modulation coefficient of surface roughness around its mean value ((x,y) panel, red and blue correspond to the maxima and minima respectively). (b) Spatially averaged streamwise velocity (i.e. mean streamwise wind) as a function of height.

BIBLIOGRAPHY

Ronald J Adrian. Hairpin vortex organization in wall turbulence. *Physics of Fluids*, 19(4): 041301, 2007.

Espen Åkervik and Magnus Vartdal. The role of wave kinematics in turbulent flow over waves. *Journal of Fluid Mechanics*, 880:890–915, 2019.

William Anderson. Amplitude modulation of streamwise velocity fluctuations in the roughness sublayer: evidence from large-eddy simulations. *J Fluid Mech*, 789:567–588, 2016. doi: 10.1017/jfm.2015.744.

Alex Ayet and Jean-Luc Redelsperger. An analytical study of the atmospheric boundary-layer flow and divergence over an sst front. *Quarterly Journal of the Royal Meteorological Society*, 145(723):2549–2567, 2019.

Scott D Bachman, Baylor Fox-Kemper, and Brodie Pearson. A scale-aware subgrid model for quasi-geostrophic turbulence. *Journal of Geophysical Research: Oceans*, 122(2):1529–1554, 2017.

Promode R Bandyopadhyay. Rough-wall turbulent boundary layers in the transition regime. *Journal of Fluid Mechanics*, 180:231–266, 1987.

T Banerjee and GG Katul. Logarithmic scaling in the longitudinal velocity variance explained by a spectral budget. *Physics of Fluids*, 25(12):125106, 2013.

T Banerjee, D Li, J-Y Juang, and G Katul. A spectral budget model for the longitudinal turbulent velocity in the stable atmospheric surface layer. *Journal of the Atmospheric Sciences*, 73(1): 145–166, 2016. doi: 10.1175/JAS-D-15-0066.1.

Michael L Banner. The influence of wave breaking on the surface pressure distribution in wind—wave interactions. *J Fluid Mech*, 211:463–495, 1990. doi: 10.1017/S0022112090001653.

Michael L Banner and Mark A Donelan. The physical consequences of wave breaking in deep water. In *Breaking waves*, pages 3–20. Springer, 1992. doi: 10.1007/978-3-642-84847-6_1.

Michael L Banner and W Kendall Melville. On the separation of air flow over water waves. *Journal of fluid mechanics*, 77(4):825–842, 1976. doi: 10.1017/S0022112076002905.

SE Belcher. Wave growth by non-separated sheltering. *Europ J Mech-B/Fluids*, 18(3):447–462, 1999. doi: 10.1016/S0997-7546(99)80041-7.

SE Belcher and JCR Hunt. Turbulent shear flow over slowly moving waves. *J Fluid Mech*, 251:109–148, 1993. doi: 10.1017/S0022112093003350.

SE Belcher and JCR Hunt. Turbulent flow over hills and waves. *Annu Rev Fluid Mech*, 30(1): 507–538, 1998. doi: 10.1146/annurev.fluid.30.1.507.

SE Belcher and JC Vassilicos. Breaking waves and the equilibrium range of wind-wave spectra. *J Fluid Mech*, 342:377–401, 1997. doi: 10.1017/S0022112097005740.

A Yu Benilov, OA Kouznetsov, and GN Panin. On the analysis of wind wave-induced disturbances in the atmospheric turbulent surface layer. *Boundary-Layer Meteorology*, 6(1-2): 269–285, 1974. doi: 10.1007/BF00232489.

DC Besnard, FH Harlow, RM Rauenzahn, and C Zemach. Spectral transport model for turbulence. *Theoretical and Computational Fluid Dynamics*, 8(1):1–35, 1996. doi: 10.1007/BF00312400.

Ron F Blackwelder and Helmut Eckelmann. Streamwise vortices associated with the bursting phenomenon. *Journal of Fluid Mechanics*, 94(3):577–594, 1979. doi: 10.1017/S0022112079001191.

Sara Bonetti, Gabriele Manoli, Costantino Manes, Amilcare Porporato, and Gabriel G Katul. Manning's formula and strickler's scaling explained by a co-spectral budget model. *J Fluid Mech*, 812:1189–1212, 2017. doi: 10.1017/jfm.2016.863.

WJT Bos, H Touil, L Shao, and J-P Bertoglio. On the behavior of the velocity-scalar cross correlation spectrum in the inertial range. *Physics of Fluids*, 16(10):3818–3823, 2004. doi: 10.1063/1.1779229.

E Bou-Zeid, X Gao, C Ansorge, and GG Katul. On the role of return to isotropy in wall-bounded turbulent flows with buoyancy. *Journal of Fluid Mechanics*, 856:61–78, 2018.

Denis Bourras, Hubert Branger, Gilles Reverdin, Louis Marié, Rémi Cambra, Lucio Baggio, Christophe Caudoux, Gérard Caudal, Simon Morisset, Nicolas Geyskens, et al. A new platform for the determination of air–sea fluxes (ocarina): Overview and first results. *Journal of Atmospheric and Oceanic Technology*, 31(5):1043–1062, 2014.

Denis Bourras, Rémi Cambra, Louis Marié, Marie-Noëlle Bouin, Lucio Baggio, Hubert Branger, Houda Beghoura, Gilles Reverdin, Boris Dewitte, Aurélien Paulmier, et al. Air-sea turbulent fluxes from a wave-following platform during six experiments at sea. *Journal of Geophysical Research: Oceans*, 124(6):4290–4321, 2019.

Edward F Bradley, RA Antonia, and AJ Chambers. Turbulence reynolds number and the turbulent kinetic energy balance in the atmospheric surface layer. *Boundary-Layer Meteorology*, 21(2):183–197, 1981.

P Bradshaw. 'inactive'motion and pressure fluctuations in turbulent boundary layers. *Journal of Fluid Mechanics*, 30(2):241–258, 1967.

Marc P Buckley and Jochen Horstmann. Field observations of coupled wind-wave dynamics using piv. In *Ocean Sciences Meeting 2020*. AGU, 2020.

Marc P Buckley and Fabrice Veron. Structure of the airflow above surface waves. *J Phys Oceanogr*, 46(5):1377–1397, 2016. doi: 10.1175/JPO-D-15-0135.1.

JA Businger. A note on the businger-dyer profiles. *Boundary-Layer Meteorol*, 42(1-2):145–151, 1988. doi: 10.1007/BF00119880.

Joost A Businger, John C Wyngaard, Y Izumi, and Edward F Bradley. Flux-profile relationships in the atmospheric surface layer. *Journal of the atmospheric Sciences*, 28(2):181–189, 1971.

Vittorio M Canuto, A Howard, Y Cheng, and MS Dubovikov. Ocean turbulence. part i: One-point closure model—momentum and heat vertical diffusivities. *Journal of Physical Oceanography*, 31(6):1413–1426, 2001. doi: 10.1175/1520-0485(2001)031<1413:OTPIOP>2.0.CO;2.

D. V. Chalikov and V. K. Makin. Models of the wave boundary layer. *Boundary-Layer Meteorol*, 56(1-2):83–99, 1991. ISSN 0042-3106. doi: 10.1007/BF00035383.

DV Chalikov and M Yu Belevich. One-dimensional theory of the wave boundary layer. *Boundary-Layer Meteorol*, 63(1-2):65–96, 1993. doi: 10.1007/BF00705377.

H Charnock. Wind stress on a water surface. *Quarterly Journal of the Royal Meteorological Society*, 81(350):639–640, 1955. doi: 10.1002/qj.49708135027.

Cheng Cheng, Weipeng Li, Adrián Lozano-Durán, and Hong Liu. Uncovering townsend's wall-attached eddies in low-reynolds-number wall turbulence. *Journal of Fluid Mechanics*, 889, 2020.

Alejandro Cifuentes-Lorenzen, James B. Edson, and Christopher J. Zappa. Air–sea interaction in the southern ocean: Exploring the height of the wave boundary layer at the air–sea interface. *Boundary-Layer Meteorol*, 169(3):461–482, Dec 2018. ISSN 1573-1472. doi: 10.1007/s10546-018-0376-0. URL https://doi.org/10.1007/s10546-018-0376-0.

Andrea Cimarelli, Elisabetta De Angelis, Javier Jimenez, and Carlo Massimo Casciola. Cascades and wall-normal fluxes in turbulent channel flows. *Journal of Fluid Mechanics*, 796: 417–436, 2016.

Timothy T Clark and Charles Zemach. A spectral model applied to homogeneous turbulence. *Physics of Fluids*, 7(7):1674–1694, 1995. doi: 10.1063/1.868485.

Timothy Truman Clark. Spectral self-similarity of homogeneous anisotropic turbulence. Technical report, Los Alamos National Lab., NM (United States), 1992.

Charles Cox and Walter Munk. Measurement of the roughness of the sea surface from photographs of the sun's glitter. *Journal of the Optical Society of America*, 44(11):838–850, 1954. doi: 10.1364/JOSA.44.000838.

GT Csanady. Air-sea momentum transfer by means of short-crested wavelets. *J Phys Oceanogr*, 15(11):1486–1501, 1985. doi: 10.1175/1520-0485(1985)015<1486:ASMTBM>2.0.CO%3B2.

J. Cuxart, P. Bougeault, and J.-L. Redelsperger. A turbulence scheme allowing for mesoscale and large-eddy simulations. *Quarterly Journal of the Royal Meteorological Society*, 126: 1–30, 2000. doi: 10.1002/qj.49712656202.

Russ E Davis. On prediction of the turbulent flow over a wavy boundary. *J Fluid Mech*, 52(2): 287–306, 1972. doi: 10.1017/S0022112072001429.

James W Deardorff. Aerodynamic theory of wave growth with constant wave steepness. *J. Oceanographical Soc. Japan*, 23(6):278–297, 1967.

Graig E Dorman and Erik Mollo-Christensen. Observation of the structure on moving gust patterns over a water surface ("cat's paws"). *Journal of Physical Oceanography*, 3(1): 120–132, 1973.

Philippe Drobinski, Pierre Carlotti, Jean-Luc Redelsperger, Valery Masson, Robert M Banta, and Rob K Newsom. Numerical and experimental investigation of the neutral atmospheric surface layer. *Journal of the atmospheric sciences*, 64(1):137–156, 2007.

Bérengère Dubrulle. Beyond kolmogorov cascades. *Journal of Fluid Mechanics*, 867, 2019.

James B Edson, Venkata Jampana, Robert A Weller, Sebastien P Bigorre, Albert J Plueddemann, Christopher W Fairall, Scott D Miller, Larry Mahrt, Dean Vickers, and Hans Hersbach. On the exchange of momentum over the open ocean. *J Phys Oceanogr*, 43(8):1589–1610, 2013. doi: 10.1175/JPO-D-12-0173.1.

JB Edson and CW Fairall. Similarity relationships in the marine atmospheric surface layer for terms in the tke and scalar variance budgets. *J Atmos Sci*, 55(13):2311–2328, 1998. doi: 10.1175/1520-0469(1998)055<2311:SRITMA>2.0.CO;2.

Walter Eifler. A hypothesis on momentum and heat transfer near the sea-atmosphere interface and a related simple model. *Journal of marine systems*, 4(2-3):133–153, 1993.

TH Ellison. Turbulent transport of heat and momentum from an infinite rough plane. *Journal of Fluid Mechanics*, 2(5):456–466, 1957.

AL Fabrikant. Quasilinear theory of wind-wave generation. izv. acad. sci. ussr. *Atmos. Oceanic Phys*, 12:524–526, 1976.

Chris W Fairall, Edward F Bradley, David P Rogers, James Bearer Edson, and George S Young. Bulk parameterization of air-sea fluxes for tropical ocean-global atmosphere coupled-ocean atmosphere response experiment. *Journal of Geophysical Research: Oceans*, 101(C2): 3747–3764, 1996.

CW Fairall, Edward F Bradley, JE Hare, AA Grachev, and JB Edson. Bulk parameterization of air–sea fluxes: Updates and verification for the coare algorithm. *J Clim*, 16(4):571–591, 2003. doi: 10.1175/1520-0442(2003)016<0571:BPOASF>2.0.CO;2.

JJ Finnigan and SE Belcher. Flow over a hill covered with a plant canopy. *Quarterly Journal of the Royal Meteorological Society*, 130(596):1–29, 2004.

John Finnigan. Turbulence in plant canopies. *Annual review of fluid mechanics*, 32(1):519–571, 2000. doi: 10.1146/annurev.fluid.32.1.519.

Katherine Fodor, Juan Pedro Mellado, and Michael Wilczek. On the role of large-scale updrafts and downdrafts in deviations from monin–obukhov similarity theory in free convection. *Boundary-Layer Meteorol*, 172(3):371–396, 2019.

Thomas Foken. 50 years of the monin–obukhov similarity theory. *Boundary-Layer Meteorology*, 119(3):431–447, 2006.

JRD Francis. Wind stress on a water surface. *Q J R Meteorol Soc*, 80(345):438–443, 1954. doi: 10.1002/qj.49708034514.

Barry A Gardiner. Wind and wind forces in a plantation spruce forest. *Boundary-Layer Meteorology*, 67(1-2):161–186, 1994.

JR Garratt and BB Hicks. Micrometeorological and pbl experiments in australia. *Boundary-layer meteorology*, 50(1-4):11–29, 1990.

JR Gemmrich, TD Mudge, and VD Polonichko. On the energy input from wind to surface waves. *J Phys Oceanogr*, 24(11):2413–2417, 1994. doi: 10.1175/1520-0485(1994)024<2413:OTEIFW>2.0.CO;2.

PR Gent and PA Taylor. A numerical model of the air flow above water waves. *Journal of Fluid Mechanics*, 77(1):105–128, 1976.

G Gioia and FA Bombardelli. Scaling and similarity in rough channel flows. *Physical review letters*, 88(1):014501, 2001.

Gustavo Gioia, Nicholas Guttenberg, Nigel Goldenfeld, and Pinaki Chakraborty. Spectral theory of the turbulent mean-velocity profile. *Physical review letters*, 105(18):184501, 2010.

Laurent Grare, Luc Lenain, and W Kendall Melville. Wave-coherent airflow and critical layers over ocean waves. *J Phys Oceanogr*, 43(10):2156–2172, 2013. doi: 10.1175/JPO-D-13-056.1.

Laurent Grare, Luc Lenain, and W Kendall Melville. Vertical profiles of the wave-induced airflow above ocean surface waves. *Journal of Physical Oceanography*, 48(12):2901–2922, 2018. doi: 10.1175/JPO-D-18-0121.1.

Semyon A. Grodsky, Vladimir N. Kudryavtsev, Abderrahim Bentamy, James A. Carton, and Bertrand Chapron. Does direct impact of SST on short wind waves matter for scatterometry? *Geophys Res Lett*, 39(12), jun 2012. doi: 10.1029/2012gl052091. URL https://doi.org/10.1029%2F2012gl052091.

Xuanting Hao and Lian Shen. Wind–wave coupling study using les of wind and phase-resolved simulation of nonlinear waves. *J Fluid Mech*, 874:391–425, 2019. doi: 10.1017/jfm.2019.444.

Tetsu Hara and Stephen E Belcher. Wind forcing in the equilibrium range of wind-wave spectra. *J Fluid Mech*, 470:223–245, 2002. doi: 10.1017/S0022112002001945.

Tetsu Hara and Stephen E Belcher. Wind profile and drag coefficient over mature ocean surface wave spectra. *J Phys Oceanogr*, 34(11):2345–2358, 2004. doi: 10.1175/JPO2633.1.

Tetsu Hara and Peter P Sullivan. Wave boundary layer turbulence over surface waves in a strongly forced condition. *J Phys Oceanogr*, 45(3):868–883, 2015. doi: 10.1175/JPO-D-14-0116.1.

Ian N Harman and John J Finnigan. A simple unified theory for flow in the canopy and roughness sublayer. *Boundary-Layer Meteorol*, 123(2):339–363, 2007. doi: 10.1007/s10546-006-9145-6.

Klaus Hasselmann, TP Barnett, E Bouws, H Carlson, DE Cartwright, K Enke, JA Ewing, H Gienapp, DE Hasselmann, P Kruseman, et al. Measurements of wind-wave growth and swell decay during the joint north sea wave project (jonswap). *Ergänzungsheft 8-12*, 1973.

W Heisenberg. On the theory of statistical and isotropic turbulence. *Proceedings of the Royal Society of London. Series A. Mathematical and Physical Sciences*, 195(1042):402–406, 1948. doi: 10.1098/rspa.1948.0127.

Tihomir Hristov. Mechanistic, empirical and numerical perspectives on wind-waves interaction. In *Procedia IUTAM*, volume 26, pages 102–111. Elsevier B.V., 2018. doi: 10.1016/j.piutam.2018.03.010.

Tihomir Hristov and Jesus Ruiz-Plancarte. Dynamic balances in a wavy boundary layer. *J Phys Oceanogr*, 44(12):3185–3194, 2014. doi: 10.1175/JPO-D-13-0209.1.

Tihomir Hristov, Carl Friehe, and Scott Miller. Wave-coherent fields in air flow over ocean waves: Identification of cooperative behavior buried in turbulence. *Phys Rev Lett*, 81(23): 5245, 1998. doi: 10.1103/PhysRevLett.81.5245.

TS Hristov, SD Miller, and CA Friehe. Dynamical coupling of wind and ocean waves through wave-induced air flow. *Nature*, 422(6927):55, 2003. doi: 10.1038/nature01382.

Julian CR Hunt and Jonathan F Morrison. Eddy structure in turbulent boundary layers. *European Journal of Mechanics-B/Fluids*, 19(5):673–694, 2000.

Nyla Husain, Tetsu Hara, Marc Buckley, Kianoosh Yousefi, Fabrice Veron, and Peter Sullivan. Boundary layer turbulence over surface waves in a strongly forced condition: Les and observation. *J Phys Oceanogr*, (2019), 2019. doi: 10.1175/JPO-D-19-0070.1.

SJ Jacobs. An asymptotic theory for the turbulent flow over a progressive water wave. *J Fluid Mech*, 174:69–80, 1987. doi: 10.1017/S0022112087000041.

Peter A. E. M. Janssen. Quasilinear approximation for the spectrum of wind-generated water waves. *J Fluid Mech*, 117:493–506, 1982. doi: 10.1017/S0022112082001736.

Peter a. E. M. Janssen. Wave-Induced Stress and the Drag of Air Flow over Sea Waves. *J Phys Oceanogr*, 19(6):745–754, 1989. doi: 10.1175/1520-0485(1989)019<0745:WISATD>2.0.CO;2.

Peter AEM Janssen. Quasi-linear theory of wind-wave generation applied to wave forecasting. *J Phys Oceanogr*, 21(11):1631–1642, 1991. doi: 10.1175/1520-0485(1991)021<1631:QLTOWW>2.0.CO;2.

Peter AEM Janssen. On the effect of ocean waves on the kinetic energy balance and consequences for the inertial dissipation technique. *J Phys Oceanogr*, 29(3):530–534, 1999. doi: 10.1175/1520-0485(1999)029<0530:OTEOOW>2.0.CO;2.

Peter AEM Janssen. *The interaction of ocean waves and wind*. Cambridge University Press, 2004.

PG Jarvis. Coniferous forest. *Vegetation and the Atmosphere*, 2:171–240, 1976.

Harold Jeffreys. On the formation of water waves by wind. *Proceedings of the Royal Society of London. Series A, Containing Papers of a Mathematical and Physical Character*, 107(742): 189–206, 1925. doi: 10.1098/rspa.1925.0015.

Qingfang Jiang, Peter Sullivan, Shouping Wang, James Doyle, and Linwood Vincent. Impact of swell on air–sea momentum flux and marine boundary layer under low-wind conditions. *Journal of the Atmospheric Sciences*, 73(7):2683–2697, 2016.

Javier Jiménez. The physics of wall turbulence. *Physica A: Statistical Mechanics and its Applications*, 263(1-4):252–262, 1999.

Javier Jiménez. Turbulent flows over rough walls. *Annu. Rev. Fluid Mech.*, 36:173–196, 2004.

Javier Jiménez. Cascades in wall-bounded turbulence. *Annual Review of Fluid Mechanics*, 44: 27–45, 2012.

Javier Jiménez. Coherent structures in wall-bounded turbulence. *Journal of Fluid Mechanics*, 842, 2018.

Javier Jiménez and Parviz Moin. The minimal flow unit in near-wall turbulence. *Journal of Fluid Mechanics*, 225:213–240, 1991.

Ian SF Jones, Yoshiaki Toba, et al. *Wind stress over the ocean*. Cambridge University Press, 2001.

J C Kaimal, JCJ Wyngaard, Y Izumi, and OR Coté. Spectral characteristics of surface-layer turbulence. *Quarterly Journal of the Royal Meteorological Society*, 98(417):563–589, 1972.

Jagadish Chandran Kaimal and John J Finnigan. *Atmospheric boundary layer flows: their structure and measurement*. Oxford university press, 1994.

Gabriel Katul and Brani Vidakovic. The partitioning of attached and detached eddy motion in the atmospheric surface layer using lorentz wavelet filtering. *Boundary-Layer Meteorology*, 77(2):153–172, 1996.

Gabriel G Katul and Costantino Manes. Cospectral budget of turbulence explains the bulk properties of smooth pipe flow. *Phys. Rev. E*, 90(6):063008, 2014. doi: 10.1103/PhysRevE.90.063008.

Gabriel G Katul, John D Albertson, Marc B Parlange, Cheng-I Hsieh, Paul S Conklin, John T Sigmon, and Ken R Knoerr. The "inactive" eddy motion and the large-scale turbulent pressure fluctuations in the dynamic sublayer. *Journal of the atmospheric sciences*, 53(17): 2512–2524, 1996.

Gabriel G Katul, Alexandra G Konings, and Amilcare Porporato. Mean velocity profile in a sheared and thermally stratified atmospheric boundary layer. *Physical review letters*, 107 (26):268502, 2011.

Gabriel G Katul, Amilcare Porporato, and Vladimir Nikora. Existence of k- 1 power-law scaling in the equilibrium regions of wall-bounded turbulence explained by heisenberg's eddy viscosity. *Physical Review E*, 86(6):066311, 2012.

Gabriel G Katul, Amilcare Porporato, Costantino Manes, and Charles Meneveau. Co-spectrum and mean velocity in turbulent boundary layers. *Physics of Fluids*, 25(9):091702, 2013.

Gabriel G Katul, Amilcare Porporato, Stimit Shah, and Elie Bou-Zeid. Two phenomenological constants explain similarity laws in stably stratified turbulence. *Physical Review E*, 89(2): 023007, 2014.

Sanshiro Kawai. Visualization of airflow separation over wind-wave crests under moderate wind. *Boundary-Layer Meteorol*, 21(1):93–104, 1981.

H Kawamura and Y Toba. Ordered motion in the turbulent boundary layer over wind waves. *J Fluid Mech*, 197:105–138, 1988. doi: 10.1017/S0022112088003192.

N Kihara, H Hanazaki, T Mizuya, and H Ueda. Relationship between airflow at the critical height and momentum transfer to the traveling waves. *Phys Fluids*, 19(1):015102, 2007. doi: 10.1063/1.2409736.

SA Kitaigorodskii. On the theory of the equilibrium range in the spectrum of wind-generated gravity waves. *J Phys Oceanogr*, 13(5):816–827, 1983. doi: 10.1175/1520-0485(1983)013<0816:OTTOTE>2.0.CO;2.

SA Kitaigorodskii and Mark A Donelan. Wind-wave effects on gas transfer. In *Gas transfer at water surfaces*, pages 147–170. Springer, 1984. doi: 10.1007/978-94-017-1660-4_14.

Sergei Aleksandrovich Kitaigorodskii. *The physics of air-sea interaction*. 1973.

Sergej A Kitaigorodskii, Yury A Volkov, and Andrey A Grachev. A note on the analogy between momentum transfer across a rough solid surface and the air-sea interface. *Boundary-layer meteorology*, 76(1-2):181–197, 1995.

SJ Kline and PW Runstadler. Some preliminary results of visual studies of the flow model of the viscous sublayer. *J. Appl. Mech*, 2:166, 1959.

EB Kraus. Wind stress along the sea surface. *Advances in Geophysics*, 12:213–255, 1967.

V. Kudryavtsev, B. Chapron, and V. Makin. Impact of wind waves on the air-sea fluxes: A coupled model. *J Geophys Res Oceans*, 46(2):1022–1037, 2014. doi: 10.1002/2013JC009412.

V. N. Kudryavtsev and V. K. Makin. Impact of swell on the marine atmospheric boundary layer. *J Phys Oceanogr*, (4):934–949, 2004. ISSN 0022-3670. doi: 10.1175/1520-0485(2004)034<0934:IOSOTM>2.0.CO;2.

V. N. Kudryavtsev, V. K. Makin, and B. Chapron. Coupled sea surface-atmosphere model: 2. Spectrum of short wind waves. *J Geophys Res*, 104(C4):7625, 1999. ISSN 0148-0227. doi: 10.1029/1999JC900005.

Vladimir Kudryavtsev and Bertrand Chapron. On growth rate of wind waves: impact of short-scale breaking modulations. *J Phys Oceanogr*, 46(1):349–360, 2016. doi: 10.1175/JPO-D-14-0216.1.

Vladimir Kudryavtsev, Alexander Myasoedov, Bertrand Chapron, Johnny A. Johannessen, and Fabrice Collard. Imaging mesoscale upper ocean dynamics using synthetic aperture radar and optical data. *J Geophys Res Oceans*, 117(C4):n/a–n/a, apr 2012. doi: 10.1029/2011jc007492. URL https://doi.org/10.1029%2F2011jc007492.

VN Kudryavtsev and VK Makin. The impact of air-flow separation on the drag of the sea surface. *Boundary-Layer Meteorol*, 98(1):155–171, 2001. doi: 10.1023/A:1018719917275.

Tobias Kukulka and Tetsu Hara. The effect of breaking waves on a coupled model of wind and ocean surface waves. part i: Mature seas. *Journal of physical oceanography*, 38(10): 2145–2163, 2008a. doi: 10.1175/2008JPO3961.1.

Tobias Kukulka and Tetsu Hara. The effect of breaking waves on a coupled model of wind and ocean surface waves. part ii: Growing seas. *J Phys Oceanogr*, 38(10):2164–2184, 2008b. doi: 10.1175/2008JPO3962.1.

Tobias Kukulka, Tetsu Hara, and Stephen E Belcher. A model of the air–sea momentum flux and breaking-wave distribution for strongly forced wind waves. *J Phys Oceanogr*, 37(7): 1811–1828, 2007. doi: 10.1175/JPO3084.1.

John E Kutzbach. Investigations of the modification of wind profiles by artificially controlled surface roughness. *Studies of the Three Dimensional Structure of the Planetary Boundary Layer*, pages 71–113, 1961.

Christine Lac, Pierre Chaboureau, Valéry Masson, Pierre Pinty, Pierre Tulet, Juan Escobar, Maud Leriche, Christelle Barthe, Benjamin Aouizerats, Clotilde Augros, et al. Overview of the meso-nh model version 5.4 and its applications. *Geoscientific Model Development*, 11: 1929–1969, 2018.

Jean Philippe Lafore, Joël Stein, Nicole Asencio, Philippe Bougeault, Véronique Ducrocq, Jacqueline Duron, Claude Fischer, Philippe Héreil, Patrick Mascart, Valéry Masson, et al. The meso-nh atmospheric simulation system. part i: Adiabatic formulation and control simulations. In *Annales geophysicae*, volume 16, pages 90–109. Springer, 1997.

LD Landau and EM Lifshitz. *Fluid mechanics*. (Addisort-Wesley, 1959.

Brian Edward Launder, G Jr Reece, and W Rodi. Progress in the development of a reynolds-stress turbulence closure. *Journal of fluid mechanics*, 68(3):537–566, 1975.

CE Leith. Diffusion approximation to inertial energy transfer in isotropic turbulence. *The Physics of Fluids*, 10(7):1409–1416, 1967.

Margaret A LeMone, Wayne M Angevine, Christopher S Bretherton, Fei Chen, Jimy Dudhia, Evgeni Fedorovich, Kristina B Katsaros, Donald H Lenschow, Larry Mahrt, Edward G Patton, et al. 100 years of progress in boundary layer meteorology. *Meteorological Monographs*, 59: 9–1, 2019. doi: 10.1175/AMSMONOGRAPHS-D-18-0013.1.

H_ Lettau. Note on aerodynamic roughness-parameter estimation on the basis of roughness-element description. *Journal of applied meteorology*, 8(5):828–832, 1969.

Dan Li. Turbulent prandtl number in the atmospheric boundary layer-where are we now? *Atmospheric Research*, 216:86–105, 2019.

Dan Li, Gabriel G Katul, and Elie Bou-Zeid. Mean velocity and temperature profiles in a sheared diabatic turbulent boundary layer. *Phys Fluids*, 24(10):105105, 2012. doi: 10.1063/1.4757660.

Dan Li, Gabriel G Katul, and Elie Bou-Zeid. Turbulent energy spectra and cospectra of momentum and heat fluxes in the stable atmospheric surface layer. *Boundary-layer meteorology*, 157(1):1–21, 2015.

Dan Li, Scott T Salesky, and Tirtha Banerjee. Connections between the ozmidov scale and mean velocity profile in stably stratified atmospheric surface layers. *Journal of Fluid Mechanics*, 797, 2016.

Qi Li, Pierre Gentine, Juan Pedro Mellado, and Kaighin A McColl. Implications of nonlocal transport and conditionally averaged statistics on monin–obukhov similarity theory and townsend's attached eddy hypothesis. *J Atmos Sci*, 75(10):3403–3431, 2018. doi: 10.1175/JAS-D-17-0301.1.

MJ Lighthill. Physical interpretation of the mathematical theory of wave generation by wind. *J Fluid Mech*, 14(3):385–398, 1962. doi: 10.1017/S0022112062001305.

Michael S Longuet-Higgins. Action of a variable stress at the surface of water waves. *Phys Fluids*, 12(4):737–740, 1969a. doi: 10.1063/1.1692549.

Michael Selwyn Longuet-Higgins. A nonlinear mechanism for the generation of sea waves. *Proceedings of the Royal Society of London. A. Mathematical and Physical Sciences*, 311 (1506):371–389, 1969b. doi: 10.1098/rspa.1969.0123.

Michael Selwyn Longuet-Higgins. A stochastic model of sea-surface roughness. i. wave crests. *Proceedings of the Royal Society of London. A. Mathematical and Physical Sciences*, 410 (1838):19–34, 1987. doi: 10.1098/rspa.1987.0026.

Adrián Lozano-Durán and Javier Jiménez. Time-resolved evolution of coherent structures in turbulent channels: characterization of eddies and cascades. *Journal of fluid mechanics*, 759: 432–471, 2014.

Adrián Lozano-Durán, Oscar Flores, and Javier Jiménez. The three-dimensional structure of momentum transfer in turbulent channels. *Journal of Fluid Mechanics*, 694:100–130, 2012.

VK Makin and VN Kudryavtsev. Coupled sea surface-atmosphere model: 1. wind over waves coupling. *J Geophys Res Oceans*, 104(C4):7613–7623, 1999. doi: 10.1029/1999JC900006.

VK Makin and C Mastenbroek. Impact of waves on air-sea exchange of sensible heat and momentum. *Boundary-Layer Meteorol*, 79(3):279–300, 1996. doi: 10.1007/BF00119442.

VK Makin, VN Kudryavtsev, and C Mastenbroek. Drag of the sea surface. *Boundary-Layer Meteorol*, 73(1-2):159–182, 1995. doi: 10.1007/BF00708935.

I Marusic, R Mathis, and N Hutchins. Predictive model for wall-bounded turbulent flow. *Science*, 329(5988):193–196, 2010.

Ivan Marusic and Jason P Monty. Attached eddy model of wall turbulence. *Annual Review of Fluid Mechanics*, 51:49–74, 2019.

C Mastenbroek, VK Makin, MH Garat, and Jean-Paul Giovanangeli. Experimental evidence of the rapid distortion of turbulence in the air flow over water waves. *Journal of Fluid Mechanics*, 318:273–302, 1996. doi: 10.1017/S0022112096007124.

Jan F Meirink and Vladimir K Makin. Modelling low-reynolds-number effects in the turbulent air flow over water waves. *J Fluid Mech*, 415:155–174, 2000. doi: 10.1017/S0022112000008624.

GL Mellor and T Yamada. Development of a turbulence closure model for geophysical fluid problems. *Reviews of Geophysics*, 20(4):851–875, 1982.

W Kendall Melville. The role of surface-wave breaking in air-sea interaction. *Annual review of fluid mechanics*, 28(1):279–321, 1996. doi: 10.1146/annurev.fl.28.010196.001431.

W Kendall Melville. Wind-wave breaking. *Procedia IUTAM*, 26:30–42, 2018.

WK Melville. Wind stress and roughness length over breaking waves. *Journal of Physical Oceanography*, 7(5):702–710, 1977. doi: 10.1175/1520-0485(1977)007<0702:WSARLO>2.0.CO;2.

John Miles. Surface-wave generation revisited. *J Fluid Mech*, 256:427–441, 1993. doi: 10.1017/S0022112093002836.

John W Miles. On the generation of surface waves by shear flows. *Journal of Fluid Mechanics*, 3(2):185–204, 1957. doi: 10.1017/S0022112057000567.

John W Miles. On the generation of surface waves by shear flows. part 2. *Journal of Fluid Mechanics*, 6(4):568–582, 1959. doi: 10.1017/S0022112059000830.

John W Miles. A note on the interaction between surface waves and wind profiles. *Journal of Fluid Mechanics*, 22(4):823–827, 1965. doi: 10.1017/S0022112065001167.

AS Monin and AM Obukhov. Basic laws of turbulent mixing in the surface layer of the atmosphere. *Contrib. Geophys. Inst. Acad. Sci. USSR*, 151(163):e187, 1954.

James A Mueller and Fabrice Veron. Nonlinear formulation of the bulk surface stress over breaking waves: Feedback mechanisms from air-flow separation. *Boundary-Layer Meteorol*, 130(1):117, 2009. doi: 0.1007/s10546-008-9334-6.

Walter Munk. An inconvenient sea truth: Spread, steepness, and skewness of surface slopes. *Annual review of marine science*, 1:377–415, 2009. doi: 10.1146/annurev.marine.010908.163940.

WH Munk. Wind stress on water: An hypothesis. *Q J R Meteorol Soc*, 81(349):320–332, 1955. doi: 10.1002/qj.49708134903.

Alan C Newell and Vladimir E Zakharov. Rough sea foam. *Physical review letters*, 69(8):1149, 1992.

J Nikuradse. Stromungsgesetz in rauhren rohren, vdi forschungshefte 361. *English translation: Laws of flow in rough pipes). Technical report, NACA Technical Memorandum*, 1292, 1933.

A Obukhov. Turbulence in thermally inhomogeneous atmosphere. *Trudy Inst. Teor. Geofiz. Akad. Nauk SSSR*, 1:95–115, 1946.

A. M. Obukhov. Turbulence in an atmosphere with a non-uniform temperature. *Boundary-Layer Meteorol.*, 2(1):7–29, 1971. ISSN 00068314. doi: 10.1007/BF00718085.

AM Obukhov. On the distribution of energy in the spectrum of turbulent flow. *Bull. Acad. Sci. USSR, Geog. Geophys.*, 5:453–466, 1941.

Kuniaki Okuda, Sanshiro Kawai, and Yoshiaki Toba. Measurement of skin friction distribution along the surface of wind waves. *Journal of the Oceanographical Society of Japan*, 33(4): 190–198, 1977.

David G Ortiz-Suslow and Qing Wang. An evaluation of kolmogorov's-5/3 power law observed within the turbulent airflow above the ocean. *Geophys Res Lett*, 2019. doi: 10.1029/2019GL085083.

S. Panchev. *Random Functions and Turbulence*, volume 32. Elsevier, 1971. doi: 10.1016/C2013-0-02360-2.

HA Panofsky. An alternative derivation of the diabatic wind profile. *Quarterly Journal of the Royal Meteorological Society*, 87(371):109–110, 1961.

Hans A Panofsky. Determination of stress from wind and temperature measurements. *Q J R Meteorol Soc*, 89(379):85–94, 1963. doi: 10.1002/qj.49708937906.

AE Perry and CJ Abell. Asymptotic similarity of turbulence structures in smooth-and rough-walled pipes. *Journal of Fluid Mechanics*, 79(4):785–799, 1977.

Anthony Edward Perry, William H Schofield, and Peter N Joubert. Rough wall turbulent boundary layers. *Journal of Fluid Mechanics*, 37(2):383–413, 1969.

Oliver M Phillips. The equilibrium range in the spectrum of wind-generated waves. *J Fluid Mech*, 4(4):426–434, 1958. doi: 10.1017/S0022112058000550.

OM Phillips. Spectral and statistical properties of the equilibrium range in wind-generated gravity waves. *J Fluid Mech*, 156:505–531, 1985. doi: 10.1017/S0022112085002221.

Owen M Phillips. On the generation of waves by turbulent wind. *J Fluid Mech*, 2(5):417–445, 1957. doi: 10.1017/S0022112057000233.

Owen M Phillips. *The dynamics of the upper ocean*. Cambridge University Press, 1977.

William J. Plant. A relationship between wind stress and wave slope. *J Geophys Res Oceans*, 87(C3):1961–1967, 1982. ISSN 2156-2202. doi: 10.1029/JC087iC03p01961.

SB Pope. *Turbulent flows*. Cambridge university press, 2000.

Nicolas Rascle, Frederic Nouguier, Bertrand Chapron, Alexis Mouche, and Aurélien Ponte. Surface roughness changes by finescale current gradients: properties at multiple azimuth view angles. *J Phys Oceanogr*, 46(12):3681–3694, 2016.

M. R. Raupach, R. A. Antonia, and S. Rajagopalan. Rough-Wall Turbulent Boundary Layers. *Applied Mechanics Reviews*, 44(1):1–25, 01 1991. ISSN 0003-6900. doi: 10.1115/1.3119492. URL https://doi.org/10.1115/1.3119492.

M_R Raupach, JJ Finnigan, and Y Brunet. Coherent eddies and turbulence in vegetation canopies: the mixing-layer analogy. In *Boundary-layer meteorology 25th anniversary volume, 1970–1995*, pages 351–382. Springer, 1996.

Nicolas Reul, Hubert Branger, and J-P Giovanangeli. Air flow separation over unsteady breaking waves. *Phys Fluids*, 11(7):1959–1961, 1999. doi: 10.1063/1.870058.

Nicolas Reul, Hubert Branger, and Jean-Paul Giovanangeli. Air flow structure over short-gravity breaking water waves. *Boundary-Layer Meteorol*, 126(3):477–505, 2008. doi: 10.1007/s10546-007-9240-3.

VP Reutov. The plasma-hydrodynamic analogy and the nonlinear stage of wind-wave instability. *Akademiia Nauk SSSR, Izvestiia, Fizika Atmosfery i Okeana*, 16:1266–1275, 1980.

Stephen K Robinson. Coherent motions in the turbulent boundary layer. *Annual Review of Fluid Mechanics*, 23(1):601–639, 1991. doi: 10.1146/annurev.fl.23.010191.003125.

JC Rotta. Statistische theorie nichthomogener turbulenz. *Zeitschrift für Physik*, 129(6):547–572, 1951.

Seyed G Saddoughi and Srinivas V Veeravalli. Local isotropy in turbulent boundary layers at high reynolds number. *Journal of Fluid Mechanics*, 268:333–372, 1994.

Scott T Salesky, Gabriel G Katul, and Marcelo Chamecki. Buoyancy effects on the integral lengthscales and mean velocity profile in atmospheric surface layer flows. *Physics of Fluids*, 25(10):105101, 2013.

William D Sellers. A simplified derivation of the diabatic wind profile. *Journal of the Atmospheric Sciences*, 19(2):180–181, 1962.

Tomoya Shimura, Nobuhito Mori, Tetsuya Takemi, and Ryo Mizuta. Long-term impacts of ocean wave-dependent roughness on global climate systems. *J Geophys Res Oceans*, 122(3): 1995–2011, 2017. doi: 10.1002/2016jc012621.

Anna Sjöblom and Ann-Sofi Smedman. The turbulent kinetic energy budget in the marine atmospheric surface layer. *J Geophys Res Oceans*, 107(C10):6–1, 2002. doi: 10.1029/2001JC001016.

Alexander J Smits, Beverley J McKeon, and Ivan Marusic. High–reynolds number wall turbulence. *Annual Review of Fluid Mechanics*, 43, 2011.

Alexander V Soloviev, Roger Lukas, Mark A Donelan, Brian K Haus, and Isaac Ginis. The air-sea interface and surface stress under tropical cyclones. *Sci. Rep.*, 4:5306, 2014. doi: 10.1038/srep05306.

Yu P Soloviev and VN Kudryavtsev. Wind-speed undulations over swell: Field experiment and interpretation. *Boundary-Layer Meteorol*, 136(3):341–363, 2010. doi: 10.1007/s10546-010-9506-z.

DT Squire, WJ Baars, N Hutchins, and I Marusic. Inner–outer interactions in rough-wall turbulence. *Journal of Turbulence*, 17(12):1159–1178, 2016.

DT Squire, N Hutchins, C Morrill-Winter, MP Schultz, JC Klewicki, and I Marusic. Applicability of taylor's hypothesis in rough-and smooth-wall boundary layers. *Journal of Fluid Mechanics*, 812:398–417, 2017.

Sricharan Srinath, JC Vassilicos, Christophe Cuvier, J-P Laval, Michel Stanislas, and J-M Foucaut. Attached flow structure and streamwise energy spectra in a turbulent boundary layer. *Physical review E*, 97(5):053103, 2018.

Richard JAM Stevens, Michael Wilczek, and Charles Meneveau. Large-eddy simulation study of the logarithmic law for second-and higher-order moments in turbulent wall-bounded flow. *Journal of fluid mechanics*, 757:888–907, 2014.

RW Stewart. The wave drag of wind over water. *Journal of fluid mechanics*, 10(2):189–194, 1961. doi: 10.1017/S0022112061000172.

RW Stewart. The air-sea momentum exchange. *Boundary-Layer Meteorol*, 6(1-2):151–167, 1974. doi: 10.1007/BF00232481.

Peter P Sullivan and James C McWilliams. Dynamics of winds and currents coupled to surface waves. *Annual Review of Fluid Mechanics*, 42, 2010. doi: 10.1146/annurev-fluid-121108-145541.

Peter P Sullivan, James C McWilliams, and Chin-Hoh Moeng. Simulation of turbulent flow over idealized water waves. *J Fluid Mech*, 404:47–85, 2000. doi: 10.1017/S0022112099006965.

Peter P Sullivan, James B Edson, Tihomir Hristov, and James C McWilliams. Large-eddy simulations and observations of atmospheric marine boundary layers above nonequilibrium surface waves. *J Atmos Sci*, 65(4):1225–1245, 2008. doi: 10.1175/2007JAS2427.1.

Peter P Sullivan, James C McWilliams, and Edward G Patton. Large-eddy simulation of marine atmospheric boundary layers above a spectrum of moving waves. *J Atmos Sci*, 71(11): 4001–4027, 2014. doi: 10.1175/JAS-D-14-0095.1.

Peter Sutherland and W Kendall Melville. Field measurements and scaling of ocean surface wave-breaking statistics. *Geophys Res Lett*, 40(12):3074–3079, 2013. doi: 10.1002/grl.50584.

Nobuhiro Suzuki, Tetsu Hara, and Peter P Sullivan. Turbulent airflow at young sea states with frequent wave breaking events: Large-eddy simulation. *J Atmos Sci*, 68(6):1290–1305, 2011. doi: 10.1175/2011JAS3619.1.

Nobuhiro Suzuki, Tetsu Hara, and Peter P Sullivan. Impact of breaking wave form drag on near-surface turbulence and drag coefficient over young seas at high winds. *J Phys Oceanogr*, 43(2):324–343, 2013. doi: 10.1175/jpo-d-12-0127.1.

Geoffrey Ingram Taylor. The spectrum of turbulence. *Proceedings of the Royal Society of London. Series A-Mathematical and Physical Sciences*, 164(919):476–490, 1938.

Chan-Mou Tchen. Transport processes as foundations of the heisenberg and obukhoff theories of turbulence. *Physical Review*, 93(1):4, 1954.

CM Tchen. On the spectrum of energy in turbulent shear flow. *Journal of Research of the National Bureau of Standards*, 50(1):51–62, 1953.

H Tennekes. Free convection in the turbulent ekman layer of the atmosphere. *Journal of the Atmospheric Sciences*, 27(7):1027–1034, 1970.

H Tennekes. The logarithmic wind profile. *Journal of the Atmospheric Sciences*, 30(2):234–238, 1973.

William Thomson. Hydrokinetic solutions and observations. *Phil. Mag*, 42(281):362–377, 1871.

AA Townsend. Equilibrium layers and wall turbulence. *Journal of Fluid Mechanics*, 11(1): 97–120, 1961.

AA Townsend. Flow in a deep turbulent boundary layer over a surface distorted by water waves. *J Fluid Mech*, 55(4):719–735, 1972. doi: 10.1017/S0022112072002101.

AAR Townsend. *The structure of turbulent shear flow*. Cambridge university press, 1976.

F Ursell. Wave generation by wind. *Surveys in mechanics*, pages 216–249, 1956.

Cornelis A. Van Duin and Peter A. E. M. Janssen. An analytic model of the generation of surface gravity waves by turbulent air flow. *J Fluid Mech*, 236:197–215, 1992. doi: 10.1017/S0022112092001393.

Douglas Vandemark, James B Edson, and Bertrand Chapron. Altimeter estimation of sea surface wind stress for light to moderate winds. *J Atmos Ocean Technol*, 14(3):716–722, 1997. doi: 10.1175/1520-0426(1997)014<0716:AEOSSW>2.0.CO;2.

Douglas Vandemark, Bertrand Chapron, J Sun, Graber H Crescenti, and Hans C Graber. Ocean wave slope observations using radar backscatter and laser altimeters. *J Phys Oceanogr*, 34 (12):2825–2842, 2004. doi: 10.1175/JPO2663.1.

Fabrice Veron, G Saxena, and SK Misra. Measurements of the viscous tangential stress in the airflow above wind waves. *Geophysical Research Letters*, 34(19), 2007. doi: 10.1029/2007GL031242.

Fabrice Veron, W Kendall Melville, and Luc Lenain. Wave-coherent air–sea heat flux. *J Phys Oceanogr*, 38(4):788–802, 2008. doi: 10.1175/2007JPO3682.1.

Ana Beatriz Villas Boas, Fabrice Ardhuin, Alex Ayet, Mark A Bourassa, Betrand Chapron, Peter Brandt, Bruce D Cornuelle, J Thomas Farrar, Melanie R Fewings, Baylor Fox-Kemper, et al. Integrated observations of global surface winds, currents, and waves: requirements and challenges for the next decade. *Frontiers in Marine Science*, 6:425, 2019. doi: 10.3389/fmars.2019.00425.

James M Wallace. Space-time correlations in turbulent flow: A review. *Theoretical and Applied Mechanics Letters*, 4(2):022003, 2014.

Chen Wang, Pierre Tandeo, Alexis Mouche, Justin E Stopa, Victor Gressani, Nicolas Longepe, Douglas Vandemark, Ralph C Foster, and Bertrand Chapron. Classification of the global sentinel-1 sar vignettes for ocean surface process studies. *Remote Sensing of Environment*, 234:111457, 2019.

Michael Wilczek, Richard JAM Stevens, and Charles Meneveau. Spatio-temporal spectra in the logarithmic layer of wall turbulence: large-eddy simulations and simple models. *J Fluid Mech*, 769, 2015.

N Robert Wilson and Roger H Shaw. A higher order closure model for canopy flow. *Journal of Applied Meteorology*, 16(11):1197–1205, 1977. doi: 10.1175/1520-0450(1977)016<1197:AHOCMF>2.0.CO;2.

John C Wyngaard. On the surface-layer turbulence. In *Workshop on micrometeorology*, pages 101–149. Amer. Meteorol. Soc., 1973.

John C Wyngaard. Atmospheric turbulence. *Annual Review of Fluid Mechanics*, 24(1):205–234, 1992.

John C Wyngaard. *Turbulence in the Atmosphere*. Cambridge University Press, 2010.

Di Yang and Lian Shen. Characteristics of coherent vortical structures in turbulent flows over progressive surface waves. *Phys Fluids*, 21(12):125106, 2009. doi: 10.1063/1.3275851.

Di Yang and Lian Shen. Direct-simulation-based study of turbulent flow over various waving boundaries. *Journal of Fluid Mechanics*, 650:131–180, 2010. doi: 10.1017/S0022112009993557.

MV Yurovskaya, VA Dulov, Bertrand Chapron, and VN Kudryavtsev. Directional short wind wave spectra derived from the sea surface photography. *J Geophys Res Oceans*, 118(9): 4380–4394, 2013. doi: 10.1002/jgrc.20296.

Vladimir Evgen'evich Zakharov and NN Filonenko. Energy spectrum for stochastic oscillations of the surface of a liquid. In *Doklady Akademii Nauk*, volume 170, pages 1292–1295. Russian Academy of Sciences, 1966.

O Zeman and H Tennekes. A self-contained model for the pressure terms in the turbulent stress equations of the neutral atmospheric boundary layer. *Journal of the Atmospheric Sciences*, 32(9):1808–1813, 1975.

Sergej S Zilitinkevich, JCR Hunt, Igor N Esau, AA Grachev, DP Lalas, Evangelos Akylas, M Tombrou, CW Fairall, HJS Fernando, AA Baklanov, et al. The influence of large convective eddies on the surface-layer turbulence. *Quarterly Journal of the Royal Meteorological Society: A journal of the atmospheric sciences, applied meteorology and physical oceanography*, 132(618):1426–1456, 2006.

SS Zilitinkevich, T Elperin, N Kleeorin, I Rogachevskii, I Esau, Thorsten Mauritsen, and MW Miles. Turbulence energetics in stably stratified geophysical flows: Strong and weak mixing regimes. *Q J R Meteorol Soc*, 134(633):793–799, 2008. doi: 10.1002/qj.264.

DOCTORAT SCIENCES BRETAGNE DE LA MER LOIRE ET DU LITTORAL

UBO Université de Bretagne Occidentale

Titre : Flux de quantité de mouvement à l'interface air-mer : approche théorique du couplage entre turbulence et vagues de vent

Mots clés : flux de quantité de mouvement, turbulence proche de paroi, budgets spectraux, vagues de vent, génération de vagues, interactions air-mer.

Résumé : Malgré de nombreuses études, le lien de causalité entre vent et vagues fait toujours l'objet de controverses : cela est dû entre autres au caractère multi-échelle d'une surface océanique réaliste, et à la présence de déferlements, qui modifient radicalement sa topologie. Dans cette thèse, ces deux questions sont abordées sous un angle théorique, à travers un modèle phénoménologique, qui relie les propriétés spectrales et moyennées de la turbulence proche de paroi en utilisant la géométrie de tourbillons attachés à celle-ci. La première partie de la thèse revisite ce modèle phénoménologique en questionnant ses hypothèses sous-jacentes et révèle, en particulier, des incohérences dans les modèles utilisés pour décrire le terme de redistribution d'énergie entre composantes turbulentes (modèle de Rotta). Le modèle phénoménologique est ensuite utilisé pour étudier le couplage entre vagues de vent longues (de l'ordre de 10m) et turbulence. Les résultats démontrent que la déformation des tourbillons attachés induite par cette interaction pourrait expliquer une partie de la variabilité des flux de quantité de mouvement à un vent moyen donné. Finalement, le couplage entre la turbulence et les vagues courtes et déferlantes est abordé en définissant une sous-couche rugueuse dans laquelle les proprietés des tourbillons attachés sont définies par la vitesse des fronts déferlants dominants pour un vent donné. Ces deux études posent les bases d'un nouveau paradigme, permettant d'étudier le couplage multi-échelle entre le spectre turbulent et le spectre des vagues. Celui-ci pourrait permettre de mieux prendre en compte l'influence de paramètres environnementaux sur les flux de quantité de mouvement et de chaleur. Il ouvre ainsi de nouvelles perspectives pour les études théoriques et pour l'exploration des données expérimentales.

Title : Air-sea momentum fluxes in the vicinity of the sea surface : a theoretical study of the coupling between turbulence and wind-waves

Keywords : momentum flux, wall-bounded turbulence, spectral budgets, wind-waves, wave generation, air-sea interactions

Abstract : Despite numerous works, the causal link between wind and waves is still a controversial subject. This is due, among others, to the multi-scale nature of a realistic ocean surface and to wave breaking, which changes its topology. In this thesis, such problems are studied from a theoretical perspective, using a phenomenological model linking the spectral and averaged properties of wall-bounded turbulence through the geometry attached eddies. The first part of the thesis revisits this phenomenological model by questioning its underlying assumptions and, in particular, reveals inconsistencies in the models used for the energy redistribution between turbulence components (the Rotta model). The phenomenological model is then used to study the coupling between long wind-waves (of order 10m) and turbulence . Results indicate that the deformation of attached eddies, induced by this interaction, could explain some of the variability in momentum fluxes for a given mean wind. Finally, the study of the coupling between turbulence and short breaking waves is approached by defining a roughness sublayer, in which the properties of the attached eddies depend solely on the speed of the dominant breaking fronts for a given wind. These two studies from the basis of a new paradigm to study the multi-scale coupling between the turbulent and wave spectra. This would allow accounting for the influence of environmental parameters on momentum and heat fluxes, and opens new paths both from a theoretical perspective and for the analysis of experimental data.